



**SUSANA CRISTINA
DOS SANTOS PINTO**

**DESENVOLVIMENTO E CARACTERIZAÇÃO DE
ESTRUTURAS HÍBRIDAS MULTIFUNCIONAIS
BASEADAS EM METAIS CELULARES**

**DEVELOPMENT AND CHARACTERIZATION OF
MULTIFUNCTIONAL HYBRID STRUCTURES BASED
ON CELLULAR METALS**



**SUSANA CRISTINA
DOS SANTOS PINTO**

**DESENVOLVIMENTO E CARACTERIZAÇÃO DE
ESTRUTURAS HÍBRIDAS MULTIFUNCIONAIS
BASEADAS EM METAIS CELULARES**

**DEVELOPMENT AND CHARACTERIZATION OF
MULTIFUNCTIONAL HYBRID STRUCTURES BASED
ON CELLULAR METALS**

Tese apresentada à Universidade de Aveiro para cumprimento dos requisitos necessários à obtenção do grau de Doutor em Engenharia Mecânica, realizada sob a orientação científica da Doutora Paula Alexandrina de Aguiar Pereira Marques, Investigadora Principal do Departamento de Engenharia Mecânica da Universidade de Aveiro e coorientação da Doutora Isabel Maria Alexandrino Duarte, Investigadora Auxiliar do Departamento de Engenharia Mecânica da Universidade de Aveiro e do Doutor Romeu da Silva Vicente, Professor Associado do Departamento de Engenharia Civil da Universidade de Aveiro.

This work was supported by the projects UIDB/00481/2020 and UIDP/00481/2020 - FCT - Fundação para a Ciência e a Tecnologia; and CENTRO-01-0145-FEDER-022083 - Centro Portugal Regional Operational Programme (Centro2020), under the PORTUGAL 2020 Partnership Agreement, through the European Regional Development Fund and FCT PhD Grant SFRH/BD/111515/2015

“Nothing under the sun is greater than education. By educating one person and sending him into the society of his generation, we make a contribution extending a hundred generations to come.”

Jigoro Kano

À minha família e amigos pelo incansável apoio.

o júri

presidente

Prof. Doutor Nuno Miguel Gonçalves Borges de Carvalho

Professor catedrático da Universidade de Aveiro

Prof.^a Doutora Ana Paula da Fonseca Piedade

Professora auxiliar da Faculdade de Ciências e Tecnologia da Universidade de Coimbra

Prof. Doutor António Joaquim Mendes Ferreira

Professor catedrático da Faculdade de Engenharia da Universidade do Porto

Prof. Doutor Nuno Ricardo Maia Peixinho

Professor auxiliar da Universidade do Minho

Prof. Doutor António Gil D'Orey de Andrade Campos

Professor auxiliar da Universidade de Aveiro

Doutora Paula Alexandrina de Aguiar Pereira Marques

Investigadora principal da Universidade de Aveiro (Orientadora)

agradecimentos

À Doutora Paula Marques e à Doutora Isabel Duarte pela disponibilidade, dedicação e partilha de conhecimentos, pelas palavras de incentivo que sempre me transmitiram e por me permitirem trabalhar num tema tão abrangente e desafiante. O meu muito obrigada por contribuírem para a minha evolução profissional e pessoal.

Ao Professor Romeu Vicente pela sua contribuição na análise de resultados e visão crítica.

Ao professor Julien Bras e a todo o grupo MatBio por me receberem no LGP2 - *Laboratoire Génie des Procédés Papetiers*, Grenoble, França.

Aos Doutores Ricardo Pinto, Nuno Henriques e à Doutora Carmen Feire do grupo CICECO da Universidade de Aveiro pela disponibilização da celulose bacteriana.

Ao Professor Matej Vesenjok da Universidade de Maribor (Eslovénia) e ao Doutor Lovre Krstulović-Opara da Universidade de Split (Croácia) pela realização de ensaios mecânicos.

Ao Professor Luís Godinho da Universidade de Coimbra pela sua disponibilidade na realização dos ensaios de absorção sonora.

À BCTECHNOLOGIES, Lda e à DOW Portugal pela disponibilização de matérias-primas.

Aos Engenheiros António Festas e Ricardo Beja pelo apoio técnico que prestaram na realização fabricação de peças e moldes.

À Vanessa e ao Gonzalo pela ajuda na realização dos ensaios de TGA e XPS.

Aos colegas do TEMA do edifício 3, em especial aos amigos de gabinete e laboratório, os que passaram pelo laboratório, os que ainda estão e os recém-chegados, Andreia, Eddy, Gil, Gonçalo, Joana. Obrigada pela ajuda, partilha de ideias e conhecimento, pelas palavras de encorajamento e especialmente pelas muitas e boas gargalhadas. Um agradecimento especial aos "Sempre a Bombar!" que me proporcionaram momentos inesquecíveis.

Ao André, pelas longas conversas, pelos passeios sem destino e pelas histórias fantásticas que tanto animaram os meus dias. À Ângela por toda a ajuda, especialmente nesta fase final, por me incentivar constantemente. Ao Nuno pela disponibilidade e paciência, pelas reconfortantes pausas para o café. À Nathalie por ouvir os meus desabaços e pelas palavras de incentivo.

Aos colegas de almoço, Alexandre, Richard e German.

Aos meus amigos de longa data, António, Cátia, Patrícia, Rita, Rui e Teresa, por mesmo longe, estarem disponíveis e aos amigos que fui fazendo durante esta jornada, Alex, Anabela, Andreia Ferreira, Ângela Cunha, Patrícia Rodrigues e Sandra.

À Universidade de Aveiro, ao Departamento de Engenharia Mecânica e ao Centro de Tecnologia Mecânica e Automação (TEMA). À Fundação para a Ciência e Tecnologia pelo suporte financeiro que me possibilitou o desenvolvimento deste doutoramento.

Finalmente à minha família, em especial aos meus pais e irmã pelos valores que me passaram, de dedicação, trabalho, solidariedade, amizade e amor.

palavras-chave

Estruturas híbridas multifuncionais, espumas abertas de alumínio, materiais poliméricos, grafeno e seus derivados, propriedades mecânicas, condutividade térmica, coeficiente de absorção de som, retardamento da chama

resumo

O interesse em materiais celulares aumentou significativamente nas últimas duas décadas, refletindo a crescente procura por estruturas leves e multifuncionais. A relação entre baixo peso e elevado desempenho mecânico, acústico e térmico, torna-os atrativos para aplicações em engenharia tais como civil, automóvel, aeroespacial, entre outras. As espumas metálicas de porosidade aberta (OCF) são materiais funcionais promissores caracterizados por baixo peso, elevada área superficial interna, reciclabilidade e inflamabilidade, no entanto são mecanicamente fracas. Os investigadores descobriram neste tópico uma oportunidade na exploração destes materiais, reforçando-os com polímeros de modo a melhorar o seu desempenho e diversificar a sua aplicação. No entanto, o trabalho desenvolvido neste campo ainda é escasso e focado principalmente no preenchimento dos poros das OCF com polímeros densos e na sua caracterização mecânica.

O objetivo deste trabalho incidiu no fabrico de diversas espumas híbridas tendo como base o preenchimento de OCF com diversos nanocompósitos poliméricos de modo a obter materiais multifuncionais, de preferência leves, fornecendo alternativas promissoras aos materiais que já existem no mercado. Foram selecionados para o preenchimento, celulose bacteriana (BC) e poliuretano (PUF) na forma de espumas, cortiça aglomerada e polidimetilsiloxano (PDMS) e epóxido (EP) como materiais densos.

Antes da incorporação na OCF, os materiais de preenchimento foram reforçados com materiais à base de grafeno (GBMs) nomeadamente óxido de grafeno (GO), óxido de grafeno reduzido (rGO) ou nanoplaquetas de grafeno (GNPs) de modo a melhorar as propriedades mecânicas, térmicas e acústicas e conferir a propriedade retardamento de chama. Globalmente, a adição de GBMs melhorou as propriedades mecânicas das espumas de BC e de PUF, mas diminuiu a resistência mecânica dos polímeros densos devido aos espaços vazios criados nas matrizes poliméricas. Adicionalmente, os GBMs utilizados não aumentaram consideravelmente a condutividade térmica, o que, para aplicações de isolamento pode ser uma mais valia. De referir a eficiência da presença dos GBMs como agentes de retardação de chama dos nanocompósitos.

Dada a variedade de propriedades dos materiais produzidos, as suas aplicações poderão ser múltiplas. As estruturas híbridas constituídas por OCF e materiais mais densos (PDMS ou EP) poderão ter aplicações como componentes estruturais, pois apresentam elevada resistência e boa capacidade de absorção de energia. As espumas híbridas resultantes do preenchimento das OCF com espumas nanocompósitas de BC ou PUF ou ainda aglomerados de cortiça com boas propriedades de isolamento acústico e térmico leveza poderão encontrar aplicações onde estas propriedades são requeridas.

keywords

Multifunctional hybrid structures, open-cell aluminium foams, polymers, graphene based materials, mechanical properties, thermal conductivity, sound absorption coefficient, fire-retardancy.

abstract

The interest in cellular materials has significantly increased in the last two decades, reflecting the growing demand for lightweight and multifunctional structures. The high stiffness-to-weight ratio and acoustic and thermal insulation features, make cellular materials attractive for many engineering applications such as civil, automotive, aerospace, amongst others. Open-cell metal foams (OCF) are one of the most promising functional materials characterized by high internal surface area, recyclability and non-flammability, however mechanically weaker. Researchers perceived this topic as an opportunity to explore these materials by reinforcing them with polymers in order to improve their performance. However, the work developed in this field is still scarce and mainly focused on filling the voids of OCF with dense polymers and on its mechanical characterization.

This work aims to fabricate novel hybrid structures by filling the voids of OCF with different polymers in order to obtain multifunctional hybrid structures, providing valuable alternatives for the materials that are available on the market. Several filling materials were selected, bacterial cellulose (BC) and polyurethanes (PUF) in the form of foams, agglomerated cork, and polydimethylsiloxane (PDMS) and epoxy (EP) as dense filling materials.

Prior to its incorporation within the OCF, the polymeric based filling materials were reinforced with graphene-based materials (GBMs) namely graphene oxide (GO), reduced graphene oxide (rGO) or graphene nanoplatelets in order to improve mechanical, thermal and acoustic properties and impart flame retardant property. Overall, the incorporation of GBMs into the polymeric based matrices improved the mechanical properties of the foamed polymers but decreased the mechanical strength of the dense polymers due to voids created within the matrices. The addition of GBMs did not considerably increase the thermal conductivity of the resulting nanocomposites, which can be used advantageous for thermal insulation applications. However, the GBMs endorsed higher sound absorption coefficients.

Given the variety of materials produced, their applications may be diversified. The hybrid structures consisting in OCF and denser materials (PDMS and EP) may find applications as structural components because they present high strength and energy absorption capacity. Hybrid structures consisting in OCF and BC, PUF, and agglomerated cork nanocomposites, besides being lightweight solutions, are good candidates for applications where acoustic and thermal insulating properties are required.

Table of Contents

List of Figures.....	vi
List of Tables.....	xi
Abbreviations and symbols	xiii
Chapter 1.	1
1.1. Scope and Motivation.....	3
1.2. Objectives	4
1.3. Dissertation outline.....	5
1.4. List of Publications.....	7
Chapter 2. Introduction and State of the Art	11
2.1. Cellular materials.....	13
2.1.1. Open and closed cell structures	15
2.1.2. Cellular polymers and metals	16
2.1.3. Stochastic and periodic cellular structures.....	23
2.1.4. Hybrid cellular structures.....	26
2.2. Polymers and polymeric nanocomposites	30
2.3. Graphene based materials.....	32
2.3.1. GBMs impact on the mechanical properties.....	34
2.3.2. GBMs impact on thermal conductivity.....	37
2.3.3. GBMs impact on sound absorption	39
2.3.4. GBMs as fire-retardants.....	40
2.4. References	46
Chapter 3. Bacterial cellulose foams.....	63
3.1. Multifunctional hybrid structures made of open-cell aluminium foam impregnated with cellulose/graphene nanocomposites	65
3.1.1. Abstract.....	66
3.1.2. Introduction.....	66

Table of Contents

3.1.3. Materials and Methods.....	68
3.1.4. Results and Discussion	71
3.1.5. Conclusions.....	83
3.1.6. References.....	84
3.2. Bacterial cellulose/graphene oxide aerogels with enhanced dimensional and thermal stability	91
3.2.1. Abstract.....	93
3.2.2. Introduction.....	93
3.2.3. Materials and Methods.....	96
3.2.4. Results and discussion	98
3.2.5. Conclusions.....	110
3.2.6. References.....	111
Chapter 4. Hybrid structures made of polyurethane/graphene nanocomposite foams embedded within aluminium open-cell foam	117
4.1. Abstract.....	119
4.2. Introduction.....	119
4.3. Materials and Methods.....	121
4.3.1. Materials	121
4.3.2. Experimental methodology.....	122
4.3.3. Characterization	123
4.4. Results and discussion	124
4.4.1. PUFs nanocomposites.....	124
4.4.2. Hybrid structures.....	131
4.5. Conclusions.....	134
4.6. References.....	134
Chapter 5. Aluminium foam–cork nanocomposite hybrid structures: fabrication and characterization.....	139

Table of Contents

5.1.	Abstract.....	141
5.2.	Introduction	141
5.3.	Materials and Methods	143
5.3.1.	Materials	143
5.3.2.	Specimens fabrication.....	144
5.3.3.	Microstructure and morphology	145
5.3.4.	Compressive behaviour.....	145
5.3.5.	Thermal conductivity	146
5.3.6.	Sound absorption	146
5.3.7.	Fire-retardancy tests.....	147
5.4.	Results and discussion.....	147
5.4.1.	Microstructure and morphology	147
5.4.2.	Compressive behaviour.....	148
5.4.3.	Sound absorption	155
5.4.4.	Thermal conductivity	156
5.4.5.	Fire-retardancy tests.....	158
5.5.	Conclusions	159
5.6.	References	160
Chapter 6.	Characterization and physical properties of aluminium foam– polydimethylsiloxane nanocomposite hybrid structures	165
6.1.	Abstract.....	167
6.2.	Introduction	167
6.3.	Materials and Methods	169
6.3.1.	Materials	169
6.3.2.	Specimen fabrication	169
6.3.3.	Thermogravimetric analysis	171

Table of Contents

6.3.4. Mechanical tests.....	171
6.3.5. Thermal tests.....	171
6.3.6. Acoustic tests.....	172
6.3.7. Flammability tests.....	172
6.4. Results and discussion.....	173
6.4.1. Thermal properties.....	173
6.4.2. Compressive behaviour.....	174
6.4.3. Thermal insulation.....	184
6.4.4. Acoustic absorption.....	185
6.4.5. Fire retardancy properties.....	187
6.5. Conclusions.....	187
6.6. References.....	189
Chapter 7. Mechanical, thermal and acoustic properties of aluminium foams impregnated with epoxy/graphene oxide nanocomposites.....	193
7.1. Abstract.....	195
7.2. Introduction.....	195
7.3. Materials and Methods.....	197
7.3.1. Materials.....	197
7.3.2. Fabrication of the Specimens.....	197
7.3.3. Morphologic Characterization.....	198
7.3.4. Mechanical Characterization.....	199
7.3.5. Thermal and Flammability Characterization.....	199
7.3.6. Acoustic Characterization.....	200
7.4. Results and Discussion.....	200
7.4.1. Weight Ratio of the Graphene Oxide.....	200
7.4.2. Microstructure.....	202

Table of Contents

7.4.3. Mechanical Properties.....	203
7.4.4. Thermogravimetric Properties	208
7.4.5. Calorimetric Properties	209
7.4.6. Thermal Properties.....	210
7.4.7. Acoustic Properties	210
7.4.8. Fire-Retardant Properties	212
7.5. Conclusions	213
7.6. References	214
Chapter 8. General discussion, conclusions and future perspectives.....	219
8.1. General discussion.....	221
8.1.1. Mechanical characterization	221
8.1.2. Sound absorption coefficient	223
8.1.3. Thermal conductivity	226
8.2. Main Conclusions	227
8.3. Future Perspectives.....	229
8.4. References	230
Chapter 9. Appendices	231
Appendix S1 Theoretic Principles	232
Mechanical properties.....	232
Thermal conductivity - Transient Plane Source (TPS).....	233
Sound absorption coefficient	235
Appendix S2.1 Supplementary information for Chapter 3.1	238
Appendix S2.2 Supplementary information for Chapter 3.2	241
Appendix S3 Supplementary information for Chapter 4	246

List of Figures

Figure 1.1 Thesis organization and outline.	5
Figure 2.1 Photographs and microphotographs examples of cellular materials existing in nature, showing their cellular structures: (a, b) bone, cork (c, b) and cedar tree (d, e) (adapted from [2])......	14
Figure 2.2 Open-cell and (a) and closed-cell of polymeric foams (b) (adapted from [18]).	16
Figure 2.3 Polymeric foams applications according density and stiffness.....	18
Figure 2.4 Applications of cellular metals according to their porosity (adapted from [17]).	21
Figure 2.5 Scheme showing cellular classification according to the regularity of cells (reproduced from [9]).	23
Figure 2.6 MHSS structures (a) [95] and APM elements [96] (b).	28
Figure 2.7 Open-cell metal foam (a) silicone filled open-cell foam and (b) epoxy open-cell filled foam (c) (adapted from [116])......	30
Figure 2.8 Classification grid for the categorization of different graphene types according to three fundamental GBM properties. The different materials drawn at the six corners of the box represent the ideal cases according to the lateral dimensions and the number of layers reported in the literature. The values of the three axes are related to the GBMs at the nanoscale, but it is feasible to expand the values to the microscale. Reproduced from [147]......	33
Figure 2.9 Scheme of fire-retardancy behaviour with and without graphene/graphene oxide (adapted from [222])......	42
Figure 3.1.1 Schematic of the preparation of the nanocomposite foams and hybrid structures.	71
Figure 3.1.2 Photographs of the upper surface of BC/PCMs10 and BC/GO10/PCMs10 foams and respective SEM images at different magnifications (the arrows at the higher SEM magnification images point to PCMs microspheres) together with photographs of flame test results for both foams.....	73

List of Figures

- Figure 3.1.3 XPS spectra survey (a) and normalized C1s core levels for BC (b), BC/GO10 (c) and BC/rGO10 (d). 75
- Figure 3.1.4 TGA under air atmosphere of BC foam, GO nanosheets, PCMs microcapsules, BC/PCMs10 foam, BC/GO10/PCMs10 foam and BC/rGO10/PCMs10 foam (a), DSC curves for PCMs microcapsules, BC, BC/PCMs10, BC/GO10/PCMs10 and BC/rGO10/PCMs10 (b). 76
- Figure 3.1.5 Water absorption capacity of BC, BC/GO10 and BC/rGO10 before and after hydrophobization (H₂O) (a). The values represent a mean \pm SD of $n=3$; and water contact values for the foams before and after hydrophobization (b). 79
- Figure 3.1.6 Photographs of OCF foam and BC/GO10 hybrid structure (OCF is inside) with and SEM images of the HS-BC/GO10 sample at different scale magnifications. 81
- Figure 3.1.7 Average stress-strain compressive curves (a) and sound absorption (b) of OCF, BC/GO10 and HS-BC/GO10. 82
- Figure 3.2.1 Schematic diagram of aerogels preparation and optical appearance. Comparison of the SEM images obtained at the cross-section of the different BC/GO aerogels, prepared with and without DMSO. 98
- Figure 3.2.2 X-ray μ tomography images of the BC/GO aerogels: 3D renderings of μ CT images (BC/GO10 a), BC/GO25 c) and BC/GO50 e) and segmented 2D slices (BC/GO10 b), BC/GO25 d) and BC/GO50 f)). 100
- Figure 3.2.3 XPS spectra BC/GO25 and its reduced forms, XPS general survey scan (a) and high resolution C1s and N1s XPS spectra (b, c). FT-IR spectra (d). 103
- Figure 3.2.4 Stress-Strain curves for 40% of strain (a), Young Modulus and compressive strength (CS) at 40% of strain (b), Stress amplitude after 1,000 cycles of compression (c) and Real image of the scaffolds under dynamic compression test in wet environment (d). 106
- Figure 3.2.5 Swelling ratio of the aerogels immersed in water as a function of time (a) and water contact angles for aerogels reduced with N₂H₄ (b) and NH₃ (c). 107
- Figure 3.2.6 Thermogravimetric analysis of BC, GO and BC/GO25 aerogels(a). Flame behaviour of BC/rGO25_{NH₃} (b) and BC (c) specimens. Figure (b) the frames captured at

List of Figures

t0 and t3s show the dimensional stability of the aerogel after flame exposure and frame t6s exhibit the ability to be handled without suffer collapse. Figure (c) the frame sequence (t0s, t3s and t6s) showed the continuous annealing degradation of the sample.	109
Figure 4.1 Scheme describing the preparation of PUF nanocomposites (A) and hybrid structures (B).....	122
Figure 4.2 Flame behaviour of PUF (a), PUF/GNPs2.5 (b) and PUF/GO2.5 (c).	125
Figure 4.3 SEM images (a), 3D μ CT rendering (b), pore size distribution (c) and cell wall thickness distribution (d) for PUF, PUF/GNPs2.5, PUF/GNPs5.0, PUF/GO2.5 and FUF/GO5.0.	128
Figure 4.4 Average stress-strain compressive curves (a) and sound absorption coefficient (b) of the different PUF based nanocomposites.	129
Figure 4.5 Specimens: OCF(a); HS-PUF/GNPs2.5 (b) and 3D- μ CT HS-PUF/GNPs2.5 (c).	132
Figure 4.6 Average stress-strain compressive curves (a) and sound absorption curves (b) of OCF, PUF/GNPs2.5 and HS-PUF/GNPs2.5.	133
Figure 5.1 Fabricated specimens: cubic specimens (a) and circular specimens (b) of OCF, Cork, nCork, HS-Cork and HS-nCork.....	145
Figure 5.2 SEM images of the OCF foam (a) and a granule of cork (b).....	147
Figure 5.3 SEM images of the Cork (a, first row) and b) nCork (b, second row) matrices.	148
Figure 5.4 The quasi-static deformation sequences showing the progressive deformation of the Cork (a), nCork (b), HS-Cork (c) and HS-nCork (d).....	148
Figure 5.5 The IR image sequences showing the dynamic progressive deformation of the of the Cork (a), nCork (b), HS-Cork (c) and HS-nCork (d).....	149
Figure 5.6 Quasi-static and dynamic compressive stress-strain relationship of OCF, Cork, nCork, HS-Cork and HS-nCork.....	150
Figure 5.7 EAD (a) and SEA (b) curves of OCF, Cork, nCork, HS-Cork and HS-nCork for quasi-static and dynamic tests.....	154

List of Figures

Figure 5.8 Sound absorption coefficient of the OCF, Cork, nCork, HS-Cork, HS-nCork.	156
Figure 5.9 Flame response of the Cork (a) and HS-nCork (b).	159
Figure 6.1 SEM images of the matrices of PDMS (a) and nPDMS matrices (b).	170
Figure 6.2 Square and cylindrical specimens: OCF (a), dense PDMS (b), nPDMS (c), HS- PDMS (d) and HS-nPDMS (e).	170
Figure 6.3 TG/DTG of the PDMS and nPDMS matrices.	173
Figure 6.4 Compressive deformation (a) and stress–strain curves (b) of dense PDMS and nPDMS specimens at quasi-static and dynamic loading conditions.	177
Figure 6.5 Compressive deformation (a) and stress–strain curves (b) of OCF specimens.	179
Figure 6.6 Compressive deformation (a) and stress–strain curves (b) of the HS-PDMS and HS-nPDMS specimens.	181
Figure 6.7 Averaged EAD (a) and SEA (b) curves for quasi-static and dynamic loading conditions.	184
Figure 6.8 Thermal conductivities and (a) Sound absorption coefficient curves (b) of the hybrid structures (HS-PDMS and HS-nPDMS) and the individual components (PDMS, nPDMS and OCF).	186
Figure 6.9 Fire retardancy sequence image for the PDMS and nPDMS.	187
Figure 7.1 Fabricated specimens (22 mm × 22 mm × 25 mm): OCF (a), EP (b), nEP (c), HS- EP (d) and HS-nEP (e).	198
Figure 7.2 Quasi-static compressive stress-strain curves (a) and Vickers Hardness (b) of the unreinforced EP and reinforced EP with different compositions of the GO.	201
Figure 7.3 SEM images of the EP (magnification factor: 1000) (a) and nEP matrices (magnification factor: 1000 (b) and 2000 (c)).	202
Figure 7.4 Micro-computed tomography images 2D slice (a) and 3D volume rendering of HS-nEP (b).	203

List of Figures

Figure 7.5 The quasi-static deformation (0.1 mm/s) sequences showing the progressive deformation of the: EP (a), nEP (b), HS-EP (c) and HS-nEP (d).	203
Figure 7.6 The quasi-static deformation (1 mm/s) deformation sequences showing the progressive deformation of the: EP (a), nEP (b), HS-EP (c) and HS-nEP (d).	204
Figure 7.7 The IR image sequences at different strain increments showing the dynamic progressive deformation of the: HS-EP (a) and HS-nEP (b) subjected to a crosshead rate of 1 mm/s.	204
Figure 7.8 Stress-strain relationship (each curve represents an average of three specimens tested) at different crosshead rates: (a) 0.1 mm/s and (b) 1 mm/s.	205
Figure 7.9 Average energy absorption and specific absorption energy capacity at crosshead rate of 0.1 mm/s (a, c) and 1 mm/s (b, d).	207
Figure 7.10 Thermograms (a) and DSC curves (b) of the EP and nEP matrices.	209
Figure 7.11 Thermal conductivity (a) and sound absorption capacity (b) of the OC, EP, nEP, HS-EP and HS-nEP.	212
Figure 7.12 Fire-retardant behaviour of the: EP (a) and nEP (b).	212
Figure 8.1 “Charts created using CES EduPack 2018, Granta Design Ltd: compressive strength vs density.	221
Figure 8.2 Averaged values with the standard deviation of EAD and SEA for a strain of 0.5 for quasi-static (a, c) and dynamic loading conditions (b, d).	222
Figure 8.3 Sound absorption coefficient vs Frequency.	224
Figure 8.4 Thermal conductivity values of the fabricated materials.	226
Figure 8.5 Main properties presented by the materials developed under the scope of this thesis.	228

List of Tables

Table 2.1 Main advantages and disadvantages presented by polymeric, metal and ceramic foams [19].	16
Table 2.2 Literature survey of polymer composites mechanically reinforced with GBMs. The % enhancement is with respect to the net polymer.	37
Table 2.3 Literature survey of thermal conductivity improvement in polymeric/graphene nanocomposites.	39
Table 2.4 Literature survey of fire-retardancy improvement in polymer/graphene nanocomposites.	43
Table 3.1.1 Relative atomic percentage of C, O and N and C/O ratio for pristine BC nanofibers and BC nanocomposite foams.	76
Table 3.1.2 Compressive results of the cellulose-based foams.	80
Table 3.2.1 C, O and N content of BC and BC/GO aerogels determined by XPS.	101
Table 3.2.2 Electric conductivities for the different BC/GO aerogels.	110
Table 4.1 Experimental data of TGA analysis.	126
Table 4.2 Apparent density, compressive Modulus and compressive strength for 10% of deformation.	128
Table 4.3 Thermal conductivity, thermal diffusivity and specific heat.	130
Table 4.4 Apparent density, stress peak, energy absorption, specific energy absorption and thermal conductivity.	133
Table 5.1 Compressive quasi-static results of Cork, nCork, HS-Cork and HS-nCork specimens.	151
Table 5.2 Compressive dynamic results of Cork, nCork, HS-Cork and HS-nCork specimens.	152
Table 5.3 Thermal conductivity and thermal diffusivity of the OCF, Cork, nCork, HS-Cork, HS-nCork.	158
Table 6.1 Compressive results of PDMS and nPDMS specimens.	175

List of Tables

Table 6.2 Compressive results of HS-PDMS and HS-nPDMS specimens.	183
Table 8.1 Acoustic parameters for fabricated specimens.	225

Abbreviations and symbols

Al	Aluminium
APM	Advanced Pore Morphology
BC	Bacterial cellulose
BC/xGO10/yPCMs10	Bacterial cellulose /graphene oxide (x = 0, 5, 10, 25 and 50 wt. %) /phase change materials (y = 0, 5 and 10 wt.%)
BC/xrGO	Bacterial cellulose/reduced graphene oxide with hydroxylamine
BC/xrGO/yPCMs	Bacterial cellulose/reduced graphene oxide with hydroxylamine (x = 0, 5 and 10 wt.%) and phase change materials (y = 0, 5 and 10 wt.%)
BC/xrGO _{N₂H₄}	Bacterial cellulose/graphene oxide reduced with hydrazine (x = 0, 10, 25 and 50)
BC/xrGO _{NH₃}	Bacterial cellulose/graphene oxide aerogels reduced with ammonia vapour (x = 0, 10, 25 and 50)
Cork	Agglomerated cork
CNTs	Carbon nanotubes
CS	Compressive Strength
DMSO	Dimethyl sulfoxide
DSC	Dynamic scanning calorimetry
DTG	Derivative thermogravimetric analysis
EAD	Energy absorption density
EB	Elongation at break
EP	Epoxy
FTIR-ATR	Attenuated Total Reflection Fourier Transform Infrared
GBMs	Graphene based materials
GO	Graphene oxide
GNPs	Graphene nanoplatelets
H_BC	Hydrophobicized bacterial cellulose
H_BC/xGO	Hydrophobicized Bacterial cellulose/graphene oxide aerogels in a proportion 90/10

Abbreviations and symbols

H_BC/xrGO	Hydrophobicized Bacterial cellulose/reduced graphene oxide aerogels with hydroxylamine
HS	Hybrid structures made of Aluminium open-cell foam incorporated with other material
HS-BC/GO10 or HS-nBC	Hybrid structure composed by aluminium open-cell foam and bacterial cellulose foam/graphene oxide 10 wt. %
HS-Cork	Hybrid structure composed by aluminium open-cell foam and agglomerated cork
HS-nCork	Hybrid structure composed by aluminium open-cell foam and agglomerated cork/graphene oxide
HS-EP	Hybrid structure composed by aluminium open-cell foam and with epoxy
HS-nEP	Hybrid structure composed by aluminium open-cell foam and epoxy/graphene oxide
HS-PDMS	Hybrid structure composed by aluminium open-cell foam and polydimethylsiloxane
HS-nPDMS	Hybrid structure composed by aluminium open-cell foam and polydimethylsiloxane/graphene oxide
HS-PUF/GNPs2.5 or HS-nPUF	Hybrid structure composed by aluminium open-cell foam and polyurethane foam/graphene nanoplatelets 2.5 wt. %
HV	Hardness of Vickers
IR	Infra-red
LbL	Layer by layer
MDI	Methylene diphenyl diisocyanate
Micro-CT (μ CT)	Micro computerized tomography
MMT	Methyl trimethoxy silane
nCork	Agglomerated cork/graphene oxide
nBC	Nanocomposite of bacterial cellulose and graphene oxide
nEP	Nanocomposite of Epoxy and graphene oxide
nPDMS	Nanocomposite of Polydimethylsiloxane and graphene oxide

Abbreviations and symbols

nPUF	Nanocomposite of polyurethane foam and graphene oxide
NFC	Nanofibrillated cellulose
NRC	Noise reduction coefficient
OCF	Open-cell aluminium foam
PCMs	Microencapsulated phase change materials
PDMS	Polydimethylsiloxane
PE	Polyethylene
PES	Poly ether sulfone
PLA	Poly lactic acid
PMMA	Polymethyl methacrylate
PP	Polypropylene
PPC	Polypropylene carbonate
PS	Polystyrene
PU	Polyurethane
PUF	Polyurethane foam
PVA	Polyvinyl alcohol
PUF/xGNPs	Polyurethane foam/graphene nanoplatelets (x = 0, 1.0, 2.5 and 5.0 wt.%)
PUF/xGO	Polyurethane foam/graphene oxide (x = 0, 1.0, 2.5 and 5.0 wt.%)
Q	Water absorption capacity
rt	Room temperature
SEA	Specific energy absorption
SEM	Scanning electron microscopy
St Dev	Standard deviation
TGA	Thermogravimetric analysis
TS	Tensile strength
WCA	Water contact angle
XPS	X-ray Spectroscopy
YM	Young Modulus

Abbreviations and symbols

α Sound absorption coefficient

Chapter 1.

This chapter contains the scope and motivation, the main objectives, the thesis outline and the publications under the scope of this thesis

1.1. Scope and Motivation

Researchers are constantly exploring materials that are lighter, more resistant, energy efficient, sustainable and with lower environmental impact. Novel materials, technologies and manufacturing processes or just the improvement of the ones already existing are now being actively developed to handle with the increasing human demand to promote better living conditions, through applications in different areas such as water treatment, structural energy storage systems, healthcare, packaging or impact absorption, among others.

Currently, cellular metals are promising materials in engineering. Closed-cell metal foams exhibit high stiffness-to-weight ratio and high energy absorption capacity; however, the irregular structure makes its use unfeasible since its behaviour cannot be predicted. On the other hand, open-cell metal foams (OCF) are characterized by high specific area, highly interconnected and regular structure, poor mechanical properties and are mostly used for functional applications. To create periodic structures with an easily reproducible unit cell, researchers are combining the OCF with dense polymers in which the polymers compensate the weak mechanical strength/behaviour of OCF. So far, the work developed in this field is still limited and mainly focused on filling the voids of OCF with dense polymers and on its mechanical characterization. There is no substantial data regarding acoustic and thermal applications or in diversifying the type of filling material. Filling the voids of these structures with different type of materials such as polymeric foams and cork powder can increase multifunctionality and thereby broaden the field of application.

In parallel, the mentioned structures can be even more complete and include new functionalities by the addition of carbon nanostructures to the filling material. The use of these nanostructures has opened up a new exciting possibility to tailor the properties of materials. In particular, graphene-based materials (GBMs) have seen their use in a variety of fields to provide or enhance many properties, such as mechanical, acoustic and thermal and fire-retardancy.

For the reasons exposed above, the research presented in this thesis was focused on the development of new hybrid cellular structures by combining a regular OCF as host matrix and cellular materials or dense polymers with or without GBMs as void fillers. Bacterial cellulose (BC), polyurethane foams (PUF) and cork granules are examples of the cellular materials explored to prepare the novel composite hybrid structures. Polydimethylsiloxane

(PDMS) and epoxy (EP) were the dense polymers studied as the void filler of the open-cell foams.

It is intended that hybrid structures constitute a competitive solution, with advanced functional value and measurable advantages in terms of mechanical, acoustic, thermal, durability, ease of production and application, making it a viable alternative to solutions currently on the market and expanding the interest of cellular materials.

1.2. Objectives

The overall objective of this thesis is to develop multifunctional hybrid structures composed by OCF filled with different polymeric-based nanocomposites materials.

The main achievement is considered at two levels. The first level is the incorporation, characterization and optimization of nanocomposites based in polymer/GBMs. The second level is the filling of the OCF voids with the optimized polymer nanocomposites followed by characterization.

The specific objectives are listed below:

- To evaluate the potential of GBMs as fire-retardant agents, mechanical and acoustic enhancers of BC and PUF foams, agglomerated cork, and PDMS and EP dense polymers;
- To characterize the void fillers regarding the dispersion of GBMs into the polymeric matrices;
- To prepare novel hybrid structures consisting in OCF filled with cellular materials (BC and PUF foams and agglomerated cork) and dense polymers (PDMS and EP) incorporating GBMs, with special focus on the development of fabrication methods;
- To characterize the novel hybrid structures developed within this PhD thesis concerning the mechanical compressive behaviour, energy absorption capability, thermal insulating and sound absorption properties;
- To compare novel hybrid structures with the available cellular materials and structures in terms of main properties, namely density, mechanical, thermal and acoustic.

1.3. Dissertation outline

This section aims to summarize the work developed throughout the PhD workplan and how it is organized and presented. For a clear understanding of the thesis outline, in Figure 1.1, is shown a flow chart listing all chapters and the main issues presented and discussed within each chapter.

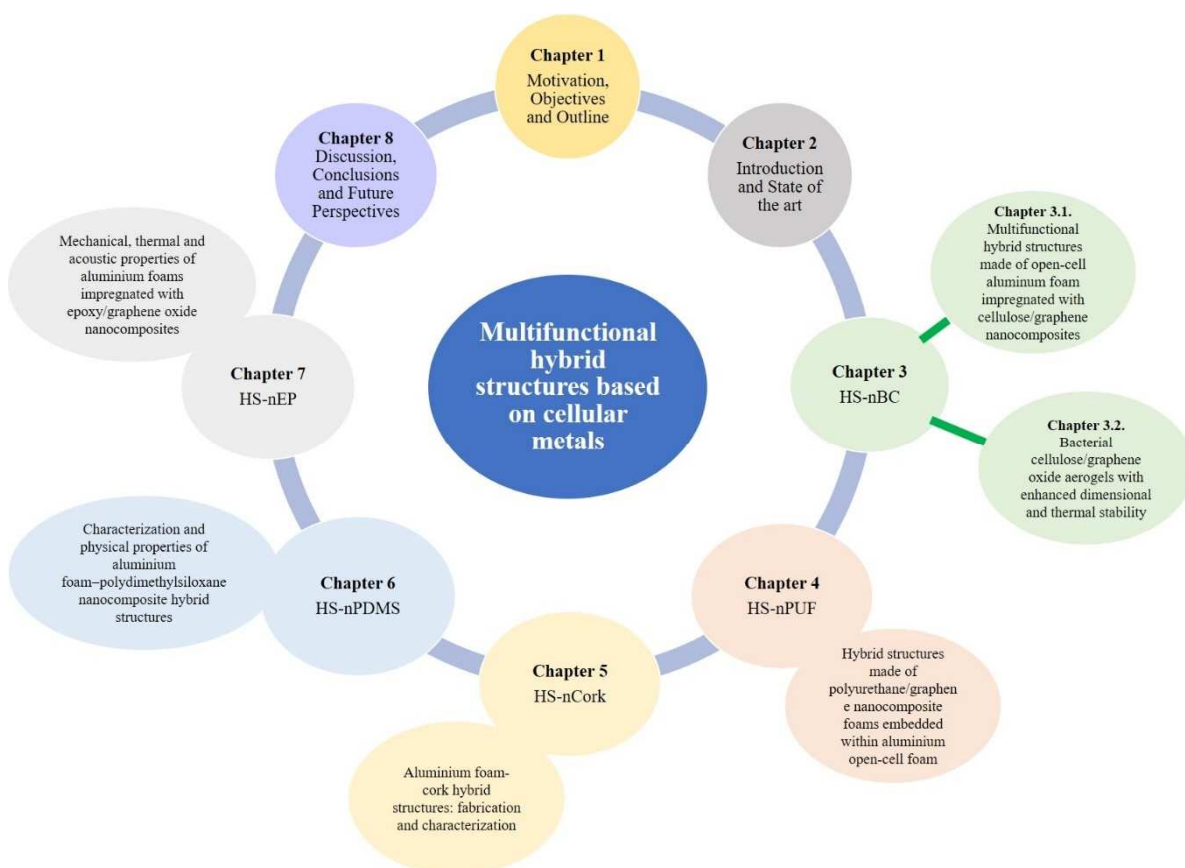


Figure 1.1 Thesis organization and outline.

The thesis comprises eight main chapters. Chapter 1 presents the scope and motivation and objectives under the thesis development, describing its outline and the list of publications. Chapter 2 provides an overview of the natural and artificial cellular materials, the main manufacturing processes, properties and applications, focusing on the cellular materials studied in this thesis. Furthermore, the effect of GBMs used as nanosized reinforcement of the polymeric matrices on the main properties (mechanical, thermal, acoustic and fire-retardant) is also discussed, since it is a transversal subject to all chapters. Chapters 3 to 7 provide the main findings, each addressing a specific problem/challenges. All of them exhibit the same structure and are based on original research work submitted or

published in peer-reviewed indexed journals. Finally, chapter 8 gathers the general discussion, final conclusions and future perspectives.

Chapter 3 presents the preparation and characterization of foamed cellulose-GBMs materials. Special focus is addressed to the cellulose composite foams preparation and optimization regarding chemical, morphological and mechanical properties. Given the increasingly importance of developing natural and new eco-friendly materials, more work has been done in this topic, aiming preparing different cellulose/GBMs based foamed nanocomposites envisaging multiple applications. Although only in sub-chapter 3.1, the cellulose/GBMs aerogels are incorporated into the OCF, the further developed aerogels (sub-chapter 3.2) can also be combined with OCF, therefore, chapter 3 is itself organized in 2 sub-chapters, 3.1 and 3.2. Sub-chapter 3.1 describes the preparation and characterization of bacterial cellulose-based foams incorporated with GBMs and phase change materials (PCMs) and its incorporation into OCF foams. A full chemical, structural, thermal and mechanical characterization was carried out for the individual and hybrid structures. Sub-chapter 3.2 reports the use of dimethyl sulfoxide (DMSO) that interfere with the water freezing point, to control the porosity in BC/GO nanocomposite foams prepared by freeze-drying and the comparison between two reducing methods applied to GO chemical reduction with hydrazine and thermal reduction with ammonia vapour.

Chapter 4 details the preparation and characterization of hybrid structures resulting from the combination of previously optimized synthetic polyurethane PUF/GBMs nanocomposite foams and OCF. A set of complementary characterization tests were carried out regarding mechanical, thermal, acoustic characterization.

Chapter 5 reports the findings of an experimental work developed to prepare the novel hybrid structures by filling the OCF with a 100% natural cork with and without GO, assessing their mechanical, thermal and acoustic properties.

Chapters 6 and 7 explore a different approach, in which, the OCFs are filled with two dense nanocomposite polymers, polydimethylsiloxane (PDMS) and epoxy resin (EP), both combined with GO. The thermal, acoustic and mechanical properties of these novel hybrid structures are also presented.

Chapter 8 summarizes the work presented in the chapters 3 to 7 by the compilation of the main results in charts and its comparison with the most recently available literature. The output is intended to target a portfolio of products developed to take advantage of the main achieved properties. Possible applications were pointed out according to the main properties presented by each material. Furthermore, main conclusions are summarized, and future work is proposed.

1.4. List of Publications

Publications in the framework of this thesis

Research articles

S.C. Pinto, P.A.A.P. Marques, M. Vesenjajk, R. Vicente, L. Krstulović-Opara and I. Duarte Aluminium foam-cork hybrid structures: fabrication and characterization (to be submitted).

S.C. Pinto, P.A.A.P. Marques, R. Vicente, L. Godinho and I. Duarte (2020) Hybrid Structures Made of Polyurethane/Graphene Nanocomposite Foams Embedded within Aluminum Open-Cell Foam. *Metals* 10(6), 768.

S. C. Pinto, N.H.C.S. Silva, R. J.B. Pinto, C.S.R. Freire, I. Duarte, R. Vicente, M. Vesenjajk and P.A.A.P. Marques (2020) Multifunctional hybrid structures made of open-cell aluminium foam impregnated with cellulose/graphene nanocomposites. *Carbohydrate Polymers*. 238, 116197.

S.C. Pinto, G. Gonçalves, S. Sandoval, A.M. López-Periago, A. Borrás, C. Domingo, G. Tobias, I. Duarte, R. Vicente and P.A.A.P. Marques (2020) Bacterial cellulose/ graphene oxide aerogels with enhanced dimensional and thermal stability. *Carbohydrate Polymers*. 230, 115598.

S.C. Pinto, P.A.A.P. Marques, M. Vesenjajk, R. Vicente, L. Godinho, L. Krstulović-Opara and I. Duarte (2019) Mechanical, thermal and acoustic properties of aluminium open-cell foams impregnated with epoxy/graphene oxide nanocomposites. *Metals*. 9(11), 1214.

S.C. Pinto, P.A.A.P. Marques, M. Vesenjajk, R. Vicente, L. Godinho, L. Krstulović-Opara and I. Duarte (2019) Mechanical, thermal, acoustic absorption and fire retardancy properties

of simple and nanocomposite polydimethylsiloxane-aluminium hybrid foams. *Composite Structures*. 230,111521.

M. Ptak, P. Kaczyński, J. Wilhelm, J.M.T. Margarido, P.A.A.P. Marques, S.C. Pinto, R.J.A. Sousa, and F.O. Fernandes (2019) Graphene-Enriched Agglomerated Cork Material and Its Behaviour under Quasi-Static and Dynamic Loading. *Materials* 12:1-12

P.T. Santos, S.C. Pinto, P.A.A.P. Marques, A.B. Pereira and R.J. Alves de Sousa (2017) Agglomerated cork: a way to tailor its mechanical properties. *Composite Structures*. 178, 277-287

Book chapters

C. Vilela, R.J.B. Pinto, S.C. Pinto, P. Marques, A. Silvestre, and C.S. da Rocha Freire Barros (2018) Polysaccharides-Based Hybrids with Metal Nanoparticles. In: *Polysaccharide Based Hybrid Materials*. Springer Briefs in Molecular Science. Springer, Cham.

A.F. Girão, S.C. Pinto, A. Bessa, G. Gonçalves, B.H., E. Pereira and P.A.A.P. Marques (2016) Graphene oxide: a unique nano-platform to build advanced multifunctional composites. In: *Advanced 2D Materials*, WILEY-Scrivener Publishing LLC, USA.

Patent

I. Duarte, S.C. Pinto, P. Marques, *Metais e estruturas metálicas porosas e celulares de porosidade aberta impregnados com cortiça, seus processos de produção e suas utilizações*, 2019. Data do depósito: 11.10.2019, N°. do pedido: 115835.

Oral communications

I. Duarte, S.C. Pinto, P.A.A.P. Marques, M. Vesenjaj, R. Vicente, L. Krstulović-Opara, *Advanced lightweight aluminium foam-cork hybrid structures*, ICCS23 & MECHCOMP6, 1- September 2020, Porto, Portugal (accepted).

I. Duarte, S.C. Pinto, P.A.A.P. Marques, M. Vesenjaj, R. Vicente, L. Krstulović-Opara, *Development and characterisation of aluminium foam-polymer hybrid structures*, ICCS23 & MECHCOMP6, 1-4 September 2020, Porto, Portugal (accepted).

S.C. Pinto, P.A.A.P. Marques, M. Vesenjaj, R. Vicente, L. Krstulović-Opara and I. Duarte, Multifunctional hybrid foams composed by aluminium open-cell foam filled with polymers, INCELL2019, 19-20 September 2019, Maribor, Slovenia.

S.C. Pinto, R.J. Pinto, I. Duarte, R. Vicente, C. Freire and P.A.A.P. Marques, Bacterial cellulose and graphene nanostructures as promising nanocomposites for the development of new insulating and fire-retardant materials, Materiais2017, 9-12 April 2017, Aveiro, Portugal.

S.C. Pinto, P.A.A.P. Marques, I. Duarte, R. Vicente. Multifunctional hybrid foams development. Science & Research GRIDS 2017, Anfiteatro do Departamento de Engenharia Mecânica, 29 March 2017, Aveiro, Portugal.

S.C. Pinto, P.A.A.P. Marques, I. Duarte, R. Vicente. Energy efficient and fire-retardant lightweight structures. RISCO Research Meeting 2015, Semana do DECivil Anfiteatro do Departamento de Geociências, 28th October 2015, Aveiro, Portugal.

S.C. Pinto, R.J. Pinto, C. Freire, I. Duarte, R. Vicente and P.A.A.P. Marques, Nanocellulose foams containing phase change materials and carbon nanostructures: a new energetic and fire-retardant foam, MatCel'2015, 7-8 September, Aveiro, Portugal.

Poster Communications

S.C. Pinto, I. Duarte, R. Vicente and P. Marques. Multifunctional lightweight celular materials, 2nd International Conference, Anfiteatro do Departamento de Engenharia Mecânica, 11-12 July 2019, Aveiro, Portugal.

S.C. Pinto, R.J. Pinto, C. Freire, I. Duarte, R. Vicente, P.A.A.P. Marques, Multifunctional aerogels by combining nanocellulose and graphene-based materials, International Conference on Nanomaterials Science and Mechanical Engineering, 16-18 July 2018, Aveiro, Portugal.

S.C. Pinto, I. Duarte, R. Vicente and P.A.A.P. Marques. Nanocellulose-aluminium hybrid foams for multifunctional applications, TEMA em questão conference, Anfiteatro do Departamento de Engenharia Mecânica, 11 June 2018, Aveiro, Portugal.

Chapter 1

S.C. Pinto, R.J. Pinto, C. Freire, I. Duarte, R. Vicente, P.A.A.P. Marques, Hybrid structures based in cellular materials, MATCEL 2017, 25-27 September 2017, Aveiro, Portugal.

S.C. Pinto, P.A.A.P. Marques, I. Duarte and R. Vicente, Cellular materials/graphene nanostructures with promising insulating and fire-retardant properties, Research day 2017, 13 June 2017, Aveiro, Portugal.

Chapter 2. Introduction and State of the Art

This chapter is divided into two parts. The first part introduces the cellular materials, providing a comprehensive review about their main characteristics, manufacturing processes, properties and applications, focusing on the polymeric and metal cellular materials. The second part, presents the graphene based materials which were used as reinforcement elements of polymeric based matrices, giving an overview of the methods used to ensure the homogeneous distribution into the matrix, as well as their main properties, in particular the effect on mechanical, thermal, sound absorption and fire-retardancy of the resulting nanocomposites.

2.1. Cellular materials

Driven by the need for new materials with the ability to perform different functions simultaneously, in the past decades, research efforts have been committed with the purpose of developing new lightweight composite structures, foreseeing applications in emergent sectors, such as construction, automotive, railway and aerospace industries. This straightforward approach resulted in energy, time and cost savings and improvement in safety and wellbeing for society. Cellular materials have been considered an interesting and viable solution in the formulation of lightweight and multifunctional materials [1].

Concerning the topic, Ashby stated [2]:

“When modern man builds large load-bearing structures, he uses dense solids: steel, concrete, glass. When nature does the same, she generally uses cellular materials: wood, bone, coral. There must be good reasons for this.”

Cellular materials can be found everywhere in nature (Figure 2.1), but also in engineering applications. Bones, cork, wood, cedar tree, bee honeycombs and coral are some examples of the natural cellular materials. Some of them, like wood and cork are extensively used in engineering applications. In fact, wood has been used for millennia in the construction of houses, furniture and boats, while cork has been used since Roman times in shoes soles [3]. Robert Hooke was the first scientist, in 1665, to relate some properties such as low density to its cellular structure, by examining a piece of cork under a rudimentary microscope. Hooke observed that cork is composed by polyhedral cavities, which he called as cells (from the Latin *cellula*, small room) [4]. Inspired by the potential of the natural materials, scientists are developing artificial cellular materials made of polymers, metals, ceramics and glasses which are designated by artificial, synthetic, man-made or bio-inspired cellular materials [5–7]. Bread and cakes are examples of fabricated man-made cellular material [3].

In 1997, Gibson and Ashby were the firsts to compile information related with cellular materials, regarding their manufacturing processes, properties and theoretical models, thereby contributing and describing in detail the mechanical deformation and failure mechanisms of some cellular materials, correlating, for example, the mechanical with structural properties, which enable the understanding and development of new cellular materials [8].

In the literature, cellular materials are often designated by other technical terms, such as foams, for example polyurethane (PU) and aluminium (Al) foams, and sponges, such as human bone. The term foam refers to a special case of porous material, which is obtained from a liquid mixture where air bubbles were dispersed. On the other hand, the term sponge, is associated to a porous material with complex and interconnected porosity, which cannot be subdivided into unitary and well-defined cells [9].

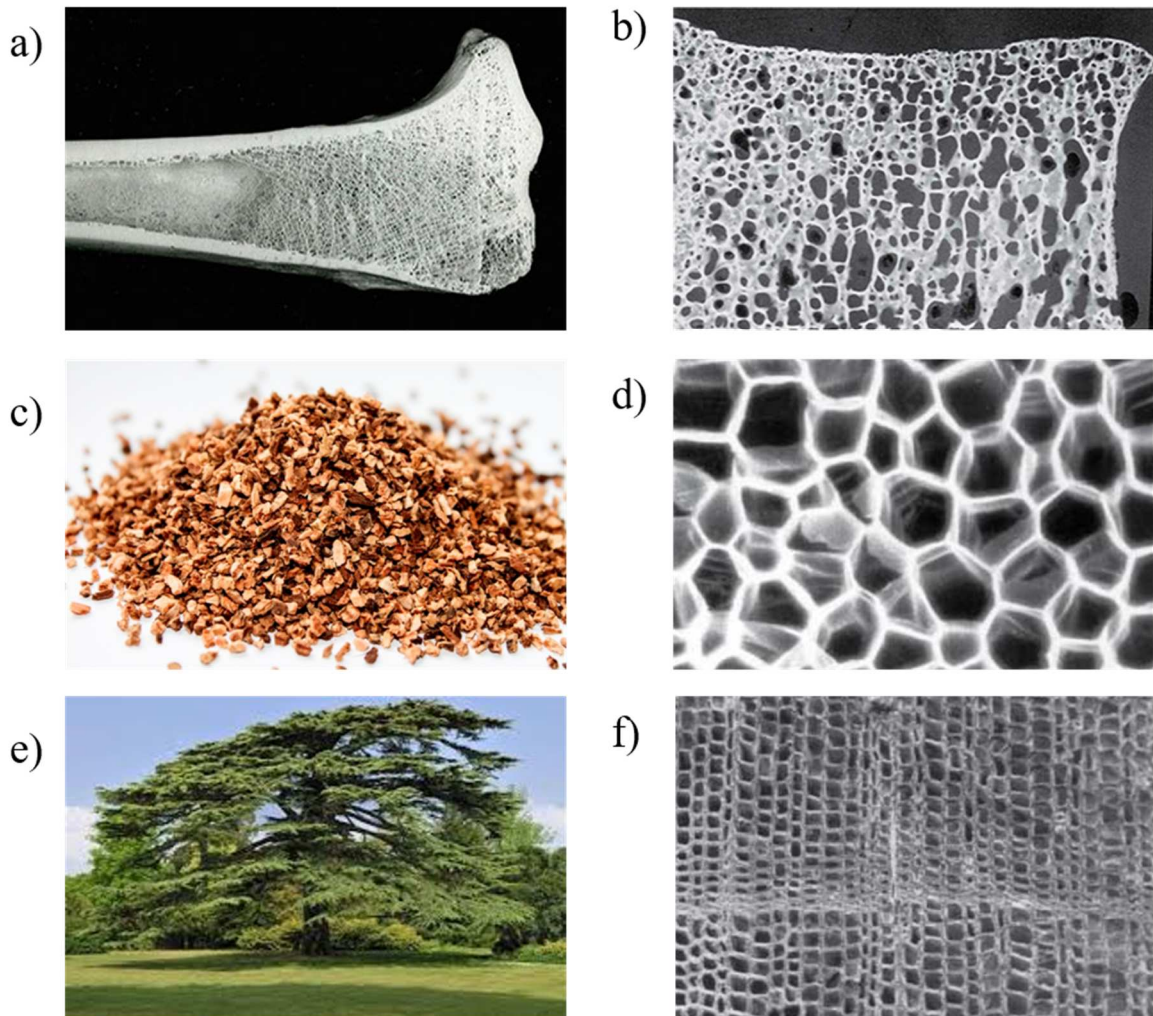


Figure 2.1 Photographs and microphotographs examples of cellular materials existing in nature, showing their cellular structures: (a, b) bone, cork (c, b) and cedar tree (d, e) (adapted from [2]).

From the structural point of view and as it can be seen in Figure 2.1, cellular materials are composed by pores or cells. Cellular solids or porous materials are composed by two phases, a continuous solid phase (base material or matrix) and a continuous or discontinuous gaseous phase (pores or cells) [10]. The resulting cellular arrangement results in an interconnected porous network of solid struts, which form the edges and/or faces of cells,

showing high porosity with values above 70% [8,11]. In fact, the final properties of the cellular materials are a balance of many characteristic, the relative density (solid volume fraction), the properties of the base material and the characteristics of the pores, such as pore type, pore size, pore shape and pore size distribution [2].

Cellular materials are of great importance since they present low weight maintaining coupled to good mechanical performance, sound absorption and thermal insulation features [12]. For example, the use of these lightweight cellular materials, in particular closed-cell metal foams into the automobile vehicles, trains, aircraft contributes to the reduction of their weight (cost savings), leading to a decrease of the fuel consumption and, therefore the reduction of the gas emissions (pollution reduction), but also to increase the safety of the passengers in case of an accident due to their excellent ability to absorb impact energy [13,14]. Other cellular materials, such as natural cork are widely used in the building construction sector, for example to produce seismic, thermal and acoustic insulating devices for buildings [15]. In the packaging industry, synthetic polymeric foams like flexible PU, polystyrene (PS) or more recently cellulose have been used to protect materials from impact [10]. The porous structure of cellular materials is also attractive in the biomedical field, namely orthopaedic applications (titanium, ceramics) and polymeric porous scaffolds for regenerating tissues, mimicking/reproducing a similar porous structure of the bones [16].

The cellular materials can be grouped and classified in several types, according to their origin (natural and synthetic), the base material (metal, polymer, ceramic), pore type (open or closed cells) and arrangement of pores in the cellular structures (stochastic and periodic), which will be presented next.

2.1.1. Open and closed cell structures

Open and closed-cell foams are stochastic cellular materials which designations are based on the cell type. In the former, the cells are interconnected by cell edges and in the later cells do not touch each other, being isolated by solid faces (Figure 2.2). Due to such different structures and respective properties, the structures will cover different technological areas. Open-cell structures are characterized by high interconnectivity, high permeability (allowing chemical leaking) and very high internal surface area, being used as functional materials. Heat-exchangers, filters, batteries, electrodes, biomedical implants, are some examples. Closed-cell foams are heavier, mechanically stronger (in particular, metal and polymeric

ones) and therefore can be used as structural materials, such as components in buildings, for cars and trains due to the excellent capability to absorb energy under impact and sound insulating properties. However, depending on the manufacturing method, the pores may contain undesirable chemicals trapped inside the cells [17,18]. When the manufacturing process is not well controlled, for example in gas forming methods, a mixture of open and closed pores can be observed.

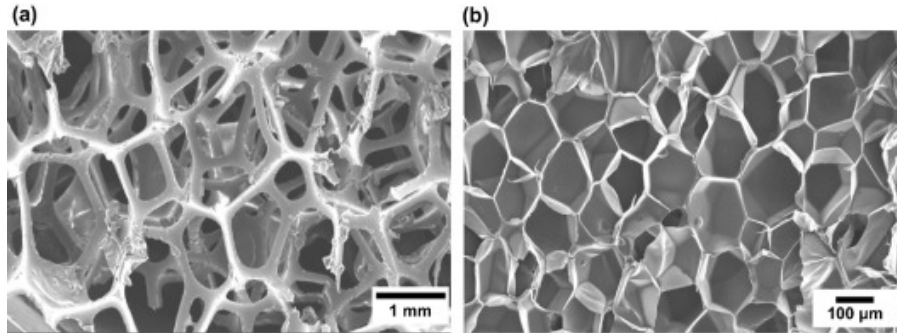


Figure 2.2 Open-cell and (a) and closed-cell of polymeric foams (b) (adapted from [18]).

2.1.2. Cellular polymers and metals

The cellular materials can also be grouped based on their base material into polymers, metals and ceramics. Table 2.1 summarizes the main advantages and disadvantages presented by these three types of cellular materials [19].

Table 2.1 Main advantages and disadvantages presented by polymeric, metal and ceramic foams [19].

	Polymeric	Metal	Ceramic
Advantages	Lightweight Soundproofing Thermal insulating High flexibility	High energy absorption Ductility Recyclable	High thermal stability Stable in corrosive environments
Disadvantages	Poor thermal stability	Heavy High corrosion Low flexibility	Low ductility

The selection of the type of the base material depends on the in-service conditions and on the required properties. Hereafter, only polymeric and metal cellular materials will be described, since these are the ones used in the scope of this thesis.

Cellular polymers

The first cellular polymer to be commercialized was a sponge rubber developed in 1914. Polystyrene foam (PS) was developed in 1931 by the Swedish Engineers Munters and Tandberg, followed by the PU in 1937 by Dr Otoo Bayer. Epoxy foams (EP) were first developed in 1949 for encapsulation of electronic components [20–22]. Currently, polymeric foams are part of the modern world, being the most manufactured type of foams. They can be found everywhere, in common daily products like disposable packaging, cushioning of furniture, mattress and seats, and acoustic and thermal insulation material [23–25]. Data from 2013 indicates that, among the cellular polymers, in terms of the amount consumed, PU occupies the largest foam market share (53%) and PS is the second one (26%) [23]. The low density (ranging from dozens to hundreds of kg/m^3 , usually located within 1-800 kg/m^3 [26], high flexibility, low thermal conductivity (0.20-0.40 $\text{W/m}\cdot\text{K}$ for polymeric foams typically used in housing insulation), good sound absorption, easy manufacturing, high ability to hold micro or nanofillers and capability for surface modification and functionalization make this type of materials suitable to be applied in many engineering applications [27]. However, they have poor thermal stability and are fire hazardous. In fire case situations, polymeric foams usually release toxic gases and burn extensively accompanied by dripping [28,29]. Polymeric foams can be classified according to their stiffness and density. Polymeric foams with low Young modulus (YM) values are designated by flexible (inferior than 68 MPa), semi-rigid (between 68 and 686 MPa) and rigid (above 686 MPa) [30]. Figure 2.3 shows a graphical image with the main applications of polymeric foams based in density and stiffness.

The preparation of polymeric foams can be performed by three different foaming processes:

- Mechanical foaming – the air bubbles are formed by external mechanical action;
- Physical foaming – low-boiling-point liquid and a polymer are blended and then foamed through pressuring and heating;
- Chemical foaming – this foaming technique can occur by the addition of a blowing to a molten polymer followed to its decomposition and gas release or by chemical reactions between two polymers with gas formation [22,31].

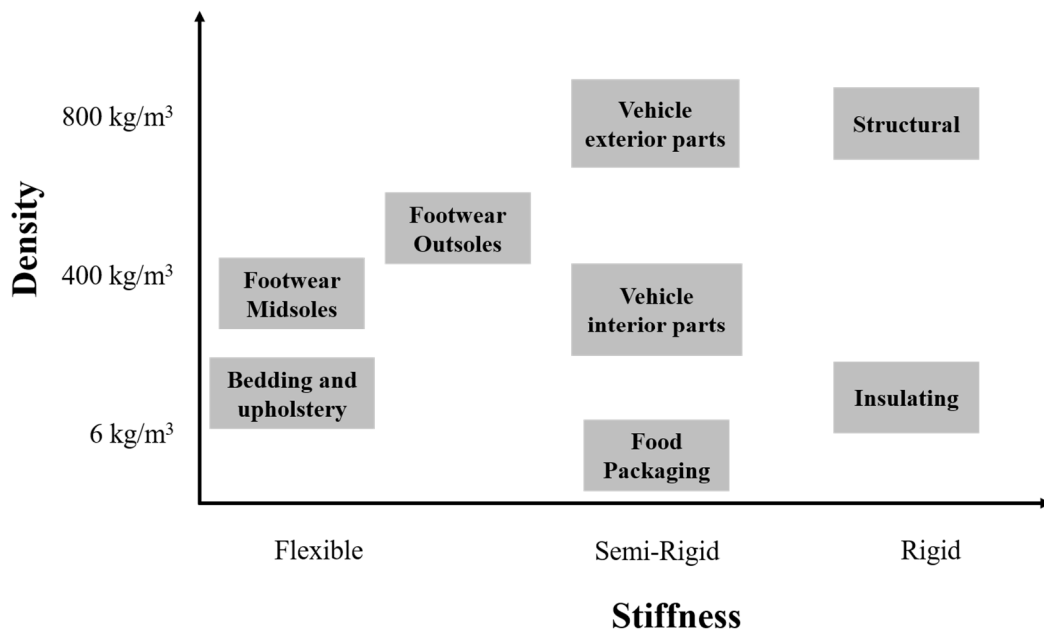


Figure 2.3 Polymeric foams applications according density and stiffness.

The foaming usually occurs at three stages (bubble nucleation, bubble growth and foam collapse). First, the cell is formed by introducing air or by adding a blowing agent into a molten polymer. The amount of the gas gradually increases accompanied by the increase in pressure inside the cell and when saturation is reached, the gas is released from the mixture, forming the cell nucleus. Foam collapse can occur due to the high pressure felt inside the small cells that can lead to the gas escape to the neighbouring cells, reaching a point where the foam system becomes unstable. Cells are usually stabilized by cooling or by adding surfactants [22,31].

Two types of blowing agents can be used, chemical or physical blowing agents. The former refers to those in which the gas of expansion is produced by a chemical reaction while, in the latter, the gas is provided to the expansion of the polymer by undergoing an irreversible phase change. This phase change can be a volatilization (change from liquid to gas) or just the release of a compressed gas trapped in a melted polymer mixture [32]. Due to the difficulties in the removal of side-products, chemical foaming is being replaced by physical foaming. Physical foaming dates back to the 90s and involves the saturation of a polymer matrix with a liquid at high pressure followed by a rapid decrease in pressure. This rapid decrease in pressure leads to phase change to a gaseous state, and volume expansion of the gas results in the formation of bubbles inside the polymer matrix.

The lack of hazardous chemical solvents during physical foaming makes this technique a very interesting and well accepted method among research community to produce polymeric foams [24,25]. This environment-friendly techniques can use supercritical fluids (SCFs) as foaming agents [25,33]. Supercritical CO₂ is a good choice because it is stable, non-toxic, non-flammable, low-cost, easy to obtain from air and recycle, and has low critical temperature and moderate critical pressure compared to other supercritical fluids [24,25,33].

The preparation methodology for common synthetic polymeric foams such as, PU, PS, polyethylene (PE), polypropylene (PP), poly(vinyl chloride) (PVC), polycarbonate (PC), poly(methyl methacrylate) (PMMA), is well described in literature as well as their main properties and potential applications [24,25].

To highlight that, besides high flammability, one negative aspect in the use of many synthetic foams is their fossil fuel dependency, since most of raw materials are petroleum based. The concerns over the reduction of petroleum resources due to environment and sustainability concerns led scientists to find alternative raw materials [34,35]. For example, the use of biopolymers from renewable resources is being explored with a particular emphasis to polysaccharides, like cellulose, lignin [36–38], starch, or chitosan [39].

Cellular metals

Metals and alloys can be also produced in the form of cellular materials. Although the first reference to metal foams dates to 1925 with a French patent presented by Meller, its commercialization only started three decades later in the USA [40]. After a period of stagnation due to high cost and difficulties in the manufacturing process [41], metal and alloys foams become again very attractive in the 90's due to the development of new technologies, which enabled their manufacturing at reasonable costs [40].

Globally, when compared to the polymeric foams, the engineering properties of metal foams are superior, for example, the stiffness values can be 1000 times higher, the thermal and electric conductivities are superior, and they are stable at elevated temperatures. In a fire case situation, metal foams will not burn or release toxic fumes. These are recyclable and thus environmentally friendly [41,42], however, metal foams present high corrosion and low flexibility. To date, among metal foams, the Al ones are the most commonly manufactured [17,43,44].

Numerous techniques have been developed for synthesizing metal foams and many classifications are possible according to their features. One possible classification is related to the state of the starting metal: vapour (e.g. direct, chemical and physical vapour deposition), liquid (e.g. foaming direct method), powdered (e.g. indirect foaming method) or from an electrolyte containing metal ions, as reported by Banhart [44]. Closed-cell foams are commonly prepared by direct and indirect foaming methods:

- Injecting an inert gas (e.g. nitrogen) or adding a blowing agent (e.g. titanium hydride) into a molten metal (e.g. Al and Zn) containing ceramic particles (e.g. calcium, alumina, silicon carbide) to enhance the viscosity of the melt, avoiding the burst of the formed or injected bubbles;
- Heating a foamable precursor material at temperatures close to the melting temperature of its metallic matrix which is prepared by the hot compaction (e.g. extrusion) of a mixture of the metallic (e.g. magnesium and Al alloys) and blowing agent powders (e.g. titanium hydride).

On the other hand, open-cell foams are commonly prepared by investment casting and direct vapour deposition:

- Producing a ceramic mould (e.g. plaster) from a wax or polymeric foam precursor with the desirable cell size and density foam, followed by the burning-out of the precursor, leaving behind a negative image of the foam with open channels which is infiltrated with liquid metal (e.g. Al, Mg, Ni-Cr, Cu and stainless steel);
- Vapour phase deposition or electrodeposition of metal onto a polymer foam that undergoes burning, leaving cell edges with hollow cores (Ni, Ti) [41–45].

The unusual combination of the properties of closed cell metal foams, namely high stiffness-to-weight ratio, high impact energy absorption capacity at low stresses (large compressive strains at near constant) and good damping (vibration attenuation) properties make these foams interesting for structural applications in automotive, aerospace, building, railway, ship and biomedical industries and also in machine construction and sport equipment [17,43,44]. Functional cellular metals are associated to open-cell metals and find applications in filtration processes, as supports in catalysis, heat exchangers, storage devices, electrodes and water purification. Furthermore, more recently, metal foams have been used as decoration pieces and art due to the visually pleasing properties [17,41–45]. Besides,

cellular metals are being studied to be applied in biomedical field, as bone implants devices [46]. More information concerning existing cellular metal material and their applications are highlight in [17,46,47]. Figure 2.4 shows the applications regarding the type of porosity.

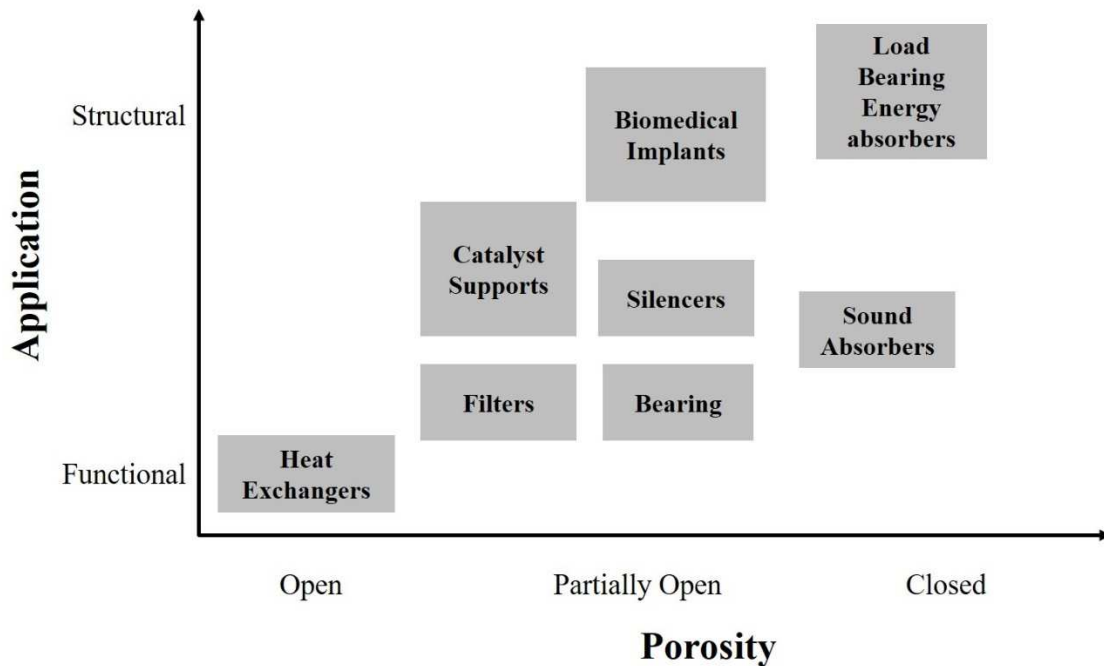


Figure 2.4 Applications of cellular metals according to their porosity (adapted from [17]).

Two other sub-groups of important engineering materials have been emerged: cellular composites and cellular nanocomposites.

In order to increase the high structural efficiency and capacity to absorb energy under both impact and sound of the existing cellular materials, without compromising its weight, scientists have been developing composite and nanocomposite cellular materials by incorporating micro-reinforcement (e.g. alumina and silicon carbide) or nano reinforcement (e.g. cellulose nanofibers, metal oxide nanoparticles, carbon nanotubes (CNTs), GBMs into the base material [24,48–50]. In fact, the nanomaterials, defined by having at least one nanometric dimension, are considered the 21st material of election to be incorporated in polymers and metals [51].

Carbon nanostructures (e.g. CNTs, carbon fibres and GBMs) have been widely used as polymer and metal reinforcement and are well known to increase the mechanical properties, enhancing the thermal and electric conductivity: In the last decade they also started to be

used as fire- and co-fire-retardant agents [24,52]. Regarding how carbon nanostructures incorporation impacts the foaming process, they can act as heterogeneous nucleation sites leading to smaller cell size formation. Furthermore, the incorporation of such nanofillers usually increases the viscosity of the materials, which prevents cell coalescence and further decreases the average cell size. The ability to have more control in the cell size is a matter of big importance as it can have a significant effect on the final properties of the foams [23,25]. There are several studies reporting the use of carbon nanostructures in polymeric foams [24,25,52]. In section 2.3, it will be discussed in detail the effect of GBMs in polymeric nanocomposites. The carbon nanostructures (e.g. graphene and its derivatives) have also been investigated as flame retardants for polymeric foams for enhancing their thermal stability, flammability and fire retardancy, without compromising their mechanical properties.

Concerning the reinforcement of metal foams with carbon nanostructures, Duarte and Ferreira [49] published a review which provides an updated overview of the different manufacturing processes of composite and nanocomposite metal foams. As for polymeric materials, the main challenge is to ensure a uniform dispersion and avoid the formation of clusters resulting from the agglomeration of filler particles. It can be achieved by a proper and strong interfacial bonding between nanofiller and matrix, for example, increasing the compatibility between nanofiller and matrix by surface modification or adding a proper surfactant. Globally, the nanofillers are incorporated at low loading to ensure good and uniform dispersion and their small amount is enough to promote good improvements, due to their outstanding properties of low density, high values of aspect ratio, mechanical strength, thermal and electric conductivities. Duarte *et al.* reported the incorporation of ceramic particles and nanoparticles, fibres and CNTs. The individually dispersed, stretched and random alignment of CNTs efficiently reinforced the Al-matrix of these closed-cell foams [53]. Graphene and its derivatives have been tested and good results were achieved in the mechanical properties [49]. This is a relatively new topic, with few articles published. Graphene was added in the manufacturing process of Al foams and results showed improvements in pore morphology [54] as well as in the tensile and yield strengths [55]. The quasi-static and dynamic compressive deformation behaviour of Al and graphene reinforced Al closed cell foams reported increments of 1.25 to 2.4 in energy absorption in static tests [56].

2.1.3. Stochastic and periodic cellular structures

Due to the urge to create periodic cellular structures with an easily reproducible unit cell to achieve predefined performances, establishing the process–structure–property relationships, several cellular metals have been emerging, leading to new classification. Figure 2.5 presents a scheme of the current classification of the cellular materials considering the arrangement of cells/pores in their cellular structures. The stochastic cellular materials cannot be characterized by a single unit cell while the periodic cellular structures can be described by a single unit cell [9].

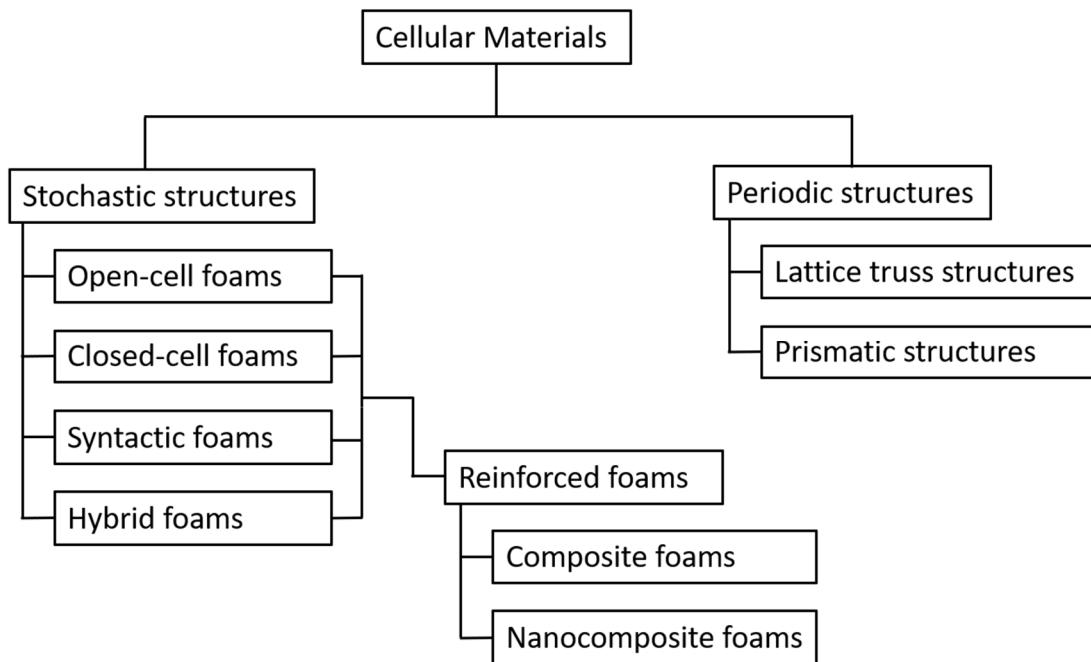


Figure 2.5 Scheme showing cellular classification according to the regularity of cells (reproduced from [9]).

Stochastic cellular materials

Open and closed cell foams and some syntactic foams are examples of the stochastic cellular structures. The difficulty to control the cellular structures (pore size, pore shape, pore size distribution) during the production of these materials, results in random pore sizes and/or in the spatial arrangement of pores [9]. For example, closed-cell Al foams prepared through foaming method (e.g. powder metallurgy or melt foaming) by using blowing agent (e.g. titanium hydride). Both manufacturing processes do not allow a rigorous control of the cellular structures in terms of their pores' shape and size, due to the difficulty to control the thermal decomposition of the blowing agent. Some improvements have been achieved for

the powder metallurgy method through the using of pre-treated blowing agent powder (e.g. titanium hydride) instead of untreated powder, ensuring that the initial decomposition temperature is close to the melting temperature of the metallic matrix [57]. Stochastic polymeric foams are also obtained by the direct and indirect foaming methods with blowing agents [47].

Some syntactic foams are a class of stochastic closed-cell cellular materials, which are developed due to the need to produce porous materials with superior mechanical performance [58,59]. The main advantage is the major control in the process and thus the ability to tailor the structure and consequently the properties. Such syntactic foams are prepared by infiltrating a metal or polymer melt into the interstices spaces of a packed hollow spheres made of metal or ceramic or porous particles [60]. There are a set of materials available either in the choice of the solid matrix and the filler materials (e.g. hollow spheres). The matrix includes molten metals (e.g. Al alloys) and polymers such as thermoplastic and thermoset resins (EP, polyimide, phenolic and silicone). The hollow spheres are, usually, low density metals and their alloys (e.g. aluminium, magnesium, zinc, nickel and copper), and carbonized microballoons [60,61]. Microballoons synthesized from polymeric materials like PU, polyimide, unsaturated polyester, carbamide, or even ceramic micro hollow spheres (e.g. alumina and silicon carbide) may also be used [61]. Expanded glass [62], perlite [63–65] and fly ash cenosphere particles perlite [66–68] are also examples of the filler particles used to prepare syntactic foams.

Recently, greener materials have been developed by Islam and Kim [69]. The authors reported the use of starch, a natural polymer, as a binder of ceramic hollow microspheres. Pumice particles, a low cost natural volcanic glass, are also used as filler material to prepare high metal matrix syntactic foam [70]. In the syntactic foams, parameters such as filler particle properties (e.g. volume fraction, particle size) can be also adjusted in order to tailor the final product with the properties of interest.

Two other sub-groups of important engineering materials have been emerged: cellular composites and cellular nanocomposites. These reinforced cellular materials have been developed through incorporating micro and nano-sized reinforcements into the bulk matrix to improve the properties of the conventional ones. For instance, ceramic micro and nano particles (e.g. alumina and silicon carbide) and carbon nanostructures (e.g. CNTs) have been

explored as mechanical reinforcements to fabricate high-strength metal foams (Duarte and Ferreira, 2010). The carbon nanostructures (e.g. graphene and its derivatives) have also been investigated as flame retardants for polymeric foams for enhancing their thermal stability, flammability and fire retardancy, without compromising their mechanical properties.

In order to enhance the performance of these cellular structures, micro and nanofillers (e.g. CNTs and GBMs) have been introduced in the matrix of syntactic foams [61]. An increase in tensile strength (TS) and modulus of syntactic foams with the addition of graphene platelets (GNPs) has been reported with the maximum strength enhancement of 15.9% attained at a concentration of 0.1 wt.% of GNPs [71]. Otherwise, Ciardiello *et al.* [72] found poor mechanical properties with the incorporation of high content of GNPs (1.0 vol.%) due to agglomeration issues. Comparing syntactic cellular materials with conventional porous materials (open and closed cell foams), high density, low porosity and high strength values were obtained due to the presence of more controlled porosity fraction and oriented spatial distribution [49]. Therefore, syntactic foams fulfil a set of requirements to be used in military and commercial applications. These can be used in various structural components including sandwich composites and in undersea/marine equipment for deep ocean current metering, anti-submarine warfare [58].

Periodic cellular structures

3D periodic structures have been emerged due to the need to create cellular structures with an easily reproducible unit cell to achieve predefined performances, establishing the process–structure–property relationships [73]. Periodic cellular structures are obtained using more expensive and sophisticated additive manufacturing methods, such as rapid prototyping and 3D printing. In 1984 Charles Hull invented the first 3D printing, named at the time of stereo-lithography [74]. In fact, the boost in the fabrication of cellular materials was driven mainly by two reasons: advances in additive manufacturing technologies, and the evolution in basic knowledge of relationship between the properties of cellular materials, mechanical, thermal and acoustic properties and the structure [75]. Furthermore, novel and well-planned design strategies associated with new computational tools (computational power and methods) have been developed and used in the design and to infer the resulting properties, for example anticipate how the materials will behave in multi-loading situations [76]. This allows a better control of the final structure, thus obtaining materials free of or

with less defects. The materials, methods, applications and challenges found in additive manufacturing are well described in literature, with works of Wadley [77], Ngo [78] and Mins [79]. Despite being an already widespread technique for polymers, 3D prototyping of metals is still very expensive. In the 1990s, the German company EOS patented the first metal 3D printing using direct metal laser sintering [74]. According to Evans *et al.* [80], there are two types of periodic structures: lattice trusses and prismatic. In the lattice trusses, all the struts converge to a node, which gives resistance and flexibility to the structures. Trusses have considerable applicability in modern engineering like bridges, scaffolding and other commercial products. Prismatic structures can have different standard cellular topologies such as periodic hexagonal, triangular, square cells, etc. These type of structures cover a range of applications such as light structures, heat exchangers, fuel cell and battery subsystems, energy absorption systems, and others [81] or used as core of sandwich structures [77]. Metal periodic structures, aluminium, copper, nickel, steel and their alloys [82], and lattice structures of polymers, namely polyamide, thermoplastic polyurethane, acrylate resins [83–86], have been fabricated by 3D printing.

2.14. Hybrid cellular structures

Recently, a new advanced type of structure by combining metal foam with other materials has received significant attention. Metal hollow spheres structures (MHSS) and advanced pore morphology (APM) structures are examples of periodic cellular structures with an easily reproducible unit cell to achieve predefined performances. MHSS was developed by Fraunhofer Institute (Dresden, Germany) in collaboration with Glatt Systemtechnik GmbH (Dresden, Germany) and later with hollomet GmbH (Dresden, Germany). MHSS are obtained from (Figure 2.6a) assemblies of hollow spheres adhered or soldered together, resulting in a cellular structure with multifunctional properties. Alternative ways of manufacturing of hollow sphere structures are adhesive bonding of sintered spheres using polymeric or ceramic adhesives as well as brazing or casting. The density, mechanical, acoustic and thermal properties can be adjusted by changing the shell thickness, cell size, sintering temperature, with an heat treatment [87,88]. MHSS have low thermal conductivity, high sound absorption coefficient, relatively high strength allowing the construction of self-supporting elements and a good heat and oxidation resistance. They can be also used as filler or core of thin-walled structures and sandwich panels [89]. Results have demonstrated that

they can be used as crash/impact energy absorbers for vehicles due to exhibit high strength-to-weight and stiffness-to-weight ratios and high energy absorption capacity [89].

New approaches like filling the spheres with phase change materials or coating the spheres with ceramics have been reported, creating multifunctionality and broadening the field of possible applications [87].

Another hybrid structure based on cellular metals was developed using the APM technology patented and by Fraunhofer Institute in Bremen, Germany [90–92]. Advanced Pore morphology (APM) metallic foam elements are simple spheres of closed-cell metal foams, which are fabricated by the powder metallurgy method using the smallest pieces of the precursor material (e.g. 1-2 mm in size). The small precursor sample sizes ensure that surface tension forces during the melting process are relatively large compared to the hydrostatic pressure, forming near spherical shapes with an easily reproducible unit cell. These APM foam elements can be coated by a polymer. The coated APM foam elements can be poured by a mould or by thin-walled structures, fabricated the APM foam-polymer hybrid structures [89]. These APM foam elements can be used bonded or non-bonded (without connecting points). APM foam elements (Figure 2.6b) present a thin solid outer shell, with cores that can range from simple to complex closed-cell internal structure [87]. The mechanical and thermal properties of APM structures strongly depend on the morphometric parameters of the APM foam elements. APMs can be applied for absorbing impact energy, vibration damping, among others [87]. Researchers are trying to provide new insights about these structures. Experimental studies have been performed to evaluate the influence of density and the diameter of the APM foam elements and polymer adhesive (e.g. epoxy and polyamide) [91-93]. Theoretical studies also helped to understand and develop new structures based on APM foam elements. Borovinšek [87] conducted a detailed investigation of how the main parameters affect the compressive behaviour of these hybrid structures by using compression tests together with supported by μ CT, and advanced digital image analysis and recognition. External (e.g. sphere shape and sphere size) and internal factors (e.g. distribution, size, number of closed pores) were studied. The thermal conductivity of such structures was also evaluated [94].

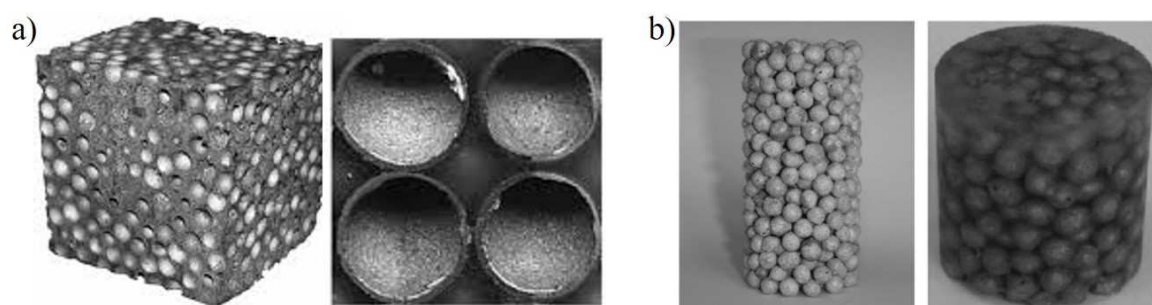


Figure 2.6 MHSS structures (a) [95] and APM elements [96] (b).

Novel hybrid structures based on the filling the pores of foams with other materials have been developed. Often designated by interpenetrating phase composites, IPCs [97], these new types of composites are composed of two different materials that are connected at a macroscopic level. They have interpenetrating structures in which both materials are interconnected three-dimensionally, forming a continuous network throughout the structure. The coexistence of these two materials allows that each component contributes to the enhancement of final properties, offering improved combinations of mechanical and physical properties [98,99]. There are various hybrid structures composed of different constituents, for example ceramic-metal [100], interpenetrating polymer network [101], metal/ceramic foams and metal porous polymer composites (MPPC) [102,103]. Among hybrid structures, the MPPC are the most common material, showing great potential to energy absorption applications without, however, significantly increase its weight. The voids (pores) of closed or open cell metal foams are filled with polymers chosen in accordance with the properties that are pursuit. Literature reports the use of thermosetting polymer [98], thermoplastic polymer [104] or elastomeric rubber [105]. These studies are mainly theoretical, where models are used to predict the mechanical response of materials.

Two studies conducted by Hadley *et al.* [106] and Yuan *et al.* [105] reported the preparation of a hybrid structure consisting of an aluminium foam (Duocell) and thermoplastic polymer. The material was fabricated by injection moulding of a polymer through the aluminium foam, with the polymer occupying the voids of the host foam. The authors found that the final composite exhibited an increase in stiffness, a reduction in strength and less ductility than the “raw” polymer. Also, an aluminium open-cell foam (OCF) was cured with polymeric filling in order to enhance their mechanical compressive response [107]. The quasi-static behaviour results of the dynamic tests showed insignificant changes in the deformation curves in the case of the unfilled open-cell foam and an

increasing energy absorption capacity in the case of the samples filled with the polymeric material. Jhaver and Tippur [103] prepared a hybrid structure by infiltrating uncured epoxy-based synthetic foam into an open-cell aluminium preform, resulting in improved compression characteristics relatively to the conventional synthetic foams. Liu *et al.* [108] studied the mechanical behaviour of Al foam – polyurethane hybrid structure (AF-PU). These composites presented different corresponding porosity and pore size under cyclic compressions and the authors found that the structures with high porosity and large pore size had a good potential for damping devices for seismic resistant structures under the condition of large strain level and preloading several cycles. Wegner and Gibson developed a numerical work to predict the mechanical behaviour and thermal expansion of hybrid structures applying finite element model [109–111].

The work conducted by Su *et al.* [112] established the relation between porous structure and mechanical behaviour of Al foam filled with Polyamide 6 (PA6/Al MPPC) and the Low-Density Polyethylene (LDPE/Al MPPC). An infiltrating technique under negative pressure was applied to fabricate open-cell metal foam and PA6/Al and LDPE/Al MPPCs. The results show that the mechanical properties of PA6/Al and LDPE/Al MPPCs are mainly influenced by the filling polymers, the type of pores, the pore size, the polymer–metal interface, the polymer volume fraction and the distribution of pores, respectively. Reinfried *et al.* [19] join together two cellular materials by filling the voids of an open-cell steel foam with expandable polystyrene (EPS) foam. The resulting structures showed a negligible increase in density and more homogeneous deformation up to a strain of 0.4 (m/m) comparatively to the metal by itself. However, the increase in compressive strength (CS) was small. The impact of silicon rubber pore filling in open-cell aluminium alloy foams with regular [113] and irregular [114] topology or silicone rubber mixtures as pore filler material in an open-cell structure made of photopolymer, FullCure M840 [115], under quasi-static and dynamic compressive loading conditions has been experimentally studied and evaluated. It was observed that the pore filler material increased the capability of energy absorption and furthermore improved and stabilized the response of a cellular structures.

More recently, Duarte and co-workers [116] developed and tested hybrid structures by combining OCF specimens with epoxy resin and silicone rubber (Figure 2.7) and after by incorporating the same into metal fine tubes [117]. Both polymer fillers contributed to the

increase of the compressive response of the hybrid foams and of the energy absorption capacity, being this effect more evident in EP filler (Figure 2.7c).

The studies performed concerning the combination of aluminium OCF with polymers were mainly focused on the mechanical characterization. There is no substantial data regarding acoustic and thermal applications or in diversifying the type of filling material.

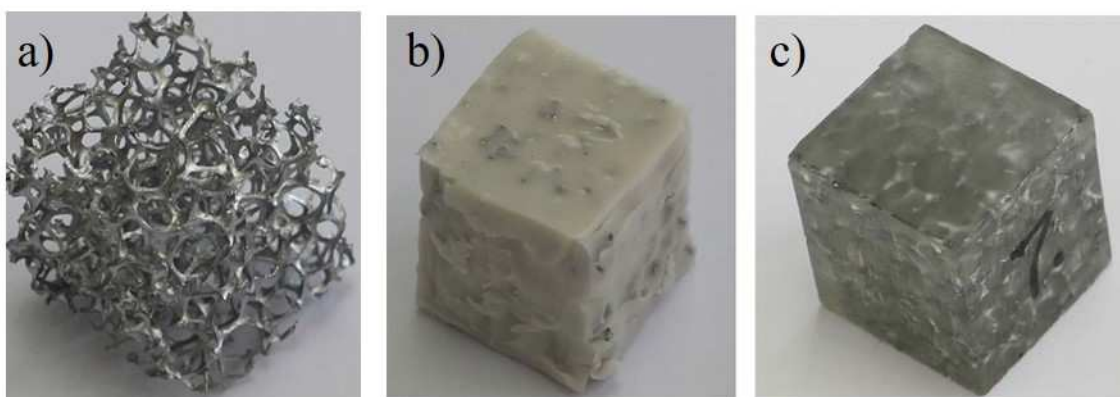


Figure 2.7 Open-cell metal foam (a) silicone filled open-cell foam and (b) epoxy open-cell filled foam (c) (adapted from [116]).

2.2. Polymers and polymeric nanocomposites

Polymers can be categorized into thermoplastic, thermoset and elastomers. Thermoplastic materials are commonly named of plastics and are characterized by long linear or slightly branched chains with relatively weak intermolecular bonds. They become mouldable at high temperatures and solidify after cooling. Multiple cycles of heating and cooling can be repeated, allowing reprocessing and recycling. As examples, it can be pointed PE, PP, PVC, being applied in toys, bottles and sports equipment, among others. Thermosetting polymers have a 3D network with high degree of cross-linking between polymer chains, which translates in high rigidity. When heated, thermosetting polymers do not melt, however undergo decomposition and do not return to its initial shape. These polymers maintain their strength and shape even when heated and are used to fabricate solid and durable components in polymeric coatings, dental fillings, polymeric reinforced composites. As examples it can be pointed EP, phenolics and polyamides. Elastomers are low crosslinked polymers with high elasticity and flexibility due to its weak intermolecular forces. Thereby elastomers generally present low YM and high failure strain compared with other thermosetting. Natural

rubber used in shoes heels, neoprene in wetsuits fabrication and polydimethylsiloxane in prosthesis, lubricants, are some examples of elastomers [118].

Among the type of nanocomposites, polymer nanocomposites are widely used as they can offer a wide range of improved properties, such as mechanical, thermal, optical and electrical, and thus, extending even more the range of applications [23,25,119-121]. Nevertheless, the surface of some nanoparticles is inert and the difference of polarity between them and the polymer matrices make their dispersion at the nanometer level, not straightforward [122-124]. Often, it is required a surface modification of the nanofillers and/or of the polymers in order to improve the compatibility between both. Many functionalization methods (chemical or physical) have been used and reported in literature and its choice is based on properties of the matrix where the fillers will be incorporated [122,125–129].

There are three main methods to prepare polymer nanocomposites: solvent casting, melt-blending and in-situ polymerization. In solvent casting, the polymer, the nanoparticles and the solvent are well mixed together and then a thin film is formed after solvent evaporation. It is worthy to mention that the solvent should dissolve completely the polymer and disperse well the nanoparticles. The role of the solvent is to allow the mobility of the polymer chains and endorse possible the intercalation between polymer chains and the nanoparticles. The melt-blending can be achieved using an internal mixer or extruder. The polymer and the nanoparticles are introduced in the extruder and subjected to an intense power mixing. In the case of in-situ polymerization, the monomer is grown at or from the nanoparticles surface. In this case, the polymer-modified nanoparticles are then mixed with the polymer matrix (of the same type of the polymer grown at the nanoparticles surface) increasing the compatibility between both [119,130,131]. Layer-by-layer (LbL) assembly of oppositely charged polymers into films and coatings is a versatile way of surface modification used to fabricate a layered structure. LbL-deposited films were first prepared in the early 1990s by the alternate deposition of cationic and anionic polymers through electrostatic interactions [132]. In this approach polymeric materials are linked to each other through attractive forces including electrostatic interactions, hydrogen bonds, covalent bonds, molecular recognition, and biological affinity. Recently it was demonstrated that GO can be assembled with other materials by LbL to produce dense polymer composites [133,134].

2.3. Graphene based materials

Graphene was firstly isolated in 2004 by Novoselov and Geim when they used pieces of sticky tape to pull off flakes of graphite and separated few layers of graphene. The impact of their discovery was so relevant that earned them the attribution of the Nobel Prize. Graphene can be produced by top-down routes, using graphite as raw material, and/or bottom-up approaches, using alternative carbon sources as raw material, such as ethanol, or methane between others, that after atomization allow graphene growth in a suitable substrate. Graphite is the most thermodynamically stable form of carbon at room temperature and has a layered and planar structure. In each layer, the carbon elements are distributed in a hexagonal lattice arrangement [135]. Graphene is a one-atom-thick planar sheet of sp^2 -bonded carbon atoms that are densely packed in a honeycomb crystal lattice. It possesses extraordinary physical properties, associated with its monolayer of covalently bonded carbon atoms. When multi layers of graphene are densely packed it receives the name of graphene nanoplatelets (GNPs). GO, a derivative of graphene, is receiving much attention since the upsurge of graphene research. It can be obtained from graphite in two steps, oxidation and exfoliation. The first step is the chemical oxidation (with strong acids) of graphite into graphite oxide, followed by simple stirring or mild sonication (mechanical process) to exfoliated graphite oxide into single layers. Thus, GO is an atomic sheet of graphite with several oxygenated functional groups (carboxylic, hydroxyl and epoxy) on its basal planes and at its edges, resulting in a hybrid structure of sp^2 and sp^3 configurations. The high oxygen content has been demonstrated to be very interesting for the chemical modification/functionalization with other molecules, thus allowing the creation of nanocomposites with interesting properties [136–138]. Globally, GO retains plenty of the properties of the graphene, but it is much easier and cheaper to prepare in bulk quantities and easier to process (better dispersion in different solvents). In fact, the chemical exfoliation of graphite in oxidative medium originates stable aqueous suspensions of GO. Brodie, Staudenmeier and Hummers *et al.* [138], developed the first procedures for the synthesis of GO that are still used today with minor modifications.

Depending on the practical application of GO, for example for electrical or thermal applications or even just due to compatibility issues, a reduced form can be more suitable to be incorporated in a matrix. Reduced graphene oxide (rGO) can be obtained by chemical, thermal, microwave, photo-chemical, photo-thermal or microbial/bacterial methods [139],

where the material can recover partial or complete hybridized sp^2 configuration [123,136,137,140–142], thus approaching to the graphene configuration [143].

Due to the already mentioned variety of GBMs, the term ‘graphene’ is often used in a generic manner to describe indifferently each of these nanostructures, thus creating misinterpretations about its properties [144–146].

Owing to the chemical and to the chemical and structural features presented by each GBMs, they have different properties that make them promising additives for specific applications. The most fundamental properties of GBMs to consider are: i) number of graphene layers, ii) average lateral size and iii) oxygen content (with a variable carbon-to-oxygen (C/O) atomic ratio) [144]. The scheme presented in Figure 2.8 helps to visualize the categorization of different graphene types according to the three fundamental GBMs properties mentioned previously [147].

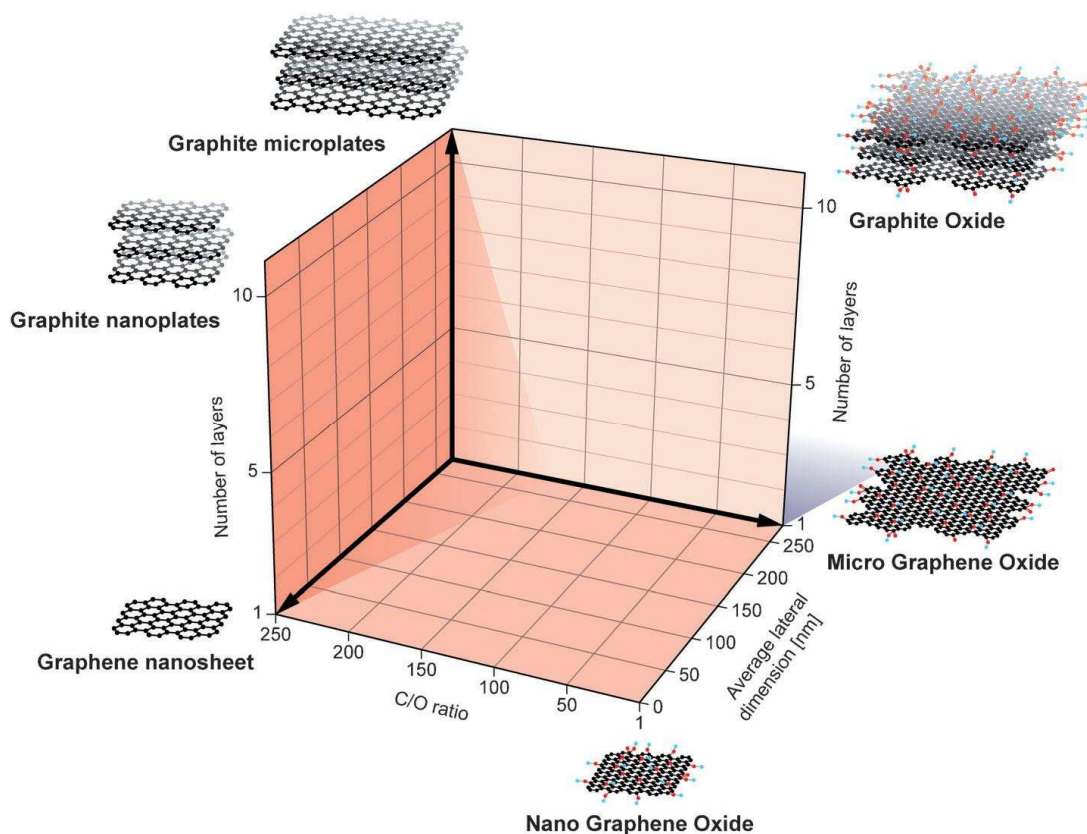


Figure 2.8 Classification grid for the categorization of different graphene types according to three fundamental GBM properties. The different materials drawn at the six corners of the box represent the ideal cases according to the lateral dimensions and the number of layers reported in the literature. The values of the three axes are related to the GBMs at the nanoscale, but it is feasible to expand the values to the microscale.

Reproduced from [147].

Although the wide use of GBMs as reinforcement in metals or ceramics, it is in polymeric matrices that they have been extensively incorporated. For example, as mechanical reinforcement, thermal conductivity and sound absorption enhancers in several, cellular or dense polymer composites envisaging structural applications in aerospace, construction, and automotive sectors [129]. Also, other properties of interest have been explored with the use of graphene and GO in composites, namely their ability to confer or improve fire-retardancy [129].

It is worth to mention that GBMs have been used successfully in other areas like water treatment, energy storage or even in the biomedical field [148].

Often, it is required the surface modification of the GBMs and/or of the polymers in order to improve the compatibility between both, making the dispersion of GBMs easier and efficient and therefore promoting stronger interactions [122-124]. Many functionalization methods (chemical, e.g. covalent bonding or physical, e.g. electrostatic interactions) have been reported in literature and its choice is based on properties of the matrix where the fillers will be incorporated [122,125-129].

2.3.1. GBMs impact on the mechanical properties

As mentioned before, due to the outstanding properties of graphene (YM of 1 TPa and an intrinsic TS of 130.5 GPa [148,148]), and its derivatives GO and rGO (YM value depending on the number of oxygen groups and structural defects), these nanofillers are being widely used as mechanical reinforcers in several polymeric composites [148]. The good dispersion of the nanofillers is the key to ensure an efficient load transfer and thus improve mechanical properties. Many times, the formation of voids due to the increase of viscosity of polymeric matrices with the addition of such nanofillers is verified and hence the enclosed air cannot be removed [122]. The literature is full of good examples describing the enhancement of mechanical properties by the incorporation of GBMs. The incorporation of GO or in some cases functionalized GO (to improve the compatibility between the matrix and the filler) in EP [150–155], polyethylene succinate (PES) [156,157], PS [158], PU [159,160], PDMS [161,162] matrices was studied. Overall, the results showed great enhancements in the mechanical properties of the final nanocomposite where the level of the nanofiller dispersion is crucial. Globally, loadings below 1 wt.% are enough to achieve large improvements in the TS and YM modulus of bulk polymeric composites. The great interest and research in this

area can be translated in the amount of reviews found through the last decade describing the preparation methods and the impact on the main properties [163–165].

Hsu *et al.* [155] studied the effect of using thermally reduced GO to reinforce an EP matrix. rGO with different amount of oxygen functional groups were used to prepare the EP/rGO nanocomposites. The results showed a better dispersion capability of the rGO with higher oxygen-containing group contents in the polymeric matrix, resulting in a significantly enhanced mechanical strength, thermal stability and thermal conductivity. These results highlight the importance of the oxygen functional groups presence to increase the compatibility and thus, the dispersion of this nanofiller in the EP matrix. Abdullah *et al.* [150] reported the addition of 1.5 vol.% of GO to an EP matrix and the TS and YM were increased by 85% and 45%, respectively. The effect of the incorporation of GO in mechanical behaviour of EP nanocomposites has been also studied by Bortz *et al.* [151], who reported an enhancement in TS of about 20% with the addition of a small amount of GO (0.1 wt.%).

In a study conducted by Balasubramanian, 0.5 vol.% of GO was incorporated to poly ether sulphone (PES). The results showed that the addition of GO to PES enhanced the TS and flexural modulus by 40% and 90%, respectively, due to the formation of continuous network, good dispersion and strong interfacial interactions [156].

Qiu *et al.* [158] incorporated GO functionalized with a novel organophosphorus oligomer (OPO-GO) into PS to enhance its dispersion and consequently enhance the performance of the matrix. The results showed that the introduction of 1 wt.% of OPO-GO increased the TS by 25% with respect to the polymer alone. The importance of the surface functionalization of GO to increase its dispersion in the polymer matrix was also highlighted by Wan *et al.* [152] who filled EP composites with GO and diglycidyl ether of bisphenol-A functionalized GO (DGEBA-GO) sheets at different filler loading levels. The results indicated that the DGEBA-GO/EP nanocomposites showed higher tensile modulus and strength than either the neat EP or the GO/EP.

Zhang *et al.* [160] introduced GO into a bio-based PU and the results showed that although the elongation at break increased by 103% with incorporation of 0.4 wt.% GO, insignificant changes in both mechanical strength and modulus were observed. Waterborne PU with rGO nanocomposites were prepared by Hu *et al.* [159] who found that although the

elongation at break decreases with increasing rGO content, the strength of the nanocomposites was rather increased. Wang *et al.* [154] incorporated nanosilica/GO (GO-NS) hybrid into EP resin and at 1 wt.% of GO-NS content the TS was increased. Forati *et al.* [157] prepared polyethersulfone (PES/GO) nanocomposite films by casting method. Tensile test showed a significant enhancement in the TS of PES films when incorporating a small amount of GO loading (1 wt.%). The incorporation of GNPs into polymer matrix was also reported, for example in PU, PVA [130] and EP [166–170] nanocomposites.

The incorporation of GBMs into polymeric foams is more recent, it reports to the last decade. GBMs started to be added to foams formulations providing to the final product superior physical and mechanical properties [171,172]. Zhou *et al.* [173] synthesized phenolic foam reinforced with GO. The results revealed that the impact toughness increased along with the GO content, with a significant enhancement when the amount reached 0.5 wt.%. Poly(propylene carbonate)/GO nanocomposite foams were prepared by Yang *et al.* [174] using supercritical CO₂ method and the results demonstrated an increase of 650% in the CS for 40% of compressive strain, after the incorporation of 1 wt.% GO in neat polypropylene carbonate. Reinforced foams based in PMMA/GO materials were prepared by Li *et al.* [175] using CO₂ as foaming agent. The compressive tests showed an enhancement in compression strength of 3 times with 1.5 wt.% GO compared with neat foam material. The addition of GBMs to PUF was also studied and for this different approaches were used: adding GBMs in powder form to the polyol [176], modifying the polyol or diisocyanate reagents used in the PUF manufacturing process with GBMs [177,178] or even impregnated (soaking) or coating the PUF with GBMs [179]. The GBMs can act as a nucleating point for the formation of the pores with smaller dimensions than the ones obtained in pristine PUF. Also, when the size of GBMs is small they locate in the struts or join struts and when there are dimensionally bigger, they stay in the pores. The tuning of pore size and cell walls thickness changes the mechanical properties, as well as other properties.

Table 2.2 summarizes the improvements in mechanical properties, tensile strength (TS), compressive strength (CS), Elongation at break (EB) and Young modulus (YM) for polymeric based materials reinforced with GBMs.

Table 2.2 Literature survey of polymer composites mechanically reinforced with GBMs. The % enhancement is with respect to the net polymer.

Polymer	GBMs concentration (%)	Property	Increase (%)	Reference
EP	GO 1.5 vol.	TS	85	[150]
PES	GO 1.5 vol.	TS	45	[156]
EP	GO 0.1 wt.	TS	20	[151]
PS	GO-OPO 1 wt.	TS	25	[158]
EP	GO-DGEBA 0.1 wt.	TS	79	[152]
PU	GO 0.4 wt.	EB	132	[160]
EP	GO 4 wt.	CS	33.5	[153]
WPU	rGO 2 wt.	TS	750	[159]
EP	GO 1 wt. GO-NS 1 wt.	TS	22 26	[154]
PES	GO 1 wt.	TS	81	[157]
PVA	graphene 1.8 vol.	TS	150	[180]
EP	TRGO 3.7 vol.	TS	105	[155]
PU	graphene 0.5 wt.	TS	28	[166]
TPU	graphene 5.1 vol.	YM	200	[181]
PPC foam	GO 1 wt.	CS	670	[174]
PMMA foam	GO 1.5 wt.	CS	200	[175]
PU foam	GNS 0.3 wt.	CS	32	[176]
PU foam	Nanoporous graphene 0.25 wt.	CS	10.7	[177]
PU foam	rUL-GO 1 wt.	TS	250	[178]
Cellulose	GON _s 0.1 wt.	CS	30	[30]
CMC	GO 5 wt.	CS	62	[30]

2.3.2. GBMs impact on thermal conductivity

One of the main applications of polymer/GBMs nanocomposites are as electrical and thermal conductive properties [182]. While graphene is widely used as thermal conductivity enhancer [183] (thermal conductivity of 3000-5000 W/m·K, in-plane thermal conductivity)

particularly to dissipate heat in electronic devices, the application of GO in the thermal conductivity enhancement of dense polymer composite is limited due to its highly oxygenated structure. In fact, GO has a very low thermal conductivity of 0.5–1 W/m·K [148]. The oxygen functional groups of GO trap electrons and block charge transport, thus hindering the flow propagation. However, some studies reported that the use of GO in polymer matrix can be advantageous to enhance the thermal conductivity since the oxygen functionalities promotes a better dispersion and the bonding between nanofiller and polymer is stronger, creating a path and facilitating the energy/thermal flow [184]. Overall the majority of the studies reported that, in order to make conductive dense nanocomposites, GO needs to be subjected to some type of modification/reduction and, for that, several strategies have been adopted to either reduce GO *ex situ*, before the preparation, or in situ during the preparation of the nanocomposites [185,186].

The effect of modified GO in EP resin was studied by many researchers for thermal conductivity enhancers purposes. Research conducted by Zhou *et al.* [187] showed that by adding 2 wt.% of multi-layer GO to an EP resin, the thermal conductivity of the composite increased by 100% comparing to the neat polymer. Wang *et al.* incorporated as-prepared nanosilica/GO (GO-NS) hybrid into EP resin and observed an increase in thermal conductivity. Specifically, the enhancement in thermal conductivity of the modified EP resin with 1.5 wt.% GO-NS was increased by 38% of that of neat EP resin [154]. The concomitant addition of GO and CNTs to poly(vinylidene fluoride) (PVDF) was explored by Zhang *et al.* [188]. They incorporated GO into PVDF/CNTs (10 wt.% of CNTs) and the results demonstrated that with only 1 wt.% GO addition, the PVDF/CNT/GO nanocomposites exhibited largely enhanced thermal conductivity compared with the PVDF/CNTs nanocomposites, at the same CNT content. They also concluded that the GO and CNTs have a great synergetic effect in the thermal conductivity improvement. Im *et al.* studied the thermal conductivity of GO/CNTs/EP nanocomposite materials. The results showed that thermal transport properties of the nanocomposites were maximized at 50 wt.% of filler (0.36 wt.% of CNTs and 49.64 wt.% of GO) with an enhancement of 100% [189]. Table 2.3 gathers some examples, however more studies can be found in literature reviews [190,191]. An increase up to 103% in thermal conductivity was reported by Ribeiro *et al.* [192], when they introduced 0.5 wt.% of modified GO with tetraethylenepentamine into EP matrix.

The effect of GBMs in polymeric foams is not easy to predict since the introduction of fillers not only alters the cell wall material but also has great influence on the pores size and morphology as reported [193,194]. The thermal conductivity value is the result of three main contributions: heat flow in the cell walls and struts, heat flow in the gas trapped in the pores and radiation between the cell walls, with the latter contribution being neglected. In cellular materials, the parameters that mainly contribute to thermal conductivity is the porosity (pore size and alignment) and cell wall material. Therefore, the changes by the incorporation of low loading of GBMs are usually small, as seen in Table 2.3. However, as one of the main applications of cellular materials is as insulating materials to the energy efficiency of buildings, keeping the thermal conductivity low can be beneficial [195]. Table 2.3 gathers thermal conductivity enhancing with GBMs incorporation in polymeric based materials.

Table 2.3 Literature survey of thermal conductivity improvement in polymeric/graphene nanocomposites.

Polymer	GO concentration (wt. %)	Increase (%)	Reference
EP	GO-NS 1.5	38	[154]
EP	MGO 2	100	[187]
PVDF	CNTs 10 /GO 1	332	[188]
EP	GO-TEPA 0.5	103	[192]
EP	(MWCNTs/GO)50	100	[189]
EP	GNPs 3	20	[196]
PU	GNPs 3	16	[169]
EP	TRGO 1	31	[155]
PU foam	GNS 0.3	-3	[176]
PU foam	GO 0.3	+2	[197]
PU foam	GO 0.033	+5	[193]

2.3.3. GBMs impact on sound absorption

Noise pollution is a serious problem in the modern world as a result of the quick development of industry, highway roads, train and plane traffic. Therefore, it is imperative to reduce noise for the wellbeing of people. Several approaches have been tested aiming the preparation of materials for damping and noise reduction in order to contribute to a healthy

environment. To achieve excellent sound-insulation property, many efforts were committed in the design and fabrication of ordered porous structures. Porous structures [198], such as, cellular materials, have superior sound insulation performance, since high dissipation occurs resulting from the friction between air flowing in and out of the cells [199] [200]. Several composites has been developed, namely wood-waste tire rubber composite, inorganic particles/polymer composites and nanocomposites, resin/hollow glass bead, poly(vinyl chloride)/mica, rubber/CNTs, polyvinylpyrrolidone/GO and so on [201]. Recently, GBMs were proved to be good nanofillers in cellular materials for sound insulating. The capacity of sound damping associated with cellular materials, like porous and honeycombs structures, has been recently improved by adding GBMs. For example, the incorporation of 0.2 wt.% of graphene in PUF led to sound absorption coefficient of 0.52 in the frequency range between 1600-2500 Hz, representing an improvement of 18% compared with pristine PUF [202]. The averaged sound absorption coefficient from 800 Hz to 6300 Hz was increased more than four times by impregnating with 15 wt.% of GO, for PUF specimens with 5 mm of thickness with density of 51 kg/m³ [203]. However, Verdejo *et al.* reported a negative influence of graphene (0.25 wt.%), and CNTs (1 wt.%) addition to a polymeric foam on damping and acoustic absorption since GBMs can alter the porous structure and stiffness in the raising process of foaming. A self-aligned and hierarchically porous graphene-PUF fabricated by electrostatic repulsion mechanism and with high sound absorption coefficient was described by Jung-Hwan *et al.* [204].

2.3.4. GBMs as fire-retardants

In spite of the huge potential for various applications presented by polymeric composites, most of them are flammable and failed in standard fire tests [25,205]. Furthermore, most of polymeric materials release toxic gases and exhibit dripping during burning. As so, concerning safety and public health, usually polymeric materials need to be submitted to some modifications in order to make them less prone to burn without being too costly. Thus, it is crucial to understand how all individual components behave in fire situations [206,207]. The phenomena that occur in the flame combustion in polymeric materials are represented in Figure 2.9. Four distinct zones can be found: the gas phase or flame zone, the char layer, the condensed region assigned to molten polymer and the underlying zone that remains intact. After an ignition source, some polymer degradation at polymer surface (molten polymer) takes place releasing some volatiles species. Simultaneously, a char layer,

originated by the post-pyrolyzed material, started to be formed delaying or avoiding the passage of the volatiles.

The flammability concept is associated with the response of a material to a small flame and it is an important topic concerning the several applications of the polymeric materials, such as in the field of electrical engineering, automotive, construction, aerospace, amongst others [208,209]. The fire-retardant performance of polymer composites is usually evaluated by three tests: UL 94 (vertical and horizontal) burner test, LOI (limiting oxygen index) and cone calorimetry assays [210,211]. All these tests should follow standard legislation, UL 94 – ASTM D 3801; LOI – ASTM D2863 or ISO 4589; Cone calorimetry – ISO 5660 or ASTM E-1354.

In LOI test, the minimum oxygen concentration required to assess the combustion of the material specimen during, at least, 3 min or the consumption of 5 cm of the specimen is evaluated. The higher LOI value, the better flame retardancy property of the material [210,211]. Cone calorimetry is one of the most complete and realistic test to predict fire-retardancy response of materials, providing simultaneously quantitative and qualitative data [212]. One of the most important parameters that can be obtained in cone calorimetry assay is peak heat rate release (PHRR) that represents the point in a fire where heat can propagate further or ignite adjacent objects. Other parameters can be obtained from this test like total heat release (THR), time to ignition (TTI), among others [210,213,214].

The positive effect of CNTs [215–219] and more recently GBMs [172,220–222] in the fire-retardancy behaviour of polymeric materials (for example EP, PVA, PLA) is documented in several studies. Interestingly, the addition of small quantities of nanofillers (between 0.5 and 10 wt.%), was proved to have a noticeable impact on the fire-retardancy of the host polymer [24,131,223–225]. GBMs emerged as good candidates and started to be explored for enhancement of the flame-retardant properties of various polymer composites [24,226,227], suppressing the limitations presented by some of the traditional fire-retardants, such as weakness of the mechanical properties, smoke release and emission of toxic gases.

The flame-retarding behaviour of GBMs can be attributed to their ability to form a continuous, protective char layer that acts as thermal insulator and barrier to mass transport [222,228,229], schematized on Figure 2.9. Furthermore, due to GBMs structure, they can act as templating substrates to char growth allowing the formation of multiple and overlapped,

stable and protective carbonaceous layers. The high superficial area of GBMs promotes the adsorption of flammable gases. In the particular case of GO, the oxygen groups, under temperature, can dehydrate and dilute the oxygen content around the ignition as well as absorb heat enabling the cooling down of the polymer surface [230,231].

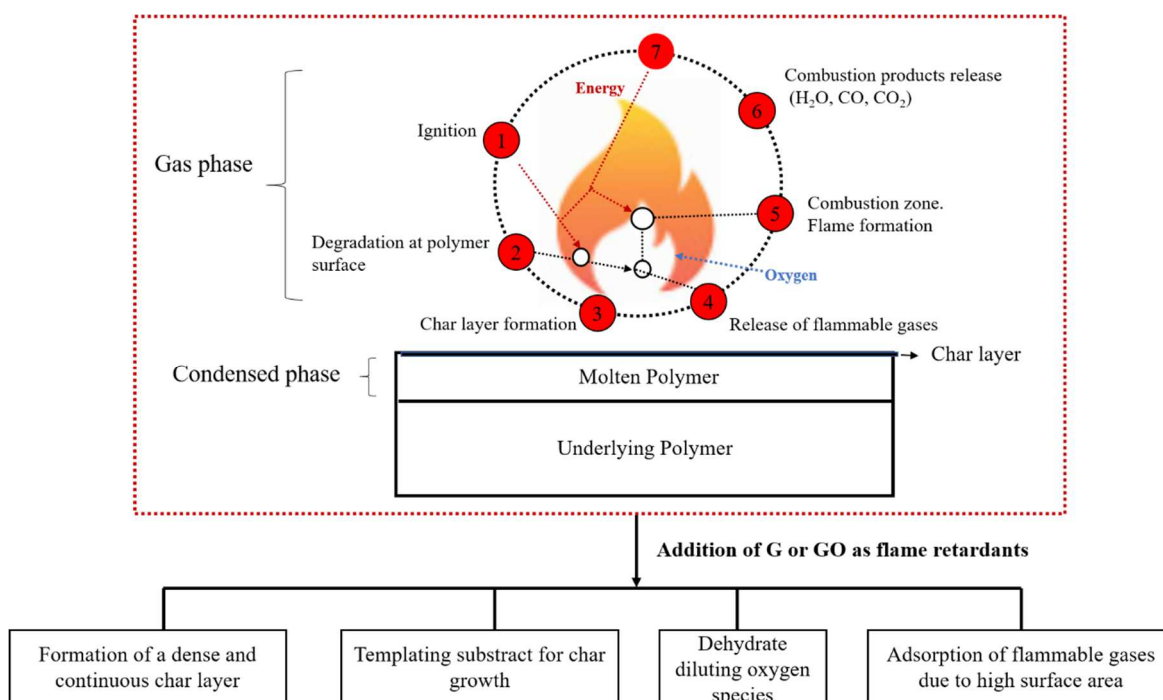


Figure 2.9 Scheme of fire-retardancy behaviour with and without graphene/graphene oxide (adapted from [222]).

When the addition of GBMs is not enough to meet the requirements of a certain application, two approaches have been attempted. In one of the cases, in addition to the carbon-based nanofillers, a traditional fire-retardant agent (IFRs) is also added directly during the mixing process of the composite, taking advantage of the synergetic effect of both compounds. The most common IFRs additives include halogen, phosphorus and nitrogen compounds, more specifically: boric acid; ammonium phosphates and borates; ammonium sulphate and chloride; zinc chloride and borate; phosphoric acid; dicyanodiamide; sodium borate; and antimony oxide [232,233]. Another approach is to functionalize the carbon nanostructures with conventional flame retardants and then incorporate them in the polymeric matrix [25,234,235]. In this case, a better dispersion of the fillers in the matrix can be achieved and simultaneously the fire-retardancy can be improved. Some examples of each situation are reported in Table 2.4. Overall, the compilation of the results in Table 2.4 shows that better results are obtained when the graphene or GO are combined with

conventional fire-retardants or if the structure of GO is covalently modified by organic molecules such as organo-phosphorus, melamine compounds.

Although GBMs are already reported as fire-retardant additives for polymers, in the particular case of polymeric foams combined with GBMs to improve fire-retardancy, the studies reported almost exclusively the use of expanded graphite. Recently, Wicklein *et al.* [172] prepared a novel fire-retardant and insulating foam material by freeze-casting of suspensions of cellulose nanofibers, GO, boric acid (BA) and sepiolite nanorods. All the components contribute to protecting the nanocellulose from self-igniting, resulting in a fire-retardant material with a better combustion resistance than polymer foams that contain halogenated flame retardants. Phosphorous hybridized graphene nanosheets at high loading were also tested against fire-retardancy in cellulose foams and results showed great improvements. More recently, GO and functionalized GO have been added to PUF [236,237]. A different strategy was reported by Zhang *et al.* [238], where a coating of several layers of GO (8.3 wt.%) in the PU foam provided fire-resistance, suggesting that the GO nanosheet is a good candidate as a flame-retardant LbL coating to reduce the flammability of PU foam.

Table 2.4 Literature survey of fire-retardancy improvement in polymer/graphene nanocomposites.

Polymer matrix	Filler	Concentration (wt.%)	Increase (%)		Decrease (%)		Reference
			LOI	TTI	PHRR	THR	
GBMs							
PVA^a	GNSs	1		39	43	5.2	[221]
		3		83	49	22	
		5		150	64	35	
EP	GNSs	0.5	20		-19	11	[239]
		1	23		-10	13	
		3	32		-5	16	
		5	35		-8	17	
WPU^a	rGO (with hydrazine)	1			16	18	[159]
		2			22	20	
EP^b	GO	1		15	10	40	[224]
PLA^a	G	2			40		[240]
PU foam	GO	12					[241]
	rGO	12					

Chapter 2

Table 2.4 *Cont.*

Polymer matrix	Filler	Concentration (wt. %)	Increase (%)		Decrease (%)		Reference
			LOI	TTI	PHRR	THR	
Blends of GBMs and conventional flame retardants							
PMMA^a	rGO	1	18	11	24	1.5	[242]
	rGO/LDHs	1/5	36	35	31	13	
	rGO/BPEA	1/10	47	-7	36	21	
	BPEA	1/5/10	62	23	45	25	
	rGO/LDHs / BPEA						
PU^a	(1MA:2M APP)	20	32				[232]
	(1MA:2M APP)-rGO	19/1	45				
	(1MA:2M APP)-rGO	18/2	55				
	(1MA:2M APP)-rGO						
PP^{d,e}	TRGO	1					[243]
	APP	27.5	111		87		
	APP/TRG	27.5/1	63		89		
	O	59	68		89		
	MH	59/1	10		91		
EP^{a,b}	PPA	20	35				[244]
	PPA/GNSs	19/1	39				
	PPA/GNSs	18/2	43				
PVA^{a,b}	GNSs	1	22				[233]
	MPP	10	34				
	G-MPP	1/10	54				
	G-MPP	1/20	74				
PP^{a,b}	CNTs	2	16		57		[245]
	RGO	2	13		61		
	CNTs/rGO	1/1	18		63		
	MPP	20	64		72		
	MPP/CNTs	18/2	67		78		
	MPP/RGO	18/2	72		80		
	MPP/CNTs /rGO	18/1/1	76		83		
PBS^a	(MA1:2M APP)	20	35				[246]
	(MA1:2M APP)/GNS	18/2	43				
	(MA1:2M APP)/GNS						

Table 2.4 *Cont.*

Polymer matrix	Filler	Concentration (wt. %)	Increase (%)		Decrease (%)		Reference
			LOI	TTI	PHRR	THR	
Modified GBMs							
PE^{a,b}	GO	1	3		8	3	[247]
	HGO	1	5		28	-2	
	GO	3	5		9	2	
	HGO	3	11		29	-6	
PS	GO-	0.5			19	5	[248]
	AEPZ				26	9	
	GO	1			39	14	
	GO	2					
PP^b	GO	2		-34	6	-7	[249]
	GO-MA			-34	29	3	
PS^{a,b}	GO	5	8		21	3	[158]
	GO-OPP		14		34	5	
EP^a	GO	10	30				[250]
	DPPES		30				
	GO-		80				
	DPPES						
EVA^b	rGO	1		7	31	14	[251]
	rGO-			32	46	22	
	PPSPB						
EP^{a,b}	DOPO	5	36				[252]
	rGO-DOPO		40				
EP^{a,b}	rGO-WPN	4	11		38	30	[220]
PU foam	GO	0.25	45				[236]
	BGO		48				
PU foam	P-GO	12.2			14.2	16.8	[237]
PU foam	GO coating	8.31				59.9	[238]
Cellulose							[172]
Cellulose	(PGN)	25			93.5	55.8	[253]

^aCone calorimeter – ISO 5660

^bLOI – ASTM D 2863

Abbreviations:

IFRs: BPEA – 1,2-Bis(5,5-dimethyl-1,3,2-dioxaphospha- cyclohexane phosphoryl amide) ethane; (1MA:2MAPP) – melamine and microencapsulated ammonium polyphosphate (weight ratio was 1:2).; PPA – Polyphosphamide; MPP – Melamine polyphosphate; (2APP:1MA) – ammonium polyphosphate and melamine (weight ratio was 2:1).

{HGO – N-aminoethyl piperazine and di(acryloyloxyethyl)methylphosphonate; AEPZ – hyper-branched flame retardant based on N-aminoethyl piperazine and phosphonate derivative; GO-MA – melamine; GO-OPP – organophosphorus oligomer modified GO

GO-DPPES – 2-(Diphenylphosphino)ethyltriethoxy silane; rGO-PPSPB – poly(piperazine spirocyclic pentaerythritol bisphosphonate); rGO-DOPO - 9,10-Dihydro-9-oxa-10-phospha-phenanthrene-10-oxide; rGO-WPN – phosphorus and nitrogen GO-NS nanosilica; PGO-Phosphorous; BGO- Boric acid} modified GO; FGP-phosphorus-hybridized graphene nanosheets.

2.4. References

- [1] T. A. Schaedler and W. B. Carter, “Architected Cellular Materials,” *Annu. Rev. Mater. Res.*, vol. 46, no. 1, pp. 187–210, Jul. 2016.
- [2] L.J. Gibson; M.F. Ashby and Brendan Harley, *Cellular Materials in Nature and Medicine*. Cambridge University Press, 2010.
- [3] S. Iannace and C. B. Park, *Biofoams: Science and Applications of Bio-Based Cellular and Porous Materials*. CRC Press, 2015.
- [4] P. H. Fortes M.A., Rosa M.E., *A cortiça*. IST Press, 2004.
- [5] P.-Y. Chen, J. McKittrick, and M. A. Meyers, “Biological materials: Functional adaptations and bioinspired designs,” *Prog. Mater. Sci.*, vol. 57, no. 8, pp. 1492–1704, Nov. 2012.
- [6] N. F. Lepora, P. Verschure, and T. J. Prescott, “The state of the art in biomimetics,” *Bioinspir. Biomim.*, vol. 8, no. 1, p. 013001, Mar. 2013.
- [7] C. Santulli and C. Langella, “Introducing students to bio-inspiration and biomimetic design: a workshop experience,” *Int. J. Technol. Des. Educ.*, vol. 21, no. 4, pp. 471–485, Aug. 2010.
- [8] L. J. Gibson and M. F. Ashby, *Cellular Solids: Structure and Properties*. Cambridge University Press, 1999.
- [9] I. Duarte, N. Peixinho, A. Andrade-campos, and R. Valente, “Special Issue on Cellular Materials,” *Sci. Technol. Mater.*, vol. 30, no. 1, pp. 1–3, 2018.
- [10] E. Solórzano and M. A. Rodriguez-Perez, “Cellular Materials,” in *Structural Materials and Processes in Transportation*, Weinheim, Germany: Wiley-VCH Verlag GmbH & Co. KGaA, 2013, pp. 371–374.
- [11] M. F. Ashby, “The properties of foams and lattices,” *Philos. Trans. R. Soc.*, vol. 364, no. November 2005, pp. 15–30, 2006.
- [12] V. . Bupesh Raja and S. Prabhu, “Processing of cellular materials - An overview,” in *International Conference on Advanced Nanomaterials & Emerging Engineering Technologies*, 2013, pp. 631–633.
- [13] W. Hou, X. Yang, W. Zhang, and Y. Xia, “Design of energy-dissipating structure with functionally graded auxetic cellular material,” *Int. J. Crashworthiness*, vol. 23, no. 4, pp. 366–376, Jul. 2018.
- [14] M. S. M. Fentahun, “Materials Used in Automotive Manufacture and Material Selection Using Ashby Charts,” *Int. J. Mater. Eng.*, vol. 8, no. 3, pp. 40–54, 2018.
- [15] S. Ma, W. Chen, and W. Zhao, “Mechanical properties and associated seismic isolation effects of foamed concrete layer in rock tunnel,” *J. Rock Mech. Geotech. Eng.*, vol. 11, no. 1, pp. 159–171, Feb. 2019.
- [16] S. Pina *et al.*, “Scaffolding Strategies for Tissue Engineering and Regenerative Medicine

- Applications,” *Materials (Basel)*., vol. 12, no. 11, p. 1824, Jun. 2019.
- [17] J. Banhart, “Manufacture, characterisation and application of cellular metals and metal foams,” *Prog. Mater. Sci.*, vol. 46, no. 6, pp. 559–632, Jan. 2001.
- [18] C. Okolieocha, D. Raps, K. Subramaniam, and V. Altstädt, “Microcellular to nanocellular polymer foams: Progress (2004–2015) and future directions – A review,” *Eur. Polym. J.*, vol. 73, pp. 500–519, Dec. 2015.
- [19] M. Reinfried, G. Stephani, F. Luthardt, J. Adler, M. John, and A. Krombholz, “Hybrid Foams - A New Approach for Multifunctional Applications,” *Adv. Eng. Mater.*, vol. 13, no. 11, pp. 1031–1036, Nov. 2011.
- [20] S. Thomas, R. Shanks, and S. Chandran, *Design and Applications of Nanostructured Polymer Blends and Nanocomposite Systems*. Elsevier Science, 2015.
- [21] N. Gama, A. Ferreira, and A. Barros-Timmons, “Polyurethane Foams: Past, Present, and Future,” *Materials (Basel)*., vol. 11, no. 10, p. 1841, Sep. 2018.
- [22] M. Berins and S. of the Plastics Industry, *Plastics Engineering Handbook Of The Society Of The Plastics Industry*. Springer US, 1991.
- [23] L. Lee, C. Zeng, X. Cao, X. Han, J. Shen, and G. Xu, “Polymer nanocomposite foams,” *Compos. Sci. Technol.*, vol. 65, no. 15–16, pp. 2344–2363, Dec. 2005.
- [24] M. Antunes and J. I. Velasco, “Multifunctional polymer foams with carbon nanoparticles,” *Prog. Polym. Sci.*, vol. 39, no. 3, pp. 486–509, Mar. 2014.
- [25] L. Chen, D. Rende, L. S. Schadler, and R. Ozisik, “Polymer nanocomposite foams,” *J. Mater. Chem. A*, vol. 1, no. 12, pp. 3837–3848, 2013.
- [26] M. A. Rodríguez-Pérez, “The Effect of Chemical Composition, Density and Cellular Structure on the Dynamic Mechanical Response of Polyolefin Foams,” *Cell. Polym.*, vol. 21, no. 2, pp. 117–136, Mar. 2002.
- [27] L. C. Brinson, Hal F., Brinson, “Polymer Engineering Science and Viscoelasticity: An Introduction - Characteristics , Applications and Properties of Polymers,” Springer S., New York, 2015, pp. 56–97.
- [28] B. E. Obi and B. E. Obi, “Overview of Applications of Polymeric Foams,” *Polym. Foam. Struct.*, pp. 3–14, Jan. 2018.
- [29] E. Aram and S. Mehdipour-Ataei, “A review on the micro- and nanoporous polymeric foams: Preparation and properties,” *Int. J. Polym. Mater. Polym. Biomater.*, vol. 65, no. 7, pp. 358–375, Dec. 2015.
- [30] J. Zhang, Y. Cao, J. Feng, and P. Wu, “Graphene-Oxide-Sheet-Induced Gelation of Cellulose and Promoted Mechanical Properties of Composite Aerogels,” *J. Phys. Chem. C*, vol. 116, no. 14, pp. 8063–8068, Apr. 2012.
- [31] F.-L. Jin, M. Zhao, M. Park, and S.-J. Park, “Recent Trends of Foaming in Polymer Processing: A Review,” *Polymers (Basel)*., vol. 11, no. 6, p. 953, Jun. 2019.
- [32] M. Altan, “Thermoplastic Foams: Processing, Manufacturing, and Characterization,” in *Recent Research in Polymerization*, InTech, 2018.
- [33] E. Reverchon and S. Cardea, “Production of controlled polymeric foams by supercritical CO₂,” *J. Supercrit. Fluids*, vol. 40, no. 1, pp. 144–152, Feb. 2007.

- [34] Z. Petrovic, "Polyurethanes from Vegetable Oils," *Polym. Rev.*, vol. 48, no. 1, pp. 109–155, Jan. 2008.
- [35] S. Hu and Y. Li, "Polyols and polyurethane foams from base-catalyzed liquefaction of lignocellulosic biomass by crude glycerol: Effects of crude glycerol impurities," *Ind. Crops Prod.*, vol. 57, pp. 188–194, Jun. 2014.
- [36] S. Ahmadzadeh, A. Nasirpour, J. Keramat, N. Hamdami, T. Behzad, and S. Desobry, "Nanoporous cellulose nanocomposite foams as high insulated food packaging materials," *Colloids Surfaces A Physicochem. Eng. Asp.*, vol. 468, pp. 201–210, Mar. 2015.
- [37] N. T. Cervin, J. Boon, S. Ng, P. Olin, and L. Bergstro, "Lightweight and Strong Cellulose Materials Made from Aqueous Foams Stabilized by Nanofibrillated Cellulose," *Biomacromolecules*, vol. 14, pp. 503–511, 2013.
- [38] M. Poletto, H. Júnior, and A. Zattera, "Native Cellulose: Structure, Characterization and Thermal Properties," *Materials (Basel)*, vol. 7, no. 9, pp. 6105–6119, Aug. 2014.
- [39] C. Vilela, R. J. B. Pinto, S. Pinto, P. Marques, A. Silvestre, and C. S. da Rocha Freire Barros, *Polysaccharide Based Hybrid Materials*. Cham: Springer International Publishing, 2018.
- [40] L.-P. Lefebvre, J. Banhart, and D. C. Dunand, "Porous Metals and Metallic Foams: Current Status and Recent Developments," *Adv. Eng. Mater.*, vol. 10, no. 9, pp. 775–787, Sep. 2008.
- [41] I. N. Ż. Ynieria and M. Ł. Owa, "Metallic foams – ultra light materials for structural applications," no. 5, pp. 823–828, 2001.
- [42] I. Duarte and M. Oliveira, "Aluminium Alloy Foams : Production and Properties," 2003.
- [43] H. P. Degischer and B. Kriszt, *Handbook of Cellular Metals: Production, Processing, Applications*. Wiley, 2002.
- [44] B. J. Banhart, "Metal Foams : Production and Stability," *Adv. Eng. Mater.*, no. 9, pp. 781–794, 2006.
- [45] G. Stephani, O. Andersen, P. Quadbeck, and B. Kieback, "Cellular Metals for Functional Applications – an Overview."
- [46] F. García-Moreno, "Commercial Applications of Metal Foams: Their Properties and Production," *Materials (Basel)*, vol. 9, no. 2, p. 85, Jan. 2016.
- [47] D. Lehmus, M. Vesenjajak, S. Schampheleire, and T. Fiedler, "From Stochastic Foam to Designed Structure: Balancing Cost and Performance of Cellular Metals," *Materials (Basel)*, vol. 10, no. 8, p. 922, Aug. 2017.
- [48] L. Chen, D. Rende, L. S. Schadler, and R. Ozisik, "Polymer nanocomposite foams," *J. Mater. Chem. A*, vol. 1, no. 12, p. 3837, 2013.
- [49] I. Duarte and J. M. F. Ferreira, "Composite and Nanocomposite Metal Foams," *Materials (Basel)*, vol. 9, no. 2, 2016.
- [50] M. S. Chavali and M. P. Nikolova, "Metal oxide nanoparticles and their applications in nanotechnology," *SN Appl. Sci.*, vol. 1, no. 6, p. 607, Jun. 2019.
- [51] J. Njuguna, K. Pielichowski, and S. Desai, "Nanofiller-reinforced polymer nanocomposites," *Polym. Adv. Technol.*, vol. 19, pp. 947–959, 2008.
- [52] I. Velasco and M. Antunes, "Progress in Polymer Science Multifunctional polymer foams with carbon nanoparticles," *Prog. Polym. Sci.*, vol. 39, pp. 486–509, 2014.

- [53] I. Duarte, E. Ventura, S. Olhero, and J. M. Ferreira, "A novel approach to prepare aluminium-alloy foams reinforced by carbon-nanotubes," *Mater. Lett.*, vol. 160, pp. 162–166, Dec. 2015.
- [54] Y. An, S. Yang, E. Zhao, Z. Wang, and H. Wu, "Fabrication of aluminum foam reinforced by graphene nanoflakes," *Mater. Lett.*, vol. 212, pp. 4–7, Feb. 2018.
- [55] S. J. Yan *et al.*, "Investigating aluminum alloy reinforced by graphene nanoflakes," *Mater. Sci. Eng. A*, vol. 612, pp. 440–444, Aug. 2014.
- [56] sourav Das, *Graphene Reinforced Aluminum Foam for Automobile and Aerospace*. Lambert Academic Publishing, 2017.
- [57] I. Duarte and M. Oliveir, "Aluminium Alloy Foams: Production and Properties," in *Powder Metallurgy*, InTech, 2012.
- [58] M. Puterman, M. Narkis, and S. Kenig, "Syntactic Foams I. Preparation, Structure and Properties," *J. Cell. Plast.*, vol. 16, no. 4, pp. 223–229, 1980.
- [59] N. Gupta and P. K. Rohatgi, *Metal Matrix Syntactic Foams: Processing, Microstructure, Properties and Applications*. DEStech Publications, Incorporated, 2014.
- [60] S. Broxtermann, M. Vesenjok, L. Krstulović-Opara, and T. Fiedler, "Quasi static and dynamic compression of zinc syntactic foams," *J. Alloys Compd.*, vol. 768, pp. 962–969, 2018.
- [61] S. Sankaran, B. N. Ravishankar, K. Ravi Sekhar, S. Dasgupta, and M. N. Jagdish Kumar, "Syntactic Foams for Multifunctional Applications," in *Composite Materials*, Berlin, Heidelberg: Springer Berlin Heidelberg, 2017, pp. 281–314.
- [62] T. Al-Salhami, K.; Taherishargh, M.; Kisi, E. and Fiedler, "Controlled Shrinkage of Expanded Glass Particles in Metal Syntactic Foams," *Materials (Basel)*, vol. 10, no. 9, p. 1073, Sep. 2017.
- [63] I. A. Chaves, M. Taherishargh, and T. Fiedler, "Long-term immersion exposure of perlite–aluminium syntactic foam in seawater," *J. Compos. Mater.*, vol. 53, no. 9, pp. 1229–1240, Apr. 2019.
- [64] H. Allameh-Haery, C. M. Wensrich, T. Fiedler, and E. Kisi, "Novel cellular perlite-epoxy foams: Effects of particle size," *J. Cell. Plast.*, vol. 53, no. 6, pp. 597–622, Nov. 2017.
- [65] M. Taherishargh, B. Katona, T. Fiedler, and I. N. Orbulov, "Fatigue properties of expanded perlite/aluminum syntactic foams," *J. Compos. Mater.*, vol. 51, no. 6, pp. 773–781, Mar. 2017.
- [66] M. Doddamani, Kishore, V. C. Shunmugasamy, N. Gupta, and H. B. Vijayakumar, "Compressive and flexural properties of functionally graded fly ash cenosphere-epoxy resin syntactic foams," *Polym. Compos.*, vol. 36, no. 4, pp. 685–693, Apr. 2015.
- [67] B. R. Bharath Kumar, M. Doddamani, S. E. Zeltmann, N. Gupta, M. R. Ramesh, and S. Ramakrishna, "Processing of cenosphere/HDPE syntactic foams using an industrial scale polymer injection molding machine," *Mater. Des.*, vol. 92, pp. 414–423, Feb. 2016.
- [68] P. K. Rohatgi, J. K. Kim, N. Gupta, S. Alaraj, and A. Daoud, "Compressive characteristics of A356/fly ash cenosphere composites synthesized by pressure infiltration technique," *Compos. Part A Appl. Sci. Manuf.*, vol. 37, no. 3, pp. 430–437, Mar. 2006.
- [69] M. M. Islam and H. S. Kim, "Manufacture of Syntactic Foams Using Starch as Binder: Post-Mold Processing," *Mater. Manuf. Process.*, vol. 23, no. 8, pp. 884–892, Oct. 2008.
- [70] M. Taherishargh, I. V. Belova, G. E. Murch, and T. Fiedler, "Pumice/aluminium syntactic foam," *Mater. Sci. Eng. A*, vol. 635, pp. 102–108, May 2015.

- [71] E. Zegeye, A. K. Ghamsari, and E. Woldesenbet, “Mechanical properties of graphene platelets reinforced syntactic foams,” *Compos. Part B Eng.*, vol. 60, pp. 268–273, Apr. 2014.
- [72] R. Ciardiello, L. T. Drzal, and G. Belingardi, “Effects of carbon black and graphene nanoplatelet fillers on the mechanical properties of syntactic foam,” *Compos. Struct.*, vol. 178, pp. 9–19, Oct. 2017.
- [73] D. T. Queheillalt and H. N. G. Wadley, “Cellular metal lattices with hollow trusses,” *Acta Mater.*, vol. 53, no. 2, pp. 303–313, Jan. 2005.
- [74] J. K. Min, B. Mosadegh, S. Dunham, and S. J. Al’Aref, *3D Printing Applications in Cardiovascular Medicine*. Elsevier Science, 2018.
- [75] C. B. Williams, J. K. Cochran, and D. W. Rosen, “Additive manufacturing of metallic cellular materials via three-dimensional printing,” *Int. J. Adv. Manuf. Technol.*, vol. 53, no. 1, pp. 231–239, Mar. 2011.
- [76] O. Abdulhameed, A. Al-Ahmari, W. Ameen, and S. H. Mian, “Additive manufacturing: Challenges, trends, and applications,” *Adv. Mech. Eng.*, vol. 11, no. 2, p. 168781401882288, Feb. 2019.
- [77] H. N. G. Wadley, N. A. Fleck, and A. G. Evans, “Fabrication and structural performance of periodic cellular metal sandwich structures,” *Compos. Sci. Technol.*, vol. 63, no. 16, pp. 2331–2343, 2003.
- [78] T. D. Ngo, A. Kashani, G. Imbalzano, K. T. Q. Nguyen, and D. Hui, “Additive manufacturing (3D printing): A review of materials, methods, applications and challenges,” *Compos. Part B Eng.*, vol. 143, pp. 172–196, Jun. 2018.
- [79] R. Mines, *Metallic Microlattice Structures: Manufacture, Materials and Application*. Springer, 2019.
- [80] A. G. Evans, J. W. Hutchinson, N. A. Fleck, M. F. Ashby, and H. N. G. Wadley, “The topological design of multifunctional cellular metals,” *Prog. Mater. Sci.*, vol. 46, no. 3–4, pp. 309–327, Jan. 2001.
- [81] C. C. Seepersad, R. S. Kumar, J. K. Allen, F. Mistree, and D. L. McDowell, “Multifunctional design of prismatic cellular materials,” *J. Comput. Mater. Des.*, vol. 11, no. 2, pp. 163–181, Jan. 2004.
- [82] S. Y. Yang, E. T. Zhao, and Y. K. An, “Research on Manufacturing the Metal Foams with Regular Cells by 3D Printing,” *Adv. Mater. Res.*, vol. 1120–1121, pp. 1233–1237, Jul. 2015.
- [83] F. N. Habib, P. Iovenitti, S. H. Masood, and M. Nikzad, “Fabrication of polymeric lattice structures for optimum energy absorption using Multi Jet Fusion technology,” *Mater. Des.*, vol. 155, pp. 86–98, 2018.
- [84] D. W. Abueidda, M. Bakir, R. K. A. Al-Rub, J. S. Bergström, N. A. Sobh, and I. Jasiuk, “Mechanical properties of 3D printed polymeric cellular materials with triply periodic minimal surface architectures,” *Mater. Des.*, vol. 122, pp. 255–267, 2017.
- [85] F. Shen *et al.*, “Energy Absorption of Thermoplastic Polyurethane Lattice Structures via 3D Printing: Modeling and Prediction,” *Int. J. Appl. Mech.*, vol. 08, no. 07, p. 1640006, 2016.
- [86] C. Ling, A. Cernicchi, M. D. Gilchrist, and P. Cardiff, “Mechanical behaviour of additively-manufactured polymeric octet-truss lattice structures under quasi-static and dynamic compressive loading,” *Mater. Des.*, vol. 162, pp. 106–118, 2019.

- [87] M. Borovinšek, M. Vesenjaj, Y. Higa, K. Shimojima, and Z. Ren, “Characterization of Geometrical Changes of Spherical Advanced Pore Morphology (APM) Foam Elements during Compressive Deformation,” *Materials (Basel)*, vol. 12, no. 7, p. 1088, Apr. 2019.
- [88] M. Vesenjaj, T. Fiedler, Z. Ren, and A. Öchsner, “Behaviour of Syntactic and Partial Hollow Sphere Structures under Dynamic Loading,” *Adv. Eng. Mater.*, vol. 10, no. 3, pp. 185–191, Mar. 2008.
- [89] M. Vesenjaj, I. Duarte, J. Baumeister, H. Göhler, L. Krstulović-Opara, and Z. Ren, “Bending performance evaluation of aluminium alloy tubes filled with different cellular metal cores,” *Compos. Struct.*, vol. 234, p. 111748, Feb. 2020.
- [90] M. Vesenjaj, F. Gačnik, L. Krstulović-Opara, and Z. Ren, “Behavior of composite advanced pore morphology foam,” *J. Compos. Mater.*, vol. 45, no. 26, pp. 2823–2831, Dec. 2011.
- [91] M. Vesenjaj, F. Gačnik, L. Krstulović-Opara, and Z. Ren, “Mechanical Properties of Advanced Pore Morphology Foam Elements,” *Mech. Adv. Mater. Struct.*, vol. 22, no. 5, pp. 359–366, May 2015.
- [92] M. A. Sulong, M. Vesenjaj, I. V. Belova, G. E. Murch, and T. Fiedler, “Compressive properties of Advanced Pore Morphology (APM) foam elements,” *Mater. Sci. Eng. A*, vol. 607, pp. 498–504, Jun. 2014.
- [93] D. Lehmhus *et al.*, “Mechanical Characterization of Particulate Aluminum Foams-Strain-Rate, Density and Matrix Alloy versus Adhesive Effects,” *Adv. Eng. Mater.*, vol. 12, no. 7, pp. 596–603, Jun. 2010.
- [94] T. Fiedler *et al.*, “Determination of the thermal conductivity of periodic APM foam models,” *Int. J. Heat Mass Transf.*, vol. 73, pp. 826–833, Jun. 2014.
- [95] M. Vesenjaj, Z. Ren, T. Fiedler, and A. Öchsner, “Impact Behavior of Composite Hollow Sphere Structures,” *J. Compos. Mater.*, vol. 43, no. 22, pp. 2491–2505, Oct. 2009.
- [96] A. Kovačič and Z. Ren, “On the porosity of advanced pore morphology structures,” *Compos. Struct.*, vol. 158, pp. 235–244, Dec. 2016.
- [97] D. R. Clarke, “Interpenetrating Phase Composites,” *J. Am. Ceram. Soc.*, vol. 75, no. 4, pp. 739–758, 1992.
- [98] Y. Liu and X. Gong, “Compressive behavior and energy absorption of metal porous polymer composite with interpenetrating network structure,” *Trans. Nonferrous Met. Soc. China*, vol. 16, pp. s439–s443, Jun. 2006.
- [99] F. Xie, Z. Lu, and Z. Yuan, “Numerical analysis of elastic and elastoplastic behavior of interpenetrating phase composites,” *Comput. Mater. Sci.*, vol. 97, pp. 94–101, 2015.
- [100] S. Roy, J. Gibmeier, V. Kostov, K. A. Weidenmann, A. Nagel, and A. Wanner, “Internal load transfer in a metal matrix composite with a three-dimensional interpenetrating structure,” *Acta Mater.*, vol. 59, no. 4, pp. 1424–1435, 2011.
- [101] X. Zhao, “Journal of the Mechanics and Physics of Solids A theory for large deformation and damage of interpenetrating polymer networks,” *J. Mech. Phys. Solids*, vol. 60, no. 2, pp. 319–332, 2012.
- [102] C. Periasamy, R. Jhaver, and H. V Tippur, “Quasi-static and dynamic compression response of a lightweight interpenetrating phase composite foam,” *Mater. Sci. Eng. A*, vol. 527, no. 12, pp. 2845–2856, 2010.

- [103] R. Jhaver and H. Tippur, "Processing, compression response and finite element modeling of syntactic foam based interpenetrating phase composite (IPC)," *Mater. Sci. Eng. A*, vol. 499, no. 1–2, pp. 507–517, Jan. 2009.
- [104] N. Dukhan, N. Rayess, and J. Hadley, "Characterization of aluminum foam–polypropylene interpenetrating phase composites: Flexural test results," *Mech. Mater.*, vol. 42, no. 2, pp. 134–141, Feb. 2010.
- [105] Z. Yuan, N. Rayess, and N. Dukhan, "Modeling of the Mechanical Properties of a Polymer-metal Foam Hybrid," *Procedia Mater. Sci.*, vol. 4, no. 2009, pp. 215–219, 2014.
- [106] J. R. Hadley and D. Q. Houston, "Mechanical Properties of Aluminum Foam-Polymer Multifunctional Hybrid Materials," pp. 1–9, 2016.
- [107] T. Doktor, P. Zlámal, and T. Fíla, "Properties of polymer-filled aluminium foams under moderate strain-rate loading conditions," *Mater. Tehnol.*, vol. 49, no. 4, pp. 597–600, Aug. 2015.
- [108] S. Liu, A. Li, S. He, and P. Xuan, "Cyclic compression behavior and energy dissipation of aluminum foam–polyurethane interpenetrating phase composites," *Compos. Part A Appl. Sci. Manuf.*, vol. 78, pp. 35–41, Nov. 2015.
- [109] L. D. Wegner and L. J. Gibson, "The mechanical behaviour of interpenetrating phase composites – I: modelling," *Int. J. Mech. Sci.*, vol. 42, no. 5, pp. 925–942, May 2000.
- [110] L. D. Wegner and L. J. Gibson, "The mechanical behaviour of interpenetrating phase composites – II: a case study of a three-dimensionally printed material," *Int. J. Mech. Sci.*, vol. 42, no. 5, pp. 943–964, May 2000.
- [111] L. D. Wegner and L. J. Gibson, "The mechanical behaviour of interpenetrating phase composites — III: resin-impregnated porous stainless steel," *Int. J. Mech. Sci.*, vol. 43, no. 4, pp. 1061–1072, Apr. 2001.
- [112] Y. Su *et al.*, "Structural modeling and mechanical behavior of Metal-Porous-Polymer-Composites (MPPCs) with different polymer volume fractions," *Compos. Struct.*, vol. 153, pp. 673–681, Oct. 2016.
- [113] M. Vesenjaj, L. Krstulović-Opara, Z. Ren, A. Öchsner, and Ž. Domazet, "Experimental Study of Open-Cell Cellular Structures with Elastic Filler Material," *Exp. Mech.*, vol. 49, no. 4, p. 501, 2008.
- [114] M. Vesenjaj, L. Krstulović-Opara, and Z. Ren, "Characterization of irregular open-cell cellular structure with silicone pore filler," *Polym. Test.*, vol. 32, no. 8, pp. 1538–1544, 2013.
- [115] M. Vesenjaj, A. Öchsner, and Z. Ren, "Characterization of open-cell cellular material structures with pore fillers," *Mater. Lett.*, vol. 62, no. 17, pp. 3250–3253, 2008.
- [116] I. Duarte, M. Vesenjaj, L. Krstulović-Opara, and Z. Ren, "Crush performance of multifunctional hybrid foams based on an aluminium alloy open-cell foam skeleton," *Polym. Test.*, vol. 67, pp. 246–256, 2018.
- [117] I. Duarte, L. Krstulović-Opara, J. Dias-de-Oliveira, and M. Vesenjaj, "Axial crush performance of polymer-aluminium alloy hybrid foam filled tubes," *Thin-Walled Struct.*, vol. 138, pp. 124–136, 2019.
- [118] E. N. Peters, "Thermoplastics, Thermosets, and Elastomers-Descriptions and Properties," in *Mechanical Engineers' Handbook*, Hoboken, NJ, USA: John Wiley & Sons, Inc., 2015, pp. 1–48.

- [119] S. Bakshi and S. Biswas, "Nanocomposites – An Overview," *Scitech J.*, vol. 01, no. 05, pp. 22–30, 2014.
- [120] T. K. Das and S. Prusty, "Graphene-Based Polymer Composites and Their Applications," *Polym. Plast. Technol. Eng.*, vol. 52, no. 4, pp. 319–331, Mar. 2013.
- [121] M. Lopez, *Advances in Polymer Nanocomposites*. Elsevier, 2012.
- [122] M. Šupová, G. S. Martynková, and K. Barabaszová, "Effect of Nanofillers Dispersion in Polymer Matrices: A Review," *Sci. Adv. Mater.*, vol. 3, no. 1, pp. 1–25, Feb. 2011.
- [123] D. Konios, M. M. Stylianakis, E. Stratakis, and E. Kymakis, "Dispersion behaviour of graphene oxide and reduced graphene oxide.," *J. Colloid Interface Sci.*, vol. 430, pp. 108–12, Sep. 2014.
- [124] J. Texter, "Graphene dispersions," *Curr. Opin. Colloid Interface Sci.*, vol. 19, no. 2, pp. 163–174, Apr. 2014.
- [125] P. Henrique, C. Camargo, K. G. Satyanarayana, and F. Wypych, "Nanocomposites : Synthesis , Structure , Properties and New Application Opportunities," vol. 12, no. 1, pp. 1–39, 2009.
- [126] B. Li, "Review on polymer/graphite nanoplatelet nanocomposites," *J. Mater. Sci.*, vol. 46, pp. 5595–5614, 2011.
- [127] J. R. Potts, D. R. Dreyer, C. W. Bielawski, and R. S. Ruoff, "Graphene-based polymer nanocomposites," *Polymer (Guildf)*, vol. 52, no. 1, pp. 5–25, Jan. 2011.
- [128] R. Garg, N. Dutta, and N. Choudhury, "Work Function Engineering of Graphene," *Nanomaterials*, vol. 4, no. 2, pp. 267–300, Apr. 2014.
- [129] C. Galande *et al.*, "Science and Engineering of Graphene Oxide," *Part. Part. Syst. Charact.*, vol. 31, no. 6, pp. 619–638, Jun. 2014.
- [130] T. Kuilla, S. Bhadra, D. Yao, N. H. Kim, S. Bose, and J. H. Lee, "Recent advances in graphene based polymer composites," *Prog. Polym. Sci.*, vol. 35, no. 11, pp. 1350–1375, Nov. 2010.
- [131] D. R. Paul and L. M. Robeson, "Polymer nanotechnology: Nanocomposites," *Polymer (Guildf)*, vol. 49, no. 15, pp. 3187–3204, Jul. 2008.
- [132] A. A. Mamedov and N. A. Kotov, "Free-Standing Layer-by-Layer Assembled Films of Magnetite Nanoparticles," *Langmuir*, vol. 16, no. 13, pp. 5530–5533, Jun. 2000.
- [133] M. Hashemi *et al.*, "Layer-by-layer assembly of graphene oxide on thermosensitive liposomes for photo-chemotherapy," *Acta Biomater.*, vol. 65, pp. 376–392, Jan. 2018.
- [134] R. B. Estevam *et al.*, "Preparation and characterization of LbL films based on graphene oxide nanoparticles interacting with 3-n-propylpyridinium silsesquioxane chloride," *Surf. Coatings Technol.*, vol. 275, pp. 2–8, Aug. 2015.
- [135] D. Jariwala, V. K. Sangwan, L. J. Lauhon, T. J. Marks, and M. C. Hersam, "Carbon nanomaterials for electronics, optoelectronics, photovoltaics, and sensing.," *Chem. Soc. Rev.*, vol. 42, no. 7, pp. 2824–60, Apr. 2013.
- [136] C. K. Chua and M. Pumera, "Chemical reduction of graphene oxide: a synthetic chemistry viewpoint.," *Chem. Soc. Rev.*, vol. 43, no. 1, pp. 291–312, Jan. 2014.
- [137] D. R. Dreyer, S. Park, C. W. Bielawski, and R. S. Ruoff, "The chemistry of graphene oxide.,"

- Chem. Soc. Rev.*, vol. 39, no. 1, pp. 228–40, Jan. 2010.
- [138] D. C. Marcano *et al.*, “Improved Synthesis of Graphene Oxide,” *ACS Nano*, vol. 4, no. 8, pp. 4806–4814, 2010.
- [139] C. Vilela, C.; Pinto, R.; Pinto, S.; Marques, P.; Silvestre, A.; Freire, *Polysaccharide Based Hybrid Materials Metals and Metal Oxides, Graphene and Carbon Nanotubes*, vol. 53, no. 30. 2014.
- [140] A. M. Dimiev *et al.*, “Mechanism of Graphene Oxide,” *Am. Chem. Soc.*, vol. 8, no. 3, pp. 3060–3068, 2014.
- [141] Y. Zhu *et al.*, “Graphene and graphene oxide: synthesis, properties, and applications,” *Adv. Mater.*, vol. 22, no. 35, pp. 3906–24, Sep. 2010.
- [142] X. Zhou, J. Zhang, H. Wu, H. Yang, J. Zhang, and S. Guo, “Reducing Graphene Oxide via Hydroxylamine: A Simple and Efficient Route to Graphene,” *J. Phys. Chem. C*, vol. 115, no. 24, pp. 11957–11961, Jun. 2011.
- [143] O. C. Compton and S. T. Nguyen, “Graphene oxide, highly reduced graphene oxide, and graphene: versatile building blocks for carbon-based materials,” *Small*, vol. 6, no. 6, pp. 711–23, Mar. 2010.
- [144] P. Wick *et al.*, “Classification framework for graphene-based materials,” *Angew. Chemie - Int. Ed.*, vol. 53, no. 30, pp. 7714–7718, 2014.
- [145] J. Kuang, Z. Dai, L. Liu, Z. Yang, M. Jin, and Z. Zhang, “Synergistic effects from graphene and carbon nanotubes endow ordered hierarchical structure foams with a combination of compressibility, super-elasticity and stability and potential application as pressure sensors,” *Nanoscale*, vol. 7, no. 20, pp. 9252–60, May 2015.
- [146] G. Raam Dheep and a. Sreekumar, “Influence of nanomaterials on properties of latent heat solar thermal energy storage materials – A review,” *Energy Convers. Manag.*, vol. 83, pp. 133–148, Jul. 2014.
- [147] P. Wick *et al.*, “Classification Framework for Graphene-Based Materials,” *Angew. Chemie Int. Ed.*, vol. 53, no. 30, pp. 7714–7718, Jul. 2014.
- [148] A. T. Smith, A. M. LaChance, S. Zeng, B. Liu, and L. Sun, “Synthesis, properties, and applications of graphene oxide/reduced graphene oxide and their nanocomposites,” *Nano Mater. Sci.*, vol. 1, no. 1, pp. 31–47, Mar. 2019.
- [149] D. G. Papageorgiou, I. A. Kinloch, and R. J. Young, “Mechanical properties of graphene and graphene-based nanocomposites,” *Prog. Mater. Sci.*, vol. 90, pp. 75–127, 2017.
- [150] S. I. Abdullah and M. N. M. Ansari, “Mechanical properties of graphene oxide (GO)/epoxy composites,” *HBRC J.*, vol. 11, no. 2, pp. 151–156, Aug. 2015.
- [151] D. R. Bortz, E. G. Heras, and I. Martin-Gullon, “Impressive Fatigue Life and Fracture Toughness Improvements in Graphene Oxide/Epoxy Composites,” *Macromolecules*, vol. 45, no. 1, pp. 238–245, Jan. 2012.
- [152] Y.-J. Wan *et al.*, “Grafting of epoxy chains onto graphene oxide for epoxy composites with improved mechanical and thermal properties,” *Carbon N. Y.*, vol. 69, pp. 467–480, Apr. 2014.
- [153] B. Zhang, R. Asmatulu, S. a. Soltani, L. N. Le, and S. S. a. Kumar, “Mechanical and thermal properties of hierarchical composites enhanced by pristine graphene and graphene oxide nano-inclusions,” *J. Appl. Polym. Sci.*, vol. 131, no. 19, p. n/a-n/a, Oct. 2014.

- [154] R. Wang *et al.*, “A novel nanosilica/graphene oxide hybrid and its flame retarding epoxy resin with simultaneously improved mechanical, thermal conductivity, and dielectric properties,” *J. Mater. Chem. A*, vol. 3, no. 18, pp. 9826–9836, 2015.
- [155] C.-H. Hsu *et al.*, “Physical study of room-temperature-cured epoxy/thermally reduced graphene oxides with various contents of oxygen-containing groups,” *Polym. Int.*, vol. 63, no. 10, pp. 1765–1770, 2014.
- [156] K. Balasubramanian, “Reinforcement of poly ether sulphones (PES) with exfoliated graphene oxide for aerospace applications,” *IOP Conf. Ser. Mater. Sci. Eng.*, vol. 40, p. 012022, Sep. 2012.
- [157] T. Forati, M. Atai, a. M. Rashidi, M. Imani, and a. Behnamghader, “Physical and mechanical properties of graphene oxide/polyethersulfone nanocomposites,” *Polym. Adv. Technol.*, vol. 25, no. 3, pp. 322–328, Mar. 2014.
- [158] S. Qiu *et al.*, “Effect of Functionalized Graphene Oxide with Organophosphorus Oligomer on the Thermal and Mechanical Properties and Fire Safety of Polystyrene,” *Ind. Eng. Chem. Res.*, vol. 54, no. 13, pp. 3309–3319, Apr. 2015.
- [159] J. Hu and F. Zhang, “Self-assembled fabrication and flame-retardant properties of reduced graphene oxide/waterborne polyurethane nanocomposites,” *J. Therm. Anal. Calorim.*, vol. 118, no. 3, pp. 1561–1568, Aug. 2014.
- [160] J. Zhang, C. Zhang, and S. a. Madbouly, “In situ polymerization of bio-based thermosetting polyurethane/graphene oxide nanocomposites,” *J. Appl. Polym. Sci.*, vol. 132, no. 13, p. n/a-n/a, Apr. 2015.
- [161] W. Qian *et al.*, “Polydimethylsiloxane incorporated with reduced graphene oxide (rGO) sheets for wound dressing application: Preparation and characterization,” *Colloids Surfaces B Biointerfaces*, vol. 166, pp. 61–71, Jun. 2018.
- [162] N.-J. Huang *et al.*, “Efficient interfacial interaction for improving mechanical properties of polydimethylsiloxane nanocomposites filled with low content of graphene oxide nanoribbons,” *RSC Adv.*, vol. 7, no. 36, pp. 22045–22053, 2017.
- [163] M. Silva, N. M. Alves, and M. C. Paiva, “Graphene-polymer nanocomposites for biomedical applications,” *Polym. Adv. Technol.*, vol. 29, no. 2, pp. 687–700, Feb. 2018.
- [164] Y. Du, D. Li, L. Liu, and G. Gai, “Recent Achievements of Self-Healing Graphene/Polymer Composites,” *Polymers (Basel)*, vol. 10, no. 2, p. 114, Jan. 2018.
- [165] A. Kumar, K. Sharma, and A. R. Dixit, “A review of the mechanical and thermal properties of graphene and its hybrid polymer nanocomposites for structural applications,” *J. Mater. Sci.*, vol. 54, no. 8, pp. 5992–6026, 2019.
- [166] X. Wang, F. Tang, X. Qi, and Z. Lin, “Mechanical, electrochemical, and durability behavior of graphene nano-platelet loaded epoxy-resin composite coatings,” *Compos. Part B Eng.*, vol. 176, p. 107103, Nov. 2019.
- [167] A. Kausar, I. Rafique, Z. Anwar, and B. Muhammad, “Perspectives of Epoxy/Graphene Oxide Composite: Significant Features and Technical Applications,” *Polym. Plast. Technol. Eng.*, vol. 55, no. 7, pp. 704–722, May 2016.
- [168] Z. Anwar, A. Kausar, I. Rafique, and B. Muhammad, “Advances in Epoxy/Graphene Nanoplatelet Composite with Enhanced Physical Properties: A Review,” *Polym. Plast. Technol. Eng.*, vol. 55, no. 6, pp. 643–662, Apr. 2016.

- [169] N. P. Singh, V. K. Gupta, and A. P. Singh, "Graphene and carbon nanotube reinforced epoxy nanocomposites: A review," *Polymer (Guildf)*, vol. 180, p. 121724, Oct. 2019.
- [170] R. Atif, I. Shyha, and F. Inam, "Mechanical, Thermal, and Electrical Properties of Graphene-Epoxy Nanocomposites—A Review," *Polymers (Basel)*, vol. 8, no. 8, p. 281, Aug. 2016.
- [171] S. a. Song, Y. S. Chung, and S. S. Kim, "The mechanical and thermal characteristics of phenolic foams reinforced with carbon nanoparticles," *Compos. Sci. Technol.*, vol. 103, pp. 85–93, Oct. 2014.
- [172] B. Wicklein *et al.*, "Thermally insulating and fire-retardant lightweight anisotropic foams based on nanocellulose and graphene oxide," *Nat. Nanotechnol.*, vol. 10, no. 3, pp. 1–7, Nov. 2014.
- [173] J. Zhou, Z. Yao, Y. Chen, D. Wei, and T. Xu, "Fabrication and mechanical properties of phenolic foam reinforced with graphene oxide," *Polym. Compos.*, vol. 35, no. 3, pp. 581–586, Mar. 2014.
- [174] G. Yang, J. Su, J. Gao, X. Hu, C. Geng, and Q. Fu, "Fabrication of well-controlled porous foams of graphene oxide modified poly(propylene-carbonate) using supercritical carbon dioxide and its potential tissue engineering applications," *J. Supercrit. Fluids*, vol. 73, pp. 1–9, Jan. 2013.
- [175] M. Li, P. Cheng, R. Zhang, G. Luo, Q. Shen, and L. Zhang, "Preparation of PMMA/graphene oxide microcellular foams using supercritical carbon dioxide," *IOP Conf. Ser. Mater. Sci. Eng.*, vol. 87, p. 012042, Jul. 2015.
- [176] D. Yan, L. Xu, C. Chen, J. Tang, X. Ji, and Z. Li, "Enhanced mechanical and thermal properties of rigid polyurethane foam composites containing graphene nanosheets and carbon nanotubes," *Polym. Int.*, vol. 61, no. 7, pp. 1107–1114, Jul. 2012.
- [177] M. Hoseinabadi, M. Naderi, M. Najafi, S. Motahari, and M. Shokri, "A study of rigid polyurethane foams: The effect of synthesized polyols and nanoporous graphene," *J. Appl. Polym. Sci.*, vol. 134, no. 26, Jul. 2017.
- [178] J. N. Gavgani, H. Adelnia, D. Zaarei, and M. Moazzami Gudarzi, "Lightweight flexible polyurethane/reduced ultralarge graphene oxide composite foams for electromagnetic interference shielding," *RSC Adv.*, vol. 6, no. 33, pp. 27517–27527, 2016.
- [179] B. Shen, Y. Li, W. Zhai, and W. Zheng, "Compressible Graphene-Coated Polymer Foams with Ultralow Density for Adjustable Electromagnetic Interference (EMI) Shielding," *ACS Appl. Mater. Interfaces*, vol. 8, no. 12, pp. 8050–8057, Mar. 2016.
- [180] X. Zhao, Q. Zhang, D. Chen, and P. Lu, "Enhanced Mechanical Properties of Graphene-Based Poly (vinyl alcohol) Composites," pp. 2357–2363, 2010.
- [181] J. Liang *et al.*, "Infrared-Triggered Actuators from Graphene-Based Nanocomposites," pp. 9921–9927, 2009.
- [182] W. Park, J. Hu, L. a. Jauregui, X. Ruan, and Y. P. Chen, "Electrical and thermal conductivities of reduced graphene oxide/polystyrene composites," *Appl. Phys. Lett.*, vol. 104, no. 11, p. 113101, Mar. 2014.
- [183] D. Verma, P. C. Gope, A. Shandilya, and A. Gupta, "Mechanical-Thermal-Electrical and Morphological Properties of Graphene Reinforced Polymer Composites: A Review," *Trans. Indian Inst. Met.*, vol. 67, no. 6, pp. 803–816, 2014.
- [184] N. K. Mahanta and A. R. Abramson, "Thermal conductivity of graphene and graphene oxide

- nanoplatelets,” in *13th InterSociety Conference on Thermal and Thermomechanical Phenomena in Electronic Systems*, 2012, pp. 1–6.
- [185] J. D. Renteria *et al.*, “Strongly Anisotropic Thermal Conductivity of Free-Standing Reduced Graphene Oxide Films Annealed at High Temperature,” *Adv. Funct. Mater.*, vol. 25, no. 29, pp. 4664–4672, Aug. 2015.
- [186] P. K. S. Mural, M. Sharma, G. Madras, and S. Bose, “A critical review on in situ reduction of graphene oxide during preparation of conducting polymeric nanocomposites,” *RSC Adv.*, vol. 5, no. 41, pp. 32078–32087, 2015.
- [187] T. Zhou, “Targeted kinetic strategy for improving the thermal conductivity of epoxy composite containing percolating multi-layer graphene oxide chains,” *Express Polym. Lett.*, vol. 9, no. 7, pp. 608–623, Apr. 2015.
- [188] W. Zhang *et al.*, “Largely enhanced thermal conductivity of poly(vinylidene fluoride)/carbon nanotube composites achieved by adding graphene oxide,” *Carbon N. Y.*, vol. 90, pp. 242–254, Aug. 2015.
- [189] H. Im and J. Kim, “Thermal conductivity of a graphene oxide–carbon nanotube hybrid/epoxy composite,” *Carbon N. Y.*, vol. 50, no. 15, pp. 5429–5440, Dec. 2012.
- [190] R. Atif, I. Shyha, and F. Inam, “Mechanical , Thermal , and Electrical Properties of,” 2016.
- [191] D. Verma and P. C. G. Abhinav, “Mechanical-Thermal-Electrical and Morphological Properties of Graphene Reinforced Polymer Composites : A Review,” vol. 67, pp. 803–816, 2014.
- [192] H. Ribeiro *et al.*, “Multifunctional nanocomposites based on tetraethylenepentamine-modified graphene oxide/epoxy,” *Polym. Test.*, vol. 43, pp. 182–192, May 2015.
- [193] M. Santiago-Calvo, V. Blasco, C. Ruiz, R. París, F. Villafañe, and M. Á. Rodríguez-Pérez, “Synthesis, characterization and physical properties of rigid polyurethane foams prepared with poly(propylene oxide) polyols containing graphene oxide,” *Eur. Polym. J.*, vol. 97, pp. 230–240, Dec. 2017.
- [194] M. Santiago-Calvo, V. Blasco, C. Ruiz, R. París, F. Villafañe, and M. Á. Rodríguez-Pérez, “Improvement of thermal and mechanical properties by control of formulations in rigid polyurethane foams from polyols functionalized with graphene oxide,” *J. Appl. Polym. Sci.*, vol. 136, no. 19, p. 47474, May 2019.
- [195] Z.-J. Cao, W. Liao, S.-X. Wang, H.-B. Zhao, and Y.-Z. Wang, “Polyurethane foams with functionalized graphene towards high fire-resistance, low smoke release, superior thermal insulation,” *Chem. Eng. J.*, vol. 361, pp. 1245–1254, Apr. 2019.
- [196] J. Seo, J. Cha, and S. Kim, “Enhancement of the thermal conductivity of adhesives for wood flooring using xGnP,” *Energy Build.*, vol. 51, pp. 153–156, 2012.
- [197] A. Lorenzetti, M. Roso, A. Bruschetta, C. Boaretti, and M. Modesti, “Polyurethane-graphene nanocomposite foams with enhanced thermal insulating properties,” *Polym. Adv. Technol.*, vol. 27, no. 3, pp. 303–307, Mar. 2016.
- [198] L. Cao, Q. Fu, Y. Si, B. Ding, and J. Yu, “Porous materials for sound absorption,” *Compos. Commun.*, vol. 10, pp. 25–35, Dec. 2018.
- [199] N. N. Najib, Z. M. Ariff, A. A. Bakar, and C. S. Sipaut, “Correlation between the acoustic and dynamic mechanical properties of natural rubber foam: Effect of foaming temperature,” *Mater. Des.*, vol. 32, no. 2, pp. 505–511, 2011.

- [200] A. Arjunan, A. Baroutaji, A. S. Praveen, A. G. Olabi, and C. J. Wang, “Acoustic Performance of Metallic Foams,” in *Reference Module in Materials Science and Materials Engineering*, Elsevier, 2019.
- [201] Y. Fei *et al.*, “Morphological Structure, Rheological Behavior, Mechanical Properties and Sound Insulation Performance of Thermoplastic Rubber Composites Reinforced by Different Inorganic Fillers,” *Polymers (Basel)*, vol. 10, no. 3, p. 276, Mar. 2018.
- [202] J. M. Kim, D. H. Kim, J. Kim, J. W. Lee, and W. N. Kim, “Effect of graphene on the sound damping properties of flexible polyurethane foams,” *Macromol. Res.*, vol. 25, no. 2, pp. 190–196, Feb. 2017.
- [203] J. Lee and I. Jung, “Tuning sound absorbing properties of open cell polyurethane foam by impregnating graphene oxide,” *Appl. Acoust.*, vol. 151, pp. 10–21, Aug. 2019.
- [204] J.-H. Oh, H. R. Lee, S. Umrao, Y. J. Kang, and I.-K. Oh, “Self-aligned and hierarchically porous graphene-polyurethane foams for acoustic wave absorption,” *Carbon N. Y.*, vol. 147, pp. 510–518, Jun. 2019.
- [205] A. Dasari, Z.-Z. Yu, G.-P. Cai, and Y.-W. Mai, “Recent developments in the fire retardancy of polymeric materials,” *Prog. Polym. Sci.*, vol. 38, no. 9, pp. 1357–1387, Sep. 2013.
- [206] R. Kozłowski and M. Władysław-przybylak, “Review Flammability and fire resistance of composites reinforced by natural fibers,” no. April, pp. 446–453, 2008.
- [207] M. Modesti and a Lorenzetti, “Halogen-free flame retardants for polymeric foams,” *Polym. Degrad. Stab.*, vol. 78, no. 1, pp. 167–173, Jan. 2002.
- [208] T. Kashiwagi, “Polymer Combustion and Flammability-Role,” *Twenty-Fifth Symp. Combust.*, pp. 1423–1437, 1994.
- [209] *Test for Flammability of Plastic Materials for Parts in Devices and Appliances*. 1996.
- [210] P. Kiliaris and C. D. Papaspyrides, “Polymer/layered silicate (clay) nanocomposites: An overview of flame retardancy,” *Prog. Polym. Sci.*, vol. 35, no. 7, pp. 902–958, Jul. 2010.
- [211] R. Verdejo, F. Barroso-Bujans, M. A. Rodriguez-Perez, J. Antonio de Saja, M. Arroyo, and M. A. Lopez-Manchado, “Carbon nanotubes provide self-extinguishing grade to silicone-based foams,” *J. Mater. Chem.*, vol. 18, no. 33, p. 3933, 2008.
- [212] M. W. Chai, S. Bickerton, D. Bhattacharyya, and R. Das, “Influence of natural fibre reinforcements on the flammability of bio-derived composite materials,” *Compos. Part B Eng.*, vol. 43, no. 7, pp. 2867–2874, Oct. 2012.
- [213] P. Zhang, Y. Hu, L. Song, J. Ni, W. Xing, and J. Wang, “Effect of expanded graphite on properties of high-density polyethylene/paraffin composite with intumescent flame retardant as a shape-stabilized phase change material,” *Sol. Energy Mater. Sol. Cells*, vol. 94, no. 2, pp. 360–365, Feb. 2010.
- [214] Q. Zhang *et al.*, “The influence of carbon nanotubes on the combustion toxicity of PP/intumescent flame retardant composites,” *Polym. Degrad. Stab.*, vol. 115, pp. 38–44, May 2015.
- [215] G. Beyer and K. E. Ag, “Carbon Nanotubes as a New Class of Flame Retardants for Polymers 3. Properties and applications of carbon,” pp. 628–633.
- [216] G. Beyer, “Short Communication : Carbon Nanotubes as Flame Retardants for Polymers,” *Fire Mater.*, vol. 26, pp. 291–293, 2002.

- [217] T. Kashiwagi, F. Du, J. F. Douglas, K. I. Winey, R. H. Harris, and J. R. Shields, "Nanoparticle networks reduce the flammability of polymer nanocomposites.," *Nat. Mater.*, vol. 4, no. 12, pp. 928–33, Dec. 2005.
- [218] T. Kashiwagi *et al.*, "Flammability properties of polymer nanocomposites with single-walled carbon nanotubes: effects of nanotube dispersion and concentration," *Polymer (Guildf.)*, vol. 46, no. 2, pp. 471–481, Jan. 2005.
- [219] T. Kashiwagi *et al.*, "Thermal and flammability properties of polypropylene/carbon nanotube nanocomposites," *Polymer (Guildf.)*, vol. 45, no. 12, pp. 4227–4239, May 2004.
- [220] B. Yu *et al.*, "Enhanced thermal and flame retardant properties of flame-retardant-wrapped graphene/epoxy resin nanocomposites," *J. Mater. Chem. A*, vol. 3, no. 15, pp. 8034–8044, 2015.
- [221] G. Huang, J. Gao, X. Wang, H. Liang, and C. Ge, "How can graphene reduce the flammability of polymer nanocomposites?," *Mater. Lett.*, vol. 66, no. 1, pp. 187–189, Jan. 2012.
- [222] B. Sang, Z. Li, X. Li, L. Yu, and Z. Zhang, "Graphene-based flame retardants : a review," *J. Mater. Sci.*, vol. 51, no. 18, pp. 8271–8295, 2016.
- [223] A. L. Higginbotham, J. R. Lomeda, A. B. Morgan, and J. M. Tour, "Graphite oxide flame-retardant polymer nanocomposites.," *ACS Appl. Mater. Interfaces*, vol. 1, no. 10, pp. 2256–61, Oct. 2009.
- [224] Z. Wang, X. Tang, Z. Yu, P. Guo, H. Song, and X. Duc, "Dispersion of graphene oxide and its flame retardancy effect on epoxy nanocomposites," *Chinese J. Polym. Sci.*, vol. 29, no. 3, pp. 368–376, Feb. 2011.
- [225] J. Wang and Z. Han, "The combustion behavior of polyacrylate ester/graphite oxide composites," *Polym. Adv. Technol.*, vol. 17, no. 4, pp. 335–340, Apr. 2006.
- [226] A. C. Idumah, C.I.; Hassan, Azman; Affam, "A review of recent developments in flammability of polymer nanocomposites," *Rev. Chem. Eng.*, vol. 31, no. 2, pp. 149–177, 2015.
- [227] C. A. W. Alexander B. Morgan, *Flame Retardant Polymer Nanocomposites*, John Wiley. Hoboken, NJ, USA: John Wiley & Sons, Inc., 2007.
- [228] J. Xu, J. Liu, and K. Li, "Application of Functionalized Graphene Oxide in Flame-Retardant Polypropylene," *J. Vinyl Addit. Technol.*, 2014.
- [229] R. Harris *et al.*, "Flammability reduction of flexible polyurethane foams via carbon nanofiber network formation," no. May, pp. 588–595, 2008.
- [230] G. Malucelli, "The Role of Graphene in Flame Retardancy of Polymeric Materials: Recent Advances," *Curr. Graphene Sci.*, vol. 2, no. 1, pp. 27–34, Oct. 2018.
- [231] X. Wang, E. N. Kalali, J.-T. Wan, and D.-Y. Wang, "Carbon-family materials for flame retardant polymeric materials," *Prog. Polym. Sci.*, vol. 69, pp. 22–46, Jun. 2017.
- [232] M. Science and H. Adelnia, "Intumescent flame retardant polyurethane / reduced graphene oxide composites with improved mechanical , thermal , and barrier properties," no. September 2016, 2014.
- [233] G. Huang, H. Liang, Y. Wang, X. Wang, J. Gao, and Z. Fei, "Combination effect of melamine polyphosphate and graphene on flame retardant properties of poly(vinyl alcohol)," *Mater. Chem. Phys.*, vol. 132, no. 2–3, pp. 520–528, Feb. 2012.
- [234] D. K. Chattopadhyay and D. C. Webster, "Thermal stability and flame retardancy of polyurethanes," *Prog. Polym. Sci.*, vol. 34, no. 10, pp. 1068–1133, Oct. 2009.

- [235] F. Laoutid, L. Bonnaud, M. Alexandre, J.-M. Lopez-Cuesta, and P. Dubois, “New prospects in flame retardant polymer materials: From fundamentals to nanocomposites,” *Mater. Sci. Eng. R Reports*, vol. 63, no. 3, pp. 100–125, Jan. 2009.
- [236] X. Chen, J. Li, and M. Gao, “Thermal Degradation and Flame Retardant Mechanism of the Rigid Polyurethane Foam Including Functionalized Graphene Oxide,” *Polymers (Basel)*, vol. 11, no. 1, p. 78, Jan. 2019.
- [237] Z.-J. Cao, W. Liao, S.-X. Wang, H.-B. Zhao, and Y.-Z. Wang, “Polyurethane foams with functionalized graphene towards high fire-resistance, low smoke release, superior thermal insulation,” *Chem. Eng. J.*, vol. 361, pp. 1245–1254, 2019.
- [238] X. Zhang, Q. Shen, X. Zhang, H. Pan, and Y. Lu, “Graphene oxide-filled multilayer coating to improve flame-retardant and smoke suppression properties of flexible polyurethane foam,” *J. Mater. Sci.*, vol. 51, no. 23, pp. 10361–10374, 2016.
- [239] S. Liu, H. Yan, Z. Fang, and H. Wang, “Effect of graphene nanosheets on morphology, thermal stability and flame retardancy of epoxy resin,” *Compos. Sci. Technol.*, vol. 90, pp. 40–47, 2014.
- [240] C. Bao *et al.*, “Preparation of graphene by pressurized oxidation and multiplex reduction and its polymer nanocomposites by masterbatch-based melt blending,” *J. Mater. Chem.*, vol. 22, no. 13, p. 6088, 2012.
- [241] H. Pan, B. Yu, W. Wang, Y. Pan, L. Song, and Y. Hu, “Comparative study of layer by layer assembled multilayer films based on graphene oxide and reduced graphene oxide on flexible polyurethane foam: flame retardant and smoke suppression properties,” *RSC Adv.*, vol. 6, no. 115, pp. 114304–114312, 2016.
- [242] G. Huang, S. Chen, P. Song, P. Lu, C. Wu, and H. Liang, “Combination effects of graphene and layered double hydroxides on intumescent flame-retardant poly(methyl methacrylate) nanocomposites,” *Appl. Clay Sci.*, vol. 88–89, pp. 78–85, Feb. 2014.
- [243] B. Dittrich, K.-A. Wartig, D. Hofmann, R. Mülhaupt, and B. Schartel, “Carbon black, multiwall carbon nanotubes, expanded graphite and functionalized graphene flame retarded polypropylene nanocomposites,” *Polym. Adv. Technol.*, vol. 24, no. 10, pp. 916–926, Oct. 2013.
- [244] V. A. Online *et al.*, “Polymer Chemistry polyphosphamide for flame retardant epoxy composites: synthesis, flammability and mechanism,” 2013.
- [245] G. Huang, S. Wang, P. Song, C. Wu, S. Chen, and X. Wang, “Combination effect of carbon nanotubes with graphene on intumescent flame-retardant polypropylene nanocomposites,” *Compos. Part A Appl. Sci. Manuf.*, vol. 59, pp. 18–25, Apr. 2014.
- [246] X. Wang, L. Song, H. Yang, H. Lu, and Y. Hu, “Synergistic Effect of Graphene on Antidripping and Fire Resistance of Intumescent Flame Retardant Poly (butylene succinate) Composites,” pp. 5376–5383, 2011.
- [247] T. R. Hull, J. Wang, and Y. Hu, “Effect of Functionalized Graphene Oxide with Hyper-Branched Flame Retardant on Flammability and Thermal Stability of Cross-Linked Polyethylene,” 2014.
- [248] W. Hu, B. Yu, S.-D. Jiang, L. Song, Y. Hu, and B. Wang, “Hyper-branched polymer grafting graphene oxide as an effective flame retardant and smoke suppressant for polystyrene,” *J. Hazard. Mater.*, vol. 300, pp. 58–66, Dec. 2015.
- [249] B. Yuan *et al.*, “Enhanced flame retardancy of polypropylene by melamine-modified graphene oxide,” *J. Mater. Sci.*, vol. 50, no. 16, pp. 5389–5401, May 2015.

- [250] K.-Y. Li *et al.*, “Preparation and properties of novel epoxy/graphene oxide nanosheets (GON) composites functionalized with flame retardant containing phosphorus and silicon,” *Mater. Chem. Phys.*, vol. 146, no. 3, pp. 354–362, Aug. 2014.
- [251] G. Huang, S. Chen, S. Tang, and J. Gao, “A novel intumescent flame retardant-functionalized graphene: Nanocomposite synthesis, characterization, and flammability properties,” *Mater. Chem. Phys.*, vol. 135, no. 2–3, pp. 938–947, Aug. 2012.
- [252] X. Qian, L. Song, B. Yu, B. Wang, B. Yuan, and Y. Shi, “Novel organic – inorganic flame retardants containing exfoliated graphene: preparation and their performance on the flame retardancy of epoxy resins,” pp. 6822–6830, 2013.
- [253] W. Guo, Y. Hu, X. Wang, P. Zhang, L. Song, and W. Xing, “Exceptional flame-retardant cellulosic foams modified with phosphorus-hybridized graphene nanosheets,” *Cellulose*, vol. 26, no. 2, pp. 1247–1260, Jan. 2019.

Chapter 3. Bacterial cellulose foams

Chapter 3 is organized in 2 sub-chapters, chapter 3.1 and chapter 3.2.

3.1. Multifunctional hybrid structures made of open-cell aluminium foam impregnated with cellulose/graphene nanocomposites

This chapter was based in the following published paper:



Carbohydrate Polymers

Volume 238, 15 June 2020, 116197



Multifunctional hybrid structures made of open-cell aluminum foam impregnated with cellulose/graphene nanocomposites

Susana C. Pinto ^a, Nuno H.C.S. Silva ^b, Ricardo J.B. Pinto ^b, Carmen S.R. Freire ^b, Isabel Duarte ^a, Romeu Vicente ^c, Matej Vesenjak ^d, Paula A.A.P. Marques ^a  

3.1.1. Abstract

Chapter 3.1 focuses on exploring combinations of disintegrated bacterial cellulose nanofibers (BC) with graphene oxide (GO) (reduced and non-reduced) and phase change materials (PCMs) prepared in the form of foam-like structures. The presence of GO remarkably improves the fire-retardancy and provides dimensional stability to the foams while PCMs gives thermal energy storage capacity. The foams were exposed to methyltrimethoxysilane (MTMS) vapour to become hydrophobic which was confirmed by measuring water absorption capacity and water contact angle. To extend the multifunctionality of these nanocomposite foams, a selected composition was impregnated into an open-cell aluminium foam (OCF) creating a hybrid structure (HS-BC/GO) with higher mechanical properties (increase in stress of 100 times) and high sound absorption coefficient (near 1 between 1000–4000 Hz). The low thermal conductivity confirms that this hybrid structure is a thermal insulator. These advantages highlight the potential applications of the proposed materials e.g. construction, automotive and aeronautical sectors.

3.1.2. Introduction

Lightweight multifunctional materials are desirable for several industrial sectors, such as transport, construction, energy, aerospace, defence, packaging and biotechnology, amongst others [1,2]. Both structural topology and composition play crucial roles in defining a material's properties. Cellular composites are of significant interest as they often possess multifunctional physical properties. Their use lead to a significant weight reduction and material savings, which are combined with other advantages, such as excellent performance in impact energy absorption, vibration damping and sound attenuation, and heat insulation [3,4]. However, the manufacturing of this type of materials at a low cost is a great challenge [5]. Notably, nature presents several elegant and complex composite structures, with dimensions spanning from the nano- to macroscale, which can be lightweight and offer superior combinations of strength and toughness [6]. Even so, polymeric, ceramic and metal foams are examples of artificial lightweight materials with a cellular structure commonly used in modern engineering fields. [7–13]

For a given application, the base material should be selected taking into account the application and environmental conditions [14]. Regular open-cell metal foams [15–17] have been considered for multifunctional applications by combining different materials in order to acquire new characteristics and increase their functionality. For example, hybrid structures have been developed by impregnating the cells of regular open-cell aluminium (OCF) foams with polymers (e.g. epoxy resins, silicone and polydimethylsiloxane) fillers [12,18] to be used in crashworthiness applications.

As a demand for cost effective biopolymer alternatives to synthetic polymers, cellulose foams are being explored for sustainable and recyclable materials, to reduce the use of fossil fuels [19–22]. Cellulose foams have high surface-to-volume ratio, low weight, high porosity, resulting in interesting properties for many applications, such as drug delivery [23–25], thermal insulation [26], energy storage [27,28] and water remediation [29–31]. The use of cellulose nanofibers with a high-aspect ratio to produce foams is very interesting since novel properties emerge at the nanoscale. Cellulose nanofibers can be obtained by the mechanical shearing process of wood pulp fibres [32,33] or by mechanical disintegration of bacterial cellulose (BC) membranes [34]. These nanofibers can form strong gels in water with highly entangled networks at concentrations above 1 wt.% [32]. These gels can be used to prepare cellulose foams using several techniques, namely ice templating [35,36], supercritical CO₂ drying [37,38] and solvent evaporation of Pickering emulsions [39]. With the objective to obtain new functional properties, recently, cellulose has been combined with graphene-based materials (GBMs) resulting in multifunctional foams [40–42]. From this combination, high performance materials can be obtained for oil and dyes absorption, insulation materials and energy storage devices [43,44]. Another important aspect is that the presence of GBMs acts as flame retardant agent of cellulose [40,44].

Graphene is a planar monolayer of carbon atoms arranged into a two-dimensional honeycomb lattice, which was isolated for the first time in 2004 [45]. It is a carbon nanomaterial with great potential; however, it is important to emphasise that the term graphene is used in a generic manner by scientists to describe many GBMs [46]. The most fundamental properties of GBMs to consider are: i) number of graphene layers, ii) average lateral size and iii) oxygen content (with a variable carbon-to-oxygen (C/O) atomic ratio) [46]. One of the most popular GBMs is graphene oxide (GO), a chemically modified

graphene prepared by oxidation and exfoliation of graphite that is accompanied by extensive oxidative modification of the basal plane (epoxy, hydroxyl and carboxyl functional groups) [47]. The oxygen content in GO can be reduced by chemical, thermal, microwave, photo-chemical, photo-thermal or microbial/bacterial methods, resulting in reduced GO (rGO) [43].

When considering multifunctional foams targeting thermal insulation applications, the energy efficiency is always the key factor. The addition of phase change materials (PCMs) to composite foams can improve the performance of the energy distribution network. It is also important for energy conservation, as they exhibit a high enthalpy of fusion (for relatively small volumes) with the ability to store and release large amounts of energy in form of latent heat during melting and solidification [48–50].

To address the previously combined challenges and develop a lightweight multifunctional hybrid structure, this work reports, in a first step, the development of cellulose nanocomposite foams with the addition of GBMs and PCMs, using disintegrated BC nanofiber as the cellulose source. These foams were characterized and optimized in order to present flame-retardancy, moisture resistance, thermal and acoustic insulation properties. In a second step, the optimized cellulose nanocomposite foam composition was produced inside the porous OCF foam structure. This final hybrid structure counterbalances the weak cellulose nanocomposite dimensional stability properties, while keeping its multifunctional nature, extending the possibility of applications in areas that require structural integrity.

3.1.3. Materials and Methods

3.1.3.1. Materials

Bacterial cellulose (BC) membranes used as a cellulose source were produced using *Gluconacetobacter sacchari* in Hestrin and Schramm (HS) based media containing glucose, sucrose, fructose, mannitol or glycerol as carbon sources, as previously reported [51]. The obtained membranes were desintegrated in water using an Ultra-Turrax®. The final concentration of the BC aqueous suspension was approx. 0.55 wt.%. GO (4 mg/mL aqueous dispersion) was purchased from Graphenea (Spain) and microencapsulated PCMs (Micronal® DS 5001 X; core – paraffin (26 °C) and shell – PMMA) were acquired from BASF (Germany). Open-cell AlSi7Mg0.3 foam (designated by OCF foams) with

pore size of 10 ppi (pores per inch) and produced by investment casting method were supplied by Mayser GmbH & Co. KG (Germany). Other chemicals (hydroxylamine, ammonia aqueous solution (25 wt.%) and methyltrimethoxysilane) were supplied by Sigma-Aldrich and used as received.

3.1.3.2. Preparation of cellulose-based nanocomposite foams

BC aqueous suspensions were well mixed with GO (at concentrations of 2.5 wt.%, 5 wt.% and 10 wt.% with respect to BC dry mass) for 1 h at room temperature, followed by the addition of PCMs (5 wt.% and 10 wt.% with respect to BC dry mass) and again stirred for 1 h at room temperature. Finally, the suspensions were placed in a cylindrical mould at -20 °C and freeze-dried in a LyoQuest-Telstar freeze dryer. Control samples of pure BC and BC with 10 wt.% of PCMs were also prepared for comparison purposes.

To evaluate the effect of rGO on the final properties of the composites, GO was reduced by adding hydroxylamine (NH₂OH.HCl) to the BC and GO suspension. Briefly, NH₂OH.HCl (1:2) and ammonia aqueous solution (25 vol.%) were added into the BC and GO suspensions prepared as described above. The suspensions were then heated in a water bath at approx. 80 °C. After 1 h, the unreacted hydroxylamine was removed by washing the suspensions with water in a centrifuge for 3 times. The BC/rGO foams were then prepared as described above.

A hydrophobization treatment was applied to the prepared foams, which consisted of placing the foams inside a glass container with a small open glass vial containing methyltrimethoxysilane (MTMS). The container was closed and heated in an oven at 70 °C for 2 h allowing the contact between the foams and the generated silane vapours. Then, the exposed samples were placed in a vacuum oven to remove the excess of MTMS. The samples submitted to the hydrophobization process were denoted as H_BC, H_BC/GO10 and H_BC/rGO10.

3.1.2.3. Preparation of OCF impregnated with cellulose/graphene nanocomposites

The OCF foam was completely immersed in the selected composition of BC/GO10 suspension. To ensure an efficient infiltration of the OCF foam with the suspension, the container was briefly subjected to sonication before freeze-drying. The final structure was denoted as HS-BC/GO10.

3.1.3.4. Characterization

The morphology of the foams was assessed using a high-resolution analytical scanning electron microscope HR-FESEM Hitachi SU-70 and a TM 4000 Plus Hitachi operating at an accelerating voltage of 15 kV. X-ray photoelectron spectroscopy (XPS) spectra were acquired in an Ultra High Vacuum (UHV) system equipped with a hemispherical electron energy analyser (SPECS Phoibos 150), a delay-line detector and a monochromatic AlK α (1486.74 eV) X-ray source. High resolution spectra were recorded at normal emission take-off angle and with a pass-energy of 20 eV. The binding energies were calibrated with reference to the C1s peak (284.8 eV). The spectra were processed with XPSPEAK 4.1 software. The thermal stability of the nanocomposite foams was assessed by a thermogravimetric analyser (Netzsch – Jupiter STA) at a scanning rate of 10 °C/min in the temperature range of 30–800 °C under an oxidative atmosphere (synthetic air). The energy storage properties of the foams, including melting/solidification temperatures and enthalpies/latent heat, were determined on a differential scanning calorimeter (DSC, PerkinElmer 4000). A complete run of the DSC test consisted of one heating and cooling cycles between 10 °C and 40 °C, with a heating/cooling rate of 1 °C/min. The thermal conductivity was evaluated with a Hot Disk TPS 2500 S instrument in the transient mode at room temperature (20 °C). The uniaxial compression tests of BC-based foams were conducted using a Microservo Magnetic Tester equipment (MMT-101N; manufactured by Shimadzu Corporation, Japan) with a 100 N load cell. These compression tests were carried out at a cross-head velocity of 1 mm/min up to a strain of 80 %. The dimensions of the cylindrical foam specimens were approx. 12 mm in diameter and 12 mm in height. The quasi-static compression tests of OCF and hybrid structures were carried out using a standard compressive testing machine. The compression tests were carried out according to the standard ISO 13314: 2011, at a cross-head velocity of 6 mm/min. The value of sound absorption coefficient was estimated from measurements made with an impedance tube according to the standard ASTM E 1050 [52]. The cylindrical shaped specimens measured 37 mm in diameter and 22 mm in thickness. The flame-retardancy test was based on the direct observation of the foam response when submitted to a flame. The test consisted of applying a flame, at the specimen's bottom using the set-up in a vertical sample position, for 3 s, plus a subsequent application (3 s) if the specimen self-extinguishes.

The water absorption ability of the BC-based foams was determined by immersing previously weighted dry specimens (diameter of 12 mm and height of 12 mm) into 50 mL of distilled water and kept at room temperature. At different time periods, the wet specimens were lifted and the excess water on their surface was removed with filter paper. Its value was determined using Eq. (3.1.1), where W_i is the weight of the material at time i and W_0 is the initial weight.

$$\text{Water absorption} \left(\frac{\text{mg}}{\text{mg}} \right) = \frac{(W_i - W_0)}{W_0} \quad (\text{Eq. 3.1.1})$$

Water contact angle measurements were carried out with OCA 20 from Dataphysics at room temperature. The specimens' water contact angles were evaluated by static contact angle measurements using the sessile drop method. The shape of the liquid–vapour interface was determined by the Young–Laplace equation.

3.1.4. Results and Discussion

3.1.4.1. Cellulose-based nanocomposite foams

The process for the preparation of the nanocomposite and hybrid foams is illustrated in Figure 3.1.1. In brief, different concentrations of the components used to prepare the nanocomposite were stirred in aqueous medium. Following two routes, without (A1) and with (A2) GO reduction, the obtained mixtures were transferred to a cylindrical mould and freeze-dried to produce the nanocomposite foams. A process of hydrophobization was applied to the foams by exposing them to MTMS vapour. After the characterization of the different nanocomposite foams, a selected composition was incorporated in an OCF foam by simply immersing the metal foam in the aqueous suspension followed by freeze-drying (B).

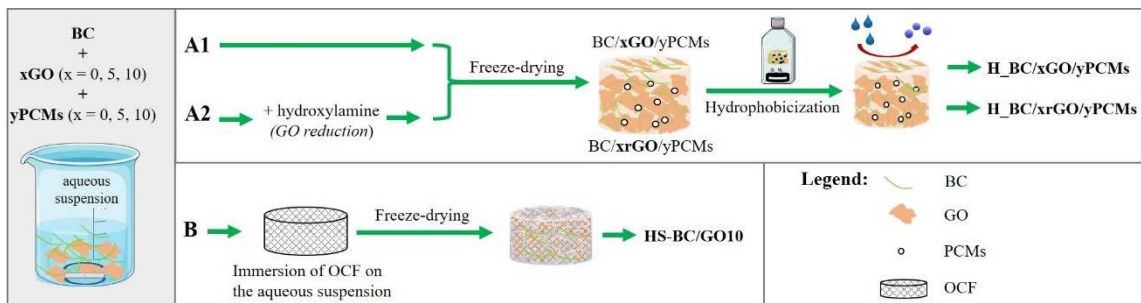


Figure 3.1.1 Schematic of the preparation of the nanocomposite foams and hybrid structures.

Morphology

The BC nanocomposite foams prepared by freeze drying are ultralight cellular structures with apparent density values between 10 kg/m^3 and 30 kg/m^3 , determined by weighting the previously conditioned samples in a desiccator for 24 h and measuring the geometric volume of the cylindrical specimens (Table S2.1.1). Although not accurate, due to a few geometric irregularities, these values are in agreement with previously reported ones for cellulose foams (1 kg/m^3 to 100 kg/m^3) [19]. The addition of 10 wt.% of PCMs increases the density of the BC foams from $9.8 \pm 1.3 \text{ kg/m}^3$ to $15.1 \pm 2.2 \text{ kg/m}^3$, while the incorporation of GO does not significantly influence the density values. However, the nanocomposite foams with rGO are denser with values of approx. 16 kg/m^3 without PCMs and 30 kg/m^3 with 10 wt.% of PCMs. These results are in accordance with the SEM images of the BC/rGO10 foams (Figure S2.1.1 (c1 and c2)) which show a denser structure when compared with BC and BC/GO10 foams (Figure S2.1.1 (a1 and a2) and (b1 and b2) respectively). The method employed to prepare the BC/xrGO/yPCMs (A2 in Figure 3.1.1) involves the *in situ* GO reduction with hydroxylamine [53] in the presence of the BC nanofiber. The *in situ* reduction was followed since the addition of previously reduced GO to the aqueous BC suspension caused the formation of rGO aggregates since rGO doesn't disperse in water due to its hydrophobic nature. This extra manipulation of the dispersion involving heating and washing by centrifugation, may be responsible to trigger more interactions between its components causing the denser structure. Additionally, a partial interaction between hydroxylamine and cellulose nanofiber cannot be excluded. In a different context, derivatives of this amine were explored to protect cellulose fibres surface before ozone bleaching of low-consistency pulp [54].

The top view photographs and SEM images of the foams BC/PCMs10 and BC/GO/PCMs10 are presented in Figure 3.1.2., The SEM images at higher magnification show a random distribution of the PCMs microcapsules which retains their physical integrity inside the foams. While it is difficult to distinguish the GO nanosheets from the BC nanofibers, the SEM images of BC/GO10/PCMs10 suggest a good dispersion between them. This is also clear from the homogeneous brown colour of the foams, characteristic of GO.

Flame tests

Regarding the flame tests, the pristine BC foams with or without PCMs burned vigorously and completely, leaving no residue as exemplified for BC/PCMs10 in Figure 3.1.2.

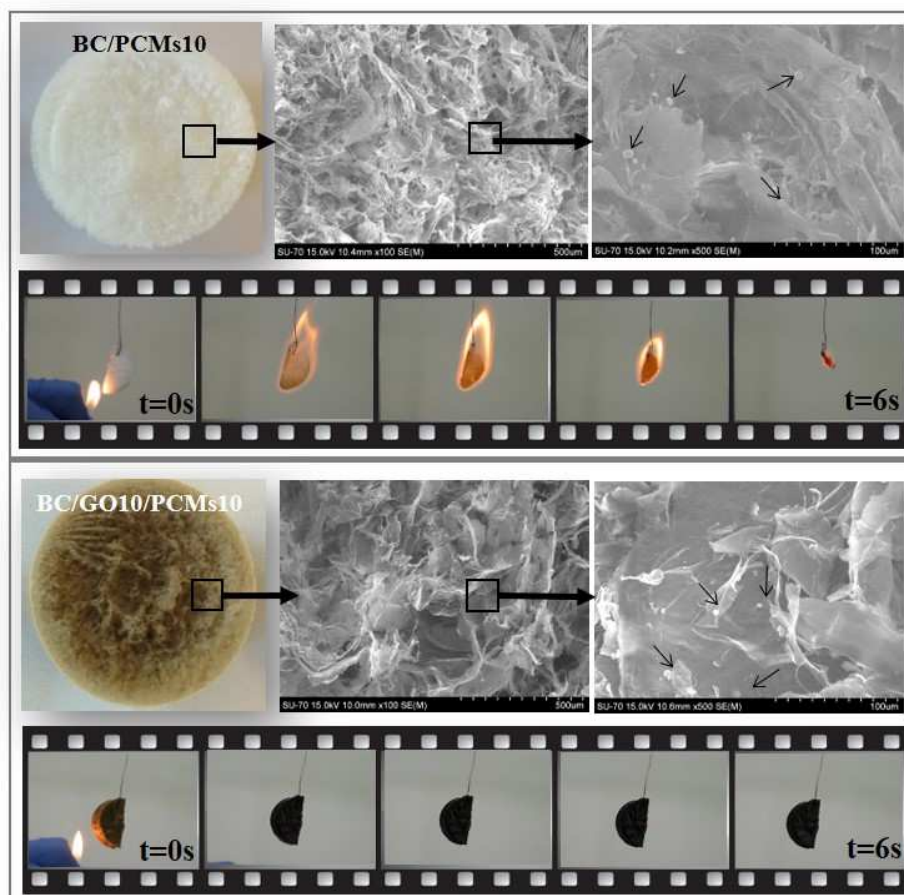


Figure 3.1.2 Photographs of the upper surface of BC/PCMs10 and BC/GO10/PCMs10 foams and respective SEM images at different magnifications (the arrows at the higher SEM magnification images point to PCMs microspheres) together with photographs of flame test results for both foams.

Remarkably, in the samples prepared with 10 wt.% GO or rGO there is no flame propagation as clearly demonstrated in Figure 3.1.2 for the BC/GO10/PCMs10 foam. In the samples prepared with 5 wt.% GO the flame takes about 2 seconds to self-extinguish (Figure S2.1.2). Additionally, there is no evident shrinkage of the samples after the flame test. Further, the SEM analysis of the foams after the flame exposure suggests that the microstructure is maintained, as exemplified for BC/GO10/PCMs10 in Figure S2.1.3, where no apparent changes of the cellular network and nanofibrous structure are detected and with the PCMs preserving the capsule integrity. GBMs have been proposed as flame retardants additives for polymer matrices, namely vegetal cellulose, due to their excellent

barrier properties that inhibit the transference of combustible gases during ignition through the formation of a char layer, which avoids the release of volatiles [55]. However, the previous studies report the use of an additional component, besides GBMs, to obtain this property, namely montemorillonite [56], sepiolite nanorods [40] or surface modified GBMs, such as phosphorus functional groups [57–59], or even the surface modification of the polymer itself to help with the compatibilization with GBMs [60]. In the present study, the good compatibility between the GO nanosheets and the BC nanofibers, was enough to, at 10 wt.% load, inhibit the flame propagation on the foam, without the need to chemically modify the GO surface or add complementary flame-retardant agent. Further and very important, the flame-retardant behaviour was not compromised by the hydrophilization method applied to the BC foams (discussed later) since the same performance was observed. Due to the importance of the fire-retardant property of these materials, the samples prepared with 10 wt. % of GO or rGO were selected for the subsequent studies.

Chemical analysis

XPS was used to characterize the surface chemistry of the nanocomposite foams. Both oxygen (O) and carbon (C) elements are present in the foams as shown in the fully scanned spectra of BC, BC/GO10 and BC/rGO10 foams (Figure 3.1.3(a)). Additionally, nitrogen (N) is present in the BC/rGO10 spectrum due to the reduction process with hydroxylamine. As mentioned previously, some chemical interactions may occur between hydroxylamine and the cellulose nanofiber justifying the N presence [54]. Table 3.1.1 presents the relative atomic concentration of C, O and N and C/O ratio for the above referred samples. The presence of the carbon nanostructures in the BC foam contributes to an increase of the C/O ratio, from 1.71 in BC to 2.30 in BC/GO10 and to 2.96 in BC/rGO10. This later value indicates the reduction of the GO, by the decrease of O at. %.

The high-resolution XPS C1s spectrum of BC foam (Figure 3.1.3(b)) can be deconvoluted into three main components, which are attributed to C-C and C-H (284.8 eV), C-O-C and C-OH (286.7 eV) and O-C-O (288.3 eV), the characteristic peaks of BC [61]. The C1s signal for BC/GO10 (Figure 3.1.3(c)) is wider in comparison with BC due to the GO contribution and after deconvolution four peaks were considered. A clear increase of the peak situated at 284.8 eV is observed, where, besides the C-C and C-H,

the presence of sp^2 carbon from GO is also assigned [62]. The peaks at 287.6 eV and 289.1 eV, attributed respectively to C=O and O-C=O linkages, also increased due to the oxygen functionalities present on the GO nanosheets and a fourth peak at 289.1 eV attributed to O-C=O is perceived [63]. The reduction of GO in the BC/rGO10 foam (Figure 3.1.3(d)) shows a significant increase of sp^2 carbon corresponding to the restoration of the graphene carbon structure due to the elimination of oxygen functional groups [64]. A new peak is present at approx. 285.7 eV corresponding to C-N from the reduction process with hydroxylamine.

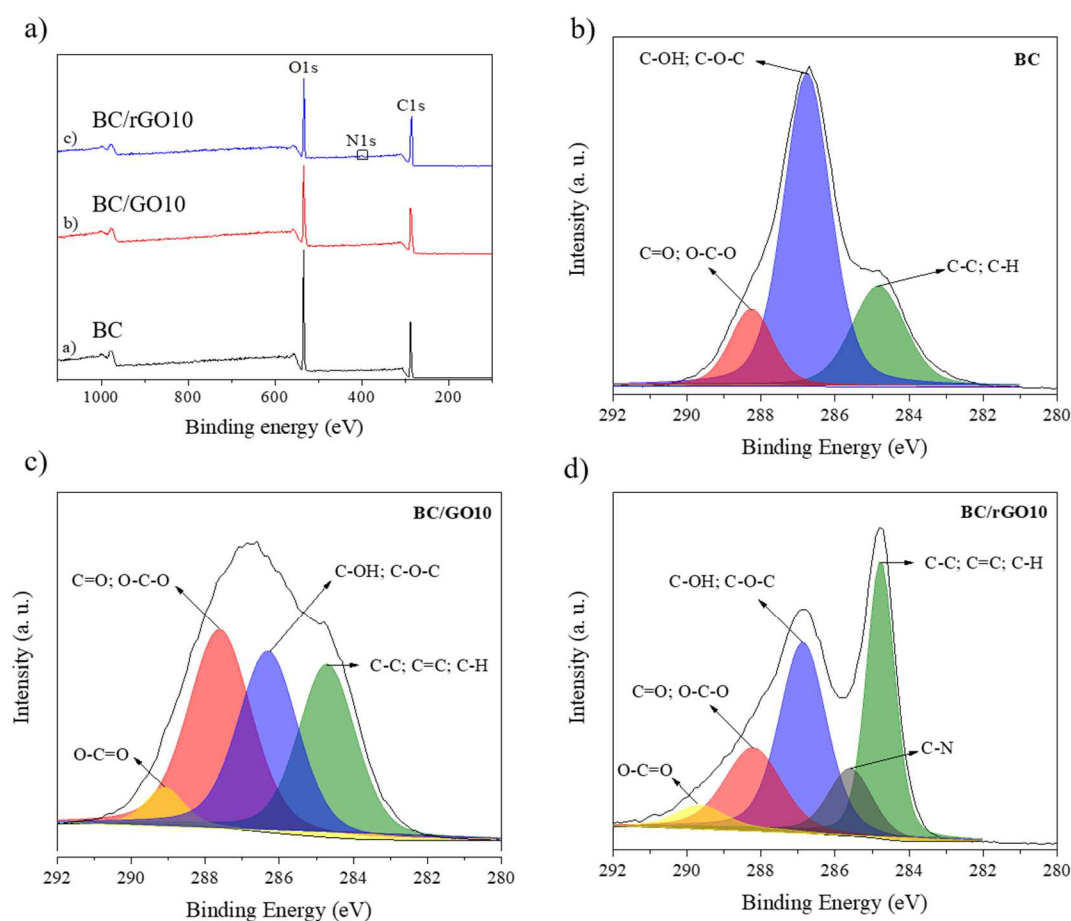


Figure 3.1.3 XPS spectra survey (a) and normalized C1s core levels for BC (b), BC/GO10 (c) and BC/rGO10 (d).

Table 3.1.1 Relative atomic percentage of C, O and N and C/O ratio for pristine BC nanofibers and BC nanocomposite foams.

	C (at. %)	O (at. %)	N (at. %)	C/O
BC	63.1	36.9	-	1.71
BC/GO10	69.6	30.4	-	2.30
BC/rGO10	73.8	24.9	1.3	2.96

Thermogravimetric and calorimetric analysis

The thermo-oxidative stability of these foams was assessed by thermogravimetric analysis (TGA) under air atmosphere (Figure 3.1.4 (a)). The TG curves of individual components, viz neat BC foam, GO nanosheets and PCMs microspheres were also obtained under the same conditions.

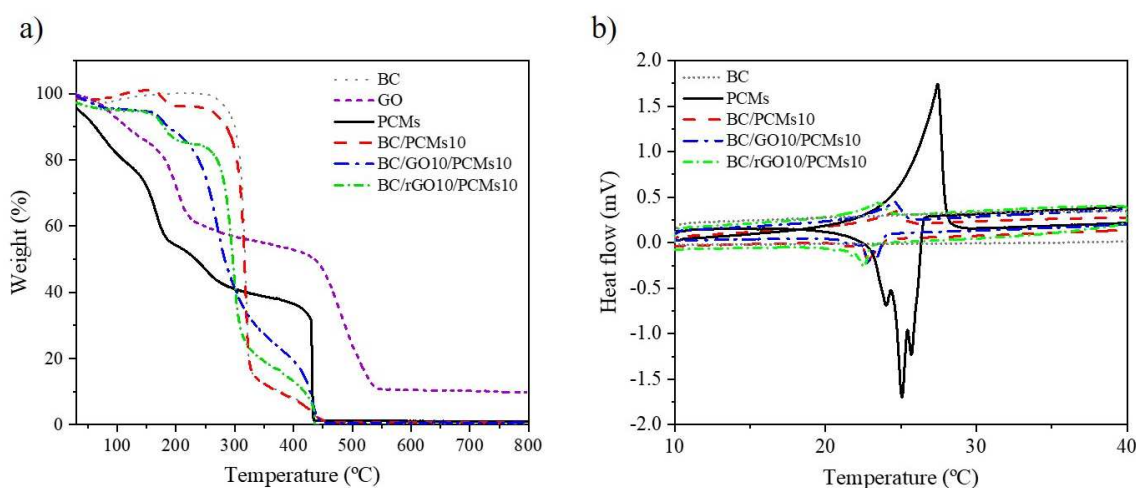


Figure 3.1.4 TGA under air atmosphere of BC foam, GO nanosheets, PCMs microcapsules, BC/PCMs10 foam, BC/GO10/PCMs10 foam and BC/rGO10/PCMs10 foam (a), DSC curves for PCMs microcapsules, BC, BC/PCMs10, BC/GO10/PCMs10 and BC/rGO10/PCMs10 (b).

Starting with the thermal behaviour of GO, the TG curve shows two significant weightlessness stages: the weight loss, between 150 °C and 230 °C, mainly attributed to the loss of labile oxygen functional groups and between 450 °C and 530 °C assigned to the reaction of the more stable carbonaceous residue in contact with the oxidizing atmosphere (calcination of the conjugated carbon skeleton of GO) [44,65]. The TG curve of the PCMs microcapsules reveals a gradual weight loss with two main weight losses between 160 °C and 280 °C due to the core paraffin decomposition [66] and an abrupt

weight loss of approx. 35 % at 432 °C attributed to the polymeric shell degradation (PMMA) [67]. The initial and continuous weight loss observed may be assigned to the core paraffin evaporation from some ruptured microcapsules, due to sample manipulation. In the case of BC foam, 90 % of its initial weight loss is observed at 318 °C due to the degradation of the polysaccharide chain, followed by a smaller degradation stage at approx. 438 °C corresponding to the generation of CO, CO₂ and H₂O [68]. For the BC/PCMs10 foam, the TG curve is dominated from the main constituent (BC) being possible to detect the initial weight loss due to the paraffin decomposition, however the PMMA shell degradation is masked due to its low content.

The TG profiles of the BC/GO10/PCMs10 and BC/rGO10/PCMs10 foams shows a small first weight loss at around 200 °C due to the PCMs presence. Then, pronounced weight loss steps with a maximum degradation temperature of 270 °C for the non-reduced foam and of 380 °C for the reduced foam are identified resulting from the combination of BC with the carbon nanostructures. For the reduced form, the main decomposition onset is slightly shifted to higher temperatures compared to the non-reduced form, suggesting the positive effect of the reduction process on the thermal stability. This improvement is attributed to the decrease in the amount of oxygen functional groups, which improved the ability of foams to tolerate high temperatures in the oxidative atmosphere [65].

DSC was used to assess the thermal phase transitions of the nanocomposite foams containing PCMs. The DSC curves are presented in Figure 3.1.4(b) and the phase change temperatures and enthalpies of BC/PCMs10, BC/GO10/PCMs10 and BC/rGO10/PCMs10 are reported in Table S2.1.2 (SI), respectively. As expected, PCMs create thermal energy storage capacity (TES) in the BC foams, the melting and solidifying enthalpies are in the range of 4–7 J/g and 3-7 J/g, respectively. These results are comparable with those reported by Borreguero *et al.* [67,69,70], where 11 wt.% of PCMs was incorporated in polyurethane foams and an enthalpy of 10 J/g was obtained. The solidification enthalpies (Table S2.1.2, SI) are generally smaller than the corresponding melting enthalpies due to an incomplete crystallization during the re-solidification processes [71].

Hydrophilic behaviour and mechanical performance

When considering the use of cellulose-based foams, the evaluation of their behaviour in contact with water is of major importance. Due to that, water absorption capacity of the foams before and after treatment with MTMS vapour was determined (according to Eq. 3.1.1) and the results are presented in Figure 3.1.5(a). Before MTMS vapour treatment BC and BC/GO10 show a high water absorption capacity, with BC foam losing its physical integrity after 1 h of water immersion while BC/GO10 maintained its physical integrity during the time of the experiment. Remarkably, after 15 min of immersion, the BC/GO10 foam shows a water absorption capacity of approx. 60 mg/mg, while pure BC absorbed approx. 39 mg/mg, (less 35%) after the same period. This highlights the strong hydrophilic nature of GO, which due to the high oxygen functional groups content, promotes strong interactions with the water molecules, resulting in a much higher water absorption capacity. This result is in accordance with a previous work [72], where a rise of water absorption capacity with the increase of GO content in cellulose (from cotton) foams was reported. However, and despite the high swelling of BC/GO10 foam, it maintains its physical integrity at least until 5 h (duration of the experiment), demonstrating a strong interaction between GO nanosheets and BC nanofibers that endorses dimensional integrity to the nanocomposite foams. It is also important to highlight the result obtained for BC/rGO10, which (although not treated with the MTMS vapour) shows a drastic reduction of the swelling capacity: a value of 2 mg/mg after 15 min was obtained. This indicates that the hydroxylamine was effective for the reduction of GO. For the foams exposed to MTMS vapour, a remarkable reduction of the water uptake was observed. This confirms the efficiency of the method to render the cellulose-based foams surface hydrophobic. Still, these foams reveal a slight increase in water absorption with time, possibly due to the capillarity effect associated with their porous structure [73].

Additionally, higher values of water contact angles (WCA) were achieved confirming the successful hydrophobization of the foams (Figure 3.1.5(b)). Images of the water droplets formed on the top of BC/GO10 and H_BC/GO10 foams, at times 0 and 3 min are shown in Figure 3.1.5(b). For BC/GO10, the water droplet, with an initially WCA of 86.3°, is completely absorbed after 5 s, contrary to what is observed for the sample H_BC/GO10, where the drop maintains a WCA of 133.1° for at least 3 min.

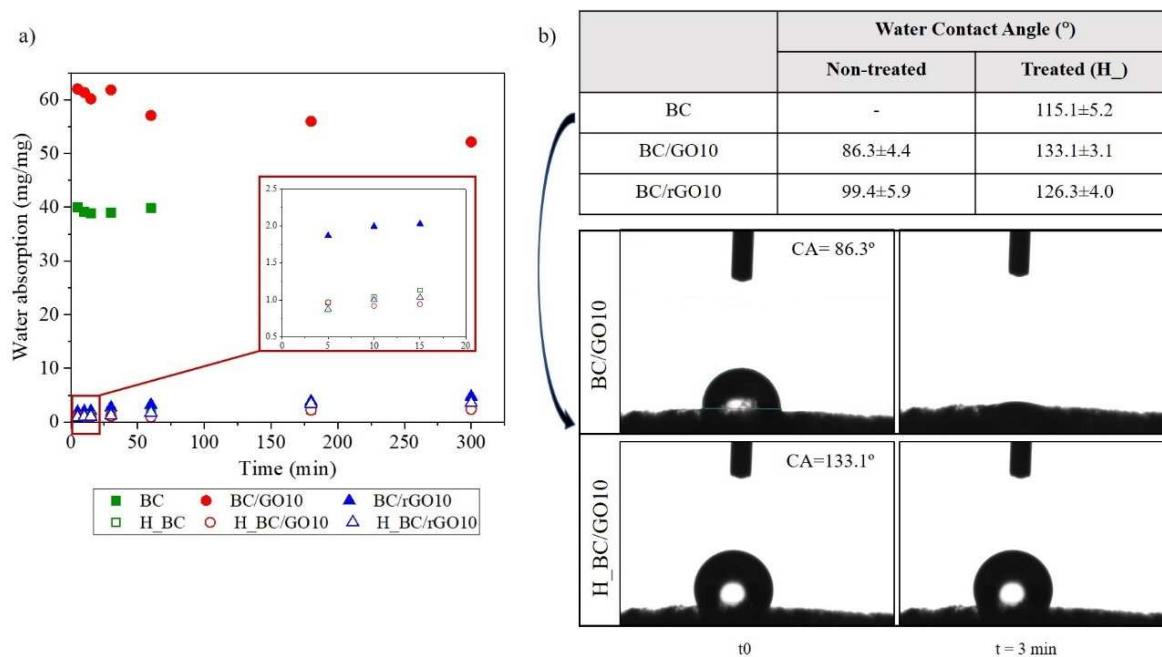


Figure 3.1.5 Water absorption capacity of BC, BC/GO10 and BC/rGO10 before and after hydrophobization (H₋) (a). The values represent a mean \pm SD of $n=3$; and water contact values for the foams before and after hydrophobization (b).

We further explored the effect of the fillers in the BC foams mechanical properties. The representative stress–strain curves of BC and BC nanocomposite foams are shown in Figure S2.1.4 and the compressive modulus and the stress values at the strain of 0.1 (at 10% of deformation) are summarized in Table 3.1.2.

Figure S2.1.4 shows that the stress increases exponentially with the increasing strain for all samples, rapidly reaching the densification. Results demonstrate also that the compressive behaviour is influenced by the presence of the PCMs and GBMs on the BC foams. The introduction of PCMs microcapsules leads to a decrease of the compression strength of the respective foam composition without PCMs, probably because the microcapsules act as defects in the foam structure, hindering the connections between BC nanofibers and the GO nanosheets. The GO addition has a positive effect in the foams. The BC/GO nanocomposite foams present the higher compressive modulus determined (23.13 ± 2.11 kPa) (Table 3.1.2). The compressive modulus and stress at 10 % of deformation of BC/GO10 are 22 % higher than for the pristine BC foams, suggesting that the hydrogen bonding between BC and GO contributes to the mechanical improvement [74]. Further, the high aspect ratio of the GO nanosheets can be advantageous to the efficient load transfer [75]. Similar studies of vegetable cellulose foams reported the

enhancement of compressive modulus and strength after addition of GO [74,76]. The BC/rGO10 and BC/rGO10/PCMs10 foam densifies earlier due to its compact structure, as previously discussed.

Table 3.1.2 Compressive results of the cellulose-based foams.

Cellulose-based foams	Compressive modulus, kPa	Stress (at strain of 0.1), kPa
BC	13.11 ± 1.86	1.22 ± 0.18
BC/PCMs10	5.52 ± 0.35	0.52 ± 0.12
BC/GO10	23.13 ± 2.11	2.20 ± 0.03
BC/GO10/PCMs10	20.46 ± 0.66	1.92 ± 0.21
BC/rGO10	11.87 ± 2.61	1.48 ± 0.90
BC/rGO10/PCMs10	4.94 ± 0.70	0.51 ± 0.09

3.1.4.2. Aluminium-cellulose hybrid structures

Structural and mechanical characterization

Subsequently, the optimized formulation of the BC/GO10 suspension was incorporated inside the OCF (Figure 3.1.1 route B), which is identified to act as a structural support. Figure 3.1.6 shows the photographs of the pure OCF foam and the HS-BC/GO10 hybrid structure. The SEM images of the later, in the transversal section of the foam wall, showed that the presence of the metallic core promoted a partial alignment of the pores of the nanocomposite during the freeze-drying. This partial orientation of the cellular pores is attributed to the presence of the metal skeleton, which may influence the freezing of the water, resulting in an anisotropic foam [19].

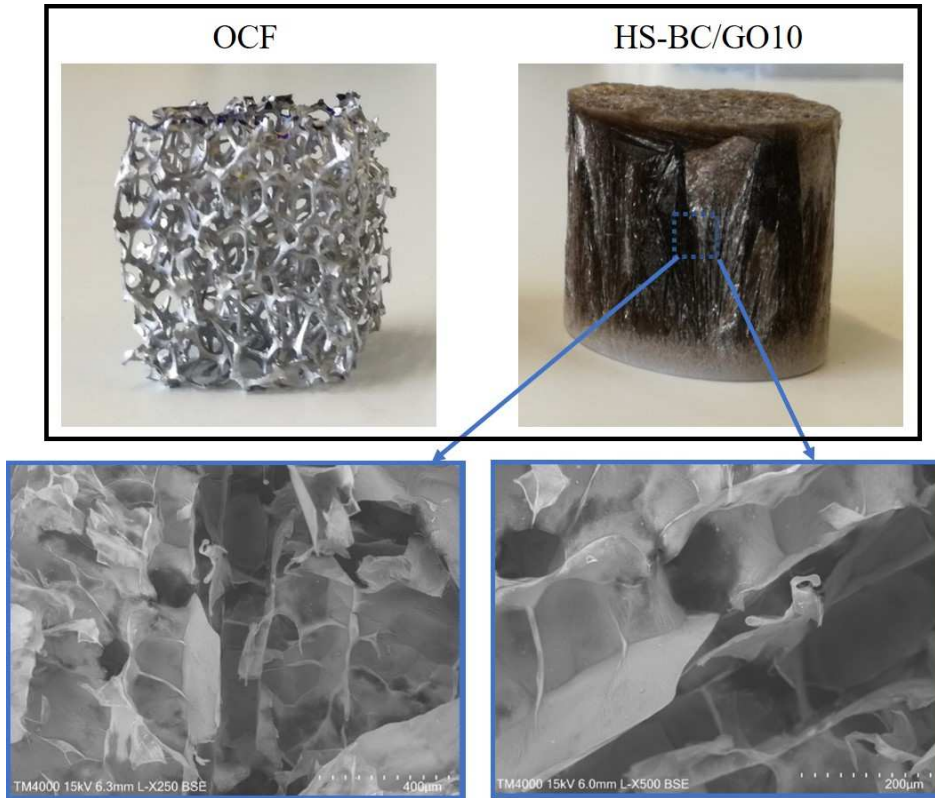


Figure 3.1.6 Photographs of OCF foam and BC/GO10 hybrid structure (OCF is inside) with and SEM images of the HS-BC/GO10 sample at different scale magnifications.

The comparison of the compressive behaviour of the OCF, BC/GO10 foam and the HS-BC/GO10 hybrid structure is shown in Figure 3.1.7(a). The typical plateau stress response of the OCF foam specimens is divided into three main regions (elastic, plateau and densification), as observed from the curves displayed in Figure 3.1.7(a). An initial elastic region, where the foam deformation is controlled by the deformation of the pore-wall due to bending and axial forces is observed, then the stress increases with the strain until reaching a peak stress, followed by a stress drop especially for OCF foam. The plateau region, where the foam exhibits a long almost constant stress due to progressive layer-by-layer pore collapse is governed by elastic buckling, plastic collapse or brittle crushing. However, this region presents some stress fluctuations, especially for the OCF foam, certainly due to the successive collapse and densification of cells at different areas during loading [12]. The presence of the BC/GO10 foam slightly decreases the stress oscillations, stabilising the compressive response of the hybrid foams. The region, where the foam densifies due to the contacts between the cell struts, results in an abrupt increase of the stiffness. The expected mechanical reinforcement, when compared with the BC/GO10 foam, was achieved since an increase in stress of approx. 100 times was

obtained. In sum, from the comparison stress-strain curves of the hybrid structures and of their individual components, it is concluded that the behaviour is governed essentially by the OCF skeleton.

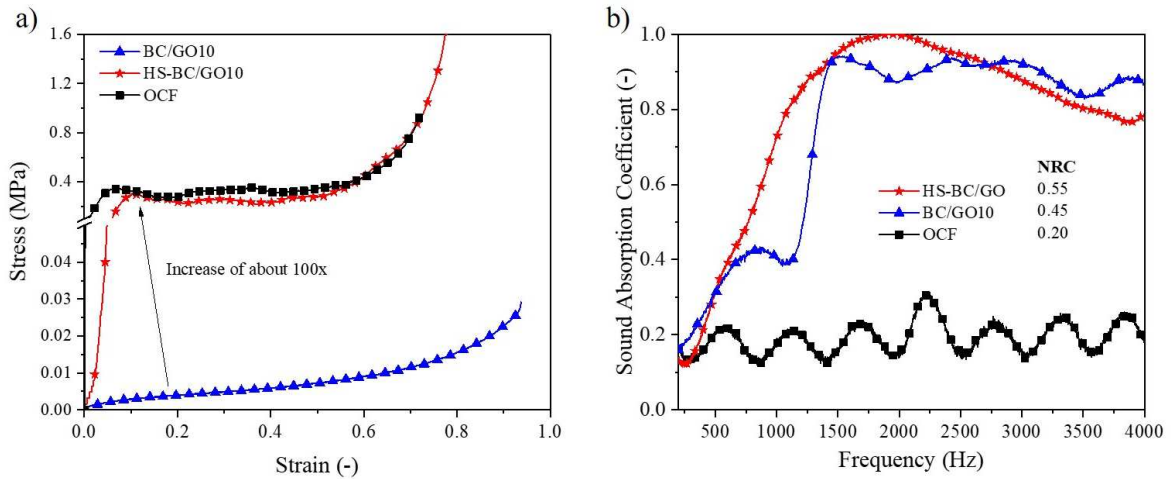


Figure 3.1.7 Average stress-strain compressive curves (a) and sound absorption (b) of OCF, BC/GO10 and HS-BC/GO10.

Sound absorption

Cellular materials are described as good sound insulating materials [77,78]. In this case, BC/GO10 and HS-BC/GO10, the sound absorption coefficient increases with frequency until 1500 Hz, followed by a small decrease and finally a subsequent stabilization between 2000 Hz and 4000 Hz, with values of 0.8 and 0.9, respectively (Figure 3.1.7(b)). The OCF foam shows a fluctuant small sound absorption capacity over the whole range of frequencies. However, when the OCF is filled with BC/GO10, the pores became smaller and more collisions between cell walls and sound waves take place. Furthermore, the cellulose cell walls are flexible and the foam structure twists and turns resulting in an increase in the friction and air viscosity consumption, thus improving the sound absorption performance [79]. In addition to the morphology (pore size and shape, porosity, interconnectivity, rigidity, density, thickness), the acoustic absorption behaviour of the material also depends on the frequency of the sound waves. It is reported that, for the propagation of sound wave in air, the heat exchange is not significant because of relatively low thermal conductivity of air. Thus, the sound absorption coefficient at low frequencies is very small [77,78]. The parameter often used to describe the sound absorption is the noise reduction coefficient (NRC). This parameter corresponds to the average of the sound absorption coefficients (at 250 Hz, 500 Hz, 1000 Hz and 2000 Hz)

and rounding the value to the nearest multiple of 0.05. The NRC values are given in Figure 3.1.7(b). The hybrid foam presents the highest sound absorption performance with NRC of 0.55. Comparing the materials analysed in this study with the ones reported in the literature, ours revealed considerable higher NRC values (0.55) for low thickness (22 mm) and density of materials (110 kg/m^3). Pedroso *et al.* [80] gathered the information regarding common and alternative insulating materials. For example, agglomerates of expanded cork exhibit NRC values of 0.4 with 50 mm of thickness and a density of 105 kg/m^3 .

Thermal conductivity

Further, the thermal conductivity of the hybrid structure was measured considering its anisotropy of the pores near the OCF skeleton. The thermal conductivity values for HS-BC/GO10 is $0.070 \text{ W/(m}\cdot\text{K)}$ in the axial direction and $0.035 \text{ W/(m}\cdot\text{K)}$ in the radial direction. It is reported that open-cell metal foams present values for thermal conductivity between $1\text{-}7 \text{ W/(m}\cdot\text{K)}$, depending on the geometry and cell wall material. Results show higher thermal conductivity values for the axial direction because the channel's direction (axial direction) is favoured. The main reason for this, is the large pore channels that reduce the solid thermal conduction of the walls in the radial direction (perpendicular to the pore direction), facilitating the heat flow along the pore direction. As so, higher values of thermal conductivity for the hybrid structures were expected due the presence of the OCF skeleton. The relatively low thermal conductivity values observed for this hybrid structures can be related with the BC/GO10 filler that reduces the heat transfer. The thermal conductivity of the isotropic BC/GO10 foam was previously determined and low values around $0.035 \text{ W/(m}\cdot\text{K)}$ were obtained. Thus, the hybrid structure is considered an insulating material.

3.1.5. Conclusions

Nanocomposite foams were prepared with disintegrated BC nanofibers and GO (reduced and non-reduced) at different loadings, with or without PCMs addition by a simple method. The samples prepared with 10 wt.% GO with respect to BC dry mass present excellent flame retardancy without the need for further fire-retardant additives. The strong electrostatic interactions between GO nanosheets and BC nanofibers provide dimensional stability to the nanocomposite foams. The hydrophobization method applied to the foams was effective without compromising the fire-retardant properties. The

presence of the 10 wt.% of PCMs create TES capacity in the foams. To take full advantage of the multifunctional properties of the nanocomposite foams, a hybrid structure was created by embedding an OCF with the BC/GO10. The resultant hybrid structure (HS-BC/GO10) presented a compressive modulus 100 times higher than the one for BC/GO10 without significantly increasing its final weight. Further, HS-BC/GO10 presents a high sound absorption performance with NRC of 0.55 and thermal isolation properties. Therefore, OCF structures impregnated with BC, GO and PCMs are thoroughly multifunctional materials with potential applications in construction, automotive and aeronautic sectors.

3.1.6. References

- [1] N. Gupta and M. Paramsothy, "Metal- and Polymer-Matrix Composites: Functional Lightweight Materials for High-Performance Structures," *J. Miner. Met. Mater. Soc.*, vol. 66, no. 6, pp. 862–865, 2014.
- [2] J. P. Thomas and M. A. Qidwai, "Mechanical design and performance of composite multifunctional materials," *Acta Biomater.*, vol. 52, pp. 2155–2164, 2004.
- [3] I. Duarte, N. Peixinho, A. Andrade-campos, and R. Valente, "Special Issue on Cellular Materials," *Sci. Technol. Mater.*, vol. 30, no. 1, pp. 1–3, 2018.
- [4] M. Wang, X. Duan, Y. Xu, and X. Duan, "Functional Three-Dimensional Graphene/Polymer Composites," *ACS Nano*, vol. 10, no. 8, pp. 7231–7247, 2016.
- [5] A. D. B. L. Ferreira, P. R. O. Nóvoa, and A. T. Marques, "Multifunctional Material Systems: A state-of-the-art review," *Compos. Struct.*, vol. 151, pp. 3–35, 2016.
- [6] Y. Yang et al., "Recent Progress in Biomimetic Additive Manufacturing Technology: From Materials to Functional Structures," *Adv. Mater.*, vol. 30, no. 36, p. 1706539, 2018.
- [7] E. Aram and S. Mehdipour-Ataei, "A review on the micro- and nanoporous polymeric foams: Preparation and properties," *Int. J. Polym. Mater. Polym. Biomater.*, vol. 65, no. 7, pp. 358–375, Dec. 2015.
- [8] U. G. K. Wegst, H. Bai, E. Saiz, A. P. Tomsia, and R. O. Ritchie, "Bioinspired structural materials," *Nat. Mater.*, vol. 14, no. 1, pp. 23–36, 2015.
- [9] B. E. Obi and B. E. Obi, "Overview of Applications of Polymeric Foams," *Polym. Foam. Struct.*, pp. 3–14, Jan. 2018.
- [10] S. Ahmad, M. A. Latif, H. Taib, and A. F. Ismail, "Short review: Ceramic foam fabrication techniques for wastewater treatment application," *Adv. Mater. Res.*, vol. 795, pp. 5–8, 2013.
- [11] V. C. Shunmugasamy and B. Mansoor, "Aluminum foam sandwich with density-graded open-cell core: Compressive and flexural response," *Mater. Sci. Eng. A*, vol. 731, pp. 220–230, Jul. 2018.
- [12] I. Duarte, M. Vesenjajk, L. Krstulović-Opara, and Z. Ren, "Crush performance of multifunctional hybrid foams based on an aluminium alloy open-cell foam skeleton," *Polym. Test.*, vol. 67, pp. 246–256, 2018.

- [13] W. Zhai et al., “Microstructure-based experimental and numerical investigations on the sound absorption property of open-cell metallic foams manufactured by a template replication technique,” *Mater. Des.*, vol. 137, pp. 108–116, 2018.
- [14] M. Reinfried, G. Stephani, F. Luthardt, J. Adler, M. John, and A. Krombholz, “Hybrid Foams - A New Approach for Multifunctional Applications,” *Adv. Eng. Mater.*, vol. 13, no. 11, pp. 1031–1036, Nov. 2011.
- [15] W. Y. Jang and S. Kyriakides, “On the crushing of aluminum open-cell foams: Part I. Experiments,” *Int. J. Solids Struct.*, vol. 46, no. 3–4, pp. 617–634, 2009.
- [16] L. J. Gibson and M. F. Ashby, *Cellular Solids: Structure and Properties*. Cambridge University Press, 1999.
- [17] D. Negri, C. Musp, V. Mussi, C. Musp, P. Aghaei, and M. Strano, “Cost-Efficient Aluminum Open-Cell Foams : Manufacture , Characterization , and Heat Transfer Measurements,” *Adv. Eng. Mater.*, vol. 20, p. 1701032, 2018.
- [18] S. C. Pinto et al., “Characterization and physical properties of aluminium foam–polydimethylsiloxane nanocomposite hybrid structures,” *Compos. Struct.*, vol. 230, p. 111521, Dec. 2019.
- [19] F. Martoia, T. Cochereau, P. J. J. Dumont, L. Orgéas, M. Terrien, and M. N. Belgacem, “Cellulose nanofibril foams: Links between ice-templating conditions, microstructures and mechanical properties,” *Mater. Des.*, vol. 104, pp. 376–391, Aug. 2016.
- [20] C. He et al., “Mechanically Resistant and Sustainable Cellulose-Based Composite Aerogels with Excellent Flame Retardant, Sound-Absorption, and Superantwetting Ability for Advanced Engineering Materials,” *ACS Sustain. Chem. Eng.*, vol. 6, no. 1, pp. 927–936, Jan. 2018.
- [21] N. Lavoine and L. Bergstrom, “Nanocellulose-based foams and aerogels: processing, properties, and applications,” *J. Mater. Chem. A*, vol. 5, no. 31, pp. 16105–16117, 2017.
- [22] A. Zaman, F. Huang, M. Jiang, W. Wei, and Z. Zhou, “Preparation, Properties, and Applications of Natural Cellulosic Aerogels: A Review,” *Energy Built Environ.*, vol. 1, no. 1, pp. 60–76, Jan. 2020.
- [23] J. Bhandari, H. Mishra, P. K. Mishra, R. Wimmer, F. J. Ahmad, and S. Talegaonkar, “Cellulose nanofiber aerogel as a promising biomaterial for customized oral drug delivery,” *Int. J. Nanomedicine*, vol. 12, pp. 2021–2031, Mar. 2017.
- [24] H. Valo et al., “Drug release from nanoparticles embedded in four different nanofibrillar cellulose aerogels,” *Eur. J. Pharm. Sci.*, vol. 50, no. 1, pp. 69–77, 2013.
- [25] Z. Ulker and C. Erkey, “An emerging platform for drug delivery: Aerogel based systems,” *J. Control. Release*, vol. 177, pp. 51–63, 2014.
- [26] Y. Kobayashi, T. Saito, and A. Isogai, “Aerogels with 3D ordered nanofiber skeletons of liquid-crystalline nanocellulose derivatives as tough and transparent insulators,” *Angew. Chem. Int. Ed. Engl.*, vol. 53, no. 39, pp. 10394–10397, 2014.
- [27] Y. Zheng, J. Monty, and R. J. Linhardt, “Polysaccharide-based nanocomposites and their applications,” *Carbohydr. Res.*, vol. 405, pp. 23–32, Mar. 2015.
- [28] X. Du, Z. Zhang, W. Liu, and Y. Deng, “Nanocellulose-based conductive materials and their emerging applications in energy devices - A review,” *Nano Energy*, vol. 35, pp. 299–320, 2017.

- [29] H. Liu, B. Geng, Y. Chen, and H. Wang, "Review on the Aerogel-Type Oil Sorbents Derived from Nanocellulose," *ACS Sustain. Chem. Eng.*, vol. 5, no. 1, pp. 49–66, 2017.
- [30] B. Geng et al., "Surface-Tailored Nanocellulose Aerogels with Thiol-Functional Moieties for Highly Efficient and Selective Removal of Hg(II) Ions from Water," *ACS Sustain. Chem. Eng.*, vol. 5, no. 12, pp. 11715–11726, 2017.
- [31] W. Caichao, L. Yun, J. Yue, J. Chunde, S. Qingfeng, and L. Jian, "Ultralight and hydrophobic nanofibrillated cellulose aerogels from coconut shell with ultrastrong adsorption properties," *J. Appl. Polym. Sci.*, vol. 132, no. 24, pp. 42037-, 2015.
- [32] W. Zhang, Y. Zhang, C. Lu, and Y. Deng, "Aerogels from crosslinked cellulose nano/micro-fibrils and their fast shape recovery property in water," *J. Mater. Chem.*, vol. 22, no. 23, pp. 11642–11650, 2012.
- [33] C. Antonini et al., "Ultra-porous nanocellulose foams: A facile and scalable fabrication approach," *Nanomaterials*, vol. 9, no. 8, pp. 1–14, 2019.
- [34] H. Abral, Kadriadi, M. Mahardika, D. Handayani, E. Sugiarti, and A. N. Muslimin, "Characterization of disintegrated bacterial cellulose nanofibers/PVA bionanocomposites prepared via ultrasonication," *Int. J. Biol. Macromol.*, vol. 135, pp. 591–599, 2019.
- [35] C. Jiménez-Saelices, B. Seantier, B. Cathala, and Y. Grohens, "Effect of freeze-drying parameters on the microstructure and thermal insulating properties of nanofibrillated cellulose aerogels," *J. Sol-Gel Sci. Technol.*, vol. 84, no. 3, pp. 475–485, 2017.
- [36] C. Jimenez-Saelices, B. Seantier, B. Cathala, and Y. Grohens, "Spray freeze-dried nanofibrillated cellulose aerogels with thermal superinsulating properties.," *Carbohydr. Polym.*, vol. 157, pp. 105–113, Feb. 2017.
- [37] Y. Medina-Gonzalez, S. Camy, and J.-S. Condoret, "Cellulosic materials as biopolymers and supercritical CO₂ as a green process: chemistry and applications," *Int. J. Sustain. Eng.*, vol. 5, no. 1, pp. 47–65, Mar. 2012.
- [38] H. Sehaqui, Q. Zhou, and L. A. Berglund, "High-porosity aerogels of high specific surface area prepared from nanofibrillated cellulose (NFC)," *Compos. Sci. Technol.*, vol. 71, no. 13, pp. 1593–1599, 2011.
- [39] N. T. Cervin, J. Boon, S. Ng, P. Olin, and L. Bergstro, "Lightweight and Strong Cellulose Materials Made from Aqueous Foams Stabilized by Nanofibrillated Cellulose," *Biomacromolecules*, vol. 14, pp. 503–511, 2013.
- [40] B. Wicklein et al., "Thermally insulating and fire-retardant lightweight anisotropic foams based on nanocellulose and graphene oxide.," *Nat. Nanotechnol.*, vol. 10, no. 3, pp. 277–83, Mar. 2015.
- [41] J. Yang, E. Zhang, X. Li, Y. Zhang, J. Qu, and Z. Z. Yu, "Cellulose/graphene aerogel supported phase change composites with high thermal conductivity and good shape stability for thermal energy storage," *Carbon N. Y.*, vol. 98, pp. 50–57, 2016.
- [42] Q. Yao, B. Fan, Y. Xiong, C. Jin, Q. Sun, and C. Sheng, "3D assembly based on 2D structure of Cellulose Nanofibril/Graphene Oxide Hybrid Aerogel for Adsorptive Removal of Antibiotics in Water," *Sci. Rep.*, vol. 7, no. December 2016, pp. 1–13, 2017.
- [43] C. Vilela, R. J. B. Pinto, S. Pinto, P. Marques, A. Silvestre, and C. S. Freire, *Polysaccharide Based Hybrid Materials*. Cham: Springer International Publishing, 2018.
- [44] S. C. Pinto et al., "Bacterial cellulose/graphene oxide aerogels with enhanced dimensional and thermal stability," *Carbohydr. Polym.*, vol. 230, p. 115598, Feb. 2020.

- [45] K. S. Novoselov, A. K. Geim, S. V Morozov, and D. Jiang, "Electric Field Effect in Atomically Thin Carbon Films," *Science* (80-.), vol. 306, pp. 666–669, 2004.
- [46] P. Wick et al., "Classification framework for graphene-based materials," *Angew. Chemie - Int. Ed.*, vol. 53, no. 30, pp. 7714–7718, 2014.
- [47] Y. Zhu et al., "Graphene and graphene oxide: synthesis, properties, and applications.," *Adv. Mater.*, vol. 22, no. 35, pp. 3906–24, Sep. 2010.
- [48] K. Pielichowska and K. Pielichowski, "Phase change materials for thermal energy storage," *Prog. Mater. Sci.*, vol. 65, pp. 67–123, Aug. 2014.
- [49] S. A. Memon, "Phase change materials integrated in building walls: A state of the art review," *Renew. Sustain. Energy Rev.*, vol. 31, pp. 870–906, Mar. 2014.
- [50] M. Pomianowski, P. Heiselberg, and Y. Zhang, "Review of thermal energy storage technologies based on PCM application in buildings," *Energy Build.*, vol. 67, pp. 56–69, Dec. 2013.
- [51] A. R. P. Figueiredo et al., "Antimicrobial bacterial cellulose nanocomposites prepared by in situ polymerization of 2-aminoethyl methacrylate," *Carbohydr. Polym.*, vol. 123, pp. 443–453, 2015.
- [52] J. da Silva, "Metodologias experimentais para a determinação do coeficiente de absorção de sonora em materiais de construção," University of Coimbra, 2008.
- [53] X. Zhou, J. Zhang, H. Wu, H. Yang, J. Zhang, and S. Guo, "Reducing Graphene Oxide via Hydroxylamine: A Simple and Efficient Route to Graphene," *J. Phys. Chem. C*, vol. 115, no. 24, pp. 11957–11961, Jun. 2011.
- [54] T. He, M. Liu, and X. Tian, "Effect of active hydroxylamine intermediates on improving cellulose protection and mass transfer in ozone bleaching of low-consistency pulp," *Ind. Crops Prod.*, vol. 143, no. April 2019, p. 111404, 2019.
- [55] B. Dittrich, K. Wartig, D. Hofmann, R. Mülhaupt, and B. Schartel, "Flame retardancy through carbon nanomaterials : Carbon black , multiwall nanotubes , expanded graphite , multi-layer graphene and graphene in polypropylene," *Polym. Degrad. Stab.*, vol. 98, no. 8, pp. 1495–1505, 2013.
- [56] G. G. Chen et al., "Fabrication of strong nanocomposite films with renewable forestry waste/montmorillonite/reduction of graphene oxide for fire retardant," *Chem. Eng. J.*, vol. 337, no. December 2017, pp. 436–445, 2018.
- [57] W. Guo, Y. Hu, X. Wang, P. Zhang, L. Song, and W. Xing, "Exceptional flame-retardant cellulosic foams modified with phosphorus-hybridized graphene nanosheets," *Cellulose*, vol. 26, no. 2, pp. 1247–1260, Jan. 2019.
- [58] W. Chen, Y. Liu, P. Liu, C. Xu, Y. Liu, and Q. Wang, "The preparation and application of a graphene-based hybrid flame retardant containing a long-chain phosphaphenanthrene," *Sci. Rep.*, no. May, pp. 1–12, 2017.
- [59] K. Li et al., "Preparation and properties of novel epoxy / graphene oxide nanosheets (GON) composites functionalized with flame retardant containing phosphorus and silicon," *Mater. Chem. Phys.*, vol. 146, no. 3, pp. 354–362, 2014.
- [60] J. Alongi et al., "Superior flame retardancy of cotton by synergetic effect of cellulose-derived nano-graphene oxide carbon dots and disulphide-containing polyamidoamines," *Polym. Degrad. Stab.*, vol. 169, p. 108993, 2019.

- [61] J. E. Song, C. Silva, A. M. Cavaco-paulo, and H. R. Kim, "Functionalization of Bacterial Cellulose Nonwoven by Poly (fluorophenol) to Improve Its Hydrophobicity and Durability," *Front. Bioeng. Biotechnol.*, vol. 7, no. November, pp. 1–10, 2019.
- [62] G. Gonçalves et al., "Reductive nanometric patterning of graphene oxide paper using electron beam lithography," *Carbon N. Y.*, vol. 129, pp. 63–75, 2018.
- [63] V. Kuzmenko, "Cellulose-derived carbon nanofibers/graphene composite electrodes for powerful compact supercapacitors," *RSC Adv.*, vol. 7, pp. 45968–45977, 2017.
- [64] S. Stankovich et al., "Synthesis of graphene-based nanosheets via chemical reduction of exfoliated graphite oxide," *Carbon N. Y.*, vol. 45, no. 7, pp. 1558–1565, 2007.
- [65] G. Gonçalves et al., "Graphene oxide modified with PMMA via ATRP as a reinforcement filler," *J. Mater. Chem.*, vol. 20, no. 44, p. 9927, 2010.
- [66] J. Giro-Paloma, G. Oncins, C. Barreneche, M. Martínez, A. I. Fernández, and L. F. Cabeza, "Physico-chemical and mechanical properties of microencapsulated phase change material," *Appl. Energy*, vol. 109, pp. 441–448, 2013.
- [67] A. M. Borreguero, J. F. Rodríguez, J. L. Valverde, T. Peijs, and M. Carmona, "Characterization of rigid polyurethane foams containing microencapsulated phase change materials: Microcapsules type effect," *J. Appl. Polym. Sci.*, vol. 128, no. 1, pp. 582–590, Apr. 2013.
- [68] A. Mautner, J. Lucenius, M. Österberg, and A. Bismarck, "Multi-layer nanopaper based composites," *Cellulose*, vol. 24, no. 4, pp. 1759–1773, 2017.
- [69] A. M. Borreguero, J. L. Valverde, T. Peijs, J. F. Rodríguez, and M. Carmona, "Characterization of rigid polyurethane foams containing microencapsulated Rubitherm® RT27. Part I," *J. Mater. Sci.*, vol. 45, no. 16, pp. 4462–4469, May 2010.
- [70] A. M. Borreguero, J. F. Rodríguez, J. L. Valverde, R. Arevalo, T. Peijs, and M. Carmona, "Characterization of rigid polyurethane foams containing microencapsulated Rubitherm® RT27: catalyst effect. Part II," *J. Mater. Sci.*, vol. 46, no. 2, pp. 347–356, Aug. 2010.
- [71] T. Barz and A. Sommer, "Modeling hysteresis in the phase transition of industrial-grade solid/liquid PCM for thermal energy storages," *Int. J. Heat Mass Transf.*, vol. 127, pp. 701–713, Dec. 2018.
- [72] S. Zhou et al., "Preparation of cellulose – graphene oxide aerogels with N -methyl morpholine- N -oxide as a solvent," *J. Appl. Polym. Sci.*, vol. 46152, pp. 1–7, 2018.
- [73] C. Demitri et al., "Preparation and characterization of cellulose-based foams via microwave curing," *J. R. Soc. interface*, vol. 4, no. 1, p. 20130053, 2014.
- [74] J. Zhang, Y. Cao, J. Feng, and P. Wu, "Graphene-Oxide-Sheet-Induced Gelation of Cellulose and Promoted Mechanical Properties of Composite Aerogels," *J. Phys. Chem. C*, vol. 116, no. 14, pp. 8063–8068, 2012.
- [75] J. R. Potts, D. R. Dreyer, C. W. Bielawski, and R. S. Ruoff, "Graphene-based polymer nanocomposites," *Polymer (Guildf.)*, vol. 52, no. 1, pp. 5–25, Jan. 2011.
- [76] X. Ge, Y. Shan, L. Wu, X. Mu, H. Peng, and Y. Jiang, "High-strength and morphology-controlled aerogel based on carboxymethyl cellulose and graphene oxide," *Carbohydr. Polym.*, vol. 197, pp. 277–283, 2018.
- [77] W. Jin et al., "Sound Absorption Characteristics of Aluminum Foams Treated by Plasma Electrolytic Oxidation," *Materials (Basel)*, vol. 8, no. 11, pp. 7511–7518, Nov. 2015.

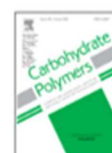
- [78] M. Nosko and J. Kováčik, “Sound Absorption Ability of Aluminium Foams,” *Met. Foam.*, vol. 1, no. 1, pp. 15–41, Jul. 2017.
- [79] C. He et al., “Mechanically Resistant and Sustainable Cellulose-Based Composite Aerogels with Excellent Flame Retardant, Sound-Absorption, and Superantiwetting Ability for Advanced Engineering Materials,” *ACS Sustain. Chem. Eng.*, vol. 6, no. 1, pp. 927–936, 2018.
- [80] M. Pedroso, J. de Brito, and J. D. Silvestre, “Characterization of eco-efficient acoustic insulation materials (traditional and innovative),” *Constr. Build. Mater.*, vol. 140, pp. 221–228, 2017.

3.2. Bacterial cellulose/graphene oxide aerogels with enhanced dimensional and thermal stability

This chapter was based in the following published paper:



Carbohydrate Polymers
Available online 11 November 2019, 115598
In Press, Journal Pre-proof ?



Bacterial cellulose/graphene oxide aerogels with enhanced dimensional and thermal stability

Susana C. Pinto ^a, Gil Gonçalves ^a  , Stefania Sandoval ^b, Ana M. López-Periago ^b, Alejandro Borrás ^b, Concepción Domingo ^b, Gerard Tobias ^b, Isabel Duarte ^a, Romeu Vicente ^c, P.A.A.P. Marques ^a  

 **Show more**

<https://doi.org/10.1016/j.carbpol.2019.115598>

Get rights and content

3.2.1. Abstract

In chapter 3.2 is presented a novel method for processing bacterial cellulose/graphene oxide (BC/GO) aerogels with improved multifunctional properties. The addition of a small amount of dimethyl sulfoxide (DMSO) to the aqueous dispersion of the nanomaterials during the gelification process showed to affect the water freezing temperature of the system and thereby affecting the porous structure of the aerogel obtained after lyophilization. The possibility to obtain small and elongated pore with axial orientation allowed a significant improvement of the structural stability of the aerogels. Moreover, the aerogels reduction by thermal treatment with ammonia vapour induced crosslinking between the different nanophases, thus giving an incremental factor for the mechanical performance of the aerogels under harsh conditions. The resulting aerogels also showed significant improvements in terms of thermal stability and electrical conductivity. These multifunctional BC-based aerogels present high potential as greener alternative materials for energy-efficient building structures, robust packaging or eco-friendly energy applications.

3.2.2. Introduction

Cellulose is the most abundant biopolymer in earth, with an annual production of about 1.5 trillion tons, mostly for paper and textile industries [1]. Indeed, humans have been exploring cellulose since ancient times due to its high availability (e.g. cotton, wood, hemp) and easy processability for daily routine materials [2]. Recently, nanotechnology is having a major impact on the development of several new approaches for processing cellulose (bacterial or vegetal). Nanocellulose arises as one of the most sustainable nanomaterial due to its high availability, biodegradability and biocompatibility, with promising applications in areas of environmental remediation, medical care, cosmetics and beyond [3]. This nanomaterial has been intensely explored for the development of multifunctional bio-based nanomaterials with several different architectures, including highly porous aerogels and mechanically strong paper or films [4,5].

Beside the potential applications of nanocellulose by itself, the incorporation of an additional nanophase can provide the appearance/improvement of outstanding properties due to the establishment of synergistic effects [5,6]. The application range of nanocellulose-based nanocomposites has thus been extended to the fields of antibacterial materials, sensors, catalysis and energy [7,8].

Recently, graphene oxide (GO) outstands as one of the most appealing nanomaterial for applications in environmental science, energy storage, and medical science [9]. Moreover, it has been widely explored as a reinforcing agent for cellulose macrostructures for the development of multifunctional materials [10]. GO nanosheets are graphene derivatives decorated with several oxygenated functional groups (carboxylic, hydroxyl and epoxy) on their basal planes and edges, resulting in a hybrid carbon nanostructure comprising a mixture of sp^2 and sp^3 domains [11,12]. Concerning the compatibility between cellulose and GO, it is reported that the highly oxygenated GO interacts with cellulose hydroxyl groups by the establishment of hydrogen bonds [13,14] resulting in the formation of mechanical stable nanocomposites with [15] with an effective three dimensional (3D) interconnected network [16]. Many studies give insights about the fabrication of cellulose/GO nanocomposite structures for several applications, e.g., to remove heavy metals, organic dyes, oils or pesticide residues from fluids and for adsorption of air pollutants [17–22]; in energy devices, such as supercapacitors [23–25], in electro-magnetic interference shielding field [26], and for biomedical applications with particular relevance in the field of tissue engineering [27–29].

The inherent interfacial compatibility of polar nanocellulose with GO provides a stimulating starting point to explore solution-based methodologies for the preparation of homogenous dispersions, in which the structural integrity of the biopolymer matrix is improved. Innovative ways should be developed to maximize the interactions between the matrix and filler, since this is the dominant and key factor in the enhancement of the specific surface area and mechanical performance. For example, the abundant oxygen containing groups in GO likely interact with the hydroxyl groups in cellulose through hydrogen bonds. This has been proven by Yao *et al.* [19] by using ultrasonic treatment for composites preparation, in which the high energy supply of ultrasounds induced fast formation of hydrogen bonds. However, the ultrasound method is not the most adequate to prepare 3D structures, since cavitation can easily break the delicate gel framework. The most popular fabrication methods of cellulose/GO in the form of aerogels/foams include freeze-casting, supercritical fluids (ethanol or carbon dioxide) and Pickering [5,30,31]. Particularly, the directional freeze-casting method could create hierarchical materials with aligned porous structures and high mechanical robustness [18,32]. Importantly, this synthetic methodology offers a high control over the pore size and density of nanocellulose-based nanocomposites.

The establishment of chemical crosslinking between nanocellulose and GO is another important strategy explored for the improvement of the dimensional stability of nanocomposite foams. Wicklein *et al.* [32] developed ultralight and anisotropic porous foams of cellulose nanofibers with GO by studying the combination of a crosslinking agent (boric acid) addition and directional freeze-casting. The foams revealed excellent combustion resistance, thermal conductivity and high radial mechanical resistance (even after exposure to 85 % rh). Recently, Ge *et al.* [33] reported the development of an ultra-strong aerogel, based on carboxymethyl cellulose and GO crosslinked also resourcing/using boric acid. This composite material produced attained fairly good compressive strength and Young modulus of 349 and 1029 kPa, respectively compatible with different applications. Other examples reporting the covalent linkage between nanocellulose and GO for the formation of macrostructures with improved properties can be easily found in the literature [34]. However, this strategy has some clear limitations, including restrained stability, complex surface chemistry, restrictions for geometrical confinement, the use of organic solvents and the need of purification of the final materials.

A simple way to improve the dimensional and mechanical stability of lightweight and hydrophilic GO based materials, especially in wet environments, consists on GO reduction, thus removing oxygen containing functional groups and, consequently, decreasing its original hydrophilicity [35,36]. Besides, the tailoring of GO surface chemistry by reduction could help to increase its reactivity for amphiphilicity-driven assembly strategy. Recently, Xiong *et al.* [36] reported an efficient approach for constructing hybrid materials based on a net of 1D cellulose nanofibers wrapped in GO nanosheets. Their findings showed that the interface-driven assembly between the two components is mainly governed by the level of reduction of GO nanosheets, where high reduced GO are tightly surrounded by a dense conformal nanocellulose network [36]. Therefore, the morphology and dimensional stability of 3D bacterial cellulose/ graphene oxide (BC/GO) aerogels can be tailor-made by exploring different reduction strategies for improved interfacial hydrophobic-hydrophilic interactions between the individual nanoelements.

This work can mean an important step forward to development of novel multifunctional BC-based aerogels reinforced with GO for improved performance in different environments envisaging greener and energy-efficient buildings structures, robust packaging materials or eco-friendly alternatives to energy applications. Taking these considerations into account,

in this study, it is presented a simple, fast, and environmentally friendly preparation method of BC/GO aerogels with different ratios, e.g., 90/10, 75/25 and 50/50. Herein, special focus was directed towards the effect of the addition of a residual amount of dimethyl sulfoxide (DMSO) to the BC/GO aqueous suspension on the structure of the resulting aerogels. Moreover, the impact of two different types of reduction treatments applied to the aerogels, either with an aqueous solution of hydrazine (N_2H_4) or with ammonia (NH_3) vapour, in their chemical and structural features was studied.

3.2.3. Materials and Methods

3.2.3.1. Synthesis of BC/GO aerogels

Bacterial cellulose (BC) aqueous suspension nano-fibrils with 1 % of solids was used as the cellulose source in this work (kindly supplied by BC TECHNOLOGIES, Lda.). BC and GO (Graphenea® in aqueous suspension of 4 mg/mL) were thoroughly mixed for 1 h at room temperature (rt). Four BC/GO sample compositions were prepared (100, 90, 75 and 50 wt. % of BC with respect to the GO dry mass), which are designated hereafter by BC, BC/GO10, BC/GO25 and BC/GO50, respectively. The composites were prepared by directly mixing both suspensions under vigorous stirring with and without the addition of DMSO (1.0 μ L and 2.5 μ L DMSO:100 μ L of aqueous suspension) during the mixture. The final blends were placed in a cylindrical mould, frozen at -20 °C and freeze-dried in a LyoQuest-Telstar freeze dryer. The samples prepared with 1.0 μ L of DMSO were reduced using two different approaches, which involve liquid and gas phase reduction of the material in presence of (N_2H_4) [37] or NH_3 [38]. In the first case, the aerogels were immersed into a (N_2H_4) solution (1 μ L/mL) at rt for 24h. Then, the aerogels were thoroughly washed with distilled water and dried again by lyophilisation. The second approach consisted in annealing the sample at 220 °C under a continuous flow of NH_3 gas. The samples processed with NH_3 were then purified by vacuum treatment to remove the residual NH_3 adsorbed on the aerogel. In both cases, treatments might lead to the N-functionalization/doping of the graphene derivative [38]. A scheme of the employed methodology is shown in Figure 3.2.1.

3.2.3.2. Characterization

The morphology of the samples was characterized using an ultra-high-resolution analytical scanning electron microscope HR-FESEM Hitachi SU-70 operating at an accelerating voltage of 15 kV. The samples (cylinders of 12 mm in diameter and 10 mm in

height) and densities (23 kg/m^3) were analysed in a micro-computed tomography (μCT) equipment from SkyScan 1275 (Bruker μCT , Belgium) with penetrative X-rays of 20 kV and 175 μA , in a high resolution mode with a pixel size of 10 μm and 450 ms of exposure time. NRecon and CTVox softwares were used for 3D-reconstruction and CTan software was used in morphometric analysis. A representative reduced volume of interest (VOI) was defined in both samples with a volume of 500 mm^3 in 3D reconstruction and morphometric analysis (pore size distribution). The chemical composition of the foams was analysed by Fourier Transform Infrared Spectroscopy - Attenuated Total Reflectance (FT-IR-ATR) (Bruker Tensor 27) spectrophotometer between 4000 and 400 cm^{-1} , with a resolution of 4 cm^{-1} and 64 scans. XPS spectra were acquired in an Ultra High Vacuum (UHV) system equipped with a hemispherical electron energy analyser (SPECS Phoibos 150), a delay-line detector and a monochromatic $\text{AlK}\alpha$ (1486.74 eV) X-ray source. High resolution spectra were recorded at normal emission take-off angle and with a pass-energy of 20 eV. The thermal stability of the composites aerogels was assessed by a thermogravimetric analyser (Netzsch, Jupiter STA) at a scanning rate of 10 $^\circ\text{C}/\text{min}$, in the temperature range of 30–800 $^\circ\text{C}$, under an oxidative atmosphere (synthetic air). For the water absorption tests, the dry specimens were allowed to hydrate in excess distilled water at rt. The weights of the hydrated samples were measured at timed intervals, following removal of excess water by gentle blotting. The water absorption capacity (Q) was determined using Equation 3.2.1, where W_i is the weight of the swollen material at time i and W_0 is the weight of the dried foam.

$$Q = \frac{(W_i - W_0)}{W_0} \quad (\text{Eq. 3.2.1})$$

Contact angle measurements were carried out with OCA 20 from Dataphysics. The measurements were performed at rt using the sessile drop method and the Laplace-Young fitting. Uniaxial compression tests and dynamic cyclic compression tests were performed using Microservo Magnetic Tester equipment (MMT-101N; manufactured by Shimadzu Corporation, Japan) equipped with a 100 N load cell. The tests were carried out for 5 % deformation, at a frequency of 0.3 Hz for 1,000 cycles and quasi-static compression at a cross-head speed of 1.0 mm/min.

3.2.4. Results and discussion

3.2.4.1. Effect of solvent composition on BC/GO aerogels

The BC/GO aerogels were prepared by vigorous stirring of mixtures of the aqueous suspensions of both individual components. In this process, BC nanofibers were dispersed and self-assembled on the surface of GO [39]. The synthesis of a BC/GO aerogel is schematically illustrated in Figure 3.2.1. The SEM observation of the as-prepared BC/GO aerogels without DMSO addition confirms the porous structure and the homogenous mixture between the cellulose fibrils and the GO sheets, being difficult to distinguish both components (Figure 3.2.1).

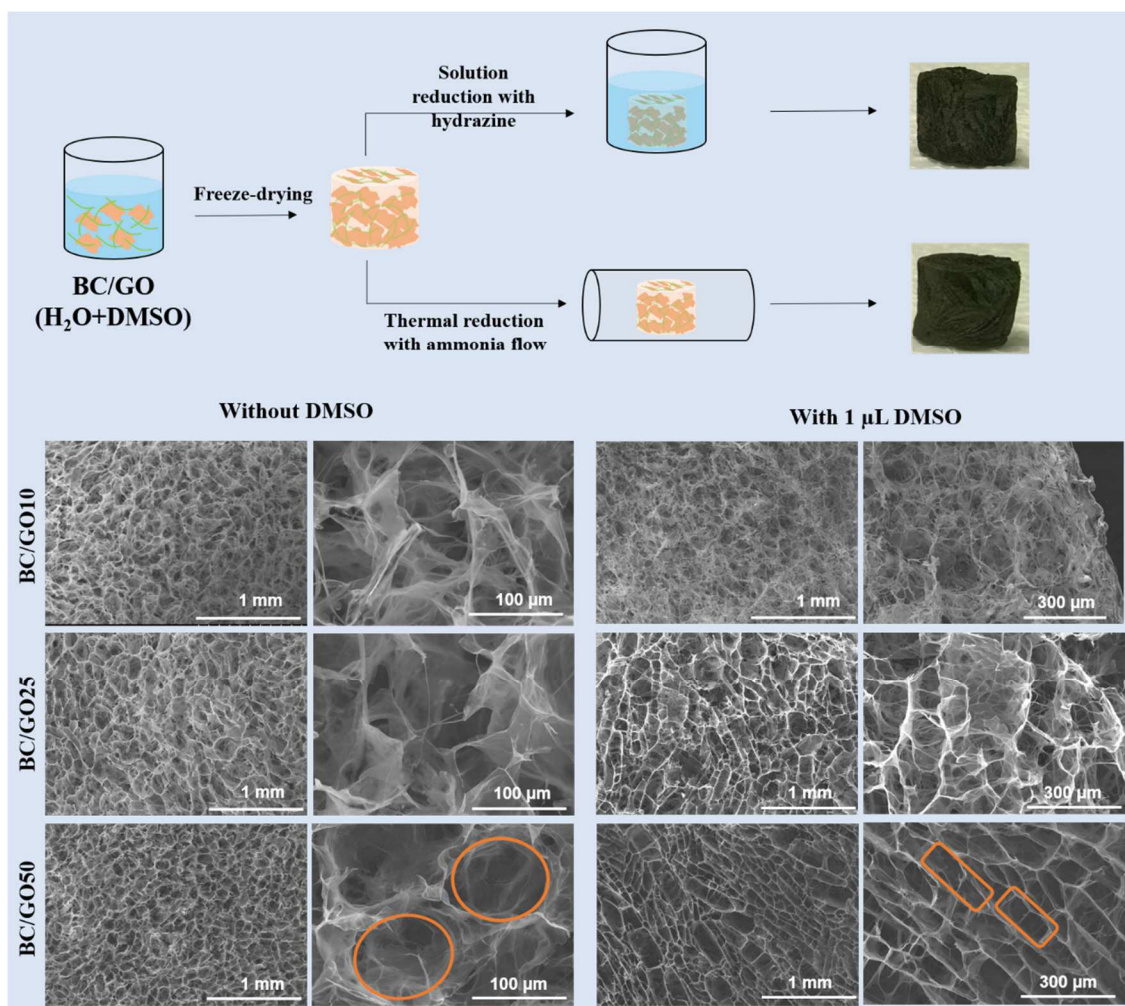


Figure 3.2.1 Schematic diagram of aerogels preparation and optical appearance. Comparison of the SEM images obtained at the cross-section of the different BC/GO aerogels, prepared with and without DMSO.

The chemical composition of both phases allows for the establishment of strong hydrophilic interactions [40] and hydrogen bonds [41], thus endorsing strong entanglement

that leads to the formation of 3D networks. Independently of the BC/GO ratio used, the aerogels exhibited an interconnected porous structure, with distribution of pore size width in the range from a few microns to hundreds of micrometers.

As mentioned, this work first explores the possibility to induce structural features of BC/GO aerogels by the DMSO addition to aqueous BC/GO suspensions during the processing of the samples. Hence, the effect of adding a small amount of DMSO to the BC/GO aqueous mixture (1.0 and 2.5 μL DMSO / 100 μL aqueous mixture) was studied. Despite the very low volumetric fraction of DMSO added, the structural changes observed on the BC/GO aerogels were remarkable (Figure S2.2.1, SI). We observed that with DMSO concentration increase (0, 1.0 and 2.5 μL), more compact structures were formed. Indeed, the samples prepared with 2.5 μL presented a collapsed porous structure closer to a film-like structure. Therefore, after these results our studies were focused with samples obtained without and with 1.0 μL of DMSO.

SEM micrographs of the BC/GO aerogels with 1.0 μL of DMSO showed that the final pore size and morphology of the later was significantly changed. In fact, in the absence of DMSO, the aerogel presents a more homogeneous porosity with round shaped pores (Figure 3.2.1). While, in the presence of DMSO, a preferential formation of small and elongated pores, with axial orientation was observed. Recently, the design of artificial interfaces has been reported by exploring the limits of GO gelation by microphase separation in water-miscible isopropanol. The low intercalation energy of water promotes the formation of an artificial liquid interface with high local concentration of GO, which after solvothermal treatment can be assembled into interconnected frameworks [42]. DMSO is a polar solvent with a freezing point of 18 $^{\circ}\text{C}$, [43,44] having capacity to accept hydrogen bonds. DMSO/water mixtures exhibit a marked freezing point depression due to the formation of stable DMSO/water complexes. For instance, it has been reported that by adding DMSO to water at a volume ratio of 1:1, the freezing point of the resulting mixture is lowered to - 52 $^{\circ}\text{C}$ [43,45].

To further investigate the different structural features of the BC/GO aerogels produced in the presence of DMSO, μCT measurements were conducted. The 3D reconstruction provides information related with the pore structure and interconnectivity as well as pore wall thickness. 3D reconstructions from μCT for BC/GO aerogels with DMSO are shown in

Figure 3.2.2. The images suggest interconnected porous structures composed mostly by open-cell pores (highly open porosity with values above 90 %). The μ CT reveals that the increase of the GO concentration in the aerogels promotes thicker pore walls formation, specially from 10 to 25 % of GO. Additionally, BC/GO50 showed lower pore size distribution. From Ctan software, the pore volume distribution was determined (Figure S2.2.2, SI). The μ CT results are in accordance with SEM analysis, showing that the BC/GO50 has a narrower pore size distribution, with 75 % of the pore size below 200 μ m, than BC/GO25 and BC/GO10, with around 60 %.

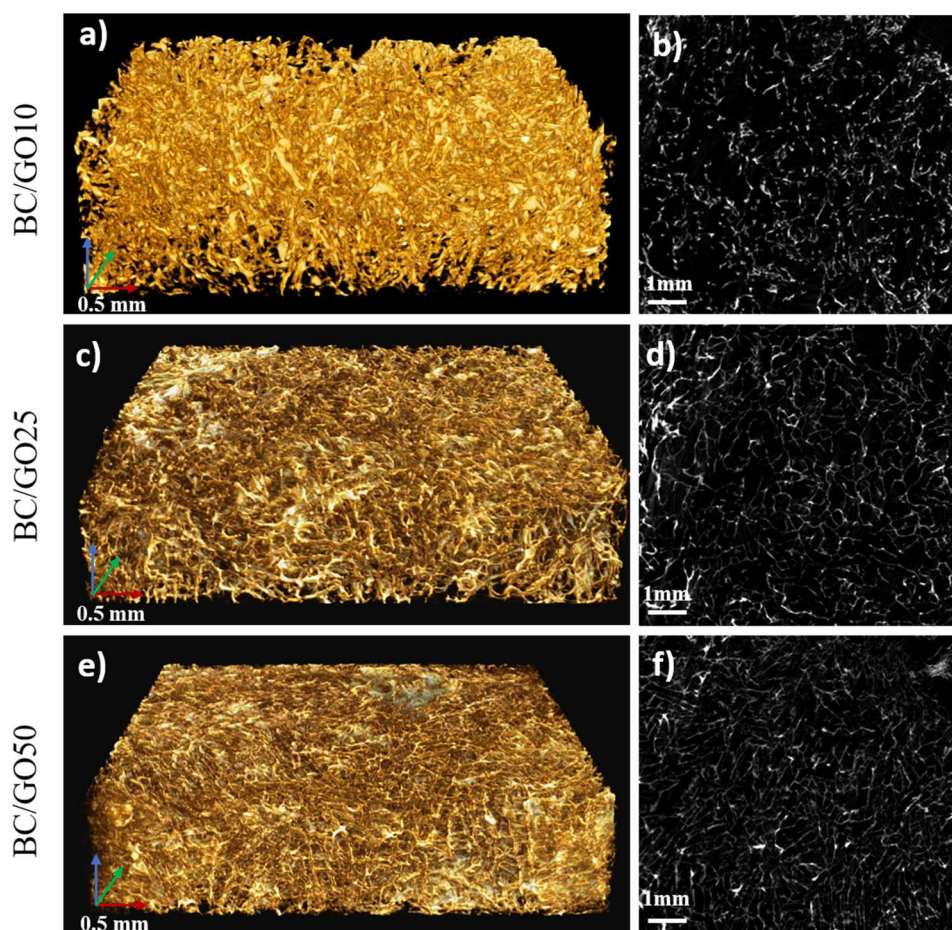


Figure 3.2.2 X-ray μ tomography images of the BC/GO aerogels: 3D renderings of μ CT images (BC/GO10 a), BC/GO25 c) and BC/GO50 e) and segmented 2D slices (BC/GO10 b), BC/GO25 d) and BC/GO50 f)).

When the suspension of BC/GO is frozen, the growth of ice crystals tends to accumulate the nanomaterials between their boundaries [19]. The increase of GO with respect to BC fibrils appears to allow its self-assembly on the ice crystal borders endorsing thicker pore

walls resulting in the establishment of stable aerogel structure. This justifies the fragile nature of the BC/GO aerogel, which has been abandoned for further studies.

3.2.4.2. Effect of reduction treatment on BC/GO aerogels

In the previous section, it was reported the structural anisotropy of the BC/GO foams induced by simple solvent mixing during the processing of the samples. The visual inspection of the BC/GO aerogels clearly evidenced the effectiveness of the GO reduction process in both cases by presenting its characteristic final black colour (Figure 3.2.1). It is important to notice that the reduction treatments applied to the aerogels do not appear to significantly affect the porous structure. Although the treatment with NH₃ gas seems to be more conservative than the solution treatment with N₂H₄, the collapse of the structure in the latter was not observed (Figure S2.2.3, SI).

XPS analysis was conducted in order to assess the surface composition of the different aerogels. Table 3.2.1 gathers the elemental composition of each aerogel as well as the O/C and N/C ratios.

Table 3.2.1 C, O and N content of BC and BC/GO aerogels determined by XPS.

Sample	C (at. %)	O (at. %)	N (at. %)	Ratio O/C	Ratio N/C
BC/GO25	70.5	29.5	-	0.42	-
BC/rGO25_{N₂H₄}	74.9	24.2	0.9	0.32	0.01
BC/rGO25_{NH₃}	77.8	13.9	8.3	0.18	0.11
BC/GO50	66.7	33.1	-	0.50	-
BC/rGO50_{N₂H₄}	74.8	23.9	1.3	0,32	0.02
BC/rGO50_{NH₃}	81.7	17.2	1.1	0.21	0.01

Analysis of the non-reduced specimens shows a high at. % for the carbon (C1s) and oxygen (O1s), which corresponds to the main elements on the starting nanomaterials. After reduction via N₂H₄ solution or thermal treatment with NH₃ gas, the at. % of the O1s was significantly reduced. The calculation of the O/C ratio provides an indirect estimation of the

extent of reduction. It was observed that the treatment with NH_3 ($\text{O/C} \sim 0.20$) is much more effective on the reduction process of GO than processing with N_2H_4 ($\text{O/C} \sim 0.32$), having into consideration the reference value of non-treated samples ($\text{O/C} \sim 0.42 - 0.50$). It is important to mention that the reduction efficiency of the aerogels is mainly governed by the effect of the treatment(s) on GO nanophase. XPS studies performed with reduced BC aerogels with NH_3 revealed a similar oxygen contents to that non-treated BC aerogels (37 at. %, Figure S2.2.4, SI).

A significant N-loading of the BC/rGO25 aerogels occurred when the reduction process via NH_3 treatment was employed, with ca. 8.3 at. % of N. However, it was observed that the at. % of N determined in the BC/GO50 aerogels was only of 1.1 at. % of N. The higher N content in the aerogels with less GO percentage suggests that the N-loading occurred preferably in the cellulose backbone by the formation of amine, amide, imide and lactam groups [46–48]. Yet, control experiment of reductive thermal treatment of pristine BC foams, under the same experimental conditions, revealed a total concentration of N lower than 1 at. %. Hence, N must be introduced in the BC/GO aerogel mainly cross-linked at the interface of GO and BC nanostructures (as verified by XPS and FTIR), instead of modifying the GO graphitic structure or BC backbone separately (Figure 3.2.3). Importantly, the results revealed that the crosslinking process is much more efficient for the sample $\text{BC/rGO25}_{\text{NH}_3}$ due to a high intensity of the signal N1s at 400 eV, which corresponds to binding energies of N moieties (Figure 3.2.3 (a)). These results can be attributed to the high miscibility of the nanophases at the ratio 75/25, which facilitates gelification under equilibrium. The saturation with the nanophases is observed at the ratio 50/50 with the appearance of small aggregates verified during gel formation.

The XPS spectrum of N1s with peak fitting for $\text{BC/rGO25}_{\text{NH}_3}$ sample is shown in Figure S2.2.5, SI. The N1s peak can be deconvoluted into three main components, which are usually assigned to graphitic N (quaternary species, N^+ 401.5 eV), pyrrolic N (400.03 eV) and pyridinic N (398.64 eV) groups [49]. However, both pyrrolic N and pyridinic N signals overlap with the binding energies corresponding to aliphatic moieties, namely amine and amide groups respectively [38]. The presence of amide groups clearly indicates the possible establishment of chemical crosslinking between the nanophases of the aerogel materials. However, the formation of structural moieties due to the substitution of C atoms from the skeleton of both BC and GO cannot be discarded. The mechanism for the establishment of

covalent bonds is not clear; however, it is anticipated here, that in case of amide groups, it can preferentially occur between the free carboxylic groups on GO, and free amine groups on BC generated during the thermal reduction (Figure S2.2.5, SI).

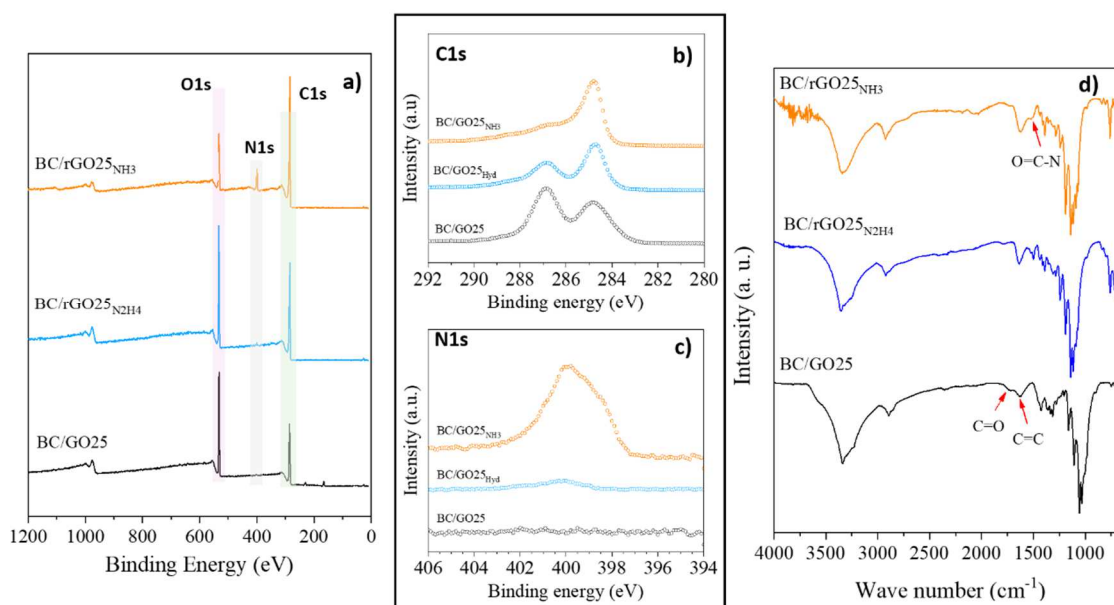


Figure 3.2.3 XPS spectra BC/GO25 and its reduced forms, XPS general survey scan (a) and high resolution C1s and N1s XPS spectra (b, c). FT-IR spectra (d).

FT-IR spectra analysis of BC/GO25 (Figure 3.2.3 (d)) reveal the presence of abundant hydrophilic oxygen containing groups, including C=O (1732 cm^{-1}), C–O (1160 cm^{-1} , 1110 cm^{-1} , and 1060 cm^{-1}), and O–H (1625 cm^{-1} bending and 3350 cm^{-1} stretching). The peaks around $2850\text{--}2950\text{ cm}^{-1}$ and $1310\text{--}1370\text{ cm}^{-1}$ are attributed to C–H vibrations [29,50]. After reduction with NH_3 or N_2H_4 , the peaks ascribed to the oxygen functionalities suffer a significant decrease of intensity [51,52]. Moreover, the reduction process also promotes the appearance of new bands originated by the incorporation of N-based functionalities into the aerogels. For instance, the peaks located at 1230 cm^{-1} , 1558 cm^{-1} and 1655 cm^{-1} can be ascribed to C–N and C=C and C=N, respectively. The band corresponding to N–H vibrations around 3200 cm^{-1} is probably overlapped with the O–H bond vibrations. Importantly, it was observed the appearance of the new band at 1430 cm^{-1} for the sample thermally treated with NH_3 [53], which can be assigned to the formation of amide groups resultant from the crosslinking between BC and GO which is in accordance with XPS analysis.

3.2.4.3. Dimensional stability of the BC/GO foams

Uniaxial compression tests were performed up to 80 % of deformation and stress–strain curves are shown in Figure 3.2.4 (a). For BC/GO25 and BC/rGO25_{NH3} a typical cellular behaviour under compression loading [54] were obtained (as represented in Figure S2.2.6, SI). First, an initial well-defined elastic stage was observed (up to 12 %), where stress changes linearly with strain, followed by plastic region in which, the materials undergo irreversible deformation (10-55 %). This region is designated by the Stress Plateau and is characterized by low stress variation with continuous deformation due to the skeleton structure collapse. Then, when the cell walls come in contact with each other, densification occurs (the stress increases abruptly). Through the compression, no cracks were observed, and the aerogels became dense and tough, with small or negligible lateral expansion. For BC/GO25 without DMSO specimen, the transition from linear to non-linear stress–strain behaviour is not clear, the initial region of linear elasticity merges itself with the long collapse zone described as the Plateau step, in which the variation of the stress is low. Some important parameters were determined from stress/strain curves, compressive strength (CS) at 40 % of deformation and Young's modulus (YM). The CS (at 40 % of strain) and YM (determined by the slope in the linear region) of BC/GO25 without DMSO, BC/GO25, BC/rGO25_{NH3} and BC/rGO25_{N2H4} are shown in Figure 3.2.4 (b).

With the addition of DMSO, there is alignment in the axial porosity and therefore high YM and CS at 40 % of deformation were observed. The CS and YM of the BC/GO25 aerogel at 40 % strain were 20 kPa and 80 kPa respectively, which were 120 and 200 % higher than that of the BC/GO25 aerogel without DMSO. The BC/rGO25_{NH3} specimen presents high stress values in the Plateau region (high load bearing capacity) and also high YM (300 % and 35 % higher than BC/GO25 without DMSO and BC/GO25, respectively). This improved performance is attributed to the crosslinking promoted by the reduction with NH₃ gas, thereby enhancing the skeleton structure of aerogel. These results are in agreement with those obtained for cyclic tests (Figure 3.2.4 (c), with the BC/rGO25_{NH3} having the best mechanical performance at low deformations. The YM values obtained are quite lower to those obtained by Ge *et al.* [33] for ultra-strong aerogel based on carboxymethyl cellulose and GO crosslinking mediated by boric acid (YM values ranging from 228 KPa to 1 MPa for aerogels with 25 kg/m³ of density), although higher to those obtained by Zhang *et al.*

[55] that prepared ultralight graphene/cellulose nanocrystal (CNC) hybrid aerogels and with values of YM (20-60 kPa).

The mechanical integrity of BC/GO foams under harsh conditions is a crucial factor to explore their potential applications. For this reason, the mechanical behaviour under dynamic cyclic compression was studied in different environments (dry and wet conditions). A strain amplitude of 5 % was selected, which was verified to be in the linear regime. After the dry dynamic cyclic compression tests, the specimens did not present significant structural changes as they recover its original shape with no mechanical failure. Besides, after a first period of accommodation, the materials present a quasi-constant value of stress amplitude. Figure 3.2.4 (c) illustrates the stress amplitude for 1,000 cycles. In a dry environment, the stress amplitude of the aerogels increases on the following order: starting with the lower value for the aerogel resultant from the simple mixture BC/GO (2.6 kPa) to the aerogel formed with addition of DMSO (3.8 kPa) and to the aerogel resultant from the thermal reduction with NH_3 (5.4 kPa). It is important to notice the impressive improvement of stress amplitude of 110 % for aerogel BC/rGO25 NH_3 . This value results from the structural synergistic effects from the synthetic process, in which the addition of DMSO to the gel mixture control the formation of axial porosity and extend crosslinking in the aerogel thermally treated with NH_3 . Besides, it is important to notice that for aerogels BC/rGO50 NH_3 a lower value of stress amplitude of 4.5 kPa was observed, which can be explained by the lower extent of crosslinking (XPS), the presence of structural defects through the formation of agglomerates of the individual components, and the non-homogeneous mixture of the nanophases of the aerogel. Contrarily, in a wet environment, the non-reduced foams easily lose their shape during the compression tests, while the reduced forms undergo the loading/unloading process without significant dimensional changes. Overall, the mechanical response in dry conditions is superior to wet conditions due to the phenomena of diffusion, and structure collapse promoted by water swelling. Despite the adverse conditions, the aerogels BC/rGO25 NH_3 reveal the highest resilience by presenting a stress amplitude of 3.5 kPa, that corresponds to an increase of 1300 % compared to the BC/GO25 aerogel (Figure 3.2.4 (c) and Figure 3.2.4 (d)).

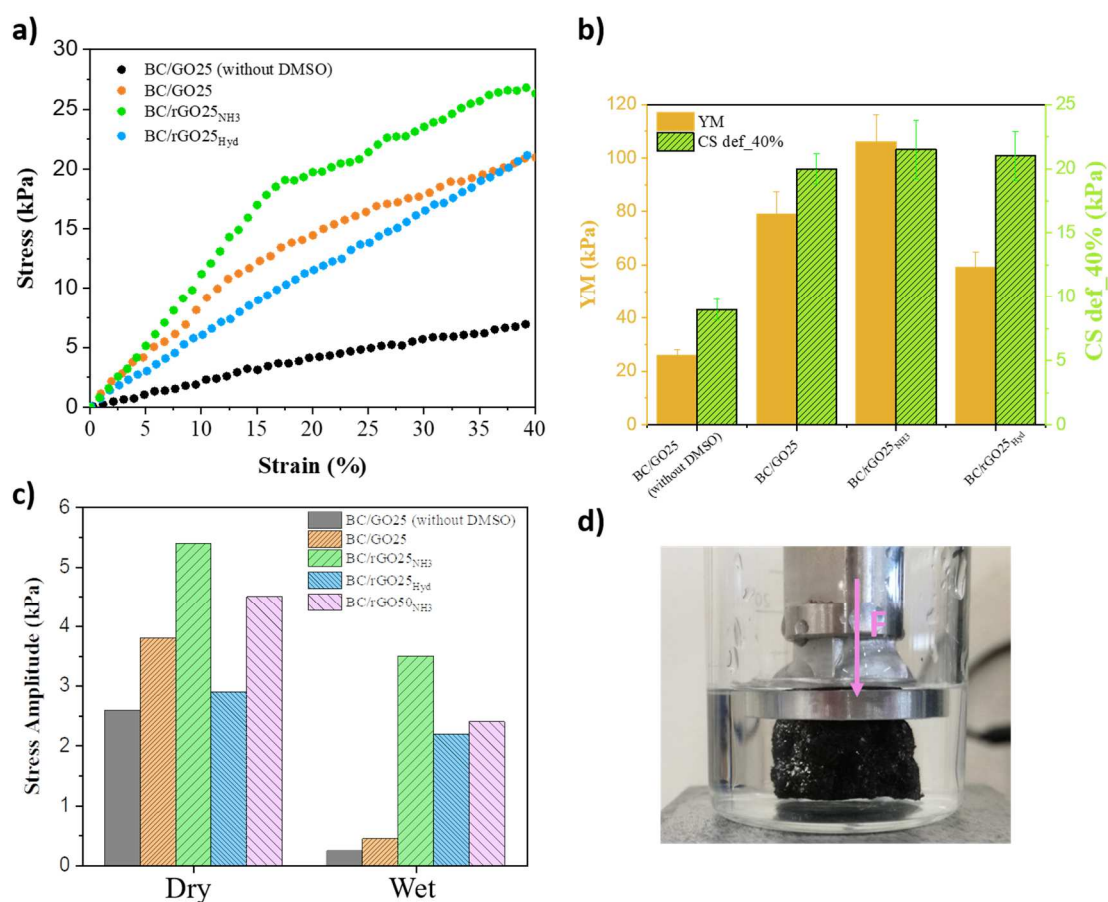


Figure 3.2.4 Stress-Strain curves for 40% of strain (a), Young Modulus and compressive strength (CS) at 40% of strain (b), Stress amplitude after 1,000 cycles of compression (c) and Real image of the scaffolds under dynamic compression test in wet environment (d).

The dimensional water stability of the produced aerogels was further studied by assessing the hydrophobic/hydrophilic nature of the aerogels, swelling (Figure 3.2.5 (a)) and water contact angle determination (Figure 3.2.5 (b) and Figure 3.2.5 (c)). Figure 3.2.5 (a) shows the swelling kinetics of the foams under study, which clearly indicates a distinct behaviour between the as-prepared foams and the foams subjected to a reduction process. The non-reduced composites present an initially high water absorption capacity (Q), followed by a gradual decrease in absorption with time indicating water loss, reaching the equilibrium stage after approximately 3 h. For the reduced composites, the opposite profile was observed, i.e., the swelling gradually increases until the equilibrium after 4 h, reaching lower Q values than the previous series. The same tendency was verified by Girão *et al.* [56] for collagen/graphene oxide scaffolds. For the non-reduced foams, the swelling behaviour is higher for the BC/GO50 than for the BC/GO25 series, most probably due to a structure collapse that closes the pores. After reduction, the dimensional stability of the aerogels

improves significantly. However, the reduction of the aerogels with NH_3 at 220 °C seems to be more effective comparatively to N_2H_4 reduction (as observed by XPS), due to the smaller swelling values. These results suggest that the thermal reduction with NH_3 increases the density of hydrophobic domains at the interface of the aerogel that limits the water flow into the pores.

The highly porous and hydrophilic surface of the BC/GO materials was revealed by water contact angle (WCA) measurements, where the water droplet was quickly absorbed on their surface, making not possible the measurement of associated WCA. This result is in agreement with the swelling tests where the BC/GO aerogels collapse fast when exposed to water solutions. Also, an immediate spread of the water droplet was observed after water drop contact with the sample reduced with N_2H_4 (Figure 3.2.5 (b)). These results can be understood by the contribution of two main factors: the oxygen-based functional groups still present at the surface of rGO, and the partial collapse of the interfacial porosity of the BC/GO aerogels during the N_2H_4 treatment in aqueous solution. The N_2H_4 reduction approach can be considered less effective to the aerogel, since the water flow partially degrades the structural porosity at the interface. Only the specimens reduced with NH_3 present high hydrophobic character with WCA values that reach ca. 120 degrees (Figure 3.2.5 (c)). These results indicate a higher effectiveness of the reduction treatment with NH_3 vs. N_2H_4 for the final dimensional water stability of the BC/GO aerogels, by promoting an extended reduction of GO on the aerogel and simultaneously preserving the structural porosity.

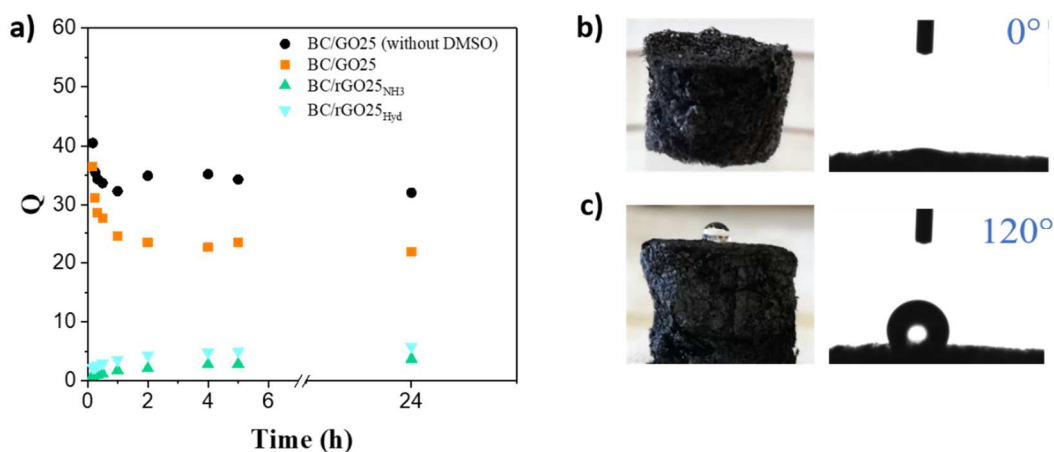


Figure 3.2.5 Swelling ratio of the aerogels immersed in water as a function of time (a) and water contact angles for aerogels reduced with N_2H_4 (b) and NH_3 (c)

3.2.4.4. Thermal stability

TGA measurements were carried out to investigate the thermal stability of the several BC/GO specimens prepared in this study. The TG curves in oxidative atmosphere of individual components (BC and GO) and BC/GO25 aerogel series are shown in Figure 3.2.6 (a). Thermogravimetric curves indicate that at ca. 400 °C, the BC/GO25 had a weight loss of 50 wt. % while BC lost up to 90 % of its initial weight. The enhanced thermal stability of the BC/GO25 aerogel comparatively to pure BC may be attributed to the interaction between BC and GO, forming an aerogel network cross-linked and restricting the movement of the polymer chains at the interface of the BC and GO, and also to the formation of a char layer that creates an indirect pathway for volatiles. The weight loss observed up to ca. 120 °C corresponds to the evaporation of absorbed water. BC, GO and BC/GO25 nanocomposites present two weight loss stages. GO has two severe weightlessness stages: the weight loss, between 150-200 °C, mainly assigned to the loss of oxygen functional groups of GO and between 450 °C and 520 °C attributed to the reaction of the more stable carbonaceous residue in presence of the oxidizing atmosphere (calcination of the conjugated carbon skeleton of GO). In the case of BC, the first stage located between 260 °C and 310 °C is assigned to the depolymerisation of BC, while the subsequent second stage situated between 310 °C and 435 °C for BC/GO25 corresponds to the generation of CO, CO₂ and H₂O [57–60]. The reduced forms of BC/GO aerogels present a later degradation. The main decomposition onset is slightly shifted to higher temperatures compared to the non-reduced forms, suggesting the positive effect of the reduction process on the thermal stability. It is believed that this improvement is due to the decrease in the amount of oxygenated functional groups, which improved the ability of aerogels to tolerate high temperatures in the oxidative atmosphere [59]. The temperature of combustion can be also correlated to the presence of N-containing fractions within the aerogel network that, as previously reported, confer enhanced thermal stability against oxidation when these species are introduced within a graphitic network [60]. The TGA results showed that the reduction of aerogels with N₂H₄ and NH₃ was not fully completed, because there is a slight weight loss that occurred over the temperature range of 160–260 °C. This thermal event can be ascribed, not only to the loss of the remaining oxygen functional groups, but also to the elimination of N-containing aliphatic moieties, which presence has been confirmed by XPS and that occurs simultaneously during the reduction step.

All the specimens were tested to evaluate the burning behaviour when a flame of an ethanol lamp is applied to the samples for three seconds. For BC/GO25 aerogels, as well as their reduced forms, the flame extinguished instantaneously, and the specimens maintained their shape during burning without dripping or smoke release (Figure 3.2.6 (b)). These results suggest that these porous materials have flame-retardant properties. A control test was performed to a BC aerogel and, in this case, the specimen burned completely (Figure 3.2.6 (c)). One possible reason for the enhanced thermal stability of BC could be the layered structure of the GO, which tends to form a char layer at the surface, which avoids or makes difficult the release of the volatile degradation products, delaying the degradation of the whole aerogel by offering indirect pathways for the volatiles release. Also, the flame temperature of an alcohol burner was lower than the combustion temperature of aerogels constituents [59].

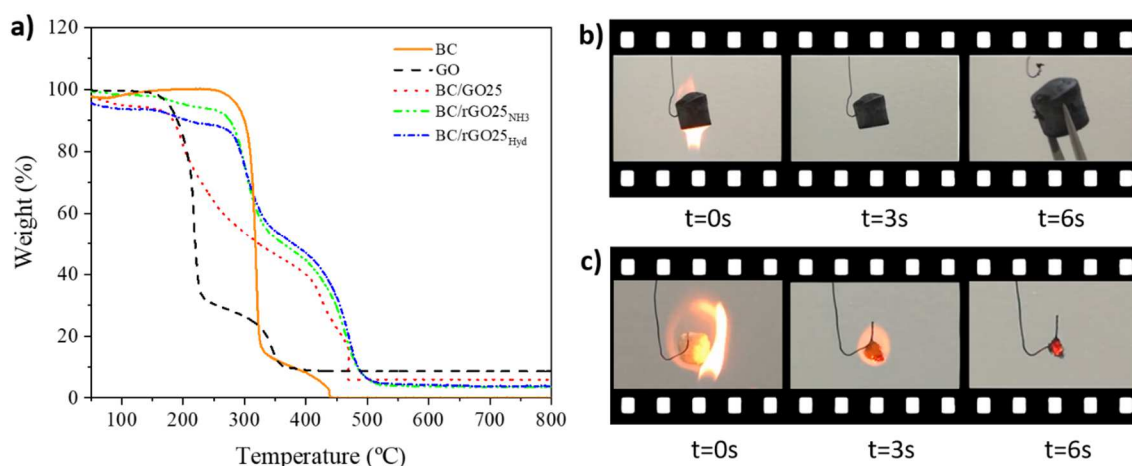


Figure 3.2.6 Thermogravimetric analysis of BC, GO and BC/GO25 aerogels(a). Flame behaviour of BC/rGO25_{NH3} (b) and BC (c) specimens. Figure (b) the frames captured at t0 and t3s show the dimensional stability of the aerogel after flame exposure and frame t6s exhibit the ability to be handled without suffer collapse. Figure (c) the frame sequence (t0s, t3s and t6s) showed the continuous annealing degradation of the sample.

3.2.4.5. Electrical properties

The electric conductivity was determined from measuring the resistance at different frequencies (Table 3.2.2). A little compression was made to ensure good contact between the rGO layers and thus a densely network with good electron transportation was obtained. The BC/GO composites have electrical insulation abilities, 5.9×10^{-07} and 1.8×10^{-06} S/m for BC/GO25 and BC/GO50, respectively, due to the presence of a large number of oxygen-containing functional groups on the surface of GO, and also in BC, which delays the

electrons transport. The reduction with NH₃ at 220 °C is more favourable to produce high BC/rGO conductors when compared to the ones reduced with N₂H₄ (Table 3.2.2). After the reduction treatments, a large fraction of the oxygen-containing groups were removed and π-π bonds were restored on the surface of rGO, which facilitates the electrons transportation [61–64]. As already mentioned, the increase of the electric conductivity for the specimens reduced with NH₃ is substantially higher, with increments of 12×10⁶ for BC/rGO25_{NH3} against materials undergoing reduction in presence of N₂H₄ (Table 3.2.2). Importantly, it was observed that the significant increase of GO concentration into the BC/GO aerogel composition from 25 % to 50 % does not correspond to a significant improvement of the values of conductivity, after the NH₃ treatment, being these of 7.2×10⁻¹ S m⁻¹ and 8.7×10⁻¹ S m⁻¹, respectively. We can thus infer that there must be a GO concentration threshold that limits the increase of the conductivity of BC/GO aerogels.

Table 3.2.2 Electric conductivities for the different BC/GO aerogels.

Sample	Electric Conductivity (S/m)
BC/GO25	5.9×10^{-7}
BC/rGO25_{Hyd}	1.7×10^{-3}
BC/rGO25_{NH3}	7.2×10^{-1}
BC/rGO50_{NH3}	8.7×10^{-1}

From the literature, this is one of the highest values of conductivity ever reported for aerogel architectures composed by a mixture of BC/GO. For example, cellulose nanofibrills films with 3 wt. % UV-reduced GO showed a substantially lower electric conductivity of 6.7×10^{-4} S m⁻¹ [62]. Higher values of electric conductivity for similar 3D materials were reported in the literature just in the cases that these were subjected to high temperature treatments (above 500 °C) and then compressed [65]. These severe treatment conditions promote the thermal decomposition of the nanocomponents promoting graphitization, thus compromising their mechanical integrity.

3.2.5. Conclusions

In summary, this work reports a new methodology for the development of multifunctional BC/GO aerogel materials with improved properties. The internal structural morphology of

BC/GO aerogels can be easily tuned by the addition of DMSO to aqueous suspensions during the gelification process. The addition of DMSO promotes the formation of small and elongated pores with axial arrangement. Thermal treatment of BC/GO samples with NH₃ revealed to be a less invasive and more efficient treatment for reduction than the use of conventional N₂H₄. Besides, NH₃ thermal treatment promoted the establishment of crosslinking between both nanophases, which enhanced the structural stability. The obtained aerogels showed improved dimensional stability under dry and wet environments, upgraded thermal resistance to oxidation and high electric conductivity (7.2×10^{-1} (S m⁻¹)).

3.2.6. References

- [1] X. Du, Z. Zhang, W. Liu, and Y. Deng, “Nanocellulose-based conductive materials and their emerging applications in energy devices - A review,” *Nano Energy*, vol. 35, pp. 299–320, 2017.
- [2] D. Klemm, B. Heublein, H.-P. Fink, and A. Bohn, “Cellulose: Fascinating Biopolymer and Sustainable Raw Material,” *Angew. Chemie Int. Ed.*, vol. 44, no. 22, pp. 3358–3393, 2005.
- [3] L. Wang, A. M. Urbas, and Q. Li, “Nature-Inspired Emerging Chiral Liquid Crystal Nanostructures: From Molecular Self-Assembly to DNA Mesophase and Nanocolloids,” *Adv. Mater.*, vol. 0, no. 0, p. 1801335, 2018.
- [4] A. Laromaine, T. Tronser, I. Pini, S. Parets, P. A. Levkin, and A. Roig, “Free-standing three-dimensional hollow bacterial cellulose structures with controlled geometry via patterned superhydrophobic–hydrophilic surfaces,” *Soft Matter*, vol. 14, no. 19, pp. 3955–3962, 2018.
- [5] N. Lavoine and L. Bergstrom, “Nanocellulose-based foams and aerogels: processing, properties, and applications,” *J. Mater. Chem. A*, vol. 5, no. 31, pp. 16105–16117, 2017.
- [6] C. Vilela, R. J. B. Pinto, S. Pinto, P. Marques, A. Silvestre, and C. S. da Rocha Freire Barros, *Polysaccharide Based Hybrid Materials*. Cham: Springer International Publishing, 2018.
- [7] A. Alonso-Díaz, J. Floriach-Clark, J. Fuentes, M. Capellades, N. S. Coll, and A. Laromaine, “Enhancing Localized Pesticide Action through Plant Foliage by Silver-Cellulose Hybrid Patches,” *ACS Biomater. Sci. Eng.*, vol. 5, no. 2, pp. 413–419, Feb. 2019.
- [8] H. Wei, K. Rodriguez, S. Rennekar, and P. J. Vikesland, “Environmental science and engineering applications of nanocellulose-based nanocomposites,” *Environ. Sci. Nano*, vol. 1, no. 4, pp. 302–316, 2014.
- [9] Z. Li, L. Wang, Y. Li, Y. Feng, and W. Feng, “Carbon-based functional nanomaterials: Preparation, properties and applications,” *Compos. Sci. Technol.*, vol. 179, pp. 10–40, 2019.
- [10] S. Zhou, L. Zhou, Y. Zhang, J. Sun, J. Wen, and Y. Yuan, “Upgrading earth-abundant biomass into three-dimensional carbon materials for energy and environmental applications,” *J. Mater. Chem. A*, vol. 7, no. 9, pp. 4217–4229, 2019.
- [11] A. Bianco et al., “All in the graphene family - A recommended nomenclature for two-dimensional carbon materials,” *Carbon N. Y.*, vol. 65, pp. 1–6, 2013.
- [12] D. R. Dreyer, S. Park, C. W. Bielawski, and R. S. Ruoff, “The chemistry of graphene oxide.”

- Chem. Soc. Rev., vol. 39, no. 1, pp. 228–40, Jan. 2010.
- [13] N. Song, D. Jiao, P. Ding, S. Cui, S. Tang, and L. Shi, “Anisotropic thermally conductive flexible films based on nanofibrillated cellulose and aligned graphene nanosheets,” *J. Mater. Chem. C*, vol. 4, no. 2, pp. 305–314, 2016.
- [14] N. Song, X. Hou, L. Chen, S. Cui, L. Shi, and P. Ding, “A Green Plastic Constructed from Cellulose and Functionalized Graphene with High Thermal Conductivity,” *ACS Appl. Mater. Interfaces*, vol. 9, no. 21, pp. 17914–17922, May 2017.
- [15] X. Wei et al., “Photo- and electro-responsive phase change materials based on highly anisotropic microcrystalline cellulose/graphene nanoplatelet structure,” *Appl. Energy*, vol. 236, pp. 70–80, 2019.
- [16] F. Jiang, S. Cui, N. Song, L. Shi, and P. Ding, “Hydrogen Bond-Regulated Boron Nitride Network Structures for Improved Thermal Conductive Property of Polyamide-imide Composites,” *ACS Appl. Mater. Interfaces*, vol. 10, no. 19, pp. 16812–16821, May 2018.
- [17] X. Wei, T. Huang, J. hui Yang, N. Zhang, Y. Wang, and Z. wan Zhou, “Green synthesis of hybrid graphene oxide/microcrystalline cellulose aerogels and their use as superabsorbents,” *J. Hazard. Mater.*, vol. 335, pp. 28–38, 2017.
- [18] H. Y. Mi, X. Jing, A. L. Politowicz, E. Chen, H. X. Huang, and L. S. Turng, “Highly compressible ultra-light anisotropic cellulose/graphene aerogel fabricated by bidirectional freeze drying for selective oil absorption,” *Carbon N. Y.*, vol. 132, pp. 199–209, 2018.
- [19] Q. Yao, B. Fan, Y. Xiong, C. Jin, Q. Sun, and C. Sheng, “3D assembly based on 2D structure of Cellulose Nanofibril/Graphene Oxide Hybrid Aerogel for Adsorptive Removal of Antibiotics in Water,” *Sci. Rep.*, vol. 7, pp. 1–13, 2017.
- [20] X. Chen, S. Zhou, L. Zhang, T. You, and F. Xu, “Adsorption of Heavy Metals by Graphene Oxide/Cellulose Hydrogel Prepared from NaOH/Urea Aqueous Solution,” *Materials (Basel)*, vol. 9, no. 7, 2016.
- [21] A. A. Yakout, R. H. El-Sokkary, M. A. Shreadah, and O. G. Abdel Hamid, “Cross-linked graphene oxide sheets via modified extracted cellulose with high metal adsorption,” *Carbohydr. Polym.*, vol. 172, pp. 20–27, 2017.
- [22] H. Luo, J. Xie, J. Wang, F. Yao, Z. Yang, and Y. Wan, “Step-by-step self-assembly of 2D few-layer reduced graphene oxide into 3D architecture of bacterial cellulose for a robust, ultralight, and recyclable all-carbon absorbent,” *Carbon N. Y.*, vol. 139, pp. 824–832, 2018.
- [23] C. Wan, Y. Jiao, and J. Li, “Flexible, highly conductive, and free-standing reduced graphene oxide/polypyrrole/cellulose hybrid papers for supercapacitor electrodes,” *J. Mater. Chem. A*, vol. 5, no. 8, pp. 3819–3831, 2017.
- [24] Q. Zheng, Z. Cai, Z. Ma, and S. Gong, “Cellulose Nanofibril/Reduced Graphene Oxide/Carbon Nanotube Hybrid Aerogels for Highly Flexible and All-Solid-State Supercapacitors,” *ACS Appl. Mater. Interfaces*, vol. 7, no. 5, pp. 3263–3271, Feb. 2015.
- [25] Y. Zhang et al., “New type multifunction porous aerogels for supercapacitors and absorbents based on cellulose nanofibers and graphene,” *Mater. Lett.*, vol. 208, pp. 73–76, 2017.
- [26] C. Wan and J. Li, “Graphene oxide/cellulose aerogels nanocomposite: Preparation, pyrolysis, and application for electromagnetic interference shielding,” *Carbohydr. Polym.*, vol. 150, pp. 172–179, 2016.
- [27] D. Ramani and T. P. Sastry, “Bacterial cellulose-reinforced hydroxyapatite functionalized

- graphene oxide: A potential osteoinductive composite,” *Cellulose*, vol. 21, no. 5, pp. 3585–3595, 2014.
- [28] D. Ege, A. R. Kamali, and A. R. Boccaccini, “Graphene Oxide/Polymer-Based Biomaterials,” *Adv. Eng. Mater.*, vol. 19, no. 12, pp. 16–34, 2017.
- [29] W. Shao, H. Liu, X. Liu, S. Wang, and R. Zhang, “Anti-bacterial performances and biocompatibility of bacterial cellulose/graphene oxide composites,” *RSC Adv.*, vol. 5, no. 7, pp. 4795–4803, 2015.
- [30] F. Martoia, T. Cochereau, P. J. J. Dumont, L. Orgéas, M. Terrien, and M. N. Belgacem, “Cellulose nanofibril foams: Links between ice-templating conditions, microstructures and mechanical properties,” *Mater. Des.*, vol. 104, pp. 376–391, Aug. 2016.
- [31] A. Borrás et al., “Preparation and Characterization of Graphene Oxide Aerogels: Exploring the Limits of Supercritical CO₂ Fabrication Methods,” *Chem. - A Eur. J.*, vol. 24, no. 59, pp. 15903–15911, Oct. 2018.
- [32] B. Wicklein et al., “Thermally insulating and fire-retardant lightweight anisotropic foams based on nanocellulose and graphene oxide,” *Nat. Nanotechnol.*, vol. 10, no. 3, pp. 1–7, Nov. 2014.
- [33] X. Ge, Y. Shan, L. Wu, X. Mu, H. Peng, and Y. Jiang, “High-strength and morphology-controlled aerogel based on carboxymethyl cellulose and graphene oxide,” *Carbohydr. Polym.*, vol. 197, pp. 277–283, 2018.
- [34] Y. Liu, J. Zhou, E. Zhu, J. Tang, X. Liu, and W. Tang, “Facile synthesis of bacterial cellulose fibres covalently intercalated with graphene oxide by one-step cross-linking for robust supercapacitors,” *J. Mater. Chem. C*, vol. 3, no. 5, pp. 1011–1017, 2015.
- [35] Y. Wen, M. Wu, M. Zhang, C. Li, and G. Shi, “Topological Design of Ultrastrong and Highly Conductive Graphene Films,” *Adv. Mater.*, vol. 29, no. 41, p. 1702831, Nov. 2017.
- [36] R. Xiong et al., “Wrapping Nanocellulose Nets around Graphene Oxide Sheets,” *Angew. Chemie Int. Ed.*, vol. 57, no. 28, pp. 8508–8513, Jul. 2018.
- [37] A. F. Girão et al., “Electrostatic self-assembled graphene oxide-collagen scaffolds towards a three-dimensional microenvironment for biomimetic applications,” *RSC Adv*, vol. 6, no. 54, pp. 49039–49051, 2016.
- [38] S. Sandoval et al., “Tuning the nature of nitrogen atoms in N-containing reduced graphene oxide,” *Carbon N. Y.*, vol. 96, pp. 594–602, 2016.
- [39] Y. Liu, J. Zhou, J. Tang, and W. Tang, “Three-Dimensional, Chemically Bonded Polypyrrole/Bacterial Cellulose/Graphene Composites for High-Performance Supercapacitors,” *Chem. Mater.*, vol. 27, pp. 7034–7041, 2015.
- [40] W. Yang et al., “Completely Green Approach for the Preparation of Strong and Highly Conductive Graphene Composite Film by Using Nanocellulose as Dispersing Agent and Mechanical Compression,” *ACS Sustain. Chem. Eng.*, vol. 5, no. 10, pp. 9102–9113, Oct. 2017.
- [41] Q. Fang, X. Zhou, W. Deng, Z. Zheng, and Z. Liu, “Freestanding bacterial cellulose-graphene oxide composite membranes with high mechanical strength for selective ion permeation,” *Sci. Rep.*, vol. 6, p. 33185, Sep. 2016.
- [42] C. Luo et al., “Realizing Ultralow Concentration Gelation of Graphene Oxide with Artificial Interfaces,” *Adv. Mater.*, vol. 31, no. 8, p. 1805075, Feb. 2019.
- [43] M. M. Ozmen, M. V. Dinu, and O. Okay, “Preparation of macroporous poly(acrylamide)

- hydrogels in DMSO/water mixture at subzero temperatures,” *Polym. Bull.*, vol. 60, no. 2, pp. 169–180, Mar. 2008.
- [44] D. B. Wong et al., “Water Dynamics in Water/DMSO Binary Mixtures,” *J. Phys. Chem. B*, vol. 116, no. 18, pp. 5479–5490, May 2012.
- [45] B. Mattiasson, A. Kumar, and I. Y. Galeaev, *Macroporous Polymers: Production Properties and Biotechnological/Biomedical Applications*. CRC Press, 2009.
- [46] W. Luo et al., “Pyrolysis of Cellulose under Ammonia Leads to Nitrogen-Doped Nanoporous Carbon Generated through Methane Formation,” *Nano Lett.*, vol. 14, no. 4, pp. 2225–2229, 2014.
- [47] R. A. N. Pertile, F. K. Andrade, C. Alves, and M. Gama, “Surface modification of bacterial cellulose by nitrogen-containing plasma for improved interaction with cells,” *Carbohydr. Polym.*, vol. 82, no. 3, pp. 692–698, 2010.
- [48] D. Cagniant et al., “Ammoxidation of cellulose—a structural study,” *J. Anal. Appl. Pyrolysis*, vol. 65, no. 1, pp. 1–23, 2002.
- [49] L. Ma et al., “Enhanced Li-S Batteries Using Amine-Functionalized Carbon Nanotubes in the Cathode,” *ACS Nano*, vol. 10, no. 1, pp. 1050–1059, Jan. 2016.
- [50] C. Li, Z.-Y. Wu, H.-W. Liang, J.-F. Chen, and S.-H. Yu, “Ultralight Multifunctional Carbon-Based Aerogels by Combining Graphene Oxide and Bacterial Cellulose,” *Small*, vol. 13, no. 25, pp. 1700453--n/a, 2017.
- [51] H. Tao et al., “N-Doping of graphene oxide at low temperature for the oxygen reduction reaction,” *Chem. Commun.*, vol. 53, no. 5, pp. 873–876, 2017.
- [52] G. S. Bang et al., “Pyridinic-N-Doped Graphene Paper from Perforated Graphene Oxide for Efficient Oxygen Reduction,” *ACS Omega*, vol. 3, no. 5, pp. 5522–5530, 2018.
- [53] S. Saska et al., “Bacterial cellulose-collagen nanocomposite for bone tissue engineering,” *J. Mater. Chem.*, vol. 22, no. 41, p. 22102, 2012.
- [54] I. Duarte, M. Vesenjajk, L. Krstulović-Opara, and Z. Ren, “Crush performance of multifunctional hybrid foams based on an aluminium alloy open-cell foam skeleton,” *Polym. Test.*, vol. 67, pp. 246–256, 2018.
- [55] X. Zhang, P. Liu, Y. Duan, M. Jiang, and J. Zhang, “Graphene/cellulose nanocrystals hybrid aerogel with tunable mechanical strength and hydrophilicity fabricated by ambient pressure drying technique,” *RSC Adv.*, vol. 7, no. 27, pp. 16467–16473, 2017.
- [56] F. Ren et al., “Facile preparation of 3D regenerated cellulose/graphene oxide composite aerogel with high-efficiency adsorption towards methylene blue,” *J. Colloid Interface Sci.*, vol. 532, pp. 58–67, 2018.
- [57] S. Gan, S. Zakaria, C. H. Chia, and H. Kaco, “Effect of graphene oxide on thermal stability of aerogel bio-nanocomposite from cellulose-based waste biomass,” *Cellulose*, vol. 25, no. 9, pp. 5099–5112, 2018.
- [58] X. Chen et al., “Construction of porous N-doped graphene layer for efficient oxygen reduction reaction,” *Chem. Eng. Sci.*, vol. 194, pp. 36–44, 2019.
- [59] Y. Cheng et al., “Enhanced mechanical, thermal, and electric properties of graphene aerogels via supercritical ethanol drying and high-temperature thermal reduction,” *Sci. Rep.*, vol. 7, no. 1, p. 1439, 2017.

- [60] S. Sandoval, N. Kumar, A. Sundaresan, C. N. R. Rao, A. Fuertes, and G. Tobias, "Enhanced Thermal Oxidation Stability of Reduced Graphene Oxide by Nitrogen Doping," *Chem. – A Eur. J.*, vol. 20, no. 38, pp. 11999–12003, 2014.
- [61] F. Liu, C. Wang, and Q. Tang, "Conductivity Maximum in 3D Graphene Foams," *Small*, vol. 14, no. 32, p. 1801458, Aug. 2018.
- [62] Y. B. Pottathara et al., "UV-Induced reduction of graphene oxide in cellulose nanofibril composites," *New J. Chem.*, vol. 43, no. 2, pp. 681–688, 2019.
- [63] Y. Beeran P. T. et al., "Mechanically strong, flexible and thermally stable graphene oxide/nanocellulosic films with enhanced dielectric properties," *RSC Adv.*, vol. 6, no. 54, pp. 49138–49149, 2016.
- [64] Y. Zhan, C. Xiong, J. Yang, Z. Shi, and Q. Yang, "Flexible cellulose nanofibril/pristine graphene nanocomposite films with high electrical conductivity," *Compos. Part A Appl. Sci. Manuf.*, vol. 119, pp. 119–126, Apr. 2019.
- [65] M. M. Perez-Madrigo, M. G. Edo, and C. Aleman, "Powering the future: application of cellulose-based materials for supercapacitors," *Green Chem.*, vol. 18, no. 22, pp. 5930–5956, 2016.

Chapter 4. Hybrid structures made of polyurethane/graphene nanocomposite foams embedded within aluminium open-cell foam

This chapter was based in following published paper:



Article

Hybrid Structures Made of Polyurethane/Graphene Nanocomposite Foams Embedded within Aluminum Open-Cell Foam

Susana C. Pinto ¹, Paula A. A. P. Marques ¹ , Romeu Vicente ², Luís Godinho ³ and Isabel Duarte ^{1,*} 

¹ Department of Mechanical Engineering, TEMA, University of Aveiro, 3810-193 Aveiro, Portugal; scpinto@ua.pt (S.C.P.); paulam@ua.pt (P.A.A.P.M.)

² Department of Civil Engineering, RISCO, University of Aveiro, 3810-193 Aveiro, Portugal; romvic@ua.pt

³ Department of Civil Engineering, ISISE, University of Coimbra, 3030-788 Coimbra, Portugal; lgodinho@dec.uc.pt

* Correspondence: isabel.duarte@ua.pt; Tel.: +350-234-370-830

4.1. Abstract

The focus of this chapter is the development of hybrid structures containing two different classes of porous materials. These are nanocomposite foams made of polyurethane combined with graphene-based materials and aluminium open-cell foams (OCF). For that, and prior to the hybrid structures preparation, the nanocomposite foams formulation was optimized. The optimization consisted of studying the effect of the addition of graphene oxide (GO) and graphene nanoplatelets (GNPs) at different loadings (1.0, 2.5 and 5.0 wt.%) during the polyurethane foam (PUF) formation and their effect on the final nanocomposite properties. Globally, the results showed enhanced mechanical, acoustic and fire-retardant properties of the PUF nanocomposites when compared with pristine PUF. The PUF nanocomposite prepared with 2.5 wt.% of GNPs (PUF/GNPs2.5) showed the better combination of properties. In a latter step, the hybrid structure was prepared by embedding the OCF with this optimized nanocomposite formulation. The process of filling the pores of the OCF was successfully achieved, with the resulting hybrid structure retaining low thermal conductivity values, around $0.038 \text{ W}\cdot\text{m}^{-1}\cdot\text{K}^{-1}$ and presenting improved sound absorption coefficient, especially for mid to high frequencies, with respect to the individual foams. Furthermore, the new hybrid structure also displayed better mechanical properties (the stress corresponding to 10% of deformation was improved in more than 10 and 1.3 times comparatively to PUF/GNPs2.5 and OCF, respectively). This study highlights the potential of these novel hybrid structures that could be adapted for applications in housing structure, aeronautics and automobile industry.

4.2. Introduction

In recent years, porous materials have attracted a huge interest from both academia and industry because they may find applications in a variety of fields such as energy storage [1], catalysis [2], drug release [3], sound and thermal insulation [4], environmental remediation [5] between others. Giving the International Union of Pure and Applied Chemistry (IUPAC) definition, porous materials can be categorized based on their pore sizes: microporous (pore size $<2 \text{ nm}$), mesoporous (2-50 nm), and macroporous ($>50 \text{ nm}$) [6] According to these categories, the properties of the porous materials and their subsequent applications will differ. Moreover, they can be found in three-dimensional (3D) and two-dimensional (2D)

structures. Common 3D porous materials are sponges, foams, wood, and bone. 2D porous materials include separation membranes, filter paper, textiles, and so on.

Depending on all the previous referred characteristics and additionally based on their chemical composition, the porous materials can present multifunctionality. Multifunctional materials present multiple characteristics that can be translated into excellent performance in existing applications and also open up avenues for untouched application fields [7]. These can exist naturally or can be engineered, with the latter being usually obtained by combining two or more materials. New functionalities arise from the synergistic combination of the individual materials properties [8].

One interesting example of porous materials are aluminium open-cell foams (OCF). This type of foams is characterized by low weight, high thermal and electrical conductivities and high internal surface area. Furthermore, they are recyclable and non-flammable [9]. However, they present a low compressive strength, when compared for example with closed pore cell foams. To overcome this drawback, OCF foams can be combined with other materials, such as silicone [10,11], epoxy [10,12] or polyurethane [13]. Even though the mechanical performance of the composite foams is compensated, their final weight is increased, which for certain applications requiring lightweight structures, is not desirable. In this context, filling these metallic skeletons with lightweight porous materials can be an interesting alternative to bulk polymers. Reinfried M. *et al.* [14] explored the concept of hybrid foams which consist of two different interpenetrating embedded foam-material classes. The idea behind the hybrid foams is to overcome the individual shortcoming of single-material foams by combining foams of two different material classes and therefore achieve synergistic property combinations that are relevant and beneficial for future applications.

Recently, our group explored the concept of lightweight multifunctional hybrid structures, by combining OCF foams with cellulose/graphene foams [15]. We reported, the impregnation of a cellulose/graphene foam into an OCF foam creating a hybrid structure with higher mechanical properties (increase in stress of 100 times) with respect to the cellulose foam. This multifunctional hybrid foam presented also high sound absorption coefficient (near 1 between 1000-4000 Hz) and low thermal conductivity.

To further explore these types of structures, in the present work we considered the incorporation of polyurethane foams (PUF) into OCF ones. PUF are known for their excellent thermal and acoustic insulation properties, low thermal conductivity, good mechanical and chemical stability and low manufacturing cost [16]. The PUF represents three quarters of the production of PU materials and the major market sectors include insulation materials in buildings, shock absorbers for vehicles, packaging, footwear and furniture [17,18]. However, due to their high flammability, the improvement of their fire retardancy properties became crucial [19]. Taking this into account, PUF precursors like polyols have been synthesized with specific chemical functional groups to confer fire-retardancy [16,20]. In addition, nanoclays (montmorillonite) [21], titanium dioxide [22], iron oxide magnetic nanoparticles [23], expandable graphite [19,24] and carbon nanostructures [25–29] have also been employed to confer flame retardancy. Often, the combinations of different fillers are used to access improved fire-retardancy behaviour due to a synergetic effect [30,31]. Interestingly, the graphene-based materials addition to polymeric matrices has been reported to provide, besides fire-retardancy, the ability to improve the mechanical properties [32,33] and sound absorption features [34,35].

Pursuing the goal to contribute to the development of lightweight multifunctional materials, this work presents, in a first step, the effect of the addition of two graphene-based materials, graphene oxide (GO) and graphene nanoplatelets (GNPs) on the PUF properties. The focus was on the fire-retardancy, mechanical, acoustic and thermal properties. After the characterization of the different PUF nanocomposites, a selected composition was incorporated in an OCF creating a lightweight multifunctional hybrid structure that was further characterized.

4.3. Materials and Methods

4.3.1. Materials

The raw materials employed in PUF synthesis were 1) methylene diphenyl diisocyanate (MDI) (VORANATE M229 from Dow Chemicals, Portugal) with average functionality of 2.7 and NCO content of 31.1% and 2) polyol with hydroxyl value of 239 mg KOH/g (VORACOR CR1112 from Dow Chemicals, Portugal).

Graphene oxide (GO) (4 mg/mL aqueous dispersion) was purchased from Graphenea (Spain) and graphene nanoplatelets (GNPs) in powder were acquired to Cheaptubes (USA). Silicone oil was acquired from Sigma-Aldrich (Germany). The open-cell AlSi7Mg0.3 foams with pore sizes of 10 ppi (pores per inch) were supplied by Mayser GmbH & Co. KG (Germany).

4.3.2. Experimental methodology

Pristine PUF and PUF nanocomposites were prepared by a two-step procedure, as schematized in Figure 4.1, route A. First, the pre-polymer (polyol), silicone oil (5 wt.%), water as blowing agent (5 wt.%) and GO or GNPs (1.0, 2.5 and 5.0 wt.%) were placed in glass beaker and homogenised for 30 seconds using a mechanical stirrer at high speed. Next, the proper amount of MDI to obtain a $R_{NCO/OH}=0.80$ (ratio between NCO groups of isocyanates and OH groups) was added and the mixture was homogenized again for 10 seconds. The PUF and PUF nanocomposites were obtained by free expansion in the cup mould at room temperature. The foams are hereafter referred as PUF, PUF/xGNPs and PUF/xGO, where x refers to the carbon nanostructure content.

For the preparation of OCF hybrids, the metal foam was placed into the cup containing the mixture right after the addition of MDI. The pores of the OCF were filled after the PUF expansion (Figure 4.1, route B). In this case only one type of specimen was prepared, OCF with the optimized PUF nanocomposite (PUF/GNPs2.5-OC). Before characterization, the samples were settled to rest for 24h at room temperature to ensure complete reaction.

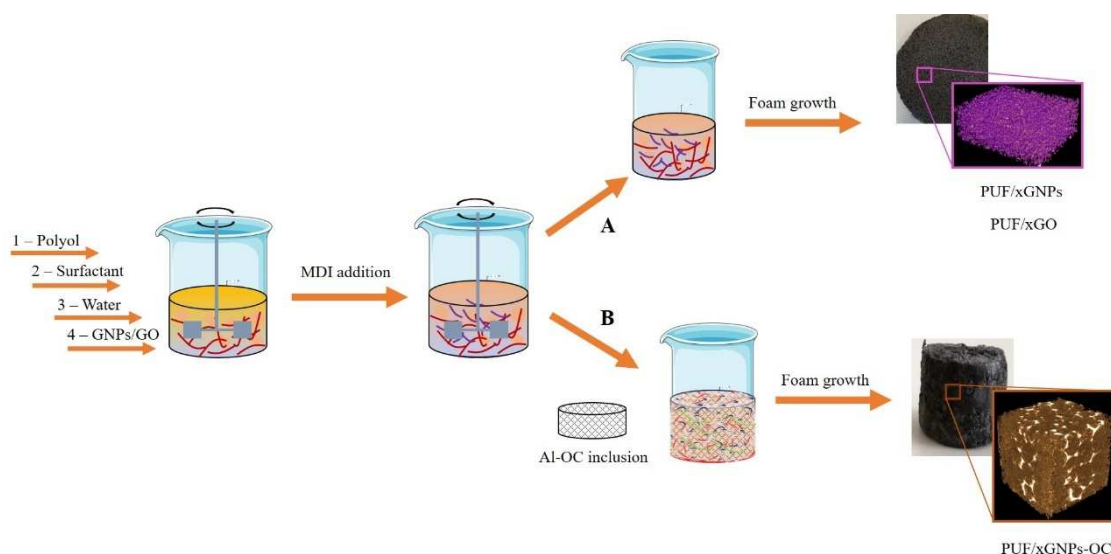


Figure 4.1 Scheme describing the preparation of PUF nanocomposites (A) and hybrid structures (B).

4.3.3. Characterization

Attenuated total reflection – Fourier Transformed Infrared spectroscopy (ATR-FTIR) spectra were collected using a Perkin Elmer FTIR System Spectrum BX Spectrometer equipped with a single horizontal Golden Gate ATR cell, in the range 4000 to 500 cm^{-1} and running 64 scans with a resolution of 4 cm^{-1} . Scanning electron microscopy (SEM) analysis was performed in a TM 4000 Plus (Hitachi, Japan) scanning electron microscope at accelerating voltage of 15.0 kV. Samples ($10 \times 10 \times 10 \text{ mm}^3$) were analysed in a μCT equipment from SkyScan 1275 (Bruker μCT , Belgium) with penetrative X-rays of 30 kV and 125 μA , in high resolution mode with a pixel size of 8 μm and 450 ms of exposure time. NRecon and CTVox software were used for 3D-reconstruction and CTan software was used in morphometric analysis (total porosity, pore size distribution and cell walls thickness). The apparent density and porosity were determined geometrically for 3 specimens of each PUF nanocomposites.

The thermal conductivity properties were evaluated with a Hot Disk TPS 2500 S instrument (Sweden), at 20 $^{\circ}\text{C}$, in accordance with the standard ISO 22007-2.2 and ASTM D7984, the specimens were cube shaped with ($25 \times 25 \times 25 \text{ mm}^3$). The value of sound absorption coefficient was estimated from measurements made with an impedance tube according standard ASTM E 1050 for cylindrical shaped specimens with 37 mm of diameter and 22 mm of thickness. The thermal stability of the nanocomposites foams was assessed by thermogravimetric analysis (TGA) using a thermogravimetric analyser (Netzsch Jupiter, Germany) at a scanning rate of 10 $^{\circ}\text{C}/\text{min}$, in the temperature range of 30–800 $^{\circ}\text{C}$, under a synthetic air atmosphere (80% N_2 and 20% O_2). The fire retardancy test was based in the direct observation of the response of the specimens when submitted to a flame. The test consisted in applying an ethanol flame, at the specimen's bottom using the set-up in vertical sample position, for 3 s, plus a subsequent application (3 s) if the specimen self-extinguishes. The tests were conducted in half of cylindrical shaped specimens, with 30 mm of diameter and 10 mm of thickness.

The mechanical testing machine (Shimadzu MMT, Japan – maximum load 101 N) was used to study the quasi-static compressive response of PUF nanocomposites under a strain rate of 1 mm/min up. The uniaxial compression test of OCF and hybrid PUF structures were performed in a Shimadzu - AGS-X-10kN (Japan) testing machine at a speed of 6 mm/min.

4.4. Results and discussion

4.4.1. PUFs nanocomposites

The success of PUF and PUF nanocomposite preparation relies on the appropriate reaction between the precursors, namely the extinction of isocyanate groups through the reaction with hydroxyl groups of the polyol and urethane formation, this was confirmed by FTIR analysis (Figure S3.1). The addition of GO or GNP, at the used concentrations, did not prevent the progression of foam formation. However, the GO and GNPs did not disperse in the same way in the polymer matrix, as can be easily observed in the left column of Figure 4.2. The photographs show a homogeneous black colour when GNPs were added suggesting a good interaction between the nanofillers and the polymer matrix. On the contrary, black spots are observed in the PUF when GO was used. GO nanosheets are directly obtained from the chemical exfoliation of graphite and contains several oxygen chemical functionalities, what makes the GO highly hydrophilic. GNPs are also obtained from graphite exfoliation, but without the use of chemical oxidants, thus resulting in a non-oxidized surface, GNPs being hydrophobic. This difference in the chemical surface structure of the carbon nanostructures determines their dispersion in the polymeric matrix.

Although the dispersion was not the same with both nanofillers, its flame retardant action was remarkable. A control test with pristine PUF showed flame propagation at some extension with smoke release, even if no dripping was observed (Figure 4.2a).

PUFs nanocomposites prepared with 2.5 wt.%, showed fire retardant properties, with the flame extinguished after 1 s. Importantly, the specimens maintained their shape during burning without dripping or smoke release (Figure 4.2b and c). Similar behaviour was observed for the compositions with 5.0 wt. % of GO or GNPs. For the lower nanofillers amount tested (1 wt.%), the results were not as good, since at 3s there was still flame propagation, mainly for PUF/GNPs1.0, with smoke release in both cases (Figure S3.2). It is worth mentioning that the pristine PUF and PUF nanocomposites with 1 wt.% of nanofillers kept their shape. Thus, the PUF with 1.0 wt.% of nanofillers were excluded in the further characterization results.

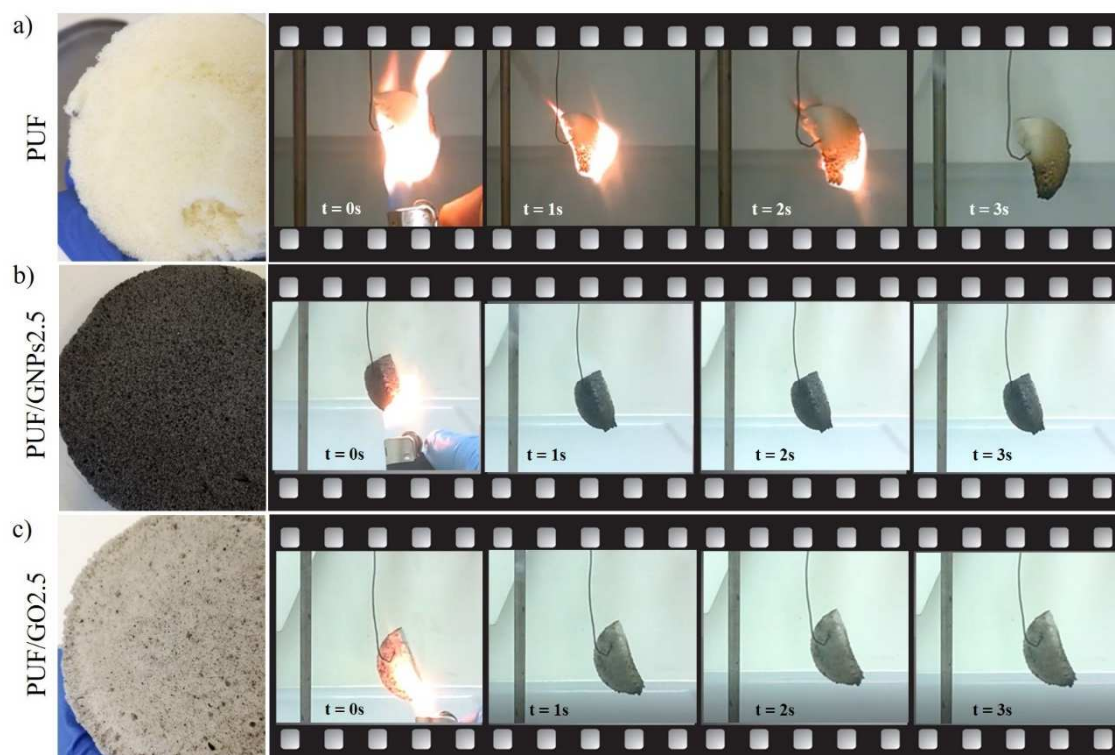


Figure 4.2 Flame behaviour of PUF (a), PUF/GNPs2.5 (b) and PUF/GO2.5 (c).

Carbon nanostructures are known to play a key role either in slowing down the flame propagation or even in providing self-extinction to thermoplastic or thermosetting polymeric matrices [36–38]. Their positive effect in the thermal stability of PUF nanocomposites may be attributed to the high specific area and layered structure of the nanofillers, which tends to form a dense and continuous char layer acting like a physical barrier at PUF surface. This barrier becomes an obstacle to the release of the volatile degradation products, preventing or causing the delay on the degradation of the whole composite [39]. It is remarkable that although GO nanosheets are not as good dispersed as GNPs, their effect on the flame retardancy was as efficient or even more than GNPs. GO benefits over graphene have been referred and are attributed to the GO oxygen functionalities that decompose and dehydrate at quite low temperatures. This causes a cool down of the polymer substrate during the combustion process and simultaneously release gaseous species that dilute the oxygen atmosphere near the ignition zone [39–41]. Graphene and GO are described mainly as co-flame-retardants, at loadings from 1.0 to 10 wt.% [41]. Also, functionalized graphene designed and prepared from expandable graphite and phosphorus-containing compounds have been described as flame retardants and smoke suppressor of PUF at 6.1 wt.% [42].

TG and DTG curves are shown in Figure S3.3a and Figure S3.3b, respectively. Pristine PUF and PUF nanocomposites showed similar TGA curves, suggesting that GNPs and GO do not significantly influence the decomposition of PUF. This finding is most likely related to the small amount of nanofillers used. The initial decomposition temperature corresponding to 5% ($T_{5\%}$), and 50% ($T_{50\%}$) of mass degradation, the maximum-rate degradation temperature (T_{max}) and mass residue at 750 °C are listed in Table 4.1.

Table 4.1 Experimental data of TGA analysis.

	$T_{5\%}$ (°C)	$T_{50\%}$ (°C)	T_{max} (°C)	Residue 750 °C (%)
PUF	173.6	349.8	312.3	5.68
PUF/GNPs2.5	197.7	404.6	314.7	5.18
PUF/GNPs5.0	188.5	392.9	316.5	5.12
PUF/GO2.5	165.4	360.7	311.4	2.42
PUF/GO5.0	149.2	355.6	312.9	1.88

Results show that GNPs had a positive effect on $T_{5\%}$ of PUF, while GO was detrimental to the early thermal stability. These results are caused by the earlier degradation of the GO oxygen functionalities at low temperature, thus accelerating the degradation of the PUF matrix. The oxygen functionalities of GO may interact with the PUF precursors during the foam formation thus interfering with crosslinking reaction, as reported by Gama *et al.* [19]. In fact, at high temperatures there is the complete burning of GO, proved by the lower percentage of residue at 750 °C [43]. The sample PUF/GNPs2.5 presents the higher thermal stability with $T_{50\%}$ of 404 °C. It was reported by Liu *et al.* [44] that graphene can act as a heat source and accelerate the decomposition of PUF. As so, the 2.5 wt.% seems to have a more positive effect on the thermal properties of PUF than 5.0 wt.%.

SEM images of pristine PUF and PUF nanocomposites (Figure 4.3a) show an inhomogeneous open-cell structure composed by quasi-spherical interconnected pores for all specimens. However, depending on the presence or absence of nanofillers, some small differences were noticed. As shown in Figure 4.3a insets, the GNPs and GO sheets are located, and sometimes wrapped, in the PUF cell walls. It is reported that carbon nanostructures have a nucleating effect during foam formation, thus altering the PUF

morphology [45]. Usually, the presence of such fillers decreases the average cell size and increase foam density improving damping properties, flame-retardancy and mechanical properties [46]. By comparing PUF/xGNPs with PUF/xGO SEM images, GO seems to promote thicker cell walls and joints which can be related with the agglomeration of GO or from the affinity of polyol and MDI with GO. GO sheets are located between adjacent cavities of the foam, and the cell wall sticks together around them, producing thicker cell walls. This effect is accentuated with the increase in the quantity of GO, PUF/GO5.0 presented bigger pore size and thicker cell walls than PUF/GO2.5. On the contrary, the increase of GNPs content in the PUF promote a pore size decrease.

The 3D reconstruction performed by μ CT analysis (Figure 4.3b) confirms the high porosity of the specimens, with porosity values of 94.4% for PUF, 93.8% for PUF/GNPs2.5, 93.5% for PUF/GO2.5, 91.9% for PUF/GNPs5.0 and 91.8% for PUF/GO5.0. μ CT images also demonstrated that the morphology of the samples is heterogeneous with wide range of pore size and wall thickness. The mean cell sizes for pristine PUF, PUF/GNPs2.5, PUF/GO2.5 and PUF/GNPs5.0 are in the range 168-328 μm , while for PUF/GO5.0 these are located between 328-468 μm (Figure 4.3c). PUF/GO5.0 nanocomposites have also higher percentage of thicker wall cells (Figure 4.3d). It is worth mentioning that due to the limitation of resolution of μ CT, only pores and cell walls thickness above 8 μm were detected.

The mechanical properties of the foams, apparent density, compressive strength at 10% of compression and compressive modulus are summarized in Table 4.2.

Table 4.2 shows that the foam's densities increase with either GO and GNPs loading. In addition, compressive strengths and compressive modulus steadily grow with the increasing of both nanofillers content. It is reported that the addition of nanofillers to cellular materials can have different effects depending on several aspects, the loading content, the size and shape, compatibility between the nanofillers and the matrix [33,47]. For the same fillers loading, GO provides higher compressive modulus and higher resistivity to undergo load without total collapse of pores (higher stress plateau) than GNPs. From the SEM images it was observed that GO induced thicker cell walls, while PUF/GNPs were similar to PUF. The improvement of compressive modulus and strength by the addition of carbon nanostructures to PUF was also reported by other experimental works, where phosphorus functionalized graphene oxide [30] and expandable graphite [19] were used.

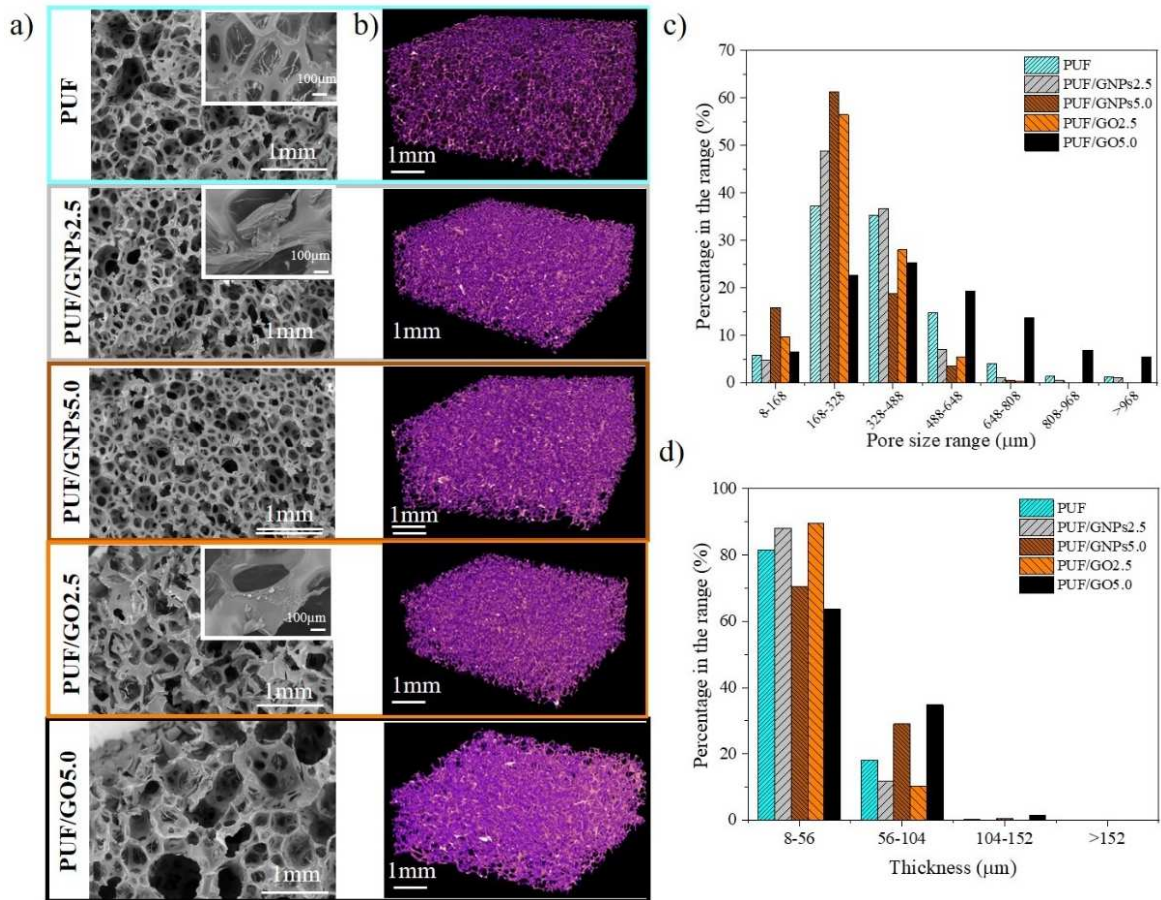


Figure 4.3 SEM images (a), 3D μ CT rendering (b), pore size distribution (c) and cell wall thickness distribution (d) for PUF, PUF/GNPs2.5, PUF/GNPs5.0, PUF/GO2.5 and PUF/GO5.0.

Table 4.2 Apparent density, compressive Modulus and compressive strength for 10% of deformation.

	Apparent density (kg/m^3)	Compressive Modulus (kPa)	Compressive strength (kPa) (Strain:0.1)
PUF	44.3 \pm 1.1	247.2 \pm 3.6	21.74 \pm 0.71
PUF/GNPs2.5	47.4 \pm 0.8	570.4 \pm 12.8	28.30 \pm 5.76
PUF/GNPs5.0	55.6 \pm 2.0	966.3 \pm 81.9	48.27 \pm 5.38
PUF/GO2.5	49.7 \pm 1.2	597.7 \pm 46.4	35.29 \pm 0.28
PUF/GO5.0	59.7 \pm 3.6	1509.6 \pm 165.4	56.28 \pm 5.02

From the average stress-strain compressive curves (Figure 4.4a), the foams exhibit the typical behaviour of cellular materials. An elastic region at low strain values (5% of strain), where stress-strain curve is linear, followed by a near constant stress until 55-60% of strain,

designated by Stress Plateau. Finally, the densification takes place, with the complete collapse of the cells and the formation of a compact material, like a thin film, which is characterized by an abrupt increase of stress.

Figure 4.4b shows the sound absorption coefficient between 100 and 4000 Hz for the PUF and PUF with 2.5 and 5.0 wt.% of GNPs and GO. Globally, the sound absorption coefficient increases with frequency until 1500 Hz, followed by a small decrease and finally a subsequent stabilization between 2000 and 4000 Hz. The sound absorption coefficient is strongly influenced by the morphology of the foams, namely the density (associated to cell wall thickness) and pore features (size, quantity, interconnectivity, tortuosity) [48].

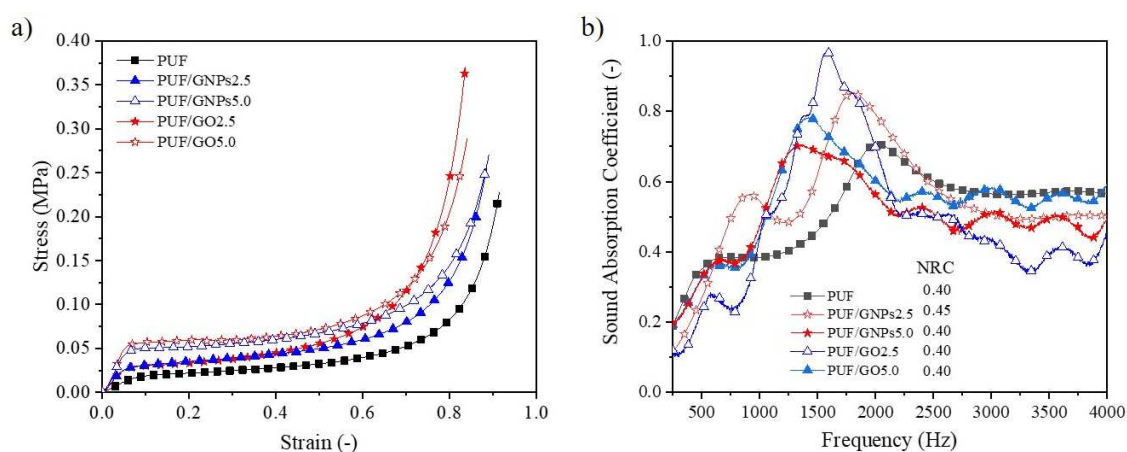


Figure 4.4 Average stress-strain compressive curves (a) and sound absorption coefficient (b) of the different PUF based nanocomposites.

It was reported that smaller interconnected pore structure gives better sound absorption coefficient due to high airflow resistivity provided by cell walls [49]. Furthermore, higher porosity, associated with low density offers less resistance to sound wave dissipation which results in low sound absorption coefficient. Many factors contribute or influence the sound absorption and therefore the overall values are a balance of all factors.[17,48,50,51]. The incorporation of GNPs and GO, increases the compressive modulus (with the later presenting higher values) and thus the cells have greater propensity to undergo cell stretching, bending and buckling without deformation. Also, by SEM and μ CT analysis it is observed that the incorporation of GNPs and GO fillers decreases the porosity and pore size. The PUF/GO2.5 has the higher sound absorption curve between 1250 and 1750 Hz, reaching the value of 1 and absorbing more than approximately 50% than PUF. In fact, between 1000 and 1750 Hz, all the PUF nanocomposites have superior sound absorption coefficient comparatively to

pristine PUF, which covers the sensitive frequency region of the human ear [34]. One parameter often used to describe sound absorption is the noise reduction coefficient (NRC). This parameter corresponds to the average of the sound absorption coefficients at the octave bands of 250, 500, 1000 and 2000 Hz, and rounding the result to the nearest multiple of 0.05. However, the use of NRC has its limitations, since equal NRC values do not necessarily translate the same curve profile. Thus, it is worthwhile to use all the available data, especially for sound absorption at frequencies below 250 Hz or above 2000 Hz. The NRC values are gathered in Figure 4.4b and results showed that, although PU/GO2.5 and PU/GO5.0 have the same NRC that PU/GNPs5.0, they have distinct profiles of sound absorption vs frequency, in this case, with PU/GO2.5 having better performance between 1200-2000Hz. Gama *et al.* [17] obtained similar NRC values around 0.40-0.45 for PUF with similar density (around 40 kg/m³) and higher thickness (approximately 40 mm).

To evaluate the possible application of these types of foams as thermal insulation materials, their thermal conductivity was evaluated (Table 4.3). A good thermal insulation material should present low thermal conductivity. The results obtained for all specimens ($\approx 0.035\text{-}0.037 \text{ W}\cdot\text{m}^{-1}\cdot\text{K}^{-1}$) are in the range of most widely used commercial insulation materials, $0.030\text{-}0.040 \text{ W}\cdot\text{m}^{-1}\cdot\text{K}^{-1}$ as reported in literature [18,52,53]. The thermal diffusivity decreases with the addition of carbon nanostructures, except for the PUF/GO5.0, as listed on Table 4.3. This could be due to the barrier effect created by the nanofillers that difficult the heat flow.

Table 4.3 Thermal conductivity, thermal diffusivity and specific heat.

	Thermal conductivity (W·m⁻¹·K⁻¹)	Thermal diffusivity (mm²·s⁻¹)	Specific heat (MJ·m⁻³·K⁻¹)
PUF	0.0352±0.0004	0.8577±0.0065	0.0410±0.0003
PUF/GNPs2.5	0.0361±0.0001	0.8037±0.0004	0.0448±0.0001
PUF/GNPs5.0	0.0393±0.0002	0.7672±0.0119	0.0486±0.0010
PUF/GO2.5	0.0355±0.0001	0.8276±0.0060	0.0429±0.0003
PUF/GO5.0	0.0366±0.0001	1.001±0.0060	0.0360±0.0002

From the combination of different materials, it is expected to create different multifunctional structures with high strength and reduced weight as a result of the synergetic

effect of the individual materials and able to be applied in different fields. In this sense, following the characterization of PUF nanocomposites regarding their fire-retardancy, mechanic, acoustic and thermal insulator properties, the optimized formulation (PUF/GNPs2.5) was selected to be incorporated in the OCF skeleton as filling material and denoted as HS-PU/GNPs2.5. However, it is worth to mention that all the developed PUF nanocomposites were suitable to be incorporated inside OCF.

4.4.2. Hybrid structures

The effect of filling the voids of OCF foams with bulky polymers has been reported [1–12,54], showing enhanced mechanical properties due to the pore filling which improves the compressive strength and energy absorption capacity of the hybrid foams. However, the use of bulky polymers to fill the voids of the OCF foams can be disadvantageous when lightweight structures are required. Here, we want to explore the properties of the hybrid structure resulting from filling the OCF foam with a porous one, thus, not compromising the lightness of the final structure. Figure 4.5a and 4.5b show the OCF and hybrid structure images, respectively and Figure 4.5c a 3D reconstruction of the hybrid structure obtained by μ CT analysis. An easy and simple process (Figure 4.1, route B) was followed. It was observed that, during the PUF expansion and when the raising PUF/GNPs2.5 came in contact with OCF struts, the cells collapsed and the PUF/GNPs2.5 structure inside the OCF foam have a different porosity and morphology from the optimized one. Although the pores are not uniform and the control of the porosity during the foaming was not possible, it was ensured that the procedure were performed under the same operating conditions. In addition, the hybrid structures were reproducible as a whole, taking into account not only the filling material but the also the OCF. Though, no chemical bonding between the metal surface and polymer was observed and even expected, an excellent form-fitting connection of the PUF/GNPs2.5 to the rough metal surface was visible by direct observation. PUF/GNPs2.5 density was increased in the vicinity of the metal surface, visible in the colour scheme (green colour Figure 4.5c).

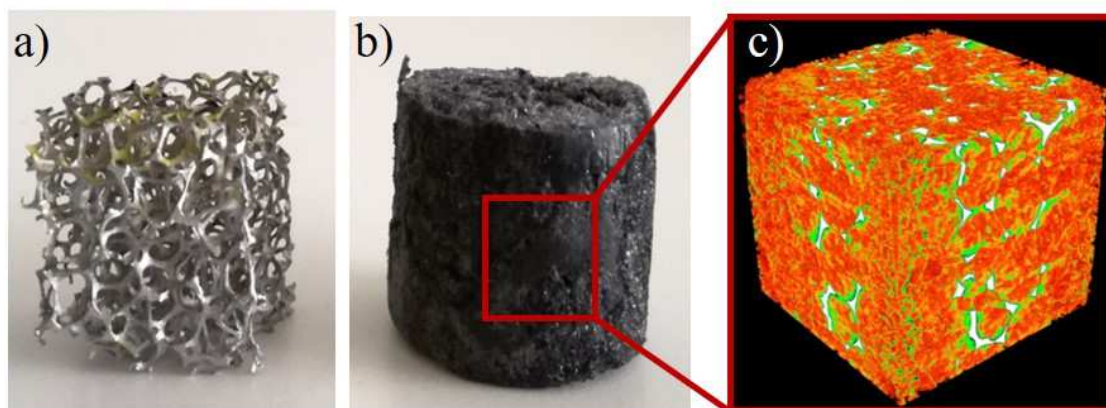


Figure 4.5 Specimens: OCF(a); HS-PUF/GNPs2.5 (b) and 3D- μ CT HS-PUF/GNPs2.5 (c).

The stress-strain curve is shown in Figure 4.6a and the energy absorption (EAD) and specific energy absorption (SEA) are illustrated in Figure S3.4. As described early for pristine PUF and PUF nanocomposite, these hybrid structures also present the typical behaviour of foams, with 3 distinct regions: elastic, stress Plateau and densification [10]. Comparing HS-PU/GNPs2.5 compressive response with OCF, a similar behaviour can be observed, however, with higher stress peak and Plateau stress values and the densification occurs earlier. The EAD is higher for hybrid structures, with improvements of 27% comparatively to the OCF foam and 13 times lower than the PUF/GNPs2.5. However, the SEA is lower suggesting that the increase in EAD do not compensate the increase in weight as found by Reinfried [14], that combined a steel open-cell foam with expanded polystyrene foam. The values of apparent density, stress peak, EAD and SEA and thermal conductivity are gathered in Table 4.4.

Contrary to the hybrid structures composed by OCF impregnated with dense polymers, epoxy [12] and polydimethylsiloxane [11], whose compressive mechanical behaviour is governed by the dense materials, in this case it is the metal skeleton (OCF) that controls the compressive response under loading, as reported in a similar study describing the OCF filled with bacterial cellulose nanocomposite foam [15]. However, it should be noted that the weight of these structures is much smaller, and a good compromise between weight and strength can be achieved.

Table 4.4 Apparent density, stress peak, energy absorption, specific energy absorption and thermal conductivity.

	Apparent density (kg·m ⁻³)	Stress Peak (MPa)	EAD (MJ·m ⁻³) Strain: 0.8	SEA (MJ·m ⁻³ ·kg ⁻¹) Strain: 0.8	Thermal conductivity (W·m ⁻¹ ·K ⁻¹)
OCF	110.2±1.6	0.338±0.0 15	0.317±0.00 4	249.0±1.5	1.1781±0.00 02
PUF/GNPs2.5	49.7±1.2	0.029±0.0 04	0.028±0.00 4	445.0±31	0.0355±0.00 01
HS-PUF /GNPs2.5	115.8±6.4	0.506±0.0 05	0.401±0.00 2	127.2±8.8	0.0377±0.00 01

The sound absorption ability of the hybrid structures (evaluated by the sound absorption coefficient) present higher sound absorption values (peak at 1200 Hz with a value of 0.8 and followed by a nearly constant value of 0.7 for higher frequencies) (Figure 4.6b) when compared with the filling material. The increase of stiffness provided by the OCF structure can improve the absorption at low frequencies. Increased sound absorption can be obtained for thick specimens [55,56]. The NRC value for HS-PUF/GNPs2.5 is of 0.45, 3 times higher than for pristine OCF. These values are comparable with other cellular materials reported in literature with similar thickness (around 22 mm) and density (120 kg/m³) [57].

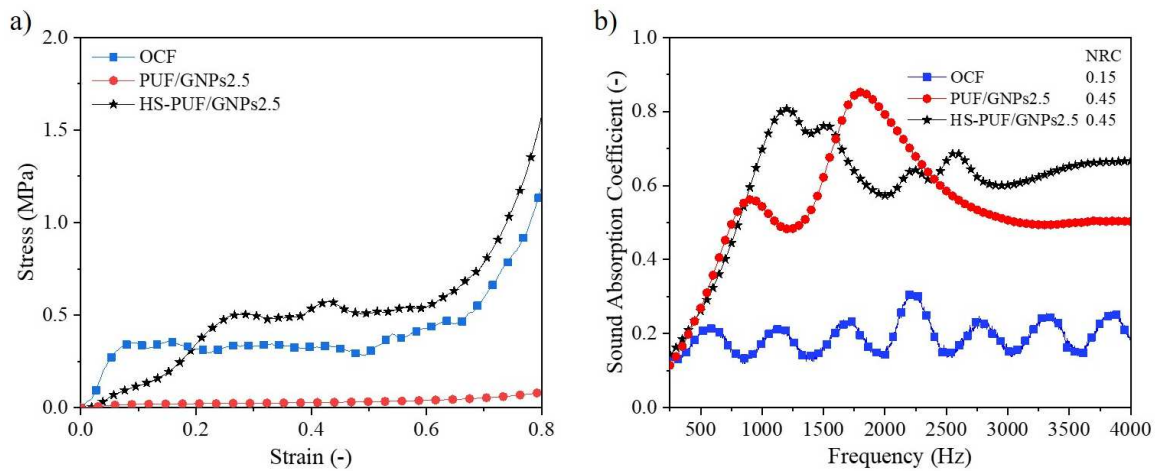


Figure 4.6 Average stress-strain compressive curves (a) and sound absorption curves (b) of OCF, PUF/GNPs2.5 and HS-PUF/GNPs2.5.

The values of thermal conductivity obtained for the hybrid foam HS-PUF/GNPs2.5 are similar to those obtained for PUF and its nanocomposites, around 0.038 (W·m⁻¹·K⁻¹),

suggesting that OCF contribution is negligible in the overall thermal conductivity value. This may be due to the small (about 1mm) layer of filler foam (PUF/GNPs2.5) surrounding the metal foam that block the heat transfer. Another aspect is related with the highly porous structure of OCF and the amount of solid material (Al-SiO₃) that would effectively increase the conductivity value is very small. The same trend is observed in previous works, in which the contribution of OCF was small regarding the filling materials [11,12,15]. Globally, hybrid HS-PUF/GNPs2.5 can be used as thermal insulation material [18,56].

4.5. Conclusions

In the present study, hybrid structures were prepared by impregnating an OCF foam with other cellular material, a PUF nanocomposite. Prior to the incorporation into the open structure of OCF foams, the stand-alone PUF nanocomposites were prepared with different amounts of GNPs and GO and fully characterized. The presence of the carbon nanostructures in the PUF nanocomposites provided PUF with excellent fire-retardancy, better mechanical strength and thermal and acoustic insulating properties. The formulation with 2.5 wt.% of GNPs was considered the more promising one. The process of filling the OCF open structure with the optimized PUF nanocomposite was successfully achieved, and the resulting hybrid structure maintain a low thermal conductivity value ($0.038 \text{ W}\cdot\text{m}^{-1}\cdot\text{K}^{-1}$), high sound absorption coefficient specially at mid to high frequencies (NRC 0.45) and better mechanical behaviour (the stress corresponding to 10% of deformation was improved in more than 10 times). Therefore, these hybrid structures are thoroughly multifunctional materials with potential applications in construction, automotive and aeronautic sectors.

4.6. References

- [1] A. D. B. L. Ferreira, P. R. O. Nóvoa, and A. T. Marques, "Multifunctional Material Systems: A state-of-the-art review," *Compos. Struct.*, vol. 151, pp. 3–35, 2016.
- [2] L. J. Gibson and M. F. Ashby, *Cellular Solids: Structure and Properties*. Cambridge University Press, 1999.
- [3] M. F. Ashby and Y. J. M. Bréchet, "Designing hybrid materials," *Acta Mater.*, vol. 51, no. 19, pp. 5801–5821, Nov. 2003.

- [4] M. F. Ashby, "The properties of foams and lattices," *R. Soc.*, no. November 2005, pp. 15–30, 2006.
- [5] I. Duarte and J. M. F. Ferreira, "Composite and Nanocomposite Metal Foams," *Materials (Basel)*, vol. 9, no. 2, p. 79, Feb. 2016.
- [6] I. Duarte, M. Vesenjajk, L. Krstulović-Opara, and Z. Ren, "Crush performance of multifunctional hybrid foams based on an aluminium alloy open-cell foam skeleton," *Polym. Test.*, vol. 67, pp. 246–256, 2018.
- [7] S. C. Pinto et al., "Characterization and physical properties of aluminium foam–polydimethylsiloxane nanocomposite hybrid structures," *Compos. Struct.*, vol. 230, p. 111521, Dec. 2019.
- [8] S. C. Pinto et al., "Mechanical, Thermal, and Acoustic Properties of Aluminum Foams Impregnated with Epoxy/Graphene Oxide Nanocomposites," *Metals (Basel)*, vol. 9, no. 11, p. 1214, Nov. 2019.
- [9] S. Liu, A. Li, S. He, and P. Xuan, "Cyclic compression behavior and energy dissipation of aluminum foam–polyurethane interpenetrating phase composites," *Compos. Part A Appl. Sci. Manuf.*, vol. 78, pp. 35–41, Nov. 2015.
- [10] M. Reinfried, G. Stephani, F. Luthardt, J. Adler, M. John, and A. Krombholz, "Hybrid Foams - A New Approach for Multifunctional Applications," *Adv. Eng. Mater.*, vol. 13, no. 11, pp. 1031–1036, Nov. 2011.
- [11] A. Kausar, "Polyurethane Composite Foams in High-Performance Applications: A Review," *Polym. Plast. Technol. Eng.*, vol. 57, no. 4, pp. 346–369, Mar. 2018.
- [12] N. Gama, A. Ferreira, and A. Barros-Timmons, "Polyurethane Foams: Past, Present, and Future," *Materials (Basel)*, vol. 11, no. 10, p. 1841, Sep. 2018.
- [13] N. Gama, R. Silva, A. P. O. Carvalho, A. Ferreira, and A. Barros-Timmons, "Sound absorption properties of polyurethane foams derived from crude glycerol and liquefied coffee grounds polyol," *Polym. Test.*, vol. 62, pp. 13–22, 2017.
- [14] N. V Gama et al., "Bio-based polyurethane foams toward applications beyond thermal insulation," *Mater. Des.*, vol. 76, pp. 77–85, 2015.
- [15] N. V Gama et al., "Enhancement of physical and reaction to fire properties of crude glycerol polyurethane foams filled with expanded graphite," *Polym. Test.*, vol. 69, pp. 199–207, 2018.
- [16] W. Xu, G. Wang, and X. Zheng, "Research on highly flame-retardant rigid PU foams by combination of nanostructured additives and phosphorus flame retardants," *Polym. Degrad. Stab.*, vol. 111, pp. 142–150, 2015.
- [17] Ł. Piszczyk, M. Danowska, A. Mietlarek-Kropidłowska, M. Szyszka, and M. Strankowski, "Synthesis and thermal studies of flexible polyurethane nanocomposite foams obtained using nanoclay modified with flame retardant compound," *J. Therm. Anal. Calorim.*, vol. 118, no. 2, pp. 901–909, Aug. 2014.
- [18] Q. Dong et al., "Investigation of Flame Retardant Flexible Polyurethane Foams Containing DOPO Immobilized Titanium Dioxide Nanoparticles," *Polymers (Basel)*, vol. 11, no. 1, p. 75, Jan. 2019.
- [19] M. M. A. Nikje, S. T. Moghaddam, and M. Noruzian, "Preparation of novel magnetic polyurethane foam nanocomposites by using core-shell nanoparticles," *Polímeros*, vol. 26, no. 4, pp. 297–303, Dec. 2016.

- [20] J. Huang, Q. Tang, W. Liao, G. Wang, W. Wei, and C. Li, "Green Preparation of Expandable Graphite and Its Application in Flame-Resistance Polymer Elastomer," *Ind. Eng. Chem. Res.*, vol. 56, no. 18, pp. 5253–5261, May 2017.
- [21] G. Pandey and E. T. Thostenson, "Carbon Nanotube-Based Multifunctional Polymer Nanocomposites," *Polym. Rev.*, vol. 52, no. 3, pp. 355–416, Jul. 2012.
- [22] C. Caglayan, I. Gurkan, S. Gungor, and H. Cebeci, "The effect of CNT-reinforced polyurethane foam cores to flexural properties of sandwich composites," *Compos. Part A Appl. Sci. Manuf.*, vol. 115, pp. 187–195, Dec. 2018.
- [23] M. Colloca, N. Gupta, and M. Porfiri, "Tensile properties of carbon nanofiber reinforced multiscale syntactic foams," *Compos. Part B Eng.*, vol. 44, no. 1, pp. 584–591, Jan. 2013.
- [24] J. Njuguna, K. Pielichowski, and S. Desai, "Nanofiller-reinforced polymer nanocomposites," *Polym. Adv. Technol.*, vol. 19, pp. 947–959, 2008.
- [25] D. Pinto, L. Bernardo, A. Amaro, and S. Lopes, "Mechanical properties of epoxy nanocomposites using titanium dioxide as reinforcement – A review," *Constr. Build. Mater.*, vol. 95, pp. 506–524, Oct. 2015.
- [26] Z.-J. Cao, W. Liao, S.-X. Wang, H.-B. Zhao, and Y.-Z. Wang, "Polyurethane foams with functionalized graphene towards high fire-resistance, low smoke release, superior thermal insulation," *Chem. Eng. J.*, vol. 361, pp. 1245–1254, 2019.
- [27] a. Gharehbaghi, R. Bashirzadeh, and Z. Ahmadi, "Polyurethane flexible foam fire resisting by melamine and expandable graphite: Industrial approach," *J. Cell. Plast.*, vol. 47, no. 6, pp. 549–565, Sep. 2011.
- [28] D. Yan, L. Xu, C. Chen, J. Tang, X. Ji, and Z. Li, "Enhanced mechanical and thermal properties of rigid polyurethane foam composites containing graphene nanosheets and carbon nanotubes," *Polym. Int.*, vol. 61, no. 7, pp. 1107–1114, Jul. 2012.
- [29] Ł. Piszczyk, P. Kosmela, and M. Strankowski, "Elastic polyurethane foams containing graphene nanoplatelets," *Adv. Polym. Technol.*, vol. 37, no. 6, pp. 1625–1634, Oct. 2018.
- [30] J. M. Kim, D. H. Kim, J. Kim, J. W. Lee, and W. N. Kim, "Effect of graphene on the sound damping properties of flexible polyurethane foams," *Macromol. Res.*, vol. 25, no. 2, pp. 190–196, Feb. 2017.
- [31] J. Lee and I. Jung, "Tuning sound absorbing properties of open cell polyurethane foam by impregnating graphene oxide," *Appl. Acoust.*, vol. 151, pp. 10–21, 2019.
- [32] J. da Silva, "Metodologias experimentais para a determinação do coeficiente de absorção de sonora em materiais de construção," University of Coimbra, 2008.
- [33] J. N. Gavvani, H. Adelnia, D. Zaarei, and M. Moazzami Gudarzi, "Lightweight flexible polyurethane/reduced ultralarge graphene oxide composite foams for electromagnetic interference shielding," *RSC Adv.*, vol. 6, no. 33, pp. 27517–27527, 2016.
- [34] Y. Cheng et al., "Enhanced mechanical, thermal, and electric properties of graphene aerogels via supercritical ethanol drying and high-temperature thermal reduction," *Sci. Rep.*, vol. 7, no. 1, p. 1439, 2017.
- [35] G. Malucelli, "The Role of Graphene in Flame Retardancy of Polymeric Materials: Recent Advances," *Curr. Graphene Sci.*, vol. 2, no. 1, pp. 27–34, Oct. 2018.

- [36] C. I. Idumah, A. Hassan, and A. C. Affam, "A review of recent developments in flammability of polymer nanocomposites," *Rev. Chem. Eng.*, vol. 31, no. 2, pp. 149–177, Jan. 2015.
- [37] B. Sang, Z. Li, X. Li, L. Yu, and Z. Zhang, "Graphene-based flame retardants : a review," *J. Mater. Sci.*, vol. 51, no. 18, pp. 8271–8295, 2016.
- [38] D. K. Chattopadhyay and D. C. Webster, "Thermal stability and flame retardancy of polyurethanes," *Prog. Polym. Sci.*, vol. 34, no. 10, pp. 1068–1133, Oct. 2009.
- [39] X. Chen, J. Li, and M. Gao, "Thermal Degradation and Flame Retardant Mechanism of the Rigid Polyurethane Foam Including Functionalized Graphene Oxide," *Polymers (Basel)*, vol. 11, no. 1, 2019.
- [40] P. Acuña, Z. Li, M. Santiago-Calvo, F. Villafañe, M. Rodríguez-Perez, and D.-Y. Wang, "Influence of the Characteristics of Expandable Graphite on the Morphology, Thermal Properties, Fire Behaviour and Compression Performance of a Rigid Polyurethane Foam," *Polymers (Basel)*, vol. 11, no. 1, p. 168, Jan. 2019.
- [41] E. Ciecierska, M. Jurczyk-Kowalska, P. Bazarnik, M. Kowalski, S. Krauze, and M. Lewandowska, "The influence of carbon fillers on the thermal properties of polyurethane foam," *J. Therm. Anal. Calorim.*, vol. 123, no. 1, pp. 283–291, Jan. 2016.
- [42] Y. Wang et al., "Magnetic graphene oxide nanocomposites: nanoparticles growth mechanism and property analysis," *J. Mater. Chem. C*, vol. 2, no. 44, pp. 9478–9488, Sep. 2014.
- [43] H. Liu et al., "Lightweight conductive graphene/thermoplastic polyurethane foams with ultrahigh compressibility for piezoresistive sensing," *J. Mater. Chem. C*, vol. 5, no. 1, pp. 73–83, 2017.
- [44] N. Gama et al., "Thermal Energy Storage and Mechanical Performance of Crude Glycerol Polyurethane Composite Foams Containing Phase Change Materials and Expandable Graphite," *Materials (Basel)*, vol. 11, no. 10, p. 1896, Oct. 2018.
- [45] M. Jawaid, R. Bouhfid, and A. K. Qaiss, *Functionalized Graphene Nanocomposites and Their Derivatives: Synthesis, Processing and Applications*. Elsevier Science, 2018.
- [46] Y. Li et al., "Effect of expandable graphite particle size on the flame retardant, mechanical, and thermal properties of water-blown semi-rigid polyurethane foam," *J. Appl. Polym. Sci.*, vol. 131, no. 3, Feb. 2014.
- [47] N. N. Najib, Z. M. Ariff, A. A. Bakar, and C. S. Sipaut, "Correlation between the acoustic and dynamic mechanical properties of natural rubber foam: Effect of foaming temperature," *Mater. Des.*, vol. 32, no. 2, pp. 505–511, 2011.
- [48] A. Arjunan, A. Baroutaji, A. S. Praveen, A. G. Olabi, and C. J. Wang, "Acoustic Performance of Metallic Foams," in *Reference Module in Materials Science and Materials Engineering*, Elsevier, 2019.
- [49] J. G. Gwon, S. K. Kim, and J. H. Kim, "Sound absorption behavior of flexible polyurethane foams with distinct cellular structures," *Mater. Des.*, vol. 89, pp. 448–454, 2016.
- [50] G. Sung, J. W. Kim, and J. H. Kim, "Fabrication of polyurethane composite foams with magnesium hydroxide filler for improved sound absorption," *J. Ind. Eng. Chem.*, vol. 44, pp. 99–104, 2016.
- [51] S. A. Al-Ajlan, "Measurements of thermal properties of insulation materials by using transient plane source technique," *Appl. Therm. Eng.*, vol. 26, no. 17, pp. 2184–2191, 2006.

- [52] B. P. Jelle, "Traditional, state-of-the-art and future thermal building insulation materials and solutions – Properties, requirements and possibilities," *Energy Build.*, vol. 43, no. 10, pp. 2549–2563, Oct. 2011.
- [53] A. R. Mahanta, N.K., Abramson, "Thermal conductivity of graphene and graphene oxide nanoplatelets," in *13th InterSociety Conference on Thermal and Thermomechanical Phenomena in Electronic Systems*, 2012, pp. 1–6.
- [54] M. Vesenjak, L. Krstulović-Opara, and Z. Ren, "Characterization of irregular open-cell cellular structure with silicone pore filler," *Polym. Test.*, vol. 32, no. 8, pp. 1538–1544, 2013.
- [55] T. J. Lu, A. Hess, and M. F. Ashby, "Sound absorption in metallic foams," *J. Appl. Phys.*, vol. 85, no. 11, pp. 7528–7539, Jun. 1999.
- [56] H. Degischer and B. Kriszt, Eds., *Handbook of Cellular Metals*. Wiley, 2002.
- [57] M. Pedroso, J. de Brito, and J. D. Silvestre, "Characterization of eco-efficient acoustic insulation materials (traditional and innovative)," *Constr. Build. Mater.*, vol. 140, pp. 221–228, 2017.

Chapter 5. Aluminium foam–cork nanocomposite hybrid structures: fabrication and characterization

This chapter was based in the following submitted national patent:

Duarte, I., Pinto, S. Marques, P., Metais e estruturas metálicas porosas e celulares de porosidade aberta impregnados com cortiça, seus processos de produção e suas utilizações, **2019**. Data do depósito: 11/10/2019, N°. do pedido: 115835

5.1. Abstract

In this chapter hybrid structures based on cellular materials were developed and studied by combining open-cell aluminium foams (OCF) with cork (natural cellular material) with and without graphene oxide (GO). More specifically, these hybrid structures were prepared by infiltrating an OCF with a mixture containing cork powders (particle size < 0.7 mm), polymer binder and graphene oxide nanosheets (GO). The mechanical, thermal, acoustic and fire retardancy properties of these aluminium foam-cork (HS-Cork) and aluminium foam-cork nanocomposite hybrid structures (HS-nCork) were evaluated and compared to their individual cellular materials (OCF, agglomerated cork (Cork) and agglomerated cork nanocomposite (nCork)). Results show that the presence of the cork as the void filler of the OCF significantly enhance their properties, namely the compressive performance and sound absorption properties. For example, the maximum coefficient sound absorption of HS-Cork is 0.990 for 1636 Hz, while is approximately 1 for HS-nCork. In general, the novel hybrid structures developed in this work are new multifunctional material exhibiting much better acoustic and mechanical properties than the individual cellular materials (OCF, Cork, nCork) being possible to obtain the characteristics necessary to satisfy the requirements for specific applications.

5.2. Introduction

Natural and artificial cellular materials (e.g. cork, wood, metallic foams, polymeric foams) are light and offer an rare combination of properties such as high stiffness-to-weight ratio, high impact energy absorption capacity at low stresses and the good damping (vibration and noise attenuation) [1,2]. Closed-cell metallic foams, in particular made of aluminium alloys have been tested and applied as filler of thin-walled hollow structures [3,4] and core of sandwich panels [5,6] for vehicles (e.g. automobile and train). However, these closed-cell foams cannot be characterised by a single unit cell, being difficult to predict their performances specially the mechanical behaviour. To overcome it, some researchers have developed and tested new hybrid foams, combining periodic cellular metals (e.g. open-cell metal foams [7,8] spheres of Advanced Pore Morphology (APM) foam elements [9,10], metal hollow spheres [11]) with polymers (e.g. epoxy (EP) and silicone) or polymeric foams (e.g. polyurethane foam) [12]. Results have shown that some of these hybrid structures have a stable and predictable crushing deformation as a

filler of thin-walled tubes made of aluminium alloy [13]. The presence of the polymers (e.g. silicone, EP and polyurethane) increases the compressive response and the energy absorption capability of the aluminium foam-polymer hybrid structures [7]. Many times, the increase in mechanical response compensates the extra weight by the filling polymeric material. The presence of the polymers changes the typical layer-wise collapse mechanism of the simple aluminium open-cell foam (OCF), preventing the self-contact of struts [7] and decreasing the stress oscillations in the plateau region of the compressive stress-strain curves observed in the OCF. Results have also shown that the crush performance and the deformation and failure modes mainly depend on the chemical nature of the polymer used [14]. For example, the brittle EP resin contributes to the development of small cracks during the fold formation under compressive loading, while the silicone rubber behaves as an elastomer showing a low adhesion and low friction coefficient between the silicone rubber and the struts of the open-cell foams, promoting a non-symmetric deformation [7]. Results have also show that the mechanical behaviour of these resulting hybrid structures could be adjusted from rubbery to brittle to ductile behaviour, selecting the polymer type and/or its curing conditions (e.g. temperature), leading to excellent energy absorption characteristics required for vehicles [15,16]. However, these hybrid foams are flammable, non-recyclable, increase fire hazards (release toxic gases and smoke in case of fire) and cannot support high temperatures due to the presence of the polymers, limiting their uses. The fire retardant of these resulting hybrid foams could be achieved by incorporating carbon nanostructures (e.g. graphene oxide (GO)) into polymer matrix [17], however, their mechanical properties diminish [16].

Herein, novel hybrid structures were developed and tested by combining the OCF (man-made foam) and cork (natural cellular material) with or without GO. Cork based products (e.g. natural cork, granulates, composite agglomerates, expanded agglomerates) are widely used in numerous applications, such as aeronautical, aerospace, automotive and buildings, footwear, outdoor furniture, decks and naval construction [18,19]. Composite agglomerates present low density (usually between 120–600 kg/m³) and have low conductivity (0.045-0.060 W/m·K) [20,21], great resistance to fire and can withstands wide variations in temperature and humidity. They are usually used as thermal and acoustic insulators and vibration control and noise solutions [22,23] due to their excellent thermal and acoustic insulation capacities and excellent damping characteristics with an

unusual compressibility and recovery characteristics [18,24]. Portugal is the main producer and processor of raw cork into products with high added value, being this one of the largest income sources for the Portuguese industry [25]. The great part of scientific outcome of the cork field is related with the properties of different types of cork [26] (e.g. natural and expanded and agglomerated cork) used as core materials of sandwich structures [27–29]. Results have indicated that the particle/granules/grains size of the cork, type and content of polymer binder, compaction pressure strongly influence the mechanical response of resulting agglomerated cork [30].

The use of graphene-based materials (GBMs) was also explored as reinforcement of the cork, studying their effects on the properties of the resulting structures.

5.3. Materials and Methods

5.3.1. Materials

An OCF panel ($300 \times 150 \times 50 \text{ mm}^3$; pore sizes of 10 pores per inch) fabricated by the investment casting method and granulated cork powder (particle size $\leq 0.7 \text{ mm}$) supplied by Amorim Revestimentos (Mozelos, Portugal) were the main materials used to prepare the new hybrid aluminium foam–cork structures, respectively. A commercial EP resin solvent free mid-viscosity glue was supplied by company KGK Ltd. (Croatia), composed by two reagents, component A (polymer density: 1.12 kg/dm^3) and component B (hardener; density 1 kg/dm^3) and the mixing ration is A:B = 2:1 (mass ratio) or 9:5 (volume ratio). An aqueous solution of 4 mg/mL GO was supplied by Graphenea (Spain). The GO sheets have a particle size $< 10 \mu\text{m}$ and $> 95 \%$ of GO content is a monolayer (nanometric in thickness). The GO has a carbon content of 49-56 % and oxygen content of 41-50 % that was determined by X-ray Photoelectron Spectroscopy (XPS).

To prepare the aluminium foam–cork (HS-Cork) and OCF-cork nanocomposite (HS-nCork) hybrid structure specimens, square ($22 \times 22 \times 25 \text{ mm}^3$) and cylindrical (diameter: 37 mm ; height: 23 mm) OCF specimens with pore sizes of 10 ppi (pores per inch) were cut from foam blocks made of AlSi7Mg0.3 ($300 \times 150 \times 150 \text{ mm}^3$) fabricated by the investment casting method. In addition, square ($25 \times 25 \times 25 \text{ mm}^3$) and cylindrical (diameter: 37 mm ; height: 22 mm) steel stainless moulds were used to prepare the studied specimens.

5.3.2. Specimens fabrication

Cubic (25 mm × 25 mm × 25 mm) and cylindrical (diameter: 37 mm; height: 22 mm) open-cell aluminum foams (OCFs), unreinforced cork (Cork), reinforced cork (nCork), aluminum foam – unreinforced cork hybrid structures (HS-Cork) and aluminum foam – reinforced cork hybrid structures (HS-nCork) were prepared and studied in this work (Figure 5.1). Cubic and cylindrical OCF specimens were previously cut by wire machining from the foam block (300 × 150 × 50 mm³; 10 pores per inch). HS-Cork and HS-nCork were prepared by pouring a mixture of cork granules with or without GO into the voids of an OCF previously placed into a mould, respectively. The mould is continuously under mechanical vibration during this step to ensure that the powder sets, filling the voids of OCF. After, the mixture was slightly compressed until reached 155 kg/m³ and 225kg/m³ for simple and hybrid structures, respectively. GO was incorporated into the cork granules via layer-by-layer method (LbL). As-received cork granules were pre-treated by immersing them in a 0.1 wt.% poly diallyldimethylammonium chloride aqueous solution for 15 min, followed of filtration and then washed with distilled water. This experimental procedure was repeated using 0.1 wt.% poly sodium 4-styrene sulfonate, followed 0.1 wt. % poly diallyldimethylammonium chloride) aqueous solutions. After, the cleaned cork granules were immersed in 0.1 wt.% GO aqueous solution for 15 min, following by filtration and then finally washed with distilled water before drying into the oven at 40 ° C for 24h.

The unreinforced and reinforced cork specimens were prepared by compressing a mixture of cork with or without GO containing 20 wt. % of EP resin that was previously poured into a mold coated with greaseproof paper to facilitate the extraction of the resulting specimen. After that, the mold containing the compressed mixture was placed into a pre-heated furnace at 80°C for 2 hours. Figure 5.1 presents the fabricated specimens.



Figure 5.1 Fabricated specimens: cubic specimens (a) and circular specimens (b) of OCF, Cork, nCork, HS-Cork and HS-nCork.

The densities of the materials were: 105.1 kg/m^3 (standard deviation: 2.1 kg/m^3), 153.4 kg/m^3 (standard deviation: 1.7 kg/m^3), 152.3 kg/m^3 (standard deviation: 3.7 kg/m^3), 223.73 kg/m^3 (standard deviation: 12.6 kg/m^3), and 221.9 kg/m^3 (standard deviation: 5.5 kg/m^3) for the OCF, Cork, nCork, HS-Cork, and HS-nCork, respectively

5.3.3. Microstructure and morphology

The microstructure and morphology of the studied specimens were analysed by scanning electron microscope (SEM) using a TM 400 Plus (Hitachi).

5.3.4. Compressive behaviour

The compressive behaviour of the HS-Cork and HS-nCork specimens and their individual components (Cork, nCork and OCF) were studied using a servo-hydraulic dynamic INSTRON 8801 testing machine (maximum load 50 kN) at crosshead rates of 0.1 mm/s (quasi-static) and 284 mm/s (dynamic). The high-resolution video camera Sony HDR-SR8 and the mid-wave infrared (IR) cooled thermal camera Flir SC 5000 were used in the quasi-static and dynamic tests in order to record the deformation and failure modes of the specimens. The density of the specimens is calculated using its weight and geometrical dimensions. The recorded load-displacement data were converted to stress-strain data. The engineering stress and engineering strain values were determined by dividing the load with the initial cross-section and by dividing the displacement with the initial specimen height, respectively. The energy absorption density (EAD) curves and the specific energy absorption (SEA) values were calculated according to the ISO 13314:

2011 by integrating the engineering stress-strain curves (from 0 up to the maximum strain attained in each test) and by dividing the EAD values by the specimen mass, respectively.

5.3.5. Thermal conductivity

The thermal conductivity properties of different types of specimens were evaluated resorting to a Hot Disk TPS 2500 S instrument using the transient plane source method at room temperature according to the standard ISO 22007-2.2 [31]. During the experiment, a small constant current is applied to the sensor inserted between two identical specimens. Since the temperature increase of the sensor is highly dependent on the two tested samples attached to it, thermal properties of the tested samples can be determined by monitoring the temperature increase for a short time period. For the measurements one pair of identical samples per material is tested at room temperature and five measurements are conducted.

5.3.6. Sound absorption

The sound absorption coefficient and sound absorption efficiency of the OCF, Cork, nCork, HS-Cork and HS-nCork specimens were evaluated using an impedance tube method according to the standard ASTM E 1050 [32]. The cylindrical specimen was placed into the testing impedance tube with the inner diameter of 37mm at one end. At the other end of the tube a sound source consisting of a loudspeaker emitting a random noise was introduced. Two microphones were placed into the tube between the sound source and the specimen to detect the sound pressure wave transmitted through the specimen and the portion of the wave that was reflected. The acoustic absorption coefficient (α) is defined as a ratio of absorbed sound intensity in a given material and the incident sound intensity that is imposed on that material. The noise reduction coefficient (NRC) is another parameter used to evaluate the sound absorption characteristics of a material. The NRC is calculated by defining an average of the sound absorption coefficients at the frequencies 250 Hz, 500 Hz, 1000 Hz and 2000 Hz and rounding off the result to the nearest multiple of 0.05. However, it should be noted that the same value of NRC for two different materials does not mean that they perform in the same way.

5.3.7. Fire-retardancy tests

The fire retardancy tests were based on the direct observation of the specimen behaviour when subjected to a live flame source. The tests consisted of applying an ethanol flame at the specimen's bottom using the set-up in vertical sample position for 3 s plus the subsequent 3 s for observing the self-extinguishing process.

5.4. Results and discussion

5.4.1. Microstructure and morphology

Both OCF and natural cork granules exhibit internal cellular structures that are nearly periodic and composed by an arrangement of open and closed polyhedral cells filled with a gas, respectively. Figure 5.2a shows the highly porous structure of OCF and Figure 5.2b shows the typical hexagonal honeycomb structure presented by the cork.

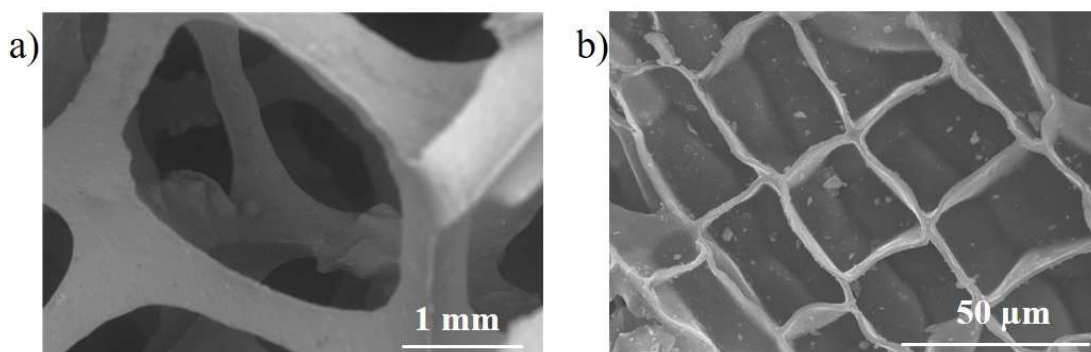


Figure 5.2 SEM images of the OCF foam (a) and a granule of cork (b).

The GO incorporation by LbL was investigated by SEM. Figure 5.3 shows the SEM images for the Cork and nCork. As previously shown in Figure 5.1, GO confers a black colour of the specimens and suggesting a good dispersion of the GO nanosheets at the cork grains surface. This was further confirmed by SEM in Figure 5.3b (second row).

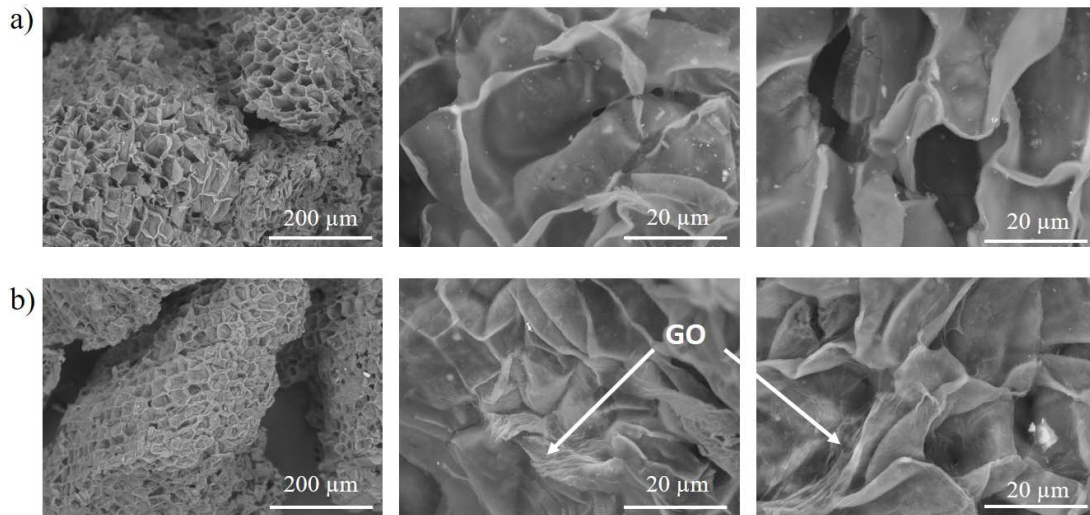


Figure 5.3 SEM images of the Cork (a, first row) and b) nCork (b, second row) matrices.

5.4.2. Compressive behaviour

Figure 5.4 and Figure 5.5 show the compressive deformation and failure modes of Cork, nCork, HS-Cork and HS-nCork under quasi-static and dynamic loading conditions, respectively.

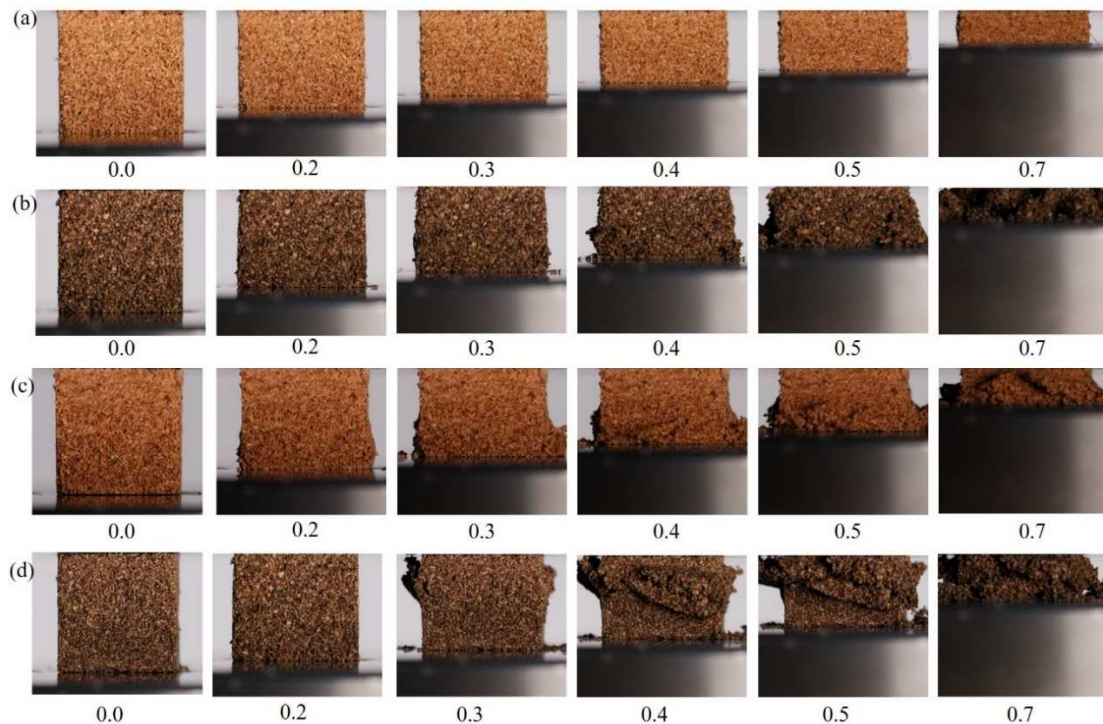


Figure 5.4 The quasi-static deformation sequences showing the progressive deformation of the Cork (a), nCork (b), HS-Cork (c) and HS-nCork (d).

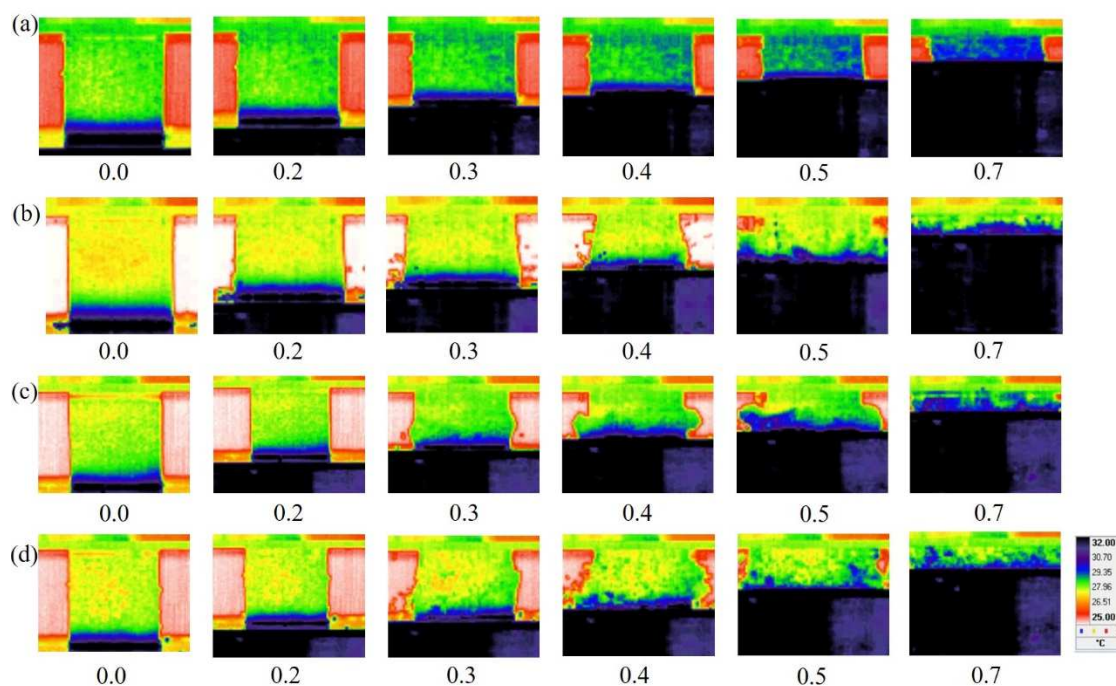


Figure 5.5 The IR image sequences showing the dynamic progressive deformation of the of the Cork (a), nCork (b), HS-Cork (c) and HS-nCork (d).

The results show that the incorporation of GO nanosheets into granulated cork strongly affects the deformation and failure modes of the cork agglomerates (Figure 5.4 and Figure 5.5). The loading rate seems to have no influence in the deformation and failure modes. When submitted to quasi-static compression, the Cork specimens exhibited a symmetric deformation, with small lateral expansion. The specimens can undergo load without failure, contrary to other polymers studied (PDMS, EP) [7]. As expected, when the load is removed and after a brief period of relaxation, significant dimensional recovery occurs due to the viscoelastic nature of the cork. Reinforced cork (containing GO) specimens have different compressive deformation and failure modes compare to those presented by the cork specimens. In nCork specimens it was observed the deagglomeration of granulated cork during loading (strains above 0.4, Figure 5.4), culminating to the total disintegration. IR images of Cork and nCork (Figure 5.5) related to dynamic loading conditions show that the specimens deform and fail in an identical mode to those observed in quasi-static compression test, suggesting that the velocity loading has no great effect on compression behaviour of cork specimens. The deformation and failure modes of the different specimens (Figure 5.4 and Figure 5.5) are directly related to the measured

compressive stress–strain curves (Figure 5.6). Tables 5.1 and Table 5.2 summarize the main quasi-static and dynamic mechanical parameters, respectively.

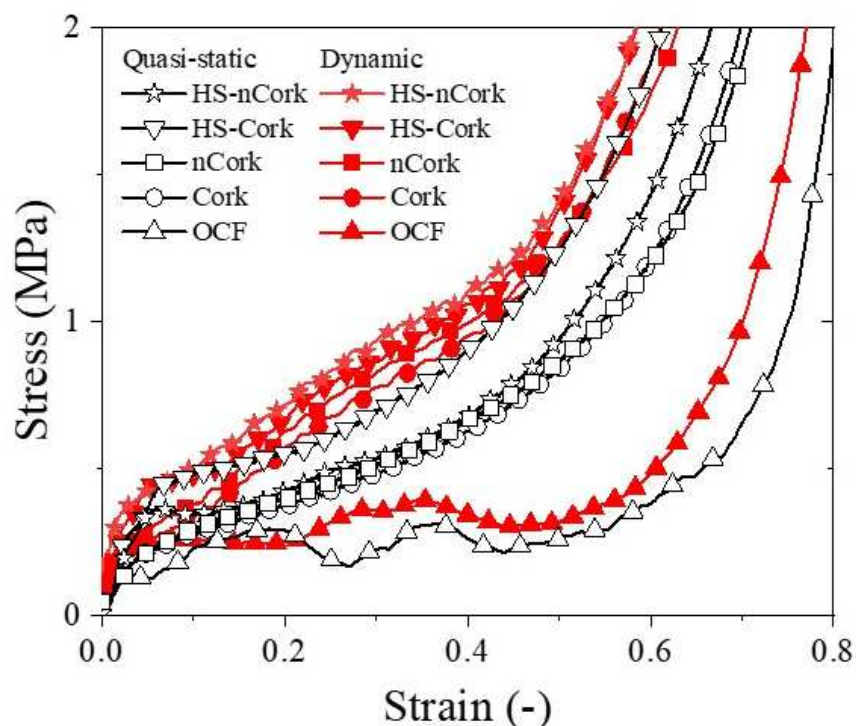


Figure 5.6 Quasi-static and dynamic compressive stress-strain relationship of OCF, Cork, nCork, HS-Cork and HS-nCork.

The shape of the quasi-static and dynamic compressive stress-strain curves for Cork and nCork is identical (Figure 5.6). They showed a typical compressive stress–strain curves typical for the agglomerated cork specimens prepared by powder or granules [19]. These curves can be divided into three main regions (elastic, plateau and densification) related to the main mechanisms responsible for their properties. The first elastic region, up to about 2% strain, corresponds to elastic bending of the cell walls. The second plateau stage region is characterizing by a slightly increasing slope, which extends to about 0.55 of strain, caused by progressive buckling of the cell walls. The densification region starts at ~0.55 of strain and correspond to the crushing of the cell walls and the complete collapse of the cells cause the curve to rise steeply. The gas inside the closed pores of the cork are responsible for its high flexibility and compressibility [19]. Moreover, the cork shows a cell-wall undulation that is responsible for the great recovery capabilities of cork. For example, when a compression load is applied, cell walls of cork are subjected to buckling, and their corrugation starts to increase, leading to the densification or collapse

of the cells without significant damaging or permanent deformation. If the compression load is removed, cell walls are free to unfold, leading to a high dimensional recovery.

Results also demonstrated that the GO has a negative effect on the compressive response, suggesting that GO not enhance their homogeneous 3D reinforcing role leading to an inefficient load transfer. The compressive curves of the nCork are below to the compressive curve of Cork. This is an agreement with other authors [33].

Both Cork and nCork specimens are sensitive to strain rate. For example, for strains of 0.2 and 0.4, the stress values for Cork specimens are 0.40 MPa (quasi-static, Table 5.1) and 0.65 MPa (quasi-static, Table 5.1) and 0.60 (dynamic, Table 5.2) and 0.92 MPa (dynamic, Table 5.2), respectively. The latter corresponds to percentage increases of 50 % and 42 % for 0.2 and 0.4 of strain, respectively.

Table 5.1 Compressive quasi-static results of Cork, nCork, HS-Cork and HS-nCork specimens.

	Strain Peak	Stress Peak (MPa)	Stress MPa (0.2)	Stress MPa (0.4)	Stress Plateau (MPa)	EAD** (MJ/m³)	SEA** (MJ/m³.kg)
Cork							
Average	*	*	0.378	0.627	0.503	0.782	365.4
St Dev			0.026	0.031	0.028	0.046	18.2
nCork							
Average	*	*	0.395	0.661	0.528	0.768	361.2
St Dev			0.030	0.060	0.045	0.124	63.9
HS-Cork							
Average	0.042	0.446	0.552	0.908	0.730	1.256	386.2
St Dev	0.016	0.077	0.085	0.121	0.102	0.248	70.7
HS-nCork							
Average	0.045	0.421	0.421	0.679	0.550	0.905	290.2
St Dev	0.004	0.062	0.045	0.053	0.048	0.135	36.4

* not determined

** determined for 0.8 of strain

Chapter 5

Table 5.2 Compressive dynamic results of Cork, nCork, HS-Cork and HS-nCork specimens.

	Strain Peak	Stress Peak (MPa)	Stress MPa (0.2)	Stress MPa (0.4)	Stress Plateau (MPa)	EAD** (MJ/m ³)	SEA** (MJ/m ³ .kg)
Cork							
Average	_*	_*	0.566	0.946	0.756	1.209	563.2
St Dev	-	-	0.033	0.061	0.046	0.110	50.8
nCork							
Average	*	*	0.630	0.996	0.813	1.113	516.1
St Dev	-	-	0.036	0.048	0.041	0.092	42.1
HS-Cork							
Average	0.048	0.456	0.683	1.062	0.872	1.403	473.9
St Dev	0.021	0.044	0.092	0.187	0.139	0.161	52.5
HS-nCork							
Average	0.026	0.471	0.721	1.108	0.915	1.407	461.4
St Dev	0.00	0.026	0.114	0.050	0.080	0.190	57.8

* not determined

** determined for 0.8 of strain

From experimental results, it could also be noticed that until 0.52 of strain the compressive curve of nCork specimens are slightly superior compared to Cork specimens. However, after 0.52 (near the densification strain), the curves of the nCork specimens are slightly inferior to the compressive curve of Cork specimens. Cork, as it well known, is composed by hexagonal cells able to undergo high loading without failure. The results indicated that the GO nanosheets lead to a poor bonding between the Cork granules. This is due to the GO nanosheets incorporated by the LBL method are coated the cells of cork, creating structural defects that cause to an inefficient load transfer. This is in agreement of our previous results in this field. Results have shown that the GBMs (e.g. graphene nanoplatelets and GO sheets) decrease the compressive strength of the resulting agglomerated cork [33] and reinforced epoxy [16] and reinforced PDMS [15].

The OCF foams exhibit the typical compressive behaviour of cellular materials (eg. Cork) in which the compressive stress-strain curves are divided by the same three main regions (elastic, plateau and densification) described above for the Cork and nCork specimens. As opposite to the Cork and nCork specimens (absence of stress oscillations

in the plateau region, Figure 5.6), the OCF foams exhibited stress oscillations in the plateau region. The local failure of cells and struts by elastic buckling, plastic yielding or brittle crushing are responsible for those oscillations [34].

Regarding the hybrid structures, the results clearly demonstrated that the presence of the Cork or nCork in the voids of the OCF prevents the self-contact of struts, changing the typical of the OCF and stabilizing the structure against buckling. The stress-strain curves in plateau region are smooth (no stress oscillations) and characterized by a slightly increasing slope (Figure 5.6), irrespective of the presence the filler void. The densification of the cork and hybrid structure specimens occurred earlier (Figure 5.6) compared with OCF due to the closed pores of the cork and also the voids of the OCF were filled with the cork (no free space). The poor bonding between the cork granules into the voids, led to the disintegration of the specimens (Figure 5.4 and Figure 5.5).

The compressive stress-strain curves of the resulting hybrid structures (HS-Cork and HS-nCork) are above the curves of its individual components (Cork, nCork, OCF). These HS-Cork and HS-nCork are also sensitive to strain rate in which the dynamic curves are superior to the quasi-static curves (Figure 5.6). This is in agreement with previous published results carried out in aluminium foam-polymer hybrid structures [7,15,16]. For example, Vesenjajak *et al.* [35] reported that the OCF foams impregnated with silicone rubber lead to an increase of 36% in the stress plateau for a similar densification strain. The same authors [14] also reported that the impregnation of silicon filler in a regular aluminium structure led to an increase in the strain densification by 41% but with similar stress plateau values.

Our previous results have shown that the void filler type, e.g. epoxy EP) [16] and silicone (PDMS) [15] used to fill the OCF is responsible to the compressive strength of the resulting hybrid structures and their sensitive of the strain rate. Both HS-EP, HS-nEP, HS-PDMS and HS-nPDMS have higher compressive strength than HS-Cork and HS-nCork. The stress plateau values are 0.66 MPa and 59 MPa for HS-PDMS and HS-EP, respectively. This means that the plateau stress of the HS-PDMS is 1.5 times superior to the HS-Cork, while the plateau stress of the HS-EP is 150 times superior to HS-Cork specimens. However, the density of the HS-EP and HS-PDMS are 6.5 times higher to the HS-Cork. In fact, the void filler contributes also to add mass to the resulting hybrid structures. This is an advantage of the cork, that is lighter than EP or PDMS.

The plateau stress average values of the Cork and nCork are between 0.50 and 0.56 MPa for the quasi-static and between 0.75 and 0.81 for the dynamic tests, respectively (Table 5.1 and Table 5.2).

The EAD and SEA curves of the HS-Cork, HS-nCork, OCF, Cork and nCork for quasi-static and dynamic conditions are shown in Figure 5.7a and Figure 5.7b, respectively. These curves were determined according to ISO 13314: 2011 and are directly related to the engineering stress-strain curves, showing the strain rate sensitivity of these specimens. Results clearly showed that the dynamic EAD and SEA curves of the different type of specimens are above the corresponding quasi-static curves (Figure 5.7 a and b). The exponential EAD curves of the HS-Cork and HS-nCork specimens are above to the curves of their individual components (Cork, nCork and OCF), indicating the high EAD capacity of resulting hybrid structures. For example, at a strain value of 0.8, the HS-Cork and HS-nCork (Tables 5.1 and 5.2) are approximately 4 times and 2.85 times higher in comparison to the OCF specimens subjected to the quasi-static loading conditions, respectively. On the other hand, results demonstrated that above strain of 0.4, the SEA curves of HS-Cork and HS-nCork specimens (Figure 5.7b) are above to the SEA curves of OCF, however below to the SEA curves of the Cork and nCork, demonstrating a higher specific energy absorption capacity.

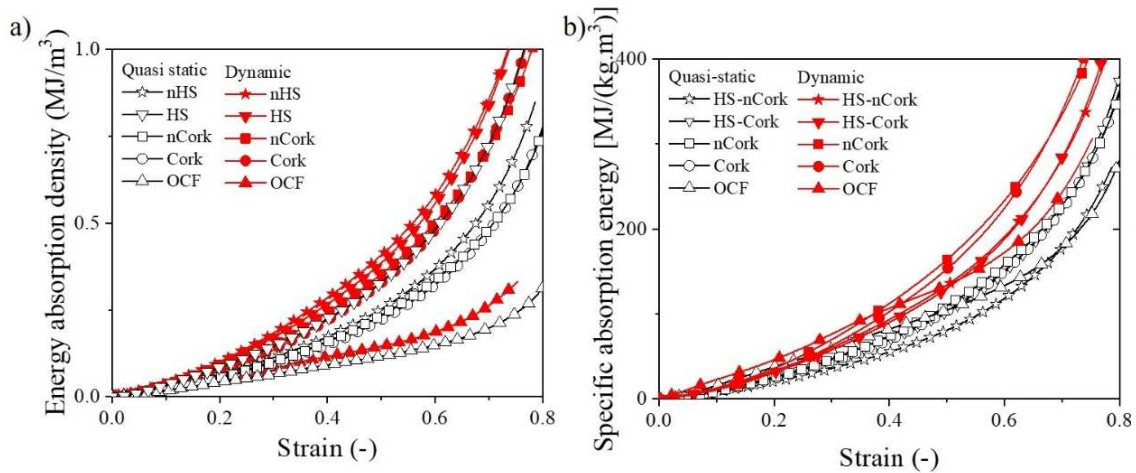


Figure 5.7 EAD (a) and SEA (b) curves of OCF, Cork, nCork, HS-Cork and HS-nCork for quasi-static and dynamic tests.

5.4.3. Sound absorption

The sound absorption coefficient values (α) of hybrid structures (HS-Cork and HS-nCork) and their individual components (OCF, Cork and nCork) between 100 and 4000 Hz are presented in Figure 5.8. Globally, the sound absorption coefficient of these specimens increases with the increase of frequency until it reached a peak (maximum value). After reaching the peak, the sound absorption coefficient starts to decrease. This sound absorption coefficient drop depends on the type of the specimens, being more pronounced in the HS-Cork (Figure 5.8). The results clearly show that the hybrid structures, in specially the HS-nCork exhibits excellent sound absorption in comparison with the individual components, reaching values of α close to 1. From the results, it is obvious that the sound absorption coefficients peaks occur in middle frequencies, between 1600 Hz and 1846 Hz for the four materials. The sound absorption coefficients peaks for the HS-nCork, HS-nCork, nCork and Cork are 0.9999(9) at 1846 Hz, 0.9900 at 1636 Hz, 0.861 at 1739 Hz and 0.682 at 1728 Hz, respectively. The maximum sound absorption coefficients of the nCork Hs are observed in the frequency range 1683 Hz–2093 Hz that keep α values close to 1 ($\alpha = 0.991$ at 1683 Hz and $\alpha = 0.985$ at 2093 Hz). Clearly, the OCF is a poor sound absorber, showing α close to 0, which means that it does not absorb any sound (0% absorption). This is due to foams are formed by open pores.

Cork materials are known to be good sound absorbers due to the viscous resistance between air molecules and its cell walls. A part of the sound energy is converted into thermal energy and be transmitted between adjacent cells which will help in faster dissipation of the converted sound energy [36]. On the other hand, the polymer-based binder (e.g. epoxy) has a more rigid structure, preventing the sound waves entering the structure leading to a reduction of the sound absorbing capability. The results also show that the presence of the GO enhanced the sound absorption of the hybrid structures and the cork. The variation of sound absorption peak can be explained by the microstructure features. This is also reported by other authors [37,38] that demonstrated that the GO nanosheets incorporated into agglomerated cork play a role in the sound absorption ability.

Results also indicated that the values of NRC of HS-Cork (0.50) and HS-nCork (0.55) are higher than individual components, Cork (0.4) and nCork (0.45) and OCF (0.05).

However, the use of NRC has its limitations, since the same value of NRC for two different materials does not mean that they perform the same way.

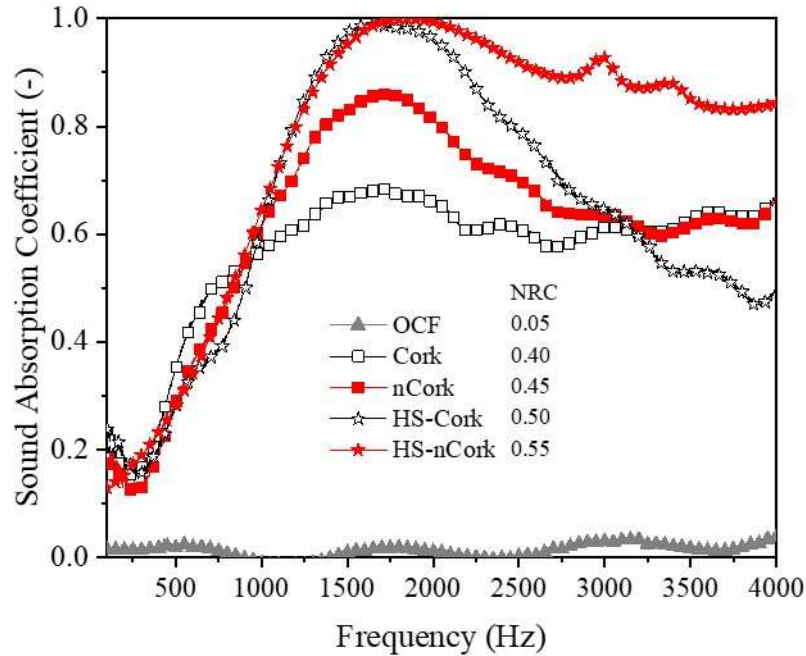


Figure 5.8 Sound absorption coefficient of the OCF, Cork, nCork, HS-Cork, HS-nCork.

5.4.4. Thermal conductivity

Table 5.3 shows the thermal conductivity and diffusivity values of OCF, Cork, nCork, HS-Cork and HS-nCork. Hot disk measurements were performed by assuming OCF, cork and cork hybrid structures as isotropic materials. This means that the structure of the materials is equal in all the directions. This is based on the literature [21], that reported that the agglomerated cork specimens having fine particles (< 0.7 mm), can be considered as isotropic materials for determining the thermal conductivity.

The results presented in Table 5.3 displayed that the hybrid structures, HS-Cork [0.091 W/(m·K)] and HS-nCork [0.101 W/(m·K)], have higher thermal conductivities values than the Cork [0.055 W/(m·K)] and nCork [0.055 W/(m·K)] specimens, however lower values than the OCF [1.611 W/(m·K)]. These are expected results, since aluminium is a metal with high thermal conductivity value [237 W/(m·K)]. The value of the OCF is 150 times lower than the dense aluminium since OCF is a highly porous material. The measured value is in accordance to the literature data. It is reported that the thermal

conductivity of open cell aluminium foams is usually between 1 W/(m·K) and 5 W/(m·K), depending of its characteristics [39].

The thermal conductivities of hybrid structures (HS-Cork and HS-nCork) increase of about 70 and 82% in relation with Cork and nCork, respectively. As expected, the aluminium network (OCF) incorporated within the cork confer to the specimens a path to heat transfer and thus high thermal conductivity values were obtained. Cork is well known by its low thermal conductivity, that makes them ideal to be used as thermal insulator. Cork agglomerates present thermal conductivities around 0.040–0.060 W/(m·K). The thermal conductivity of the agglomerated cork depends on the fabrication method and the particle/granules/grain size, polymer-based binder type and content and compacting pressure and its final density [21].

The values of thermal conductivity for Cork specimens with 155 kg/m³ of density is 0.055 W/m·K (Table 5.3). This is in agreement with the published data [21,40–43]. For agglomerated cork specimens with densities between 120 to 200 kg/m³, the thermal conductivity values are from 0.040 W/m·K to 0.060 W/m·K [21]. For agglomerated cork specimens having a density of 145 kg/m³ the thermal conductivity value is 0.04 W/m·K [40]. Roseta and dos Santos [42] obtained thermal conductivity values from 0.039 to 0.042 W/m·K for specimen (80 mm thickness) having densities between 100 and 120 kg/m³. Matias *et al.* [43] reported a maximum value of 0.049 W/(m K) for specimens (thickness range: 30–50 mm) with densities between 95 and 135 kg/m³.

Results showed that the incorporation of GO into the cork-based material (filler void) slightly increases the thermal conductivity of these specimens. The distortion of cell morphology with GO incorporation can decrease the amount of air trapped inside the cells, thus contributing to this increase.

The same trend in the thermal diffusivity values was observed since the presence of the OCF and GO increases the rate of heat propagation through the material. Although the OCF cell walls are mainly composed by aluminium, a high conductor material, they are highly porous and therefore the thermal diffusivity is not as high as for the hybrid structures [45].

Table 5.3 Thermal conductivity and thermal diffusivity of the OCF, Cork, nCork, HS-Cork, HS-nCork.

	Thermal conductivity (W/(m·K))	Thermal diffusivity (mm²/s)
OCF	1.611±0.075	0.450±0.009
Cork	0.055±0.0001	0.244±0.002
nCork	0.057±0.0002	0.248±0.003
HS-Cork	0.091±0.0004	0.773±0.014
HS-nCork	0.101±0.0004	1.795±0.023

5.4.5. Fire-retardancy tests

Cork presents slow combustion showing no smoke or toxic gases release [21], as observed in Figure 5.9. The fact of some flame propagation was observed in Figure 5.9a. This is due to the presence of the epoxy (EP) binder that is a well-known flammable polymer, burning easily with flame propagation. The results demonstrated that the incorporation of GO within the cork granules improves the fire response, by the quick extinction of the flame only after 2 s. The incandescent points (red points, Figure 5.9b) observed in the HS-nCork specimen, are related where the binder is located. This is in agreement with other works [18,19]. In the available literature, it is reported that the carbon nanostructures (e.g. GO) act as fire-retardants by creating a physical barrier and char layer on the surface of the material, avoiding or delaying the release of volatiles from the thermal decomposition [17,45].

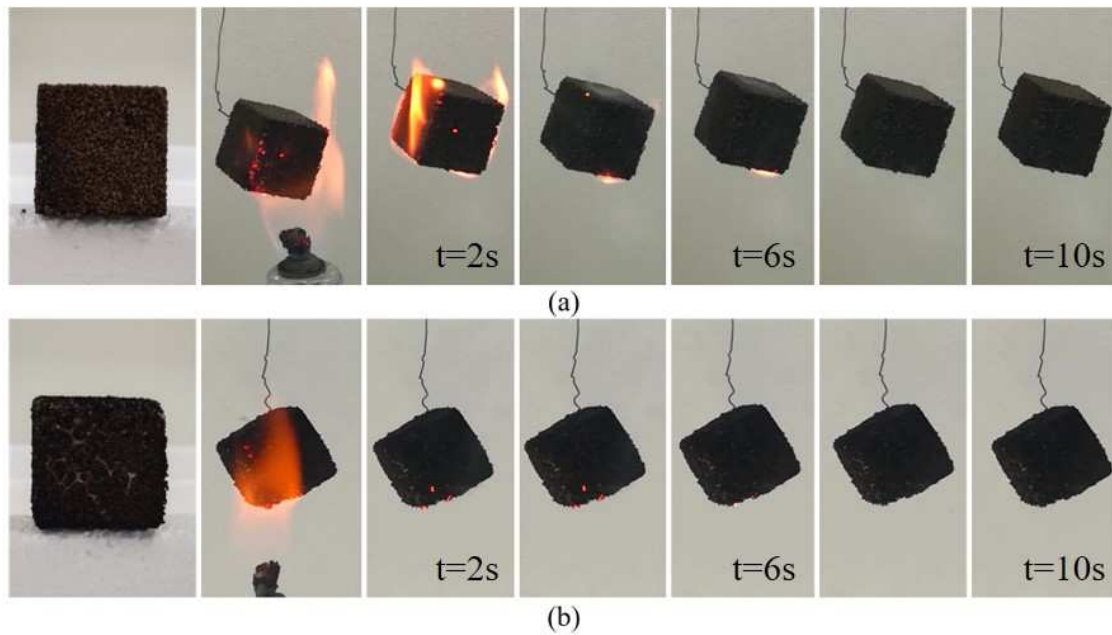


Figure 5.9 Flame response of the Cork (a) and HS-nCork (b).

5.5. Conclusions

The present study contributed to the development of a novel hybrid foam by combining two promising cellular materials, OCF and granulated cork, a natural sub-product of stoppers industry. The structural, mechanical, acoustic and thermal properties of the novel aluminium foam-cork hybrid structures and their individual components (OCF, Cork, nCork) were evaluated, exploring the GO as nanosized reinforcement of cork. The compressive response of these hybrid structures and their individual components under quasi-static and dynamic loading conditions was investigated, studying their deformation and failure modes. The results showed that:

- i) The GO sheets improve the sound absorption coefficient of the novel hybrid structures, conferring them fire-retardancy;
- ii) The GO sheets have a negative effect on the quasi-static and dynamic compressive behaviour of the hybrid structures;
- iii) The hybrid structures present higher values of EAD compared to the individual components, but presents lower values of SEA compared to Cork and nCork specimens for strain values above 0.4;

- iv) The hybrid structures are good sound absorption insulators that is improved with the incorporation of GO.
- v) The hybrid structures are good thermal insulators, with thermal conductivity around $0.1 \text{ W}/(\text{m}\cdot\text{K})$;
- vi) The cork agglomerates provides a natural, renewable alternative to traditional synthetic materials that combined with the OCF creates products with more functionality to be used in the building, automotive and aerospace industries.

5.6. References

- [1] H. P. Degischer and B. Kriszt, *Handbook of Cellular Metals: Production, Processing, Applications*. Wiley, 2002.
- [2] J. Banhart, "Manufacture, characterisation and application of cellular metals and metal foams," *Prog. Mater. Sci.*, vol. 46, no. 6, pp. 559–632, Jan. 2001.
- [3] I. Duarte, L. Krstulović-Opara, and M. Vesenjak, "Axial crush behaviour of the aluminium alloy in-situ foam filled tubes with very low wall thickness," *Compos. Struct.*, vol. 192, pp. 184–192, 2018.
- [4] I. Duarte, M. Vesenjak, L. Krstulović-Opara, and Z. Ren, "Static and dynamic axial crush performance of in-situ foam-filled tubes," *Compos. Struct.*, vol. 124, pp. 128–139, 2015.
- [5] B. J. and S. H.-W., "Aluminium Foam Sandwich Panels: Manufacture, Metallurgy and Applications," *Adv. Eng. Mater.*, vol. 10, no. 9, pp. 793–802.
- [6] D. Lehmhus, M. Busse, A. Herrmann, and K. Kayvantash, *Structural Materials and Processes in Transportation*. Wiley, 2013.
- [7] I. Duarte, M. Vesenjak, L. Krstulović-Opara, and Z. Ren, "Crush performance of multifunctional hybrid foams based on an aluminium alloy open-cell foam skeleton," *Polym. Test.*, vol. 67, pp. 246–256, 2018.
- [8] Z. Wang, J. Gao, K. Chang, L. Meng, N. Zhang, and Z. Guo, "Manufacturing of open-cell aluminum foams via infiltration casting in super-gravity fields and mechanical properties," *RSC Adv.*, vol. 8, no. 29, pp. 15933–15939, 2018.
- [9] K. Stöbener, D. Lehmhus, M. Avalle, L. Peroni, and M. Busse, "Aluminum foam-polymer hybrid structures (APM aluminum foam) in compression testing," *Int. J. Solids Struct.*, vol. 45, no. 21, pp. 5627–5641, 2008.
- [10] I. Duarte, M. Vesenjak, L. Krstulović-Opara, and Z. Ren, "Compressive performance evaluation of APM (Advanced Pore Morphology) foam filled tubes," *Compos. Struct.*, vol. 134, pp. 409–420, 2015.
- [11] O. Friedl, C. Motz, H. Peterlik, S. Puchegger, N. Reger, and R. Pippan, "Experimental Investigation of Mechanical Properties of Metallic Hollow Sphere Structures," *Metall. Mater. Trans. B*, vol. 39, no. 1, pp. 135–146, 2008.
- [12] M. Reinfried, G. Stephani, F. Luthardt, J. Adler, M. John, and A. Krombholz, "Hybrid Foams - A New Approach for Multifunctional Applications," *Adv. Eng. Mater.*, vol. 13, no. 11, pp. 1031–1036, Nov. 2011.

- [13] I. Duarte, M. Vesenjak, and L. Krstulovic, "Static and dynamic axial crush performance of in-situ foam-filled tubes," vol. 124, pp. 128–139, 2015.
- [14] M. Vesenjak, L. Krstulović-Opara, and Z. Ren, "Characterization of photopolymer cellular structure with silicone pore filler," *Polym. Test.*, vol. 31, no. 5, pp. 705–709, 2012.
- [15] S. C. Pinto et al., "Characterization and physical properties of aluminium foam–polydimethylsiloxane nanocomposite hybrid structures," *Compos. Struct.*, vol. 230, p. 111521, Dec. 2019.
- [16] S. C. Pinto et al., "Mechanical, Thermal, and Acoustic Properties of Aluminum Foams Impregnated with Epoxy/Graphene Oxide Nanocomposites," *Metals (Basel)*, vol. 9, no. 11, p. 1214, Nov. 2019.
- [17] B. Sang, Z. Li, X. Li, L. Yu, and Z. Zhang, "Graphene-based flame retardants : a review," *J. Mater. Sci.*, vol. 51, no. 18, pp. 8271–8295, 2016.
- [18] L. Gil, "Cork Composites: a Review," *Materials (Basel)*, pp. 776–789, 2009.
- [19] L. Gil, "New Cork-Based Materials and Applications," *Materials (Basel)*, vol. 8, no. 2, pp. 625–637, 2015.
- [20] C. Barreca, F and Fichera, "Thermal insulation performance assessment of agglomerated cork boards," *Wood Fiber Sci.*, vol. 48, no. 2, 2016.
- [21] V. Santos, T., Amaral, JS., Costa, AF and Amaral, "Thermal Conductivity of Agglomerate Cork," in *Cork Science and its Applications*, Millersville PA: Materials Research Forum LLC., 2017, pp. 1–10.
- [22] J. Sargianis, H. Kim, and J. Suhr, "Natural Cork Agglomerate Employed as an Environmentally Friendly Solution for Quiet Sandwich Composites," *Sci. Rep.*, vol. 2, p. 403, May 2012.
- [23] F. A. O. Fernandes, R. T. Jardim, A. B. Pereira, and R. J. A. de Sousa, "Comparing the mechanical performance of synthetic and natural cellular materials," *Mater. Des.*, vol. 82, pp. 335–341, 2015.
- [24] S. Knapic, V. Oliveira, J. S. Machado, and H. Pereira, "Cork as a building material: a review," *Eur. J. Wood Wood Prod.*, vol. 74, no. 6, pp. 775–791, 2016.
- [25] J. Sierra-Pérez, J. Boschmonart-Rives, and X. Gabarrell, "Production and trade analysis in the Iberian cork sector: Economic characterization of a forest industry," *Resour. Conserv. Recycl.*, vol. 98, no. Complete, pp. 55–66, 2015.
- [26] O. Anjos, C. Rodrigues, J. Morais, and H. Pereira, "Effect of density on the compression behaviour of cork," *Mater. Des.*, vol. 53, pp. 1089–1096, 2014.
- [27] O. Castro, J. M. Silva, T. Devezas, A. Silva, and L. Gil, "Cork agglomerates as an ideal core material in lightweight structures," *Mater. Des.*, vol. 31, no. 1, pp. 425–432, 2010.
- [28] I. Duarte and J. M. F. Ferreira, "Composite and Nanocomposite Metal Foams," *Materials (Basel)*, vol. 9, no. 2, p. 79, Feb. 2016.
- [29] A. Mancuso, G. Pitarresi, and D. Tumino, "Mechanical Behaviour of a Green Sandwich Made of Flax Reinforced Polymer Facings and Cork Core," *Procedia Eng.*, vol. 109, pp. 144–153, 2015.
- [30] P. T. Santos, S. Pinto, P. A. A. P. Marques, A. B. Pereira, and R. J. A. de Sousa, "Agglomerated cork: A way to tailor its mechanical properties," *Compos. Struct.*, vol. 178, pp. 277–287, 2017.

- [31] “ISO 22007-2.2. Plastics - Determination of thermal conductivity and thermal diffusivity - Part 2: Transient plane heat source (hot disc) method.”
- [32] “ASTM E1050-12 Standard Test Method for Impedance and Absorption of Acoustical Materials Using a Tube, Two Microphones and a Digital Frequency Analysis System.”
- [33] M. Ptak et al., “Graphene-Enriched Agglomerated Cork Material and Its Behaviour under Quasi-Static and Dynamic Loading,” *Materials (Basel)*, vol. 12, no. 1, p. 151, Jan. 2019.
- [34] P. Schüller, S. F. Fischer, A. Bührig-Polaczek, and C. Fleck, “Deformation and failure behaviour of open cell Al foams under quasistatic and impact loading,” *Mater. Sci. Eng. A*, vol. 587, pp. 250–261, 2013.
- [35] M. Vesenjajk, L. Krstulović-Opara, and Z. Ren, “Characterization of irregular open-cell cellular structure with silicone pore filler,” *Polym. Test.*, vol. 32, no. 8, pp. 1538–1544, 2013.
- [36] N. Gama, R. Silva, A. P. O. Carvalho, A. Ferreira, and A. Barros-Timmons, “Sound absorption properties of polyurethane foams derived from crude glycerol and liquefied coffee grounds polyol,” *Polym. Test.*, vol. 62, pp. 13–22, 2017.
- [37] A. Arjunan, A. Baroutaji, A. S. Praveen, A. G. Olabi, and C. J. Wang, “Acoustic Performance of Metallic Foams,” in *Reference Module in Materials Science and Materials Engineering*, Elsevier, 2019.
- [38] J. M. Kim, D. H. Kim, J. Kim, J. W. Lee, and W. N. Kim, “Effect of graphene on the sound damping properties of flexible polyurethane foams,” *Macromol. Res.*, vol. 25, no. 2, pp. 190–196, Feb. 2017.
- [39] R. Dyga and S. Witczak, “Investigation of Effective Thermal Conductivity Aluminum Foams,” *Procedia Eng.*, vol. 42, pp. 1088–1099, 2012.
- [40] M. Pedroso, J. de Brito, and J. D. Silvestre, “Characterization of eco-efficient acoustic insulation materials (traditional and innovative),” *Constr. Build. Mater.*, vol. 140, pp. 221–228, 2017. pedroso
- [41] B. P. Jelle, “Traditional, state-of-the-art and future thermal building insulation materials and solutions – Properties, requirements and possibilities,” *Energy Build.*, vol. 43, no. 10, pp. 2549–2563, Oct. 2011.
- [42] S. Knapic, C. P. dos Santos, H. Pereira, and J. S. Machado, “Performance of Expanded High-Density Cork Agglomerates,” *J. Mater. Civ. Eng.*, vol. 29, no. 2, p. 04016198, Feb. 2017.
- [43] C. Barreca, F. and Fichera, “Thermal Insulation Performance assessment of Agglomerated Cork Boards,” *Wood Fiber Sci.*, vol. 48, no. 2, pp. 1–18, 2016.
- [44] M. Roseta and C. P. dos Santos, “Study in Real Conditions and in Laboratory of the Application of Expanded Agglomerated Cork as Exterior Wall Covering,” *Key Eng. Mater.*, vol. 634, pp. 367–378, Dec. 2014.
- [45] L. Matias, C. Santos, M. Reis, and L. Gil, “Declared value for the thermal conductivity coefficient of insulation corkboard,” *Wood Sci. Technol.*, vol. 31, no. 5, pp. 355–365, 1997.
- [46] N. V. Gama et al., “Bio-based polyurethane foams toward applications beyond thermal insulation,” *Mater. Des.*, vol. 76, pp. 77–85, 2015.

[47] N. V Gama et al., “Enhancement of physical and reaction to fire properties of crude glycerol polyurethane foams filled with expanded graphite,” *Polym. Test.*, vol. 69, pp. 199–207, 2018.

Chapter 6. Characterization and physical properties of aluminium foam–polydimethylsiloxane nanocomposite hybrid structures

This chapter was based in the following published paper:



Composite Structures
Volume 230, 15 December 2019, 111521



Characterization and physical properties of aluminium foam–polydimethylsiloxane nanocomposite hybrid structures

Susana C. Pinto ^a, Paula A.A.P. Marques ^a, Matej Vesenjak ^b, Romeu Vicente ^c, Luís Godinho ^d, Lovre Krstulović-Opara ^e, Isabel Duarte ^a  

 [Show more](#)

<https://doi.org/10.1016/j.compstruct.2019.111521>

[Get rights and content](#)

6.1. Abstract

This chapter reports on the fabrication and characterization of simple and nanocomposite polydimethylsiloxane-aluminium hybrid structures, which are prepared by impregnating an aluminium open-cell foam (OCF) with only polydimethylsiloxane (PDMS) and PDMS reinforced with graphene oxide (GO), respectively. The effect of the PDMS and the GO on the mechanical, thermal, acoustic absorption and fire retardancy properties of the resulting hybrid structures were studied and compared to the individual components (simple PDMS and nanocomposite polydimethylsiloxane (nPDMS), OCF). Results demonstrate that the use of the PDMS cured at 65 °C, as void filler of the OCF changes from rubbery to brittle behaviour, reaching a high level of strength (quasi-static: ~5 MPa; dynamic: > 15 MPa) in the resulting hybrid structures, due to the low chain mobility of the polymer and effective adhesion with struts of the OCF. Furthermore, these simple and nanocomposite hybrid structures are extremely sensitive to strain-rate, exhibiting a maximum compressive stress increase of more than 300 % and 200 %, respectively. The presence of the GO within the PDMS ensures the non-flammability of the hybrid structures and increases the sound absorption coefficient.

6.2. Introduction

The search for high-performance lightweight multifunctional materials has increasingly become a target for commercial, industrial and military purposes [1]. Solid cellular (porous) materials [2,3] and nanocomposites [4,5] are examples of these multifunctional materials. Both have tremendous potential to develop high-performance structural components, reducing weight, while improving efficiency, safety and versatility. They offer notable properties and functionalities, which cannot be achieved with the traditional materials. The properties of the solid cellular metals result from their porous cellular structures (open or closed cells) together with the properties of the metal they are made of [6]. Open-cell foams are used as functional materials, e.g. as filters, batteries, electrodes, heat exchangers and biomedical implants, while the closed-cell foams are used as structural materials as lightweight impact energy and sound absorbers, e.g. in construction, vehicles, devices and other equipment [7]. In the last decades, several cellular metals have been developed in order to achieve the control of the size and shape of the cells. It is possible to distinguish two main

groups: stochastic and periodic cellular metals [3]. Stochastic cellular metals exhibit irregular cellular structures [8]. The stochastic cellular metals cannot be characterized by a single unit cell, which makes difficult to predict their final properties. Closed-cell metal foams prepared by direct [9] and indirect [10] foaming methods are examples of stochastic foams. To overcome this problem, periodic cellular metals are being developed in order to establish the relationship between the cellular structures and the properties. Syntactic foams are an example of periodic cellular metals with an easily reproducible unit cell, which are prepared by incorporating porous particles or hollow spheres made of ceramic or metal into the metallic matrix [11,12]. The porous particles or hollow spheres are packed into a predefined random dense arrangement and a molten metal is infiltrating through the interstitial spaces between the particles or hollow spheres. Periodic cellular structures with complex topologies and graded materials prepared by additive manufacturing technologies (e.g. 3D printing, laser sintering) have been also developed and tested [13–15]. Despite their properties can be easily tailored with a specific control of their topologies, some of the tailored cellular metals (density greater than 1g/cm^3) have a higher density compared to the stochastic foams (density less than 1g/cm^3) that might limit their application [16]. More recently, cellular composites and cellular nanocomposites [17] have been developed, in which the metallic bulk matrix is reinforced by micro (e.g. ceramic particles) [18] and nano-sized reinforcements (e.g. carbon nanotubes) [19] mainly for enhancing the mechanical properties [17]. Recently, based on the multi-material concept, hybrid structures have been developed by combining the periodic open-cell aluminium foams (OCF) [20–25] or APM foam elements [26–30] with polymers in which the voids of an OCF foams are completely infiltrated with a polymer. Results have demonstrated that the polymer lead to an enhancement of the compressive strength and energy absorption of the resulting hybrid structures compared to the conventional OCF. The level of enhancement strongly depends on the stiffness of the polymer. The results have also indicated that the deformation and failure modes of these hybrid structures strongly depend on the chemical nature of the polymer [24–25]. For example, the silicone rubber (gel-like material) promotes non-symmetric deformation, while the brittle epoxy resin promotes symmetric deformation [24–25]. Herein, new polymer-OCF hybrid structures were developed, fabricated and analysed to assess their mechanical, thermal, acoustic and fire-retardant properties. More specifically, polydimethylsiloxane (PDMS) and polydimethylsiloxane nanocomposites (nPDMS) were

used as void fillers of simple OCF. The effect of the GO in the polymer matrix on the mechanical, thermal, acoustic and fire-retardant properties of the resulting hybrid structures was investigated and compared to the individual components.

6.3. Materials and Methods

6.3.1. Materials

The polydimethylsiloxane (PDMS) Sylgard® 184 was supplied by Dow Corning comprising of two components: a liquid silicone rubber base and a curing agent. An aqueous solution of 4 mg/mL graphene oxide (GO) was provided by Graphenea (Spain). To prepare the PDMS–OCF hybrid structure (HS-PDMS) and PDMS nanocomposite – OCF hybrid structure (HS-nPDMS) specimens, square ($22 \times 22 \times 25 \text{ mm}^3$) and cylindrical (diameter: 37 mm; height: 22 mm) open-cell Al alloy foams (OCF) specimens with pore sizes of 10 ppi (pores per inch) were cut from foam blocks made of AlSi7Mg0.3 ($300 \times 150 \times 150 \text{ mm}^3$) fabricated by the investment casting method [24]. Thin walled tubes made of Al alloy AA6060 T66 (0.35–0.60% Mg; 0.3–0.6% Si; 0.1% Cu; 0.1% Mn; 0.05% Cr; 0.15% Zn; 0.1%Ti) with the inner diameter of 22 mm and thickness of 1.5 mm. Cylindrical moulds made of Al alloy AA6060 T66 with the inner diameter of 50 mm and height of 25 mm were also manufactured for acoustic absorption specimens.

6.3.2. Specimen fabrication

Within this study, four different types of square and cylindrical specimens were prepared: dense PDMS specimens, dense PDMS reinforced with 0.25 wt.% graphene oxide (nPDMS) specimens, PDMS-OCF hybrid structure (HS-PDMS) specimens and PDMS nanocomposite-OCF hybrid structure (HS-nPDMS) specimens. The PDMS specimens were prepared by filling a mould with liquid PDMS mixture prepared by mixing the liquid silicone rubber base with curing agent (component mixing ratio ~ 10:1 in wt.%) in a vacuum chamber for 30 min. After this period, the mould containing the liquid PDMS mixture was placed in a pre-heated furnace and cured at 65 °C for 4 h. For preparing the nPDMS specimens, the GO was dispersed into the PDMS matrix by ultrasonic and mechanical stirring. For that, the liquid PDMS liquid was first well mixed together with 0.25 wt.% of GO using a mechanic stirrer at 1000 rpm for 1 h. The resulting liquid nPDMS mixture was submitted for 30 min into an ultrasonic bath during 1 h approximately. Then, the curing agent was added, mixed and degassed under a vacuum chamber for 30 min. Finally, the resulting liquid nPDMS

mixture was poured into a mould (square or cylindrical), followed by the curing process at 65 °C for 4 h. Figure 6.1 shows the Scanning Electron Microscope (SEM) images of PDMS (Figure 6.1a) and nPDMS (Figure 6.1b) matrices assessed by Hitachi TM 4000 Plus using 15 kV voltage with different magnifications. The SEM images clearly show the sheets of the GO (Figure 6.1b) in the PDMS matrix.

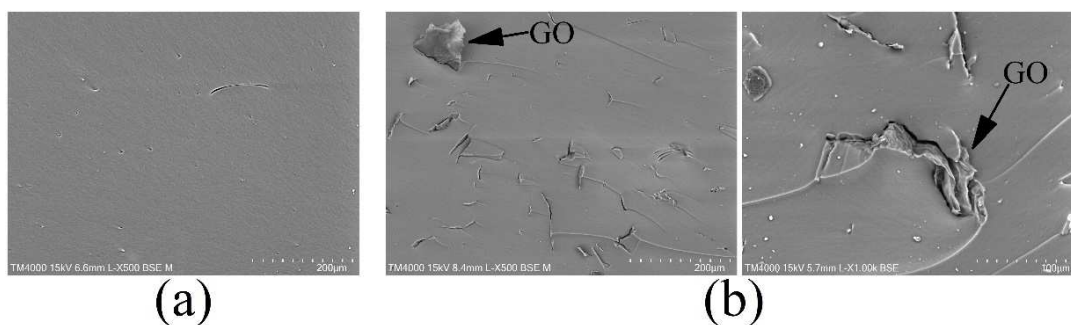


Figure 6.1 SEM images of the matrices of PDMS (a) and nPDMS matrices (b).

The hybrid structure (HS-PDMS and HS-nPDMS) specimens were prepared by previously inserting an OCF into the mould, followed by pouring and curing of the liquid polymer mixture (simple PDMS and nPDMS). The HS-PDMS or HS-nPDMS were cured at 65 °C for 4 h. The resulting HS-PDMS and HS-nPDMS were extracted from the mould after the polymer filler cured completely. For easily extracting, the inner surface of the mould was previously cleaned, polished and greased before inserting the OCF specimen. Figure 6.2 shows the fabricated specimens: conventional OCF (Figure 6.2a), simple dense PDMS (Figure 6.2b), dense nPDMS (Figure 6.2c), HS-PDMS (Figure 6.2d) and HS-nPDMS (Figure 6.2e).

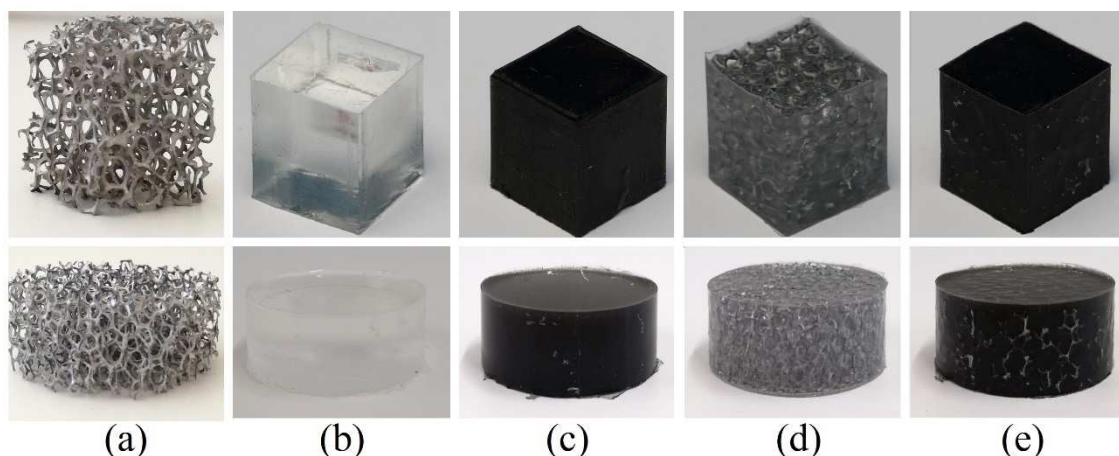


Figure 6.2 Square and cylindrical specimens: OCF (a), dense PDMS (b), nPDMS (c), HS-PDMS (d) and HS-nPDMS (e).

The average bulk densities for conventional OCF, dense PDMS, dense nPDMS, HS-PDMS and HS-nPDMS are: 943 kg/m³ (std. deviation: 31.1 kg/m³), 1076 kg/m³ (std. deviation: 24.8 kg/m³), 1068 kg/m³ (std. deviation: 12.1 kg/m³), 1087 kg/m³ (std. deviation: 32.3 kg/m³) and 1090 kg/m³ (std. deviation: 4.5 kg/m³), respectively.

6.3.3. Thermogravimetric analysis

The thermal stability of the PDMS and nPDMS matrices was assessed by a thermogravimetric analyser (Shimadzu TGA-50) at a scanning rate of 10 °C/min in the temperature range between 30 and 800 °C under an oxidative atmosphere (air).

6.3.4. Mechanical tests

The compressive behaviour of the HS-PDMS and HS-nPDMS specimens and their individual components (PDMS, nPDMS and OCF) were studied using a servo-hydraulic dynamic INSTRON 8801 testing machine (maximum load 50 kN) at crosshead rates of 0.1 mm/s (quasi-static) and 284 mm/s (dynamic). The high-resolution video camera Sony HDR-SR8 and the mid-wave infrared (IR) cooled thermal camera Flir SC 5000 [31] were used to record the quasi-static and dynamic tests in order to follow the deformation and failure modes of the specimens. The temperature (heat) distribution on the specimen surface and the plastification front propagation can be efficiently observed by IR thermography to detect plastification zones in structures based on cellular metals [31]. The weight, width and height of each specimen were measured to calculate the density (weight/volume). The recorded load-displacement data were converted to stress-strain data. The engineering stress and engineering strain values were determined by dividing the load with the initial cross-section and by dividing the displacement with the initial specimen height, respectively. The energy absorption density (EAD) curves and the specific energy absorption (SEA) values were according to the ISO 13314: 2011 calculated by integrating the engineering stress-strain curves (from 0 up to the strain at the end of each test) and by dividing the EAD values by the specimen mass, respectively.

6.3.5. Thermal tests

The thermal conductivity properties of different types of specimens were evaluated with a Hot Disk TPS 2500 S instrument using the transient plane source method at room temperature according to the standard ISO 22007-2.2 [32] and ASTM D7984 [33]. During

the experiment, a small constant current is applied to the sensor inserted between two identical specimens. Since the temperature increase of the sensor is highly dependent on the two tested samples attached to it, thermal properties of the tested samples can be determined by monitoring the temperature increase for a short time period. For the measurements one pair of identical samples per material is tested at room temperature and five replicate measurements are conducted.

6.3.6. Acoustic tests

The sound absorption coefficient and sound absorption efficiency of the OCF, PDMS, nPDMS, HS-PDMS and HS-nPDMS specimens was evaluated using an impedance tube according to the standard ASTM E 1050 [34]. The cylindrical specimen was placed into the testing impedance tube with the inner diameter of 37 mm at one end. The other end of the tube was positioned at the sound source that consists of an RG10 noise generator, emitting a random noise. Two microphones were placed into the tube between the sound source and the specimen to detect the sound pressure wave transmitted through the specimen and the portion of the wave that was reflected. The acoustic absorption coefficient (α) is defined as a ratio of absorbed sound intensity in a given material and the incident sound intensity that is imposed on that material. The sound absorption coefficient varies with the frequency. The α varies from 0 (0 % sound absorption) to 1 (100 % sound absorption). The value 0 means no sound is absorbed, while the value 1 means all sound energy is absorbed. For example, a material that has an acoustic absorption coefficient of 0.5 at a given frequency, absorbs half of the sound and either reflects or passes the rest. The materials with a sound absorption coefficient equal to or higher than 0.5 are usually considered efficient sound absorption materials [35]. The noise reduction coefficient (NRC) is another parameter used to evaluate the sound absorption characteristics of a material. The NRC is calculated by defining an average of the sound absorption coefficients at the frequencies 250 Hz, 500 Hz, 1000 Hz and 2000 Hz and rounding off the result to the nearest multiple of 0.05. However, it should be noted that the same value of NRC for two different materials does not mean that they perform in the same way.

6.3.7. Flammability tests

The fire retardancy tests were based on the direct observation of the specimen responses when subjected to a flame source. The tests consisted of applying an ethanol flame at the

specimen's bottom using the set-up in vertical sample position for 3 s plus the subsequent 3 s for observing the self-extinguishment.

6.4. Results and discussion

6.4.1. Thermal properties

Figure 6.3 shows the TG and the corresponding DTG curves of PDMS and nPDMS samples in air.

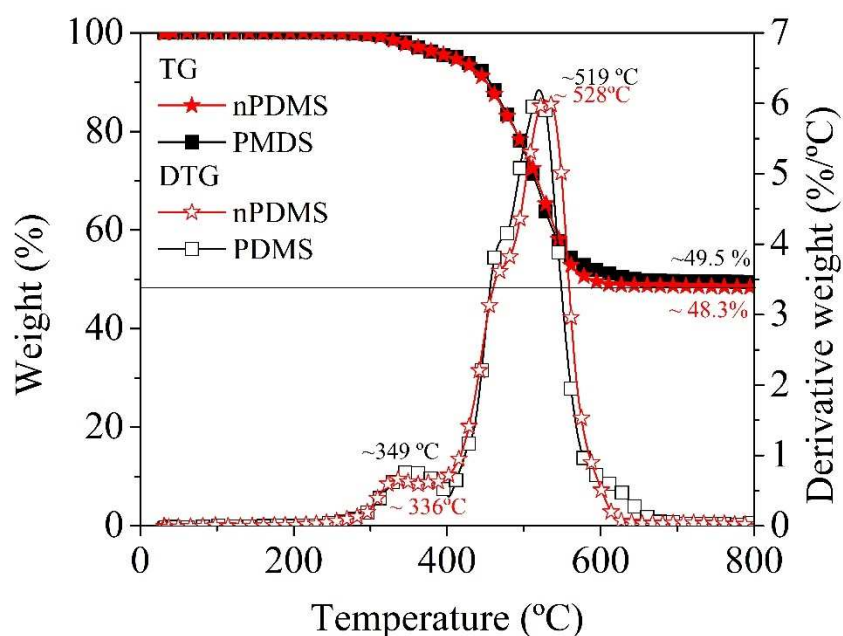


Figure 6.3 TG/DTG of the PDMS and nPDMS matrices.

The shape of the TG/DTG curves is identical for both PDMS and nPDMS specimens. From room temperature to 270 °C, the weight loss is negligible. Then two distinct degradation steps were observed. After an initial gradual weight loss, a significant weight loss was observed above 400 °C, corresponding to a high peak in the DTG curves. After ~600 °C, the weight loss remained constant. The total weight loss of PDMS and nPDMS was 49.5% and 48.3%, respectively. Both specimens showed a two-stage degradation processes in which DTG curves show the initial peak at 349 °C and 336 °C, followed by the next peak at 519 °C and 528 °C for the PDMS and nPDMS, respectively. This two-stage oxidative degradation process was reported by Camino *et al.* [36]. They proposed that the

oxygen catalyses the depolymerization reaction of PDMS to volatile cyclic oligomers, leading to a lower temperature when the weight starts to decrease. The small difference in the curves TG/DTG is due to the interaction between the GO and the molecule chains of silicon rubber. It seems to decrease of the total weight loss of the resulting PDMS nanocomposites. With the addition of the GO, the maximum DTG is located at a higher temperature (528 °C), suggesting a slight improvement in the thermal stability.

6.4.2. Compressive behaviour

6.4.2.1. Compression behaviour of PDMS and nPDMS

Figure 6.4 shows the compressive deformation and failure modes (Figure 6.4a) and the stress-strain curves (Figure 6.4b) of simple dense PDMS and nPDMS specimens subjected to quasi-static and dynamic loading conditions.

The results clearly show that the deformation and failure modes of the PDMS changed due to the presence of the GO within the polymer matrix (Figure 6.4a) and due to the loading velocity. Under quasi-static compression, the simple PDMS exhibited a symmetric deformation, showing a barrelling in the centre of the specimen, accompanied by the propagation of several internal cracks formed during the uniaxial compression, followed by the brittle failure of the specimens (quasi-static loading, Figure 6.4a). On the other hand, the simple nPDMSs under quasi-static compression displayed an initial symmetric deformation that changed to an unstable non-symmetric deformation accompanied by the tilting of the specimen (strains above 0.5, Figure 6.4a), followed by the brittle failure of the specimens leading to its disintegration. From IR image sequences for the PDMS and nPDMS under dynamic loading conditions (Figure 6.4a), it can be concluded that the specimens deform in an identical deformation and failure mode, but very different in comparison to quasi-static loading condition (Figure 6.4a). No tilting of the specimens was observed during the compression tests performed under dynamic loadings as it was the case for the nPDMS specimen compressed under quasi-static loading conditions. The deformation and failure modes of the PDMS and nPDMS specimens are directly related to the diagram shape of the measured stress–strain curves (Figure 6.4).

The shape of the PDMSs and nPDMSs curves is identical (Figure 6.4b) and can be divided into three main regions: initial linear elastic response at small strains, followed by a nonlinear increase in stress up to the maximum compressive stress (peak stress) and a drop stress

before failure. The region, where the stress starts drastically to decrease is characterized by unstable oscillations in stress when the specimens were subjected to dynamic loading conditions.

The experimental results also reveal that PDMS and nPDMS are highly sensitive to strain-rate, exhibiting an obvious positive strain rate sensitivity. The dynamic compressive curves (red curves, Figure 6.4b) of PDMS and nPDMS are much higher in comparison to the curves at quasi-static loading (black curves, Figure 6.4b). For example, the peak stresses for PMDS specimens are 32.91 MPa (quasi-static) and 71.42 MPa (dynamic), while for nPDMSs specimens, they are 30.21 MPa (quasi-static) and 54.92 MPa (dynamic), as illustrated in Table 6.1. These represent percentage increases of 117 % and 82 % for PMDS and nPDMS specimens, respectively.

Table 6.1 Compressive results of PDMS and nPDMS specimens.

Specimen	Loading conditions	Density	Peak		Decay		
			Strain (-)	Stress (MPa)	Strain (-)	Stress (MPa)	
PDMS	Quasi static	1056	0.71	40.11	0.73	1.58	
		1073	0.62	22.44	0.68	1.12	
		1092	0.67	36.19	0.68	0.79	
		Average	1074	0.67	32.91	0.70	1.16
St Dev	18.0	0.04	9.28	0.03	0.39		
PDMS	Dynamic	1039	0.81	96.80	-	-	
		1094	0.71	61.40	0.75	43.05	
		1103	0.71	56.06	0.75	39.82	
		Average	1079	0.75	71.42	0.75	41.44
		St Dev	34.7	0.05	22.14	0.00	2.28

Table 6.1 *Cont.*

Specimen	Loading conditions	Density	Peak		Decay		
			Strain (-)	Stress (MPa)	Strain (-)	Stress (MPa)	
nPDMS	Quasi-static	1060	0.68	33.26	0.70	1.16	
		1068	0.68	32.25	0.69	1.14	
		1079	0.64	25.12	0.69	1.37	
		Average	1069	0.67	30.21	0.70	1.22
St Dev	9.5	0.02	4.44	0.01	0.13		
nPDMS	Dynamic	1047	0.69	47.94	0.72	35.85	
		1075	0.70	54.12	0.74	32.49	
		1076	0.74	62.71	0.76	35.59	
		Average	1066	0.71	54.92	0.74	34.64
		St Dev	15	0.03	7.42	0.02	1.87

From these experimental results, it could be also noticed that the PMDS specimens present a higher compressive strength compared to the nPDMS. After the first peak stress (Figure 6.4b), the PDMSs and nPDMSs specimens subjected to the quasi-static loading conditions quickly reached very low values of stress (PDMS: ~1.16 MPa; nPDMS: ~1.22 MPa) without stress oscillations, while the specimens subjected to the dynamic loading conditions exhibited several stress oscillations. Clearly, the compressive behaviour of the PDMS specimens subjected to the dynamic loading was changed with the presence of the GO within the PDMS matrix. The presence of the GO leads to lower values of the peak stress but provides for a recoverable deformation after the first peak stress, showing a strong non-linear behaviour. For the nPDMS specimens, the stress increases (~12.95 MPa) up to the strain of ~0.7 (Figure 6.4b). The mechanical response of these specimens is related to their chemical nature [36–39].

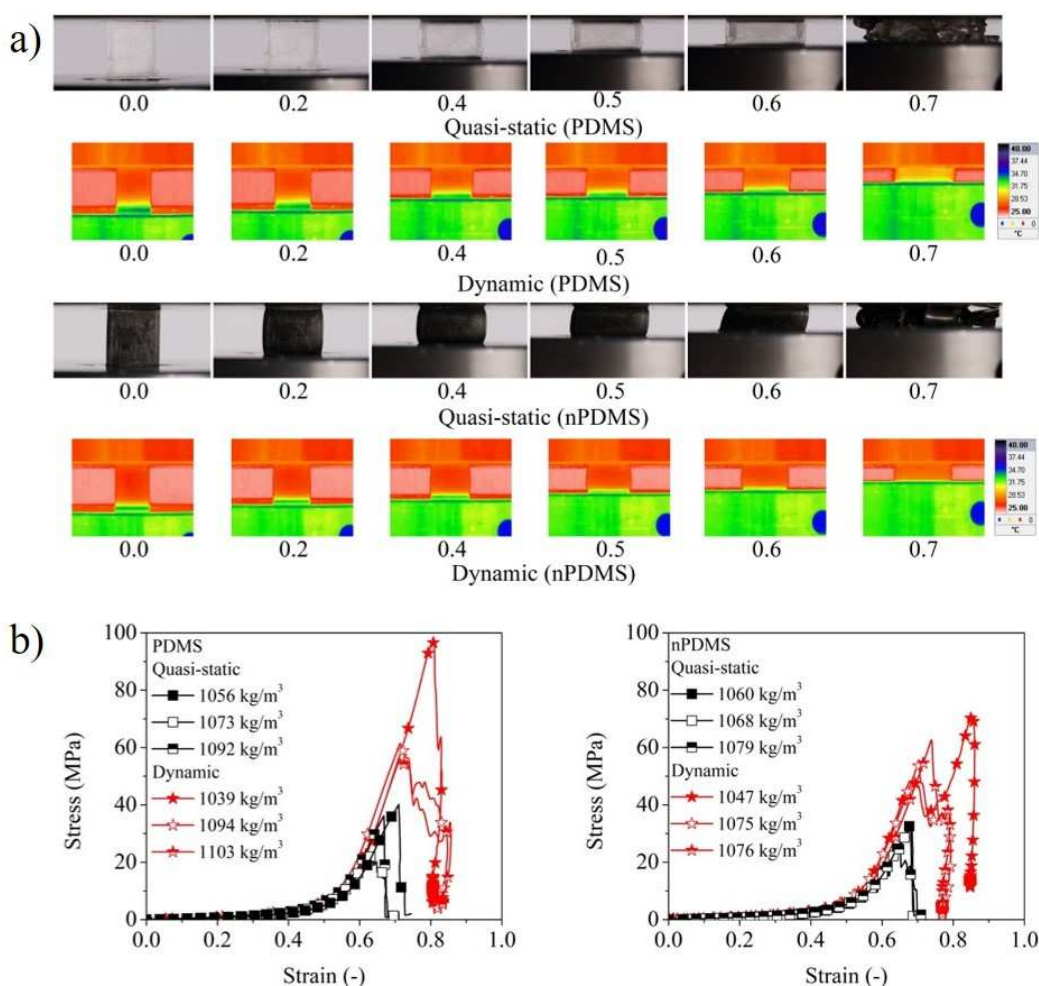


Figure 6.4 Compressive deformation (a) and stress–strain curves (b) of dense PDMS and nPDMS specimens at quasi-static and dynamic loading conditions.

As it well known, the mechanical response of a polymer depends on the temperature, strain rate and loading conditions. In particular, the mechanical response of most polymer rubbers (e.g. PDMS) may change from rubbery (elasticity) to ductile (plasticity) or even to brittle due to temperature and strain rate changes. These polymers exhibit large and recoverable strain hardened deformation. In fact, the PDMS became softer and could be compressed further without fracture and failure. Such unique mechanical properties of elastomers are related to the 3D network structure (comprising of long and flexible polymer chains) that is characterized by several parameters, such as the length of the network strands, functionality of cross-links and the number of entanglements, dangling chains and loops. The PDMS is considered as one of the most flexible polymers. Their high flexibility can be explained by the structural features of the Si–O bonds that have a longer bond length, larger

bond angle and significantly lower torsional potential than C–C bonds. This leads to a very low glass transition temperature for the PDMS. The PDMS experiences crystallization at substantially low temperatures (below 30 °C). No strain-induced crystallization at room temperature is observed for the cross-linked PDMS and they behave as elastomers. The mechanical strength of the specimens was enhanced by decreasing the hybrid structure density. The drop-in stress for dense specimens subjected to dynamic loading conditions is much lower (PDMS: 42 %; nPDMS: 36.9 %) compared to those subjected to quasi-static loading conditions (PDMS: 96.5 %; nPDMS: 96 %).

6.4.2.2. Compression behaviour of OCF

The compressive deformation and failure modes (Figure 6.5a) and stress-strain curves (Figure 6.5b) of simple OCF specimens are shown in Figure 6.5.

As expected, the compressive response of OCF specimens is divided into three regions [24]: elastic, plateau and densification. In the initial elastic region, the deformation of the foam is controlled by the deformation of the pore walls due to bending and buckling, followed the plateau region, where the foam exhibits a long (almost) constant stress due to progressive layer-by-layer collapse (plastic deformation, buckling, fracture and brittle collapse). Finally, the foam densifies due to the contact between the cell struts, exhibiting an abrupt increase of the stress. In fact, the OCF starts to deform at weak points (IR images, Figure 6.5a), followed by a band formation. The stress fluctuations are observed in the plateau region (Figure 6.5b) due to their layer-wise brittle collapse [17]. These results (Figure 6.5b) confirm our previous findings [24] that the OCF is slightly sensitive to the strain rate, in which the dynamic curves (red curves) are slightly superior (higher peak stresses) in comparison to the quasi-static ones (black curves).

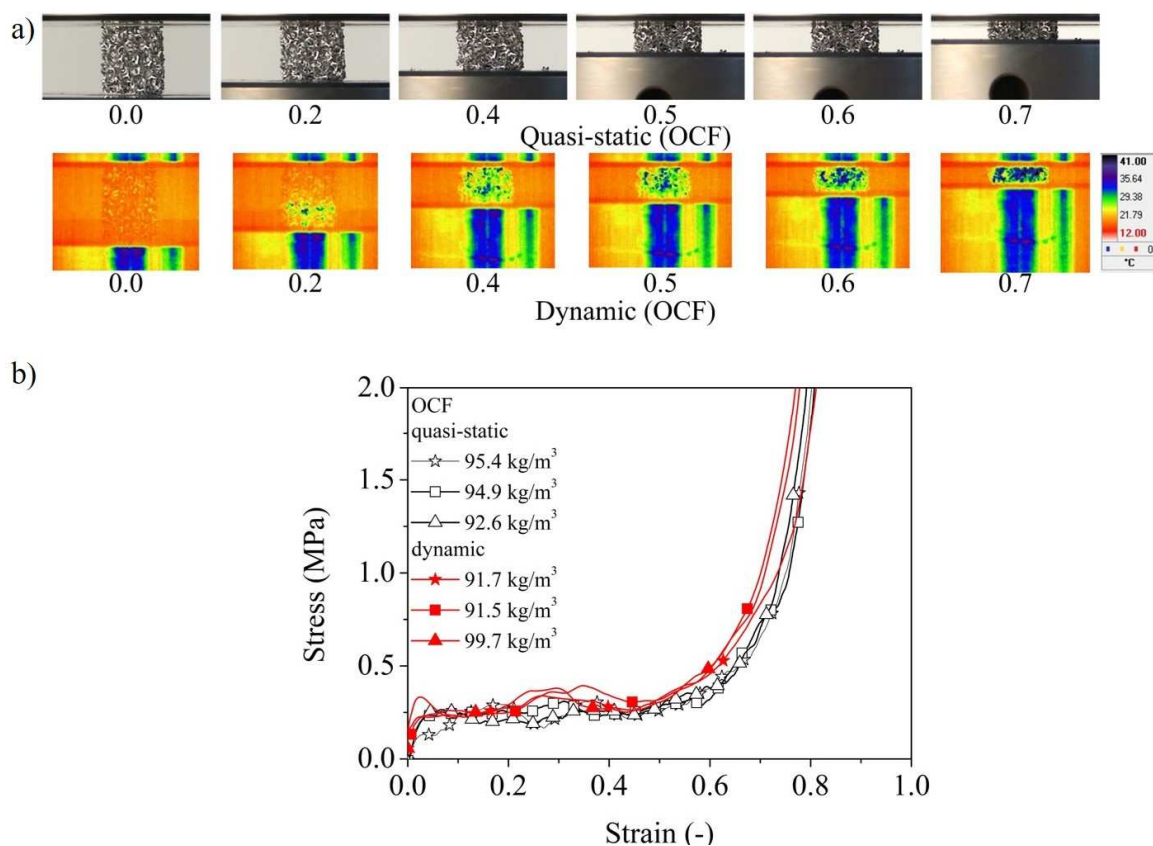


Figure 6.5 Compressive deformation (a) and stress–strain curves (b) of OCF specimens.

6.4.2.3. Compression behaviour of HS-PDMS and HS-nPDMS

Figure 6.6 shows the compressive deformation and failure modes (Figure 6.6a) and stress-strain curves (Figure 6.6b) of the simple HS-PDMS and HS-nPDMS specimens. The dynamic failure and deformation modes of the HS-PDMS and HS-nPDMS specimens were also studied using the IR thermography. The experimental results confirm that the presence of the polymer filler (PDMS and nPDMS) in the voids of the OCF changes the deformation and failure modes of the simple OCF characterized by layer-wise collapse. The polymer filler prevents the self-contact of struts. Additionally, no deformation bands are visible. The PDMS and nPDMS promotes symmetric deformation in HS-PDMS and HS-nPDMS specimens by folding in the middle at both (quasi-static and dynamic) loading conditions as can be seen in Figure 6.6a. The HS-PDMS and HS-nPDMS hybrid structures exhibit a brittle behaviour under compressive loads, leading to the development of cracks during the fold formation (i.e. barrelling in the centre of the specimens). Furthermore, the deformation and failure modes of the HS-PDMS and HS-nPDMS specimens are completely different from those observed in identical hybrid structures developed and studied in our previous work

[24]. In [24], hybrid structures specimens were prepared by impregnating the same OCF as used in this study, with PDMS cured at room temperature for 24 h (designated by HS-R). Herein, the HS-PDMS and HS-nPDMS specimens were prepared by infiltrating the OCF with PDMS and cured at 65 °C for 4 h. Obviously, the difference of the deformation and failure modes between the HS and HS-R specimens is due to the thermal curing cycle during fabrication. The PDMS changes from rubbery [24] to brittle (Figure 6.6a) when subjected to different curing temperatures, i.e. from room temperature to 65 °C, respectively. Therefore, the HS and HS-R specimens exhibit a rubber-like and brittle behaviour, respectively. This is related to the chemical nature of the PDMS, where the silicon atoms are linked to carbon, hydrogen and oxygen atoms. Their structural features, such as Si–O–Si angles, Si–O bond length, dissociation energy, the freedom of rotation and the weak intermolecular forces among polymer chains with a high chain mobility make them very flexible with unique physical (mechanical and thermal) and chemical properties. A low adhesion between the silicone and the struts of the OCF and a lower friction coefficient is observed in the HS-R specimens [24,25]. Furthermore, the silicone rubbers behave differently in comparison to the other polymers, since their structure is highly deformable and self-restoring. Published results have demonstrated that the mechanical properties of silicone increases with the increasing of the curing time. Therefore, the brittleness of HS-PDMS and HS-nPDMS specimens might be a result of the high curing temperature (65 °C) used in their fabrication, leading to a high adhesion between the silicone and the struts of the OCF, diminishing its chain mobility. The deformation and failure modes of the HS-PDMS and HS-nPDMS specimens are identical to the OCF specimens embedded with brittle epoxy resin [24], displaying a negligible chain mobility. The epoxy resin promotes a symmetric deformation in the resulting hybrid structures at both (quasi-static and dynamic) loading conditions, as in the case of the HS-PDMS and HS-nPDMS specimens. On the other hand, the HS-R experienced a non-symmetric deformation at both (quasi-static and dynamic) loading conditions [24]. In this case, the Si–O bonds are longer with fewer alkyl groups than C–C bonds, these shows a lower mechanical strength compared to the HS prepared in this study. Figure 6.6b shows the compressive stress-strain curves of the HS-PDMS and HS-nPDMS specimens for both (quasi-static and dynamic) loading conditions. The HS-PDMS and HS-nPDMS hybrid structures are significantly more sensitive to strain rate than the HS-R and the simple OCF [24]. The dynamic curves of HS-PDMS and HS-nPDMS specimens (red

curves) are much higher to the quasi-static curves (black curves), as shown in Figure 6.6b. For example, the values of the first peak stress change from 5.25 MPa (quasi-static, Table 6.2) to 13.94 MPa (dynamic, Table 6.2) and from 4.93 MPa (quasi-static, Table 6.2) to 12.97 MPa (dynamic, Table 6.2) for HS-PDMS and HS-nPDMS specimens, respectively.

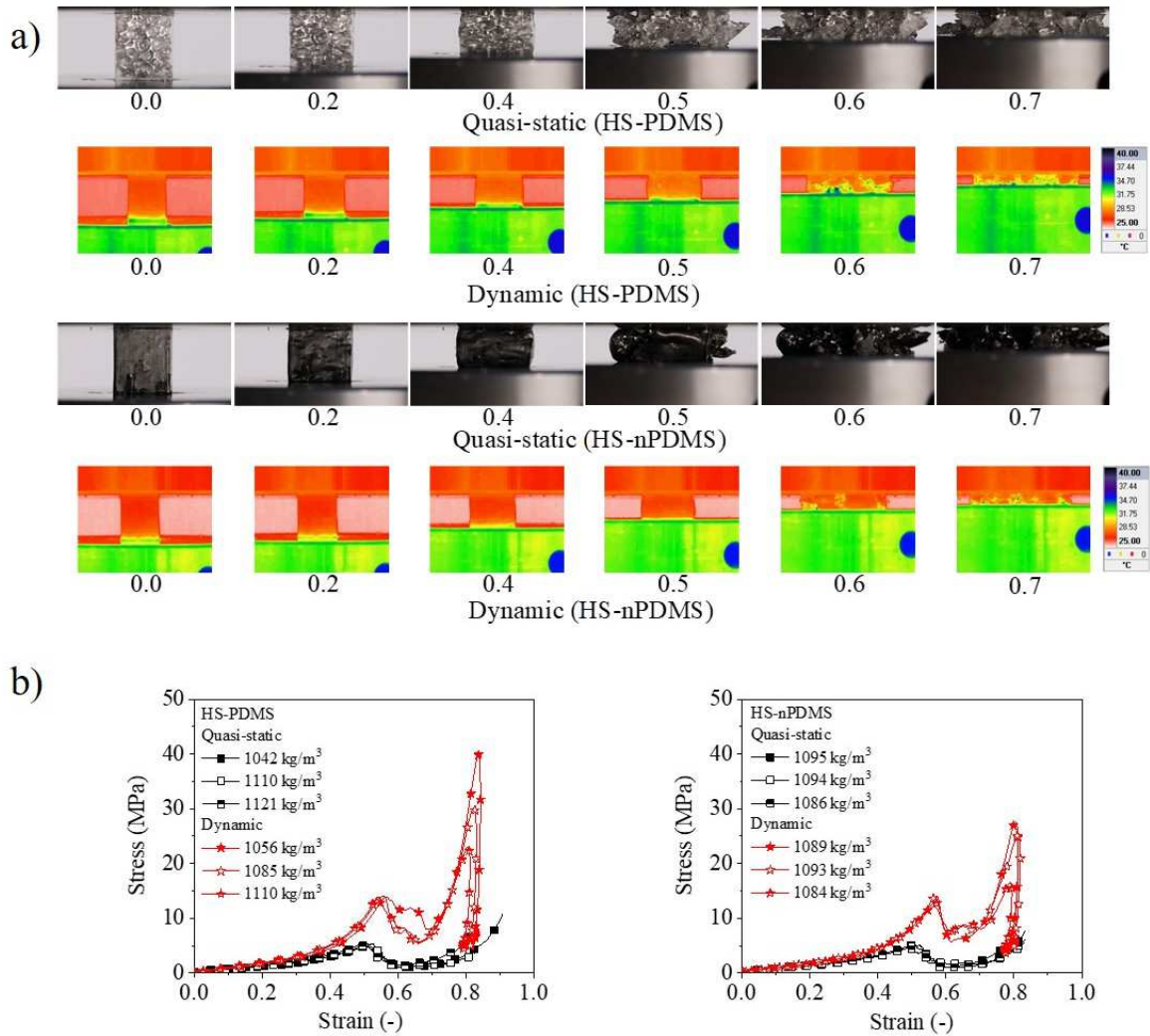


Figure 6.6 Compressive deformation (a) and stress–strain curves (b) of the HS-PDMS and HS-nPDMS specimens.

Results in this field have demonstrated that some others cellular metals have showed only a slight strain-rate sensitivity, where the dynamic response was only slightly above the quasi-static response at moderate dynamic loading velocities (284 mm/s) [24,25,40]. For example, the values of the first peak stress of the simple OCF change from 0.28 MPa to 0.31 MPa for the quasi-static and dynamic loading conditions. However, the dynamic response of the HS-R is below the quasi-static response [24], in the initial region up to strain of ~ 0.2 . The HS-

PDMS and HS-nPDMS specimens exhibit a significantly higher level of compressive stress, reaching a stress value of 5 MPa and over 20 MPa for quasi-static and dynamic loading conditions, respectively (Figure 6.6b). The diagram shape of the compressive stress-strain curves of the HS-PDMS and HS-nPDMS specimens are different from the curves of HS-R specimens. This is attributed to the different characteristics of the polymers that are subjected to different curing temperature, as described above. Results also indicated that the diagram shape depends on the (quasi-static and dynamic) loading conditions.

The diagram shape of quasi-static curves for the HS-PDMS and HS-nPDMS specimens is divided into the following four regions: the initial linear elastic, followed by a nonlinear increase in stress up to the maximum compressive stress, drop in stress and a visible recoverable deformation. However, the diagram shape of dynamic curves for the HS-PDMS and HS-nPDMS specimens can be divided into the following regions: the initial linear elastic region, followed by a nonlinear increase in stress up to the first peak stress, followed by a minor drop in stress to a given minimum stress value, followed by a stress fluctuation exhibiting a sequence of peaks reaching the maximum compressive stress before the failure. For example, the HS-PDMS specimens reached the first peak stress of 13.92 MPa (at strain of 0.45), followed the recoverable deformation, reaching the maximum compressive stress of 42 MPa (at strain of 0.8). These experimental results show that the HS and HS-nPDMS exhibit large and recoverable strain hardening deformation. The HS-PDMS and HS-nPDMS do not display the typical plateau-stress response, exhibiting by the HS-R and conventional OCF specimens (Figure 6.5b). Moreover, the silicone in the HS-R effectively smoothens and stabilizes the response of the OCF specimens, decreasing the stress oscillations in the plateau region and increasing the values of their mechanical properties. The compressive stress-strain responses of the HS and HS-nPDMS specimens (Figure 6.6a) are inferior to the dense PDMS and nPDMS specimens (Figure 6.4a). The measured hardness of the PDMS samples also increased linearly with increasing the curing temperature. The compressive responses of the HS increase by decrease of the OCF's density. The presence of the GO within the PDMS matrix effectively smoothens and stabilizes the response of the HS, decreasing the stress oscillations, achieving similar values of the first peak stress and the maximum compressive stress.

Chapter 6

Table 6.2 Compressive results of HS-PDMS and HS-nPDMS specimens.

Specimen	Loading conditions	Density	Peak		Decay	
			Strain (-)	Stress (MPa)	Strain (-)	Stress (MPa)
HS-PDMSs	Quasi static					
1		1042	0.51	5.25	0.60	0.95
2		1110	0.53	5.31	0.60	0.95
3		1112	0.49	5.19	0.62	1.38
Average		1088	0.51	5.25	0.61	1.09
St Dev		39.9	0.02	0.06	0.01	0.25
HS-PDMS	Dynamic					
1		1056	0.57	13.92	0.61	11.46
2		1085	0.56	14.05	0.59	7.68
3		1100	0.55	13.85	0.60	8.40
Average		1080	0.56	13.94	0.60	9.18
St Dev		22.4	0.01	0.10	0.01	2.01
HS-nPDMS	Quasi-static					
1		1086	0.487	4.569	0.607	0.959
2		1094	0.523	5.074	0.603	1.526
3		1095	0.502	5.156	0.597	1
Average		1092	0.504	4.933	0.602	1.162
St Dev		4.9	0.018	0.318	0.005	0.316
HS-nPDMS	Dynamic					
1		1084	0.568	12.834	0.617	7.569
2		1089	0.566	12.042	0.614	5.725
3		1093	0.571	14.02	0.605	7.195
Average		1088.7	0.568	12.965	0.612	6.830
St Dev		4.5	0.003	0.996	0.006	0.975

6.3.2.4. Energy absorption capabilities

The EAD for the HS-PDMS and HS-nPDMS specimens in comparison to the individual components (OCF, nPDMS and PDMS) is shown in Figure 6.7. The dynamic EAD curves of HS-PDMS and HS-nPDMS specimens are higher in comparison to the PDMS and nPDMS specimens.

From Figure 6.7, it can be observed that the HS-PDMS and HS-nPDMS specimens are the ones that present higher capacity of the EAD. The quasi-static and dynamic EAD curves of the HS-PDMS and HS-nPDMS specimens are above the curves of the individual components (PDMS, nPDMS and OCF). At strain of 0.5, the HS-PDMS and HS-nPDMS are approximately 4 times and 6 times higher in comparison to the OCF specimens subjected to the quasi-static and dynamic loading conditions, respectively. Furthermore, above strain of 0.4, the SEA curves of HS-PDMS and HS-nPDMS specimens are also above the ones of individual components (PDMS, nPDMS and OCF), indicating that the HS-PDMS and HS-nPDMS have a higher energy absorb capacity.

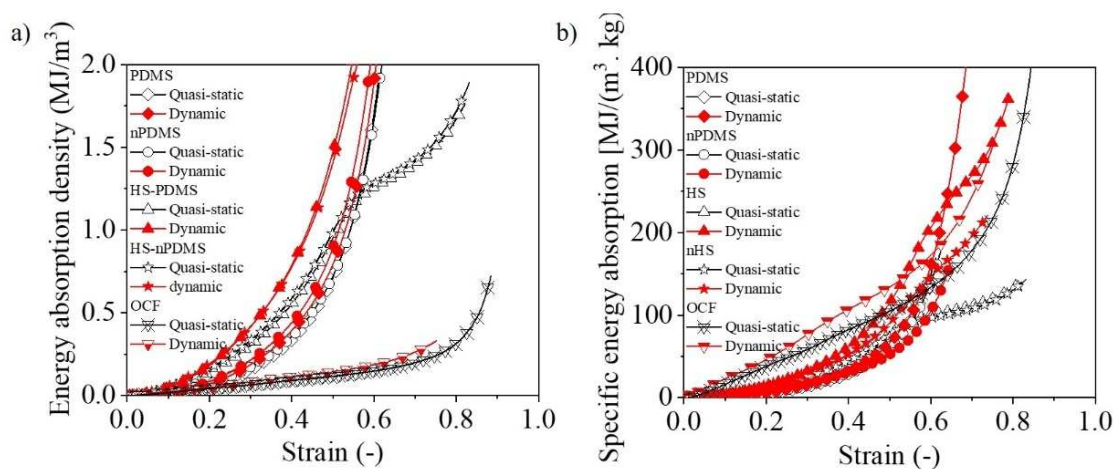


Figure 6.7 Averaged EAD (a) and SEA (b) curves for quasi-static and dynamic loading conditions.

6.4.3. Thermal insulation

Figure 6.8a illustrates the effects of the presence of the polymer in the voids of the OCF and the presence of the GO within the polymer matrix on the thermal conductivity. As expected, the OCF specimens present higher thermal conductivity (1.611 W/m·K), while the dense the PDMS and nPDMS show lower values (0.181 W/m·K and 0.187 W/m·K). The thermal conductivity of the PDMS specimens (0.181 W/m·K) is in accordance with values reported in literature (0.15-0.20 W/m·K) [41]. Results indicate that the presence of the GO

within the polymer matrix has a positive effect on the thermal conductivity. For example, the thermal conductivity increases from 0.181 to 0.187 W/m·K for dense PDMS and nPDMS specimens, leading to an increase of approximately 3.5 %. The main reasons for this include: (i) the percentage of incorporation of the GO (0.25 wt.%) within the PDMS matrix is very low for allowing the formation of a conductive network that will provide an effective pathway for the phonon movement in the insulator matrix, leading to higher thermal conductive values, (ii) even at low level of incorporation, the formation of aggregates may occur, which restricts the heat transport. In fact, aggregates reduce the aspect ratio, decrease the contact area and trap or scatter phonons. Similar studies that describe the incorporation of carbon nanostructures drive special attention towards the uniform dispersion of fillers in the matrix in order to reduce the mismatch by reducing the interfacial resistance. Similar positive effect is also observed in the hybrid structures in which the effective thermal conductivity increases from 0.241 (HS-PDMS) to 0.291 W/m K (HS-nPDMS). From these experimental results, it can be observed that the thermal conductivities of the OCF (1.611 W/m K) significantly decreased when the voids were filled by polymers (PDMS and nPDMS). The presence of an Al network structure interconnected facilitates the heat transfer.

6.4.4. Acoustic absorption

The sound absorption coefficient curves of hybrid structures (HS-PDMS and HS-nPDMS) and the individual components (PDMS, nPDMS and OCF) are presented in Figure 6.8b. Herein, the effect of the PDMS and the GO on the acoustic absorption properties is shown.

As described above, the PDMS is a semi-crystalline thermoplastic polymer composed of a chain of alternating silicon and oxygen atoms. Each silicone has two methyl groups attached to it by Van der Waal's forces. The main intermolecular interactions between the chains are weak forces. Their structure is long with highly flexible chains, resulting in rubber-like elasticity. Moreover, the PDMS exhibits both elastic and viscous properties. This means that it acts like a viscous liquid (e.g. honey) or an elastic solid (e.g. rubber) when subjected to high and low temperatures, respectively. Moreover, when the PDMS chains undergo vibrations, part of the energy is stored (elastic) and part is dissipated as heat (viscous) within the polymer. This viscous nature results in loss of vibration energy as heat, consequently enhancing the sound absorption [42]. The incorporation of the GO within the

PDMS matrix, create voids in the PDMS matrix, as observed by SEM (Figure 6.1) and as suggested in the compression tests, leading to an increase in the sound absorption. In this case, an increase of approximately 80 % in the frequency range from 500 Hz to 1250 Hz was observed. The enhancement of sound absorption coefficient of foamed materials impregnated with carbon nanoparticles was also reported by other authors [43]. This could be attributed to the large surface of the GO sheets that can be responsible for the dissipation by interfacial sliding and stick-slip behaviour. In the case of the HS-PDMS, an enhancement in the sound absorption was also observed, due to the voids created around the metal skeleton. A peak increase of more than 150 % was observed for the HS-PDMS in comparison to the PDMS. The better sound absorption was obtained for HS-nPDMS with values around 0.5 at frequency of 1000 Hz.

The comparison of results with other reported in literature is not easy since there are limited studies reporting on sound absorption. It is well known that sound waves propagate fast in solid materials, contrary to fluids. When the sound wave hits a solid surface, the material vibrates, the molecules that compose the material collide one another and the kinetic energy is passed from molecule to molecule. Furthermore, the transmission of energy is higher when molecules are closer to each other and stronger bonded [44]. As so, the dense materials are not widely used for sound absorbers like foamed materials. However, they are used as coatings or sheets to dampen vibrations and sound [45].

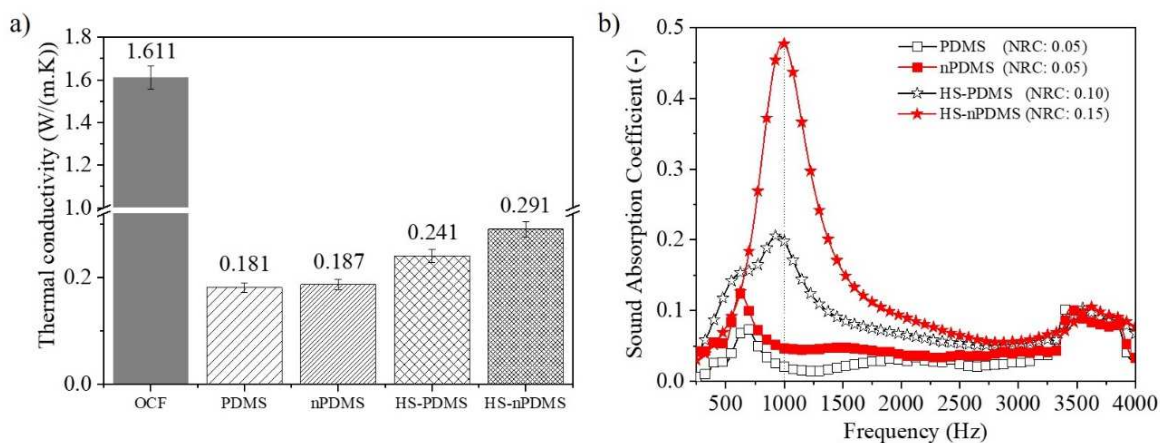


Figure 6.8 Thermal conductivities and (a) Sound absorption coefficient curves (b) of the hybrid structures (HS-PDMS and HS-nPDMS) and the individual components (PDMS, nPDMS and OCF).

6.4.5. Fire retardancy properties

The effect of the GO on the fire retardancy properties of the nPDMS was evaluated. Figure 6.9 shows the sequence image for the PDMS and nPDMS specimens. As expected, the PDMS matrix exhibited a rapid and complete combustion, along with extensive dripping from the specimens. The incorporation of the GO within the PDMS matrix results in a significant reduction of the PDMS flammability, as shown in Figure 6.9. No flame is observed for the nPDMS, while the flame for the PDMS extinguishes after 5 s. Similar results were observed previously for polymer nanocomposites [46]. It has been demonstrated that carbon nanostructures are efficient for the elastomers in terms of fire retardancy. In specific conditions, the accumulation of nanoparticles in polymer is beneficial to avoid the flow of the molten polymer and consequent physical defects in the protecting layer.

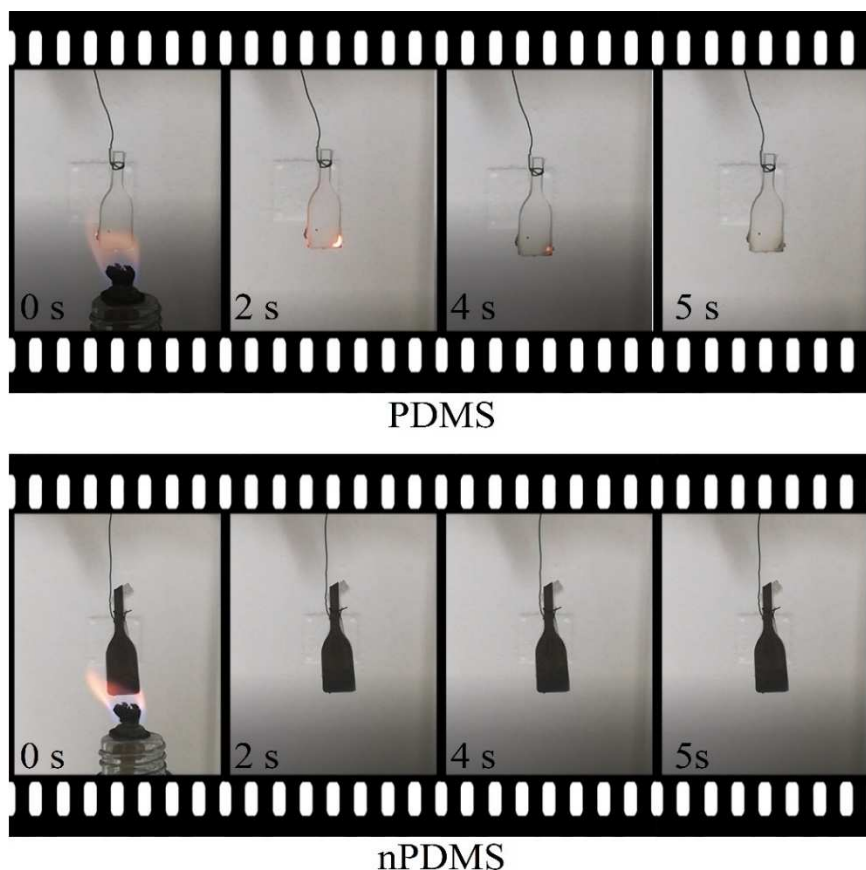


Figure 6.9 Fire retardancy sequence image for the PDMS and nPDMS.

6.5. Conclusions

Simple and nanocomposite hybrid structures (HS-PDMS and HS-nPDMS) were developed by impregnating an OCF with PDMS or PDMS reinforced with GO (nPDMS),

respectively. The thermal curing cycle lasted at 65 °C for 4 h. The mechanical, thermal, acoustic absorption and fire retardancy properties of the hybrid structures were compared to the individual components (PDMS, nPDMS and OCF). Results demonstrate that the compressive response, e.g. the shape of the curves, deformation modes and failure, of hybrid structures is notably influenced by the curing temperature of the PDMS. The mechanical response of the PDMS may change from rubbery to brittle via ductile plasticity by the thermal curing cycle, in particular the curing temperature. The use of high curing temperature (65 °C) of the silicone leads to a brittle behaviour of the resulting hybrid structure reaching a high level of strength (quasi-static: ~5 MPa; dynamic: > 15 MPa), due to the low chain mobility of the polymer and high adhesion between the struts of the OCF. Contrary, the use of the low temperature (room temperature) leads to a rubbery behaviour of the hybrid structure reaching a low level of compressive strength (~0.47 MPa), due to the high chain mobility of the polymer and low adhesion between the silicone and the struts of the OCF.

The HS-PDMS and HS-nPDMS specimens with brittle behaviour are extremely sensitive to the strain-rate compared to other cellular metals and hybrid structures based on silicone cured at room temperature. The HS-PDMS and HS-nPDMS specimens exhibited a compressive stress increase of more than 300 % and 200 %, respectively. The silicone with rubbery behaviour (gel-like material) promotes non-symmetric deformation in the hybrid structure specimens, while the silicone with brittle behaviour promotes symmetric deformation in the HS-PDMS and HS-nPDMS specimens by folding in the middle of the specimens at both (quasi-static and dynamic) loading conditions. The hybrid structure prepared by high curing temperature (65 °C) exhibited a brittle behaviour under compressive loads, leading to the development of cracks during the fold formation (i.e. barrelling in the centre of the specimens). Results also demonstrate that the presence of the GO within the PDMS matrix (even as low as 0.25 wt.%) provides voids in the HS-nPDMS, which efficiently increase the sound absorption coefficient of 0.5 at frequency of 1000 Hz. Furthermore, the presence of the GO within the PDMS matrix ensured that the hybrid structure was able to maintain the typical non-flammable characteristic of metals.

6.6. References

- [1] A.D.B.L. Ferreira, P.R.O. Nóvoa, A.T. Marques. Multifunctional Material Systems: A state-of-the-art review. *Composite Structures* 2016. 151. 3-35.
- [2] J. Banhart. Manufacture, characterisation and application of cellular metals and metal foams. *Progress in Materials Science* 2001. 46 (6). 2001. 559-632.
- [3] I. Duarte, N. Peixinho, A. Andrade-Campos, R. Valente. Editorial - Special Issue on Cellular Materials. *Science and Technology of Materials* 2018; 30: 1–3.
- [4] Tjong, S.C. Structural and mechanical properties of polymer nanocomposites. *Materials Science and Engineering: R: Reports* 2006. Volume 53. Issues 3–4. 30 August 2006. Pages 73-197.
- [5] Tjong, S.C. Recent progress in the development and properties of novel metal matrix nanocomposites reinforced with carbon nanotubes and graphene nanoplates. *Materials Science and Engineering: R: Reports* 2013. Volume 74. 281-350.
- [6] Hans-Peter Degischer; Dr. Brigitte Kriszt. *Handbook of Cellular Metals: Production, Processing, Applications*. Copyright © 2002 Wiley-VCH Verlag GmbH & Co. KGaA.
- [7] F. Garcia-Moreno. *Commercial Applications of Metal Foams: Their Properties and Production*. Materials (Basel). 2016 Jan 29;9(2). pii: E85.
- [8] M. Ulbin, M. Vesenjak, M. Borovinšek, I. Duarte, Y. Higa, K. Shimojima, Z. Ren. Detailed Analysis of Closed-Cell Aluminum Alloy Foam Internal Structure Changes during Compressive Deformation. *Adv. Eng. Mater.* 2018. 20 (8). Article number 1800164.
- [9] T. Miyoshi, M. Itoh, S. Akiyama, A. Kitahara. ALPORAS Aluminum Foam: Production Process, Properties, and Applications. *Advanced Engineering Materials* 2000. 2(4): 179-183.
- [10] I. Duarte, JMF Ferreira. 2D quantitative analysis of metal foaming kinetics by hot-stage microscopy. *Advanced Engineering Materials* 2014, 16: 33-39.
- [11] Orbulov, I.N., Szlancsik, A. On the Mechanical Properties of Aluminum Matrix Syntactic Foams. *Advanced Engineering Materials*. 20(5).1700980
- [12] Taherishargh, M., Katona, B., Fiedler, T., Orbulov, I.N. Fatigue properties of expanded perlite/aluminum syntactic foams. *Journal of Composite Materials* 2017. 51(6): 773-781.
- [13] Wadley, H.N.G. Multifunctional periodic cellular metals. *Phil. Trans. R. Soc. A* (2006) 364. 31–68.
- [14] N. Novak, M. Vesenjak, Z. Ren. Auxetic Cellular Materials – a Review. *Journal of Mechanical Engineering* 2016, 62(9): 485-493.
- [15] N. Novak, L. Starčević, M. Vesenjak, Z. Ren. Blast response study of the sandwich composite panels with 3D chiral auxetic core. *Composite Structures* 2019, 210: 167-178.
- [16] N. Gupta, P.K. Rohatgi (Eds.). *Metal Matrix Syntactic Foams: Processing, Microstructure, Properties and Applications*. DESTech Publications Inc.
- [17] I. Duarte, JMF Ferreira. Composite and nanocomposite metal foams. *Materials* 2016. 9(2).79.
- [18] Liu, J.; Yu, S.; Zhu, X.; Wei, M.; Li, S.; Luo, Y.; Liu, Y. Correlation between ceramic additions and compressive properties of Zn-22 Al matrix composite foams. *J. Alloy. Compd.* 2009. 476. 220–225.
- [19] I. Duarte, E. Ventura, S. Olhero, JMF Ferreira. A new class of closed-cell aluminium foams

- reinforced with carbon nanotubes. *Ciencia e Tecnologia dos Materiais*. 28(1): 5-8.
- [20] M. Vesenjāk. L. Krstulović-Opara. Z. Ren. A. Öchsner. Ž. Domazet. Experimental Study of Open-Cell Cellular Structures with Elastic Filler Material. *Exp. Mech.* 49 (2009) 501–509.
- [21] M. Vesenjāk. L. Krstulović-Opara. Z. Ren. Z. Domazet. Cell shape effect evaluation of polyamide cellular structures. *Polymer Testing* 2010, 29: 991–994.
- [22] M. Vesenjāk. L. Krstulović-Opara. Z. Ren. Characterization of photopolymer cellular structure with silicone pore filler. *Polym. Testing* 31 (2012) 705–709.
- [23] M. Vesenjāk. L. Krstulović-Opara. Z. Ren. Characterization of irregular open-cell cellular structure with silicone pore filler. *Polym. Test.* 32 (2013) 1538–1544.
- [24] I. Duarte. M. Vesenjāk. L. Krstulović-Opara. Z. Ren. Crush performance of multifunctional hybrid foams based on an aluminium alloy open-cell foam skeleton. *Polymer Testing* 2018; 67: 246–256.
- [25] I. Duarte. M. Vesenjāk. L. Krstulović-Opara. J. Dias-de-Oliveira. M. Vesenjāk Axial crush performance of polymer-aluminium alloy hybrid foam filled tubes. *Thin-walled Structures* 2019. 138. 124-136.
- [26] M. Reinfried. G. Stephani. F. Luthardt. J. Adler. M. John. A. Krombholz. Hybrid foams – a new approach for multifunctional. Applications. *Adv. Eng. Mater.* 13 (2011) 1031-1036.
- [27] K. Stöbener. G. Rausch. Aluminium foam–polymer composites: processing and characteristics. *J. Mater. Sci.* 44 (2009) 1506–1511.
- [28] L. Carrino. M. Durante. S. Franchitti. L. Sorrentino. Mechanical performance analysis of hybrid metal-foam/composite samples. *Int. J. Adv. Manuf. Technol.* 60 (2012) 181–190.
- [29] S. Kishimoto. Q. Wang. Y. Tanaka. Y. Kagawa. Compressive mechanical properties of closed-cell aluminium foam–polymer composites. *Composites Part B* 64 (2014) 43–49.
- [30] J. Yuan. X. Chen. W. Zhou. Y. Li. Study on quasi-static compressive properties of aluminium foam-epoxy resin composite structures. *Composites Part B* 79 (2015) 301–310.
- [31] L. Krstulović-Opara, M. Vesenjāk, I. Duarte, Z. Ren, Z. Domazet. Infrared Thermography as a Method for Energy Absorption Evaluation of Metal Foams. *Mater. Today Proc.* 3 (2016) 1025–1030.
- [32] ISO 22007-2.2. Plastics - Determination of thermal conductivity and thermal diffusivity - Part 2: Transient plane heat source (hot disc) method.
- [33] ASTM D7984 Standard Test Method for Measurement of Thermal Effusivity of Fabrics Using a Modified Transient Plane Source (MTPS) Instrument thermal.
- [34] ASTM E1050-12 Standard Test Method for Impedance and Absorption of Acoustical Materials Using a Tube, Two Microphones and a Digital Frequency Analysis System.
- [35] The materials with a sound absorption coefficient equal to or greater than 0.5 are usually considered efficient sound absorption materials
- [36] G. Caminoa, S.M. Lomakinb, M. Lazzari. Polydimethylsiloxane thermal degradation Part 1. Kinetic aspects, *Polymer* 2001, 42: 2395-2402
- [37] C. R. Siviour, J. L. Jordan. High Strain Rate Mechanics of Polymers: A Review. *Journal Dynamic Behavior Material* 2016, 2:15–32.
- [38] K. Urayama, T. Kawamura, S. Kohjiy, Structure–mechanical property correlations of model

- siloxane elastomers with controlled network topology. *Polymer* 2009, 50: 347–356.
- [39] W.S. Lee, K.S. Yeo, A. Andriyana, Y.G. Shee, F.R. Mahamd Adikan. Effect of cyclic compression and curing agent concentration on the stabilization of mechanical properties of PDMS elastomer. *Materials and Design* 96 (2016) 470–475.
- [40] I. Duarte, L. Krstulović-Opara, M. Vesenjak, Axial crush behaviour of the aluminium alloy in-situ foam filled tubes with very low wall thickness. *Composite Structures* 2018, 192: 184-192.
- [41] J.E. Mark. *Polymer Data Handbook*. 2nd edition. Oxford University Press, 2009.
- [42] A. Mata, A. J. Fleischman, and S. Roy. Characterization of Polydimethylsiloxane (PDMS) Properties for Biomedical Micro/Nanosystems,” *Biomed. Microdevices* 2005, 7 (4): 281–293.
- [43] J. M. Kim, D. H. Kim, J. Kim, J. W. Lee, and W. N. Kim. Effect of graphene on the sound damping properties of flexible polyurethane foams,” *Macromol. Res.* 2017, 25 (2): 190–196.
- [44] V. G. Geethamma, R. Asaletha, N. Kalarikkal, and S. Thomas. Vibration and sound damping in polymers,” *Resonance*, vol. 19, no. 9, pp. 821–833, 2014.
- [45] N. N. Najib, Z. M. Ariff, A. A. Bakar, and C. S. Sipaut, Correlation between the acoustic and dynamic mechanical properties of natural rubber foam: Effect of foaming temperature, *Mater. Des.* 2011, 32 (2): 505–511.
- [46] Prashant S. Khobragade, D.P. Hansora, Jitendra B. Naik, Aniruddha Chatterjee. Flame retarding performance of elastomeric nanocomposites: A review. *Polymer Degradation and Stability* 2016,130: 194-244.

Chapter 7. Mechanical, thermal and acoustic properties of aluminium foams impregnated with epoxy/graphene oxide nanocomposites

This chapter was based in the following published paper:



Article

Mechanical, Thermal, and Acoustic Properties of Aluminum Foams Impregnated with Epoxy/Graphene Oxide Nanocomposites

Susana C. Pinto ¹, Paula A.A.P. Marques ¹, Matej Vesenjak ², Romeu Vicente ³, Luís Godinho ⁴, Lovre Krstulović-Opara ⁵ and Isabel Duarte ^{1,*}

¹ Department of Mechanical Engineering, TEMA, University of Aveiro, 3810-193 Aveiro, Portugal; scpinto@ua.pt (S.C.P.); paulam@ua.pt (P.A.A.P.M.)

² Faculty of Mechanical Engineering, University of Maribor, 2000 Maribor, Slovenia; matej.vesenjak@um.si

³ Department of Civil Engineering, University of Aveiro, 3810-193 Aveiro, Portugal; romvic@ua.pt

⁴ Department of Civil Engineering, ISISE, University of Coimbra, 3030-788 Coimbra, Portugal; lgodinho@dec.uc.pt

⁵ Faculty of Electrical Eng., Mech. Eng. and Naval Architecture, University of Split, 21000 Split, Croatia; Lovre.Krstulovic-Opara@fesb.hr

* Correspondence: isabel.duarte@ua.pt; Tel.: +350-234-370-830

7.1. Abstract

Hybrid structures with epoxy (EP) embedded in the open-cell aluminium foam (OCF) were developed by combining OCF specimens with unreinforced and reinforced EP resin using graphene oxide (GO). These new hybrid structures were fabricated by infiltrating an OCF specimen with pure EP or mixtures of EP and GO, completely filling the pores. The effects of GO on the mechanical, thermal and acoustic performance of EP/GO-based nanocomposites are reported. Mechanical compression analysis was conducted through quasi-static uniaxial compression tests at two loading rates (0.1 mm/s and 1 mm/s). Results show that the thermal stability and the sound absorption coefficient of the hybrid structures were improved by the incorporation of the GO within the EP matrix. However, the incorporation of the GO into the EP matrix can create voids inside the epoxy resin, leading to a decrease of the compressive strength of the hybrid structures, thus no significant increase in the energy absorption capability was observed.

7.2. Introduction

Metal foams have gained special attention in the last years due to their outstanding properties [1]. The first reference to metallic foams is a French patent published in 1925 by Meller; however, its commercialization only started three decades later in the United States of America (USA). After the stagnation period, and with the development of new technologies that allowed the decrease of cost and difficulties in the manufacturing process, there was a boost in their development that is still ongoing [2]. With these recent developments, metal foams have become commercially available in a wide variety of structures [3]. There are many interesting combinations of different properties, such as high stiffness associated with low specific weight or high compression strength combined with good energy absorption efficiency, making them suitable for automotive industry, ship building, aerospace industry, civil engineering, and medicine [1–5]. Thus, it is important to predict their mechanical behaviour prior their application. While the behaviour of closed-cell foams is difficult to predict, since often, non-regular structures are obtained by the existent manufacturing methods [6], open-cell foams, used mainly for functional applications, frequently present regular structures—therefore, their behaviour is easier to estimate [7]. Cellular metals with regular structures have been developed, e.g., open-cell metal foams [8], advanced pore morphology (APM) foam elements [9–11], and

metal hybrid hollow structures [12], to be used as fillers of thin-walled structures [13]. The low compressive strength of open-cell structures limits their application. In this context, the uprising research of the hybrid structure concept, resulting from filling open-cell structures with stronger materials that provide suitable resistance, has brought new insights in this field [8,14,15]. Epoxy (EP)-based materials possess competitive advantages, such as high compressive resistance, low cost, and simple processing. However, EP materials are characterized by low fracture toughness, poor crack resistance, and brittle fracture under loading [16]. Besides this, EP—as many other organic materials—presents a risk of high flammability [17]. It is reported that the addition of fillers (or a combination of different fillers) to the EP matrix can improve or confer important features to the final product [17]. Among the most commonly used, the following can be pointed out: phosphorous, nitrogen-based fillers, nanoclays, carbon nanotubes, and graphene-based materials [18]. The inclusion of graphene oxide (GO), a two-dimensional (2D) structure formed by a flat monolayer of carbon atoms arranged in a hexagonal lattice and decorated by a variety of functional groups (such as epoxides, carbonyls, hydroxyls), as well as its reduced form (with no or less oxygen functionalities and recovering the sp^2 hybridization configuration), has been the subject of considerable interest and analysis [19]. It is documented that graphene and its derivatives greatly improve the fatigue characteristics and toughness of EP resins, as well as induce fire-resistance [20]. Several methods (e.g., ball milling, solvent-assisted, ultrasonication, or surface modification) [20] have been explored for preparation of these type of nanocomposite materials in order to ensure the good dispersion of nanofillers into the polymer matrix. The work herein follows the previous pioneering studies performed by Duarte *et al.* [8,21], where they evaluated the quasi-static and dynamic crush compressive performance of simple multifunctional hybrid structures based on an open-cell aluminium foam (OCF) impregnated with polymers (e.g., EP resin) and their performance as fillers of square thin-walled tubes. Results demonstrate that the polymer–aluminium hybrid structure stabilizes the tube and prevents the unstable global bending or mixed buckling mode. Studies show that the OCF–EP hybrid structure-filled structures are more efficient in terms of crashworthiness [21]. Herein, the graphene oxide at a low content load of 0.25 wt.% was studied as reinforcement of the EP matrix, used as a void filler of the OCF. Additionally, its effects on the mechanical, thermal, and acoustic properties were evaluated.

7.3. Materials and Methods

7.3.1. Materials

An AlSi7Mg0.3 open-cell foam (OCF) block made of AlSi7Mg0.3 with pore sizes of 10 ppi (pores per inch) fabricated by the replication casting method was supplied by Mayser GmbH & Co. KG (Lindenberg, Germany) (formely M-pore). The OCF was fully filled by the epoxy resin (EP).

A commercial EP resin solvent-free mid-viscosity glue was supplied by company KGK Ltd. (Barilović, Croatia), and when cured at 20 °C for 25 min had a density of 1100 kg/m³, compression strength of 90.4 MPa, bending strength of 38.9 MPa, and tensile strength of 14.8 MP. It was composed of two reagents, component A (polymer) and component B (hardener), and the mixing ratio was A:B = 2:1 (mass ratio) or 9:5 (volume ratio). The component A had a density of 1.12 kg/dm³, while the component B had a density of 1 kg/dm³. Graphene oxide (GO) was acquired from Graphenea Inc. (San Sebastián, Spain) in an aqueous dispersion with 4 mg/mL. The GO sheets had a particle size <10 μm and >95% of GO content was a monolayer (nanometric in thickness). The GO had a carbon content of 49–56% and oxygen content of 41–50%, which was determined by X-ray photoelectron spectroscopy (XPS). Before incorporation in the EP, diluted GO suspension was freeze-dried to be used in powder form.

7.3.2. Fabrication of the Specimens

The dense pure EP and EP reinforced with the GO (nEP) specimens were prepared by pouring the pure EP or nEP mixtures into an empty thin-walled tube. The OCF–EP hybrid structure (HS-EP) and OCF–nEP nanocomposite hybrid structure specimens (HS-nEP) were fabricated by pouring the pure EP or nEP mixtures into an empty thin-walled tube containing an OCF specimen (22 × 22 × 25 mm³). The inner surfaces of the thin-walled tubes were previously cleaned, polished, and greased to facilitate the specimen removal. The components A and B were mixed together well at the mass ratio of 2:1. In the case of the nEP specimens, the EP component A was first mixed together well with the GO with a mechanical stirrer at 1000 rpm for 1 h. After that, the mixture was submitted for 30 min to an ultrasonic bath and another 1 h to mechanical stirring. Then, component B was added and mixed with a mechanical stirrer at 250 rpm for 10 min to avoid bubble formation, followed by 20 min of degassing under vacuum. The specimens were extracted

from the thin-walled tubes after the filler polymer was completely cured (at room temperature for 7 days).

Preliminary uniaxial quasi-static tests at 0.1 mm/s and Vickers hardness were carried out to assess the dispersion of the GO into the EP. For this purpose, three compositions of GO were tested: 0.1, 0.25, and 0.5 wt.%. These concentrations of GO were in the final epoxy (A + B) mixture. Figure 7.1 shows the fabricated specimens: OCF (Figure 7.1a), pure EP (Figure 7.1b), nEP (Figure 7.1c), HSEP (Figure 7.1d), and HS-nEP (Figure 7.1e).

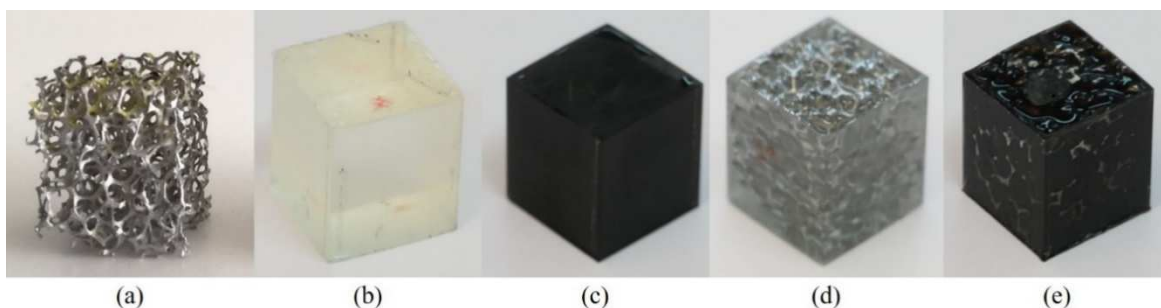


Figure 7.1 Fabricated specimens (22 mm × 22 mm × 25 mm): OCF (a), EP (b), nEP (c), HS-EP (d) and HS-nEP (e).

The densities of the materials were: 105.1 kg/m³ (standard deviation: 2.1 kg/m³), 1105 kg/m³ (standard deviation: 29.7 kg/m³), 1130.3 kg/m³ (standard deviation: 6.1 kg/m³), 1162.4 kg/m³ (standard deviation: 14.3 kg/m³), and 1169.3 kg/m³ (standard deviation: 7.7 kg/m³) for the OCF, EP, nEP, HS-EP, and HS-nEP, respectively.

7.3.3. Morphologic Characterization

To investigate the dispersion of the GO into the EP matrix, Scanning Electron Microscopy (SEM) analysis was applied. The TM 400 Plus (Hitachi, Tokyo, Japan) was used at an accelerating voltage of 15 kV and in backscattering electron mode.

The specimens (22 × 22 × 25 mm³) were analysed in a micro-computed tomography (μCT) equipment from SkyScan 1275 (Bruker, Belgium) with penetrative X-rays of 80 kV and 125 μA, 1 mm Al filter, in a high resolution mode with a pixel size of 18 μm and 45 ms of exposure time. NRecon (Bruker, Belgium), CTVox (Bruker, Belgium), and CTAn (Bruker, Belgium) softwares were used for slicing, three-dimensional (3D) reconstruction, and morphometric analysis.

7.3.4. Mechanical Characterization

Uniaxial compression tests were used to study the quasi-static compressive response of the hybrid structures (HS-EP and HS-nEP) and the individual components (OCF, EP, and nEP). The servo-hydraulic dynamic INSTRON 8801 testing machine (Instron, Norwood, MA, United States of America) with maximum load 50 kN and the electro-mechanical RAAGEN testing machine (RAAGEN Material Testing Machines, Ankara, Turkey) with maximum load 250 kN were used for quasi-static tests at 0.1 mm/s and 1 mm/s loading rates, respectively. The quasi-static tests were recorded by using a high-resolution video camera. A high cooled middle-wave infrared (IR) thermal camera FLIR SC 5000 [22] was also used to study the deformation and failure modes of the specimens subjected to the loading rate of 1 mm/s. The IR camera detected IR energy emitted from objects, converted it to temperature, and displayed an image of temperature distribution from the specimen surface. Temperature was measured in real time from a fixed distance without contacting the specimen. The load–displacement data were converted to the engineering stress–strain data. The energy absorption density (EAD) and specific energy absorption (SEA) were determined according to the ISO 13314: 2011 [23]. Vickers hardness measurements were carried out on samples using a diamond Vickers indenter Tester HMV-2000 (Shimadzu, Kyoto, Japan) where a 0.025 kgf load was applied for 10s.

7.3.5. Thermal and Flammability Characterization

The thermal stability of the EP and nEP was assessed by a thermogravimetric (TG) analyser (Netzsch, Selb, Germany) at a scanning rate of 10 °C/min, in the temperature range of 30–800 °C, under 50 mL/min of synthetic air (80% of N₂ and 20% O₂). The dynamic scanning calorimetry (DSC) method was used in order to measure cure heat (ΔH). The DSC analysis was carried out using the Perkin Elmer 4000 device (Perkin Elmer, Buckinghamshire, UK). Immediately after adding the hardener, the EP and nEP resins were submitted to a heating cycle from 30 to 220 °C with a heat rate of 10 °C/min under nitrogen atmosphere. The thermal conductivity properties were evaluated with the Hot Disk TPS 2500 S instrument (Hot Disk, Gothenburg, Sweden) in the transient mode, at room temperature (20 °C), in accordance with the standards ISO 22007-2.2 [24] and ASTM D7984 [25]. The sensor, a thin nickel foil in a double spiral pattern, which was embedded in between two thin layers of Kapton polyimide protective films, was sandwiched between two identical samples (22 × 22 × 25 mm³). Three measurements

were performed for each specimen type. During the measurement, electrical heat current passed through the nickel spiral and created an increase in temperature. The heat generated dissipated through the sample on either side at a rate which depended on the thermal transport characteristics of the material. By recording the temperature versus time with the sensor, these characteristics could accurately be calculated by a computational algorithm based on Hot Disk Thermal analyser software.

The fire retardancy tests were based on the direct observation of the response of the specimens when subjected to a flame. Each test consisted of applying an ethanol flame to the specimen's bottom using the set-up in the vertical sample position. A test lasted for 3 s, plus a subsequent application of 3 s if the specimen self-extinguished.

7.3.6. Acoustic Characterization

The value of the sound absorption coefficient was estimated from measurements made with an impedance tube according to the standard ASTM E 1050 [26]. The cylindrical specimens had a diameter of 37 mm and a height of 22 mm. The tests consisted of placing the specimens at the end of an impedance tube with a diameter of 37 mm [27] and a length of 700 mm. The sound source, an RG10 noise generator that emits a random noise signal, connected to a loudspeaker, was positioned at the opposite end of the impedance tube. Two microphones were placed inside the tube, separated by 30 mm between the sound source and the specimen, allowing to analyse a frequency range between 115 and 4500 Hz. The measurement allowed calculation of the sound absorption coefficient (α), which refers to the ratio between the amount of sound energy that is dissipated or absorbed by a given material and the sound wave that is passed to the material. The higher the sound absorption coefficient value, the greater the effectiveness of the insulation. Another parameter is the noise reduction coefficient (NRC) indicator, which is the arithmetic mean value of the sound absorption coefficients at frequencies of 250, 500, 1000, and 2000 Hz, and is used to compare and evaluate the performance of commercial materials.

7.4. Results and Discussion

7.4.1. Weight Ratio of the Graphene Oxide

In order to ensure an uniform dispersion of the GO within the EP, a preliminary study was performed by using quasi-static uniaxial compression and Vickers hardness (HV)

tests. For that, three compositions of GO were tested: 0.1, 0.25, and 0.5 wt.%. Visually, it was observed that until 0.25 wt.%, the dispersion of the GO was satisfactory, with no aggregates observed. Above 0.25 wt.% of GO, the formation of several aggregates was observed and persisted even after vigorous mechanical stirring. Figure 2 shows the average compressive stress–strain curves (Figure 7.2a) and the HV values (Figure 7.2b) measured for dense unreinforced EP and reinforced EP with different amounts of GO. Results clearly indicate that the diagram shape of the stress–strain curves of the unreinforced and reinforced EP are similar. The reinforced EP shows an inferior stress–strain behaviour when compared to the EP without GO. However, stress–strain curves of the reinforced EP with 0.25 wt.% and 0.5 wt.% are more stable when compared to the unreinforced (pure) EP, in which the first peak stress values are similar (~80 MPa). Furthermore, after the second peak stress, the reinforced EP compositions show a lower decrease in stress in comparison to the unreinforced EP specimens. This could be attributed to the development of pores in the region near to the GO region. The specimen with 0.25 wt.% of GO showed a HV value of 17.7, which is 10% higher than the value 16.1 obtained for the pure EP. The values are in agreement with the one reported by Ho and co-workers [28]. It appears that the GO additions significantly increase the variability in the hardness, since also high standard deviation was observed. The high variability of the hardness may be attributed to the GO dispersion in the polymer matrix, which can affect the final properties. Based on these preliminary results, the 0.25 wt.% of GO was selected as the composition for the specimens in subsequent studies and is denoted from now on by nEP and HS-nEP.

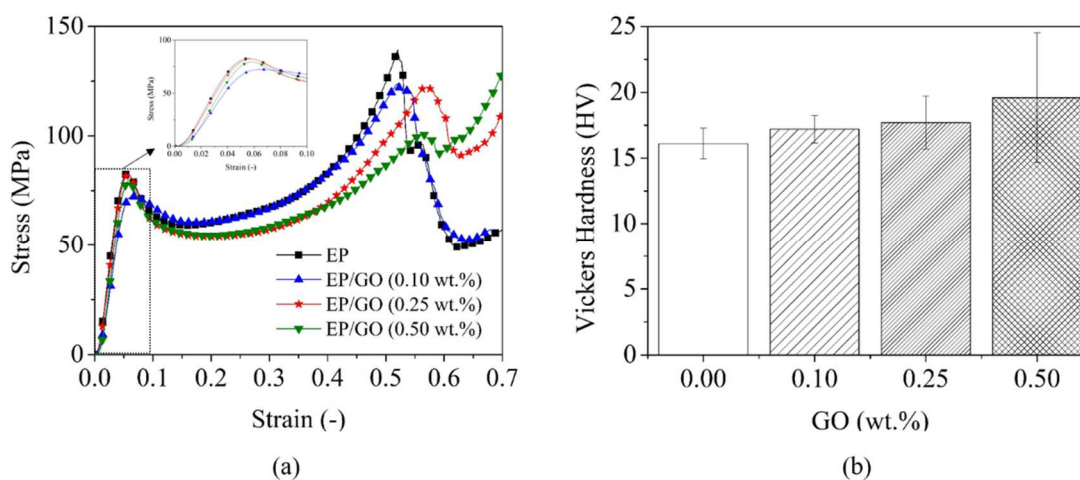


Figure 7.2 Quasi-static compressive stress-strain curves (a) and Vickers Hardness (b) of the unreinforced EP and reinforced EP with different compositions of the GO.

7.4.2. Microstructure

The representative scanning electron microscopy (SEM) images in Figure 7.3 show fractured cross-section of the EP and nEP specimens, which were obtained by breaking of the frozen specimens under liquid nitrogen. The results show that the GO sheets are well dispersed and randomly oriented within the polymer. No aggregates are visible in the SEM images. As shown in Figure 7.3a, the fracture surface of the unreinforced EP exhibits low river patterns and a smooth surface. Additionally, the cracks spread randomly, revealing a weak resistance to the crack initiation and propagation within EP. The failure process of unreinforced EP is a typical brittle fracture pattern, as reported by other authors [29]. Contrary, the nEP composites exhibit a rougher fracture surface (Figure 7.3b) and several river patterns, in which numerous and deep cracks can be observed. It seems that a continuous network of the GO was not formed due to the low content of GO. Furthermore, at higher magnification (Figure 7.3c), the presence of GO agglomerates within the EP matrix is not observed.

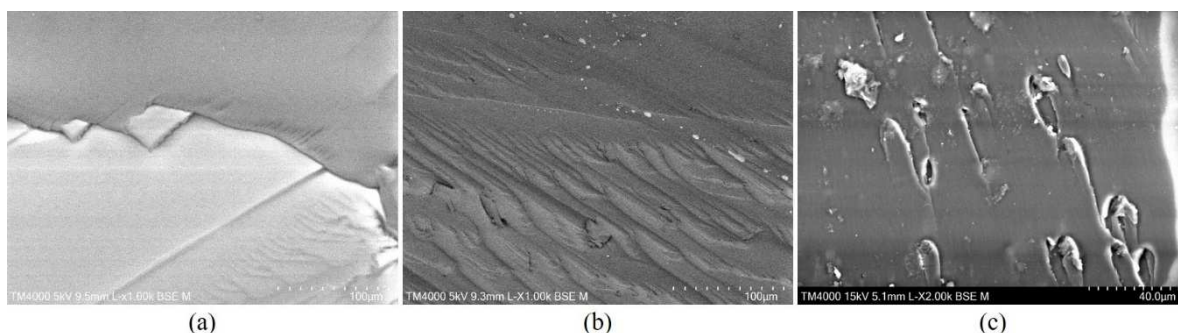


Figure 7.3 SEM images of the EP (magnification factor: 1000) (a) and nEP matrices (magnification factor: 1000 (b) and 2000 (c)).

The μ CT results reveal that the values of the total porosity of HS-nEP and HS-EP are 0.008% and 0.048%, respectively. Despite that both types of specimens present very low values, the HS-nEP has a higher percentage of total porosity that can be attributed to the formation of the voids in the EP matrix due to the GO. Figure 7.4 presents a 2D slice and 3D volume rendered image of the HS-nEP hybrid structures, using the NRecon and CTvox, respectively.

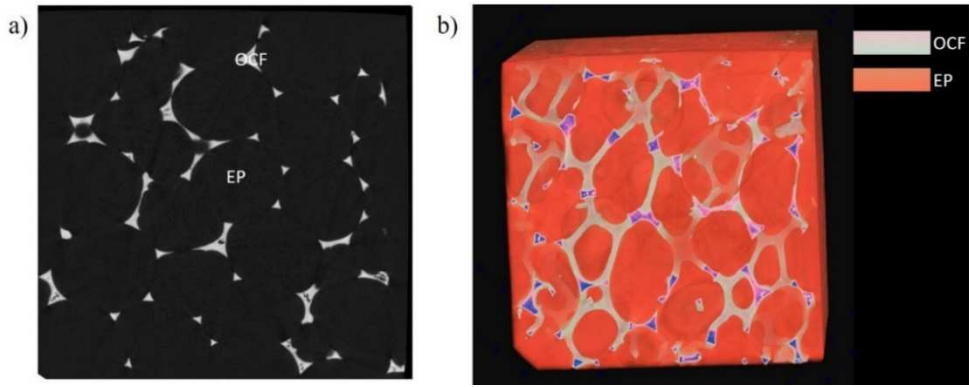


Figure 7.4 Micro-computed tomography images 2D slice (a) and 3D volume rendering of HS-nEP (b).

7.4.3. Mechanical Properties

This study is the continuation of the study conducted by Duarte *et al.* [8], in which the OCF voids were filled with EP. Herein, however, GO was added to the EP matrix to increase the toughness and provide thermal stability. The EP and nEP specimens, as well as their respective hybrid structures (HS-EP and HS-nEP), were subjected to uniaxial compression loading at two different deformation rates. Figures 7.5 and Figure 7.6 show the deformation stages during the quasi-static loading at 0.1 mm/s and 1 mm/s, respectively.

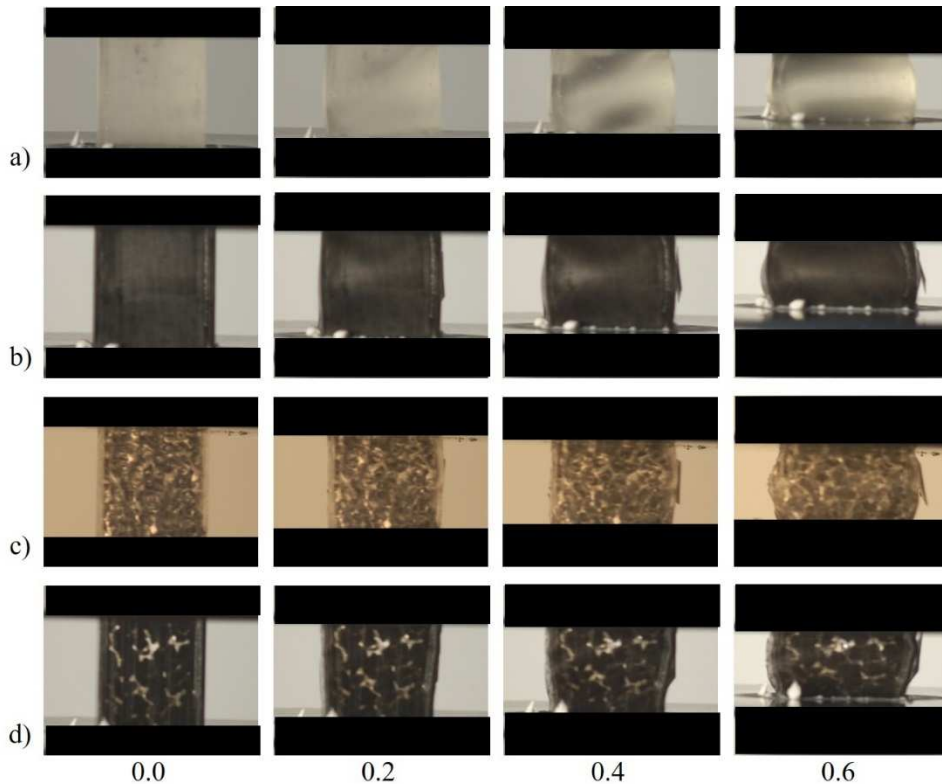


Figure 7.5 The quasi-static deformation (0.1 mm/s) sequences showing the progressive deformation of the: EP (a), nEP (b), HS-EP (c) and HS-nEP (d).

The EP, nEP, HS-EP, and HS-nEP exhibited symmetric deformation, i.e., barrelling in the centre of the specimen during the slower loading rate (0.1 mm/s). Contrary, at loading rate of 1 mm/s, asymmetric deformation was observed. However, the incorporation of 0.25 wt.% of GO had no significant influence on the deformation mode for both tested velocities. Furthermore, the IR thermography (Figure 7.7) also allowed to study the deformation and failure modes of the hybrid structures (HS-EP, and HS-nEP) at low crosshead rates (1 mm/s), as it was also confirmed in [30].

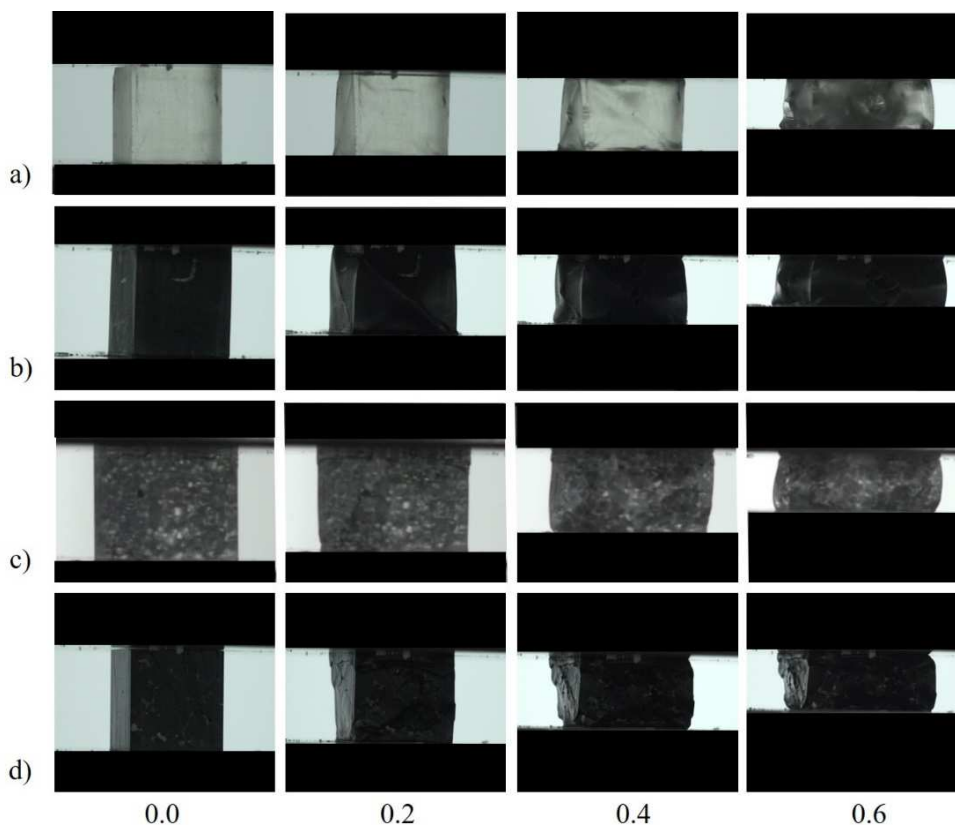


Figure 7.6 The quasi-static deformation (1 mm/s) deformation sequences showing the progressive deformation of the: EP (a), nEP (b), HS-EP (c) and HS-nEP (d).

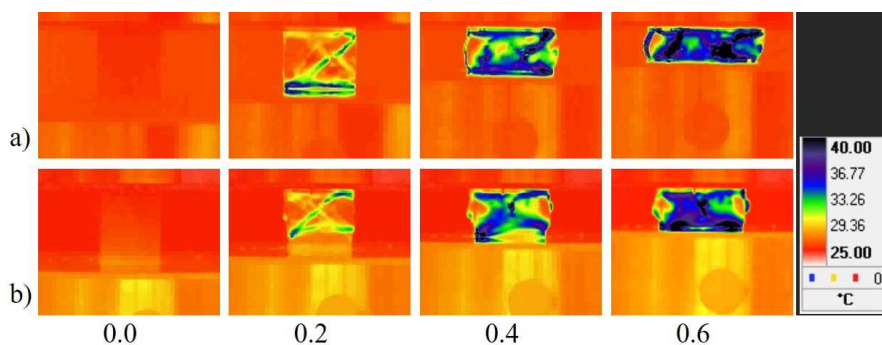


Figure 7.7 The IR image sequences at different strain increments showing the dynamic progressive deformation of the: HS-EP (a) and HS-nEP (b) subjected to a crosshead rate of 1 mm/s.

The regions subjected to higher strain were located near the metal foam skeleton and the specimens started to fail by development of cracks in the EP matrix. These cracks progressed and aggravated their amplitude and group until the final failure.

Figure 7.8 shows the quasi-static compressive stress–strain curves of the tested specimens (EP, nEP, HS-EP and HS-nEP) subjected to 0.1 mm/s (Figure 7.8a) and 1 mm/s (Figure 7.8b).

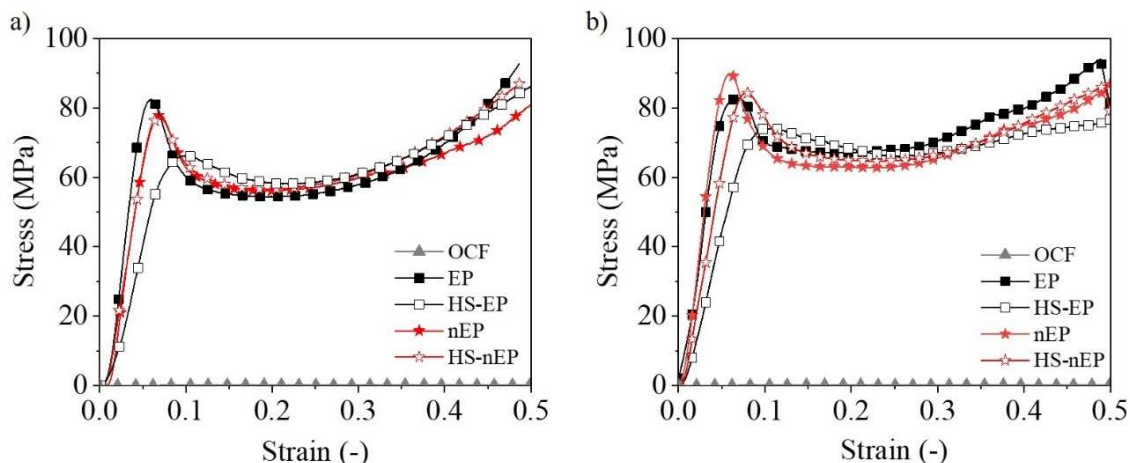


Figure 7.8 Stress-strain relationship (each curve represents an average of three specimens tested) at different crosshead rates:(a) 0.1 mm/s and (b) 1 mm/s.

Quasi-static compressive stress–strain curves (Figure 7.8a,b) show very similar diagram shapes between EP, nEP, HS-EP, and HS-nEP for both loading rates. The EP and nEP specimens, as well as the corresponding hybrid structures (HS-EP, and HS-nEP), do not exhibit a typical metal foam stress–strain behaviour. The compressive stress–strain curves of the EP, nEP, HS-EP, and HS-nEP specimens are very similar to the compressive response obtained from the empty aluminium tubes, *in-situ* closed-cell foam-filled tubes and polymer-open-cell aluminium foam-filled tubes [21,31,32]. The initial quasi-linear elastic region up to the peak stress is followed by a rapid stress drop region to a given minimum value of stress, and then by the stress fluctuation region until the abrupt final densification. These results are also in agreement with the previous results [8], in which the HS-EP specimens reach high values of the initial peak stress (~75 MPa). The experiments conducted at 0.1 mm/s revealed that the first peak stress values of 82.5 and 78.6 MPa were obtained for strain values of 0.060 and 0.067 for the EP and nEP, respectively. It is noteworthy to state that the stress values for the EP are in agreement with those in the literature [8]. The EP is a polymer composed of long carbon chains with

strong chemical bonds between the carbon atoms and oxygen (epoxy groups). Thus, the EP is a tough and brittle polymer, resulting in high stress values during loading [33]. The decrease in the peak stress at the incorporation of GO, even at low loading velocity, can be attributed to some voids created in the EP and to the fact that GO can decrease the high crosslinking of the EP chains during curing process. Simultaneously, the strain at the peak stress is higher for the nEP, suggesting a higher mobility of molecule chains. The stress–strain behaviour of the OCF structure ($22 \times 22 \times 25 \text{ mm}^3$) shows a significant lower stiffness ($\sim 0.31 \text{ MPa}$), which was already described in [8].

The compressive behaviour of the hybrid structures is mainly governed by the filling polymer, EP and nEP, since similar profile curves were obtained with and without the OCF. The peak stress values of HS-EP were 66.21 MPa (0.1 mm/s) and 73.95 MPa (1 mm/s), while the peak stress values of HS-nEP were 77.39 MPa (0.1 mm/s) and 84.25 MPa (1 mm/s). Interestingly, slightly inferior peak stress values were obtained since the OCF structure acts like a defect (confirmed by IR tomography), since the EP has a much higher stiffness than the OCF. In comparison with the OCF, the hybrid structures present a significant increase in strength and a different stress–strain response. Comparing the OCF with the filled ones, an increase of the peak stress of more than 40 times was registered. In the case of the hybrid structures, high peak stresses occurred for low strain rates, followed by a minor decrease in stress until 0.25 of strain, after which the stress started to increase again up to the densification. The decrease after the first peak is related to the initial formation and propagation of cracks, which is a typical behaviour of the brittle cured EP. All specimens are strain rate sensitive. Globally, the specimens subjected to 1 mm/s show a higher stiffness in comparison to the ones subjected to 0.1 mm/s .

The energy absorption density (EAD) to strain relationship for the tested specimens is shown in Figure 7.9. The EAD curves of the hybrid structures were compared to the EAD curves of the pure EP specimens. The EAD curves were calculated by integrating the compressive stress–strain curve from undeformed state up to the strain corresponding to the second stress peak of each test. Specific energy absorption (SEA) was obtained by dividing energy absorption with the mass of each corresponding specimen.

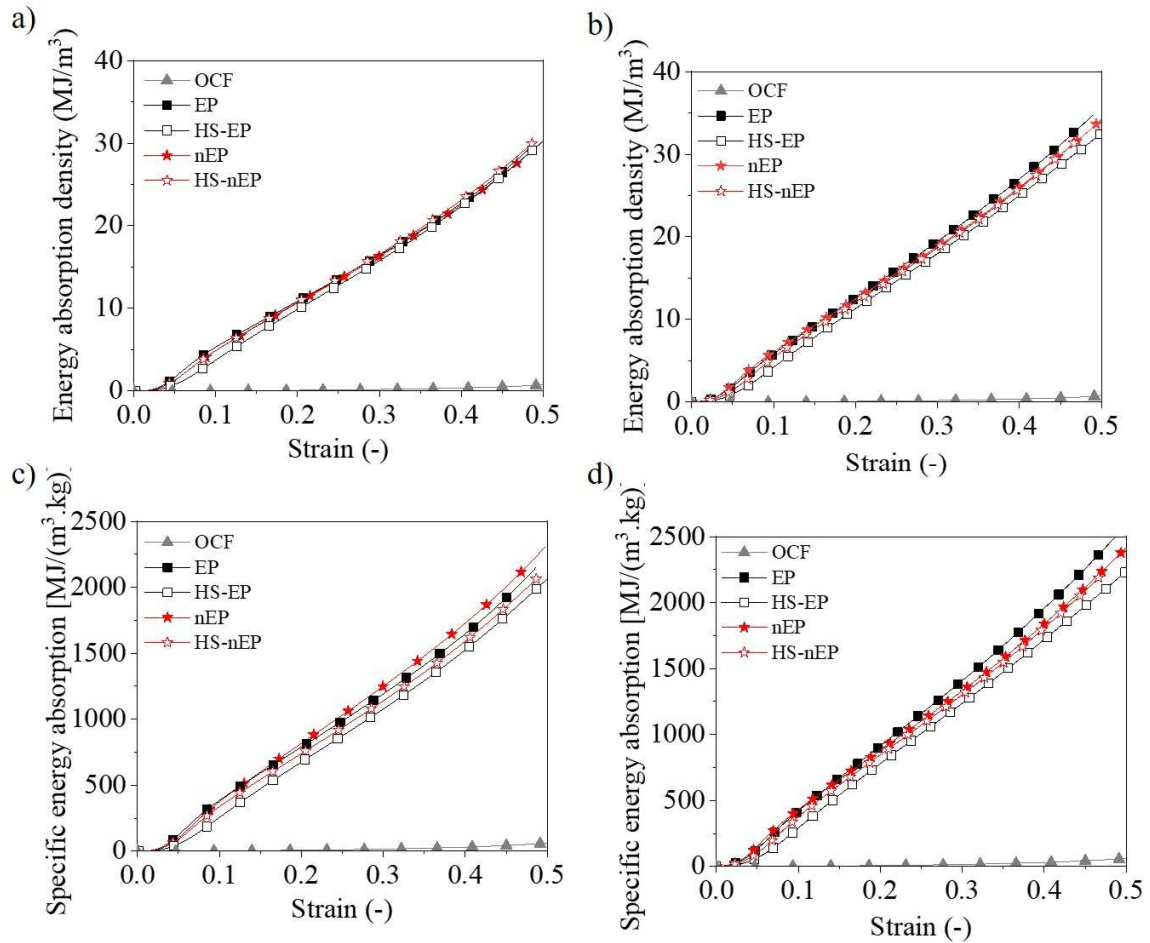


Figure 7.9 Average energy absorption and specific absorption energy capacity at crosshead rate of 0.1 mm/s (a, c) and 1 mm/s (b, d).

From Figure 7.9, it can be observed that the EP and nEP significantly contribute to the increase of the energy absorption in comparison to the OCF (Figure 7.9a) and that the increase is linear for all samples at both crosshead rates. The linear energy absorption curves indicate that these hybrid structures are ideal materials to be used as energy absorbers. The hybrid structure specimens present very high energy absorption capacity (Figure 7.9b) when compared to the OCF, and even if compared to the closed-cell aluminium foam [30]. It can be observed that the polymer filler, either EP or nEP, greatly contributes to the increase of the energy absorption capacity of the OCF specimens. However, there is a negligible difference between EP and nEP with or without OC skeleton (HS-EP and HS-nEP). Comparing the materials with and without the OCF, the values of EAD and SEA are similar, which indicates that the mechanical properties are governed by the polymer. However, the higher energy absorption capacity (Figure 7.9c,d) compensates for the increase in higher mass of the specimens. The incorporation of GO

does not reveal a significant increase in the mechanical properties. From the diagrams, it was also observed that the energy absorption capacity is also strongly strain rate sensitive.

7.4.4. Thermogravimetric Properties

Figure 7.10a contains the thermogravimetric (TG) and derivative thermogravimetric (DTG) curves of the EP and nEP specimens under synthetic air atmosphere. The EP and nEP specimens show the typical degradation curve of the EP in air atmosphere, with expected three mass loss steps [34]. Both specimens exhibit similar thermal response, since the plotted curves are practically overlapping and suggesting that the presence of GO did not significantly change the degradation mechanism of the EP matrix and that GO is well mixed within the EP matrix.

The first mass loss was observed between 100–250 °C and represents approximately 20% of its total mass initiated by degradation of the weakest and unstable linkages, oxygen functional groups (hydroxyl, carboxyl, and carbonyl groups), and the unreacted epoxy or any other impurity traces that began to decompose. The unstable oxygen functional groups transformed into CO, CO₂, and water vapor. As temperature further increased, the main major mass loss (300–380 °C) occurred in which the DTG peaks are 358 and 354 °C for EP and nEP, respectively. This can be attributed to the degradation of the main epoxy chain. The final weight lost, 450–600 °C, can be assigned to the degradation of the skeleton of the carbon atoms. The inclusion of GO 0.25 wt.% increased T₅₀ by 1 °C and decreased T₁₀ by 14 °C (Figure 7.10a). This reduction can be attributed to the defects generated in the EP network caused by possible agglomerated GO sheets (although not observed in the SEM analysis) or weak interaction between GO and the EP (weaker than the crosslinking of the EP monomer). A similar response was detected by Chhetri *et al.* [35]. However, in the temperature range between 420–520 °C, the thermal stability of the nEP was slightly improved in comparison to the EP. This might be attributed to a good dispersion of the GO into the EP matrix, which helped to develop efficient interfacial interaction within the nanocomposites. Furthermore, the high aspect ratio of the GO structure may also serve as barrier to prevent the diffusion of small gaseous molecules produced by the thermal degradation. The residue after 750 °C was less than 1% (0.25% for the EP and 0.30% for the nEP), since both specimens decomposed into gas such as CO₂ and water vapour.

7.4.5. Calorimetric Properties

Figure 7.10b shows the DSC heat flow curves obtained for the EP and nEP mixtures, immediately after adding the hardener. The heat of reaction (ΔH) was measured from the areas enclosed by the thermograms. During the curing reaction, the epoxy started to polymerize, cross-link, and then harden. The onset curing temperatures for both mixtures were located around 55 °C and the specimens were fully cured at 200 °C. The peak at which the cure reaction happened slightly decreased with the incorporation of GO, from 93.3 °C for EP to 92.4 °C to nEP. Although this temperature decrease is less than 1%, it is suggested that GO acts as a catalyst, accelerating the epoxy curing reaction. A similar behaviour was observed by Park and Kim [36], where a decrease of 2 °C was found with the incorporation of 0.5 wt.% of graphene nanoplatelets. These authors suggested that the interactions between the amino groups present in EP resin and the remaining hydroxyl groups in graphene nanomaterial are the main reason for the lowering in peak temperature. Regarding the ΔH associated with the cure reactions, the ΔH value decreased from 312.6 for EP to 290.0 J/g for nEP, suggesting that GO interferes with the cure reaction of EP. The steric hindrance effect of GO resulting from the high surface area of GO nanosheets could have contributed to the lower cross-linking degree in the EP mixture [37,38]. Galpaya *et al.* [39] reported declines of 14%, from 137.1 to 117.3 J/g, in ΔH of curing in epoxy matrices with the incorporation of only 0.3 wt.% of GO.

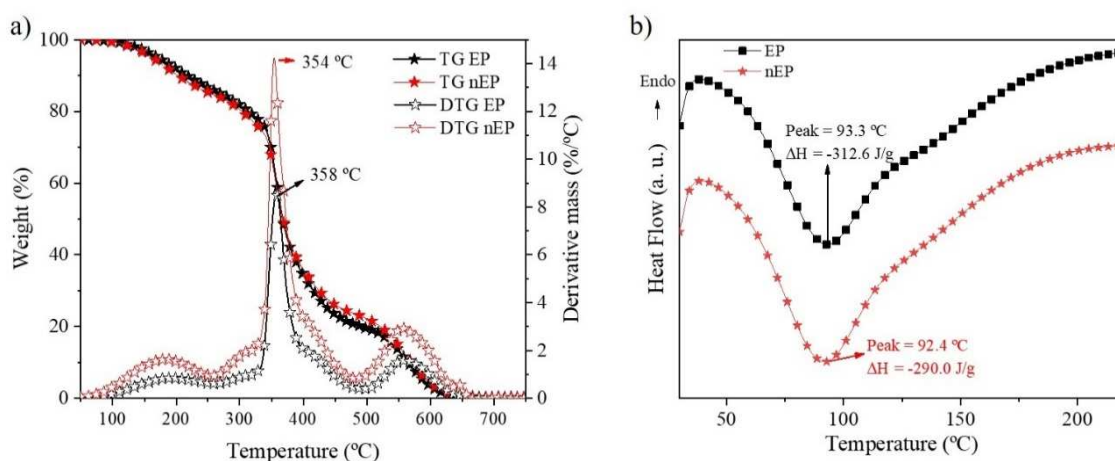


Figure 7.10 Thermograms (a) and DSC curves (b) of the EP and nEP matrices.

7.4.6. Thermal Properties

Figure 7.11a shows the thermal conductivity values of the tested specimens. The thermal conductivity values obtained for the EP specimens (0.20 W/m·K) are in accordance with the values reported in literature (0.15–0.20 W/m·K) [40]. With the incorporation of 0.25 wt.% of GO, a slight increase of approximately 10% relative to the pure EP specimens was observed. The study by Aradhana *et al.* [41] reported an increase of more than 200% in thermal conductivity with 0.5 wt.% of GO within the EP. An increase of 20% and 90% in thermal conductivity was obtained by Kim *et al.* [42] for 1 wt.% and 3 wt.%, respectively. Both studies stated the importance and the key role of GO dispersion for the increase of thermal conductivity. SEM analysis can be helpful to understand the reason for a smaller increase of the thermal conductivity in this study. The content of GO used in this work is lower than in the described studies and might be too low to allow the formation of a conductive network that would provide an effective pathway for the phonon movement in the insulator matrix, leading to higher thermal conductivity values. On the other hand, even a low level of GO in the EP could result in the formation of aggregates, due to the high content of oxygen functionalities and ability to form intra/intermolecular bonds that restrict heat transport. Aggregates reduce the aspect ratio, decrease the contact area, and trap or scatter phonons [35]. The thermal conductivity value of the hybrid structures raised up to 0.32 and 0.40 W/m·K without and with GO, respectively. The presence of the interconnected OCF structure facilitated the heat transfer and promoted a substantial increase of approximately 60% in thermal conductivity. The presence of the GO seems to reduce the interfacial resistance and enhance heat flow [43,44]. In this case, the enhancement was approximately 100% compared to the nEP.

7.4.7. Acoustic Properties

The sound absorption coefficient values are represented in Figure 7.11b, displaying the measured values for samples EP, HS-EP, nEP, and HS-nEP. In general, it should be said that the values of sound absorption coefficient registered for all samples are quite low (lower than 0.3) throughout the frequency range, which is attributed to the non-porous and high stiff structure of the EP matrix.

Indeed, when the sound absorption curve determined for the EP sample was analyzed, very low values were registered, generally below 0.05, and with only two small peaks (at

500 and 3500 Hz) exhibiting a value around 0.1. The isolated addition of both the OCF skeleton and of the GO reinforcement seemed to be beneficial in what concerns sound absorption, although with a concentrated effect around the first peak occurring at a lower frequency. Further improvement was obtained when both the OCF skeleton and the GO reinforcement were used (HS-nEP), for which case, a maximum peak around 0.25 at 750Hz was registered, and with higher absorption at a somewhat broader frequency range (values above 0.1 were registered between approximately 500 and 1500 Hz). Interestingly, high frequency sound absorption was very low (below 0.1 in all cases), a behaviour that can, once again, be strongly related to the low porosity and high stiffness of all samples. This behaviour contrasts with the typical sound absorption of porous and fibrous materials (broadly used in acoustic applications), which may exhibit peak sound absorption values around 1.0, and allow significant high frequency sound absorption (see, for example, the reference book by Cox and d'Antonio [45]).

To better understand the above-described behaviour, it is important to bear in mind that sound waves propagate fast in solid materials, but not as much in air and liquids. When the sound wave hits a solid surface, the material vibrates, the molecules that compose the material collide between each other, and the kinetic energy resulting from those collisions is passed from molecule to molecule. The transfer/transmission of energy is higher when molecules are closer to each other and have stronger bonding [5,6]. Chemically, the EP is composed of long carbon chains with very strong chemical bonds between the carbon atoms [33], and therefore lacks in chain mobility and high transmission of energy. The incorporation of GO introduces voids into the EP matrix, increasing the chain mobility, and when the sound propagates through the voids, oscillations of air molecules occur, leading to a frictional loss. Furthermore, the inclusion of GO can contribute to a rougher surface, which also results in a higher sound absorption coefficient. The hybrid structures present a higher sound absorption coefficient, since the OCF structure allows for a higher chain mobility, while in the filling process, some voids are additionally introduced at the metal–polymer interface. The noise reduction potential of cellular metals was studied by Hinze *et al.* [46] using the impedance method. They demonstrated that the acoustic absorption mainly depends on pore morphology, porosity, and the thickness of the specimen. They reported that the acoustic absorption is only achieved if sound waves can cross through the absorber. The reflection of sound waves from the absorber surface is reduced if the porosity of absorbers is high (80 to 95%). Also,

similar sound absorption levels with material containing bigger pores are achieved if the thickness of the absorber is high.

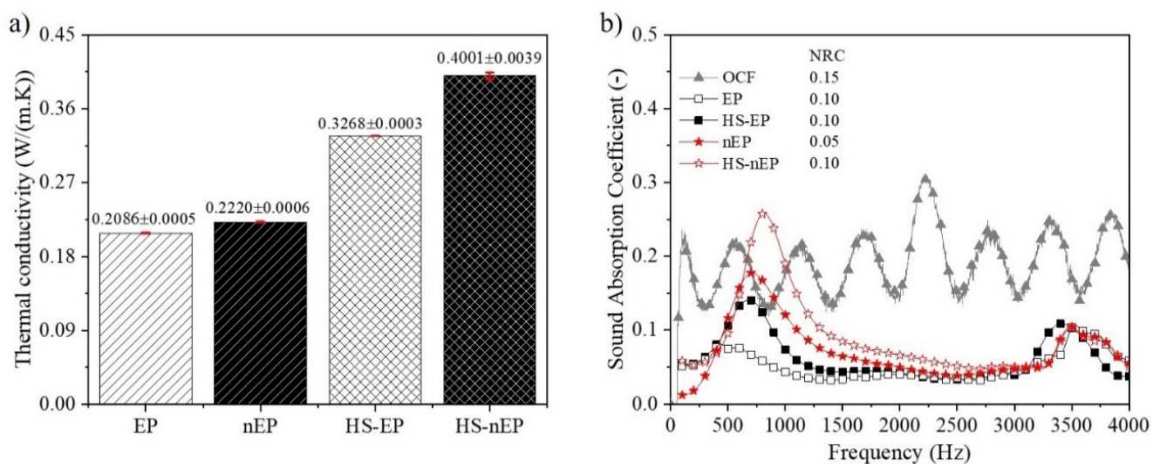


Figure 7.11 Thermal conductivity (a) and sound absorption capacity (b) of the OC, EP, nEP, HS-EP and HS-nEP.

7.4.8. Fire-Retardant Properties

The EP presents high flammability, as reported in literature [47]. Figure 7.12 shows the burning behaviour of the EP and nEP. For the EP specimen, the flame self-extinguishes after 5 s; in the case of nEP, the flame self-extinguishes after only 3 s, suggesting a better (flame-retardant) behaviour of GO.

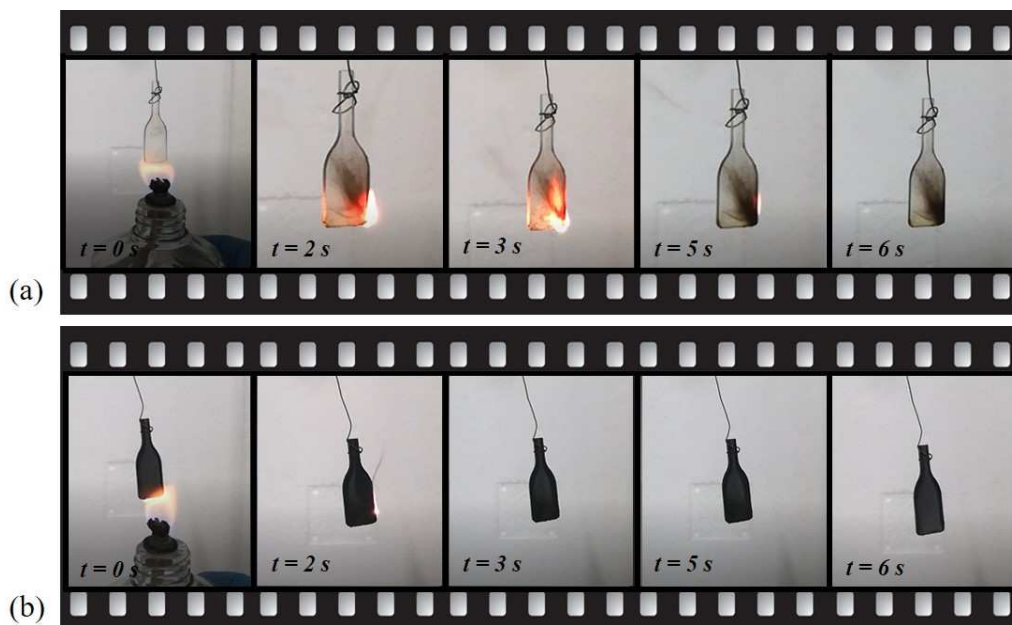


Figure 7.12 Fire-retardant behaviour of the: EP (a) and nEP (b).

Several authors have focused on the enhancement of polymers' fire-retardant properties. The incorporation of graphene and its derivatives can improve fire-retardant properties by forming a char layer on the surface of the polymer that avoids or delays the escape of volatiles from the decomposition process by creating a complex path. As such, it reduces the volatiles in gaseous phase available for fire propagation and returns heat back to the surface of the polymer [48,49]. Since GO presents no toxicity or environmental issues, it presents great potential to be one of the most promising fire-retarding fillers for epoxy nanocomposites [36].

7.5. Conclusions

This work analyses the influence of GO that was carefully dispersed in the EP matrix on the mechanical, thermal, and sound absorbing properties. For that purpose, the EP and GO dispersed within the EP (nEP) and the hybrid structures, the HS-EP and HS-nEP (EP and nEP infiltrated in the OCF), were fabricated and tested. The motivation of this work was to study the influence of the incorporation of GO within the EP to obtain superior mechanical, thermal, and acoustic properties for advanced multifunctional structures. The main results of the study allow to point out the following conclusions:

- The EP, nEP, and the epoxy–aluminium hybrid structures (HS-EP and HS-nEP) are sensitive to strain rate.
- The presence of the EP and nEP decreases the oscillations in stress plateau that are usually observed in the OCF, since the shape of the stress–strain diagram is governed by the characteristics of the polymer filler.
- The presence of the EP increases the compressive strength and energy absorption of the OCF.
- The use of GO as a reinforcement of the EP matrix decreases the compressive strength at quasi-static uniaxial mechanical tests, thus no significant increase in the energy absorption capability was observed.
- GO induces thermal stability to the EP, as observed by TGA and fire-retardant tests.

- The thermal conductivity increases with the addition of GO, and the hybrid structures present even higher thermal conductivity due to the presence of the OCF skeleton.
- Although the sound absorption of the specimens was low, it was noted that the nanofillers, as well as the aluminium structure, increase the sound absorption coefficient, especially at low frequencies.

7.6. References

- [1] J. Banhart, "Manufacture, characterisation and application of cellular metals and metal foams," *Prog. Mater. Sci.*, vol. 46, no. 6, pp. 559–632, Jan. 2001.
- [2] L.-P. Lefebvre, J. Banhart, and D. C. Dunand, "Porous Metals and Metallic Foams: Current Status and Recent Developments," *Adv. Eng. Mater.*, vol. 10, no. 9, pp. 775–787, Sep. 2008.
- [3] I. Duarte, M. Vesenjajk, and M. J. Vide, "Automated Continuous Production Line of Parts Made of Metallic Foams," *Metals (Basel)*, vol. 9, no. 5, p. 531, May 2019.
- [4] J. Banhart and J. Baumeister, "Production Methods for Metallic Foams," *MRS Proc.*, vol. 521, p. 121, Feb. 2011.
- [5] B. J. Banhart, "Metal Foams : Production and Stability," *Adv. Eng. Mater.*, no. 9, pp. 781–794, 2006.
- [6] M. Ulbin et al., "Detailed Analysis of Closed-Cell Aluminum Alloy Foam Internal Structure Changes during Compressive Deformation," *Adv. Eng. Mater.*, vol. 20, no. 8, p. 1800164, 2018.
- [7] I. Duarte, N. Peixinho, A. Andrade-campos, and R. Valente, "Special Issue on Cellular Materials," *Sci. Technol. Mater.*, vol. 30, no. 1, pp. 1–3, 2018.
- [8] I. Duarte, M. Vesenjajk, L. Krstulović-Opara, and Z. Ren, "Crush performance of multifunctional hybrid foams based on an aluminium alloy open-cell foam skeleton," *Polym. Test.*, vol. 67, pp. 246–256, 2018.
- [9] K. Stöbener, D. Lehnhus, M. Avale, L. Peroni, and M. Busse, "Aluminum foam-polymer hybrid structures (APM aluminum foam) in compression testing," *Int. J. Solids Struct.*, vol. 45, no. 21, pp. 5627–5641, 2008.
- [10] I. Duarte, M. Vesenjajk, L. Krstulović-Opara, and Z. Ren, "Compressive performance evaluation of APM (Advanced Pore Morphology) foam filled tubes," *Compos. Struct.*, vol. 134, pp. 409–420, 2015.
- [11] I. Duarte and J. M. F. Ferreira, "2D Quantitative Analysis of Metal Foaming Kinetics by Hot-Stage Microscopy," *Adv. Eng. Mater.*, vol. 16, no. 1, pp. 33–39, 2014.
- [12] O. Friedl, C. Motz, H. Peterlik, S. Puchegger, N. Reger, and R. Pippan, "Experimental Investigation of Mechanical Properties of Metallic Hollow Sphere Structures," *Metall. Mater. Trans. B*, vol. 39, no. 1, pp. 135–146, 2008.
- [13] I. Duarte, L. Krstulović-Opara, and M. Vesenjajk, "Axial crush behaviour of the aluminium alloy in-situ foam filled tubes with very low wall thickness," *Compos. Struct.*, vol. 192, pp. 184–192, 2018.

- [14] M. F. Ashby and Y. J. M. Bréchet, "Designing hybrid materials," *Acta Mater.*, vol. 51, no. 19, pp. 5801–5821, Nov. 2003.
- [15] M. F. Ashby, *Materials Selection in Mechanical Design*. Elsevier Science, 2010.
- [16] X. Mi et al., "Fabrication of halloysite nanotubes/reduced graphene oxide hybrids for epoxy composites with improved thermal and mechanical properties," *Polym. Test.*, vol. 76, pp. 473–480, Jul. 2019.
- [17] A. Kausar, I. Rafique, Z. Anwar, and B. Muhammad, "Recent Developments in Different Types of Flame Retardants and Effect on Fire Retardancy of Epoxy Composite," *Polym. Plast. Technol. Eng.*, vol. 55, no. 14, pp. 1512–1535, Sep. 2016.
- [18] E. D. Weil and S. Levchik, "A Review of Current Flame Retardant Systems for Epoxy Resins," *J. Fire Sci.*, vol. 22, no. 1, pp. 25–40, Jan. 2004.
- [19] D. R. Bortz, E. G. Heras, and I. Martin-Gullon, "Impressive Fatigue Life and Fracture Toughness Improvements in Graphene Oxide/Epoxy Composites," *Macromolecules*, vol. 45, no. 1, pp. 238–245, Jan. 2012.
- [20] N. Domun, H. Hadavinia, T. Zhang, T. Sainsbury, G. H. Liaghat, and S. Vahid, "Improving the fracture toughness and the strength of epoxy using nanomaterials – a review of the current status," *Nanoscale*, vol. 7, no. 23, pp. 10294–10329, 2015.
- [21] I. Duarte, L. Krstulović-Opara, J. Dias-de-Oliveira, and M. Vesenjak, "Axial crush performance of polymer-aluminium alloy hybrid foam filled tubes," *Thin-Walled Struct.*, vol. 138, pp. 124–136, 2019.
- [22] L. Krstulović-Opara, M. Vesenjak, I. Duarte, Z. Ren, and Ž. Domazet, "Infrared Thermography as a Method for Energy Absorption Evaluation of Metal Foams," *Mater. Today Proc.*, vol. 3, no. 4, pp. 1025–1030, 2016.
- [23] ISO 13314:2011: Mechanical Testing of Metals-Ductility testing-Compression Tests for Porous and Cellular Metals; International Organization for Standardization: Geneva, Switzerland, 2011.
- [24] ISO 22007-2.2. Plastics - Determination of thermal conductivity and thermal diffusivity - Part 2: Transient plane heat source (hot disc) method.
- [25] ASTM D7984 Standard Test Method for Measurement of Thermal Effusivity of Fabrics Using a Modified Transient Plane Source (MTPS) Instrument thermal.
- [26] ASTM E1050-12 Standard Test Method for Impedance and Absorption of Acoustical Materials Using a Tube, Two Microphones and a Digital Frequency Analysis System. Iso
- [27] J. da Silva, "Metodologias experimentais para a determinação do coeficiente de absorção de sonora em materiais de construção," University of Coimbra, Coimbra, Portugal, 2008.
- [28] M.-W. Ho, C.-K. Lam, K. Lau, D. H. L. Ng, and D. Hui, "Mechanical properties of epoxy-based composites using nanoclays," *Compos. Struct.*, vol. 75, no. 1, pp. 415–421, 2006.
- [29] J. Tang, H. Zhou, Y. Liang, X. Shi, X. Yang, and J. Zhang, "Properties of Graphene Oxide/Epoxy Resin Composites," *J. Nanomater.*, vol. 2014, pp. 1–5, 2014.
- [30] L. Krstulović-Opara, M. Surjak, M. Vesenjak, Z. Tonković, J. Kodvanj, and Ž. Domazet, "Comparison of infrared and 3D digital image correlation techniques applied for mechanical testing of materials," *Infrared Phys. Technol.*, vol. 73, pp. 166–174, Nov. 2015.

- [31] I. Duarte, L. Krstulović-Opara, and M. Vesenjak, "Characterisation of aluminium alloy tubes filled with aluminium alloy integral-skin foam under axial compressive loads," *Compos. Struct.*, vol. 121, pp. 154–162, Mar. 2015.
- [32] I. Duarte, M. Vesenjak, L. Krstulović-Opara, and Z. Ren, "Static and dynamic axial crush performance of in-situ foam-filled tubes," *Compos. Struct.*, vol. 124, pp. 128–139, Jun. 2015.
- [33] Y. T. Park et al., "Epoxy Toughening with Low Graphene Loading," *Adv. Funct. Mater.*, vol. 25, no. 4, pp. 575–585, Jan. 2015.
- [34] S. Ma, W. Liu, C. Hu, Z. Wang, and C. Tang, "Toughening of epoxy resin system using a novel dendritic polysiloxane," *Macromol. Res.*, vol. 18, no. 4, pp. 392–398, Apr. 2010.
- [35] S. Chhetri, N. C. Adak, P. Samanta, N. C. Murmu, and T. Kuila, "Functionalized reduced graphene oxide/epoxy composites with enhanced mechanical properties and thermal stability," *Polym. Test.*, vol. 63, pp. 1–11, Oct. 2017.
- [29] J. Wei, T. Vo, and F. Inam, "Epoxy/graphene nanocomposites – processing and properties: a review," *RSC Adv.*, vol. 5, no. 90, pp. 73510–73524, 2015.
- [30] S. Ganguli, H. Aglan, P. Dennig, and G. Irvin, "Effect of Loading and Surface Modification of MWCNTs on the Fracture Behavior of Epoxy Nanocomposites," *J. Reinf. Plast. Compos.*, vol. 25, no. 2, pp. 175–188, Jan. 2006.
- [31] H. Hu et al., "Preparation and properties of graphene nanosheets–polystyrene nanocomposites via in situ emulsion polymerization," *Chem. Phys. Lett.*, vol. 484, no. 4–6, pp. 247–253, Jan. 2010.
- [3] D. Galpaya, M. Wang, G. George, N. Motta, E. Waclawik, and C. Yan, "Preparation of graphene oxide/epoxy nanocomposites with significantly improved mechanical properties," *J. Appl. Phys.*, vol. 116, no. 5, p. 53518, 2014.
- [6] S. Chhetri, P. Samanta, N. Chandra Murmu, S. Kumar Srivastava, and T. Kuila, "Electromagnetic interference shielding and thermal properties of non-covalently functionalized reduced graphene oxide/epoxy composites," *AIMS Mater. Sci.*, vol. 4, no. 1, pp. 61–74, 2016.
- [2] Y. T. Park et al., "Epoxy Toughening with Low Graphene Loading," *Adv. Funct. Mater.*, vol. 25, no. 4, pp. 575–585, Jan. 2015.
- [37] C.-C. Teng et al., "Thermal conductivity and structure of non-covalent functionalized graphene/epoxy composites," *Carbon N. Y.*, vol. 49, no. 15, pp. 5107–5116, Dec. 2011.
- [38] M. G. Prolongo, C. Salom, C. Arribas, M. Sánchez-Cabezudo, R. M. Masegosa, and S. G. Prolongo, "Influence of graphene nanoplatelets on curing and mechanical properties of graphene/epoxy nanocomposites," *J. Therm. Anal. Calorim.*, vol. 125, no. 2, pp. 629–636, Aug. 2016.
- [39] D. Galpaya, M. Wang, G. George, N. Motta, E. Waclawik, and C. Yan, "Preparation of graphene oxide/epoxy nanocomposites with significantly improved mechanical properties," *J. Appl. Phys.*, vol. 116, no. 5, p. 53518, 2014.
- [40] M. R. S. and S. M. Z. Craig Dixon, "Transient Plane Source Technique for Measuring Thermal Properties of Silicone Materials Used in Electronic Assemblies," *Int. Microelectron. Packag. Soc.*, vol. 23, 2000.
- [41] R. Aradhana, S. Mohanty, and S. K. Nayak, "Comparison of mechanical, electrical and thermal properties in graphene oxide and reduced graphene oxide filled epoxy nanocomposite adhesives," *Polymer (Guildf.)*, vol. 141, pp. 109–123, Apr. 2018.

- [42] J. Kim, B. Yim, J. Kim, and J. Kim, "The effects of functionalized graphene nanosheets on the thermal and mechanical properties of epoxy composites for anisotropic conductive adhesives (ACAs)," *Microelectron. Reliab.*, vol. 52, no. 3, pp. 595–602, Mar. 2012.
- [43] X. He et al., "Improved thermal conductivity of polydimethylsiloxane/short carbon fiber composites prepared by spatial confining forced network assembly," *J. Mater. Sci.*, vol. 53, no. 20, pp. 14299–14310, 2018.
- [44] Y.-F. Zhang, Y.-J. Ren, H.-C. Guo, and S. Bai, "Enhanced thermal properties of PDMS composites containing vertically aligned graphene tubes," *Appl. Therm. Eng.*, vol. 150, pp. 840–848, 2019.
- [45] T. J. Cox and P. D'Antonio, *Acoustic Absorbers and Diffusers: Theory, Design and Application*. Taylor & Francis, 2004.
- [46] B. Hinze, J. Rösler, and N. Lippitz, "Noise Reduction Potential of Cellular Metals," *Metals (Basel)*, vol. 2, no. 2, pp. 195–201, Jun. 2012.
- [47] B. Yu et al., "Enhanced thermal and flame retardant properties of flame-retardant-wrapped graphene/epoxy resin nanocomposites," *J. Mater. Chem. A*, vol. 3, no. 15, pp. 8034–8044, 2015.
- [48] S. Hamdani, C. Longuet, D. Perrin, J.-M. Lopez-cuesta, and F. Ganachaud, "Flame retardancy of silicone-based materials," *Polym. Degrad. Stab.*, vol. 94, no. 4, pp. 465–495, 2009.
- [49] B. Sang, Z. Li, X. Li, L. Yu, and Z. Zhang, "Graphene-based flame retardants : a review," *J. Mater. Sci.*, vol. 51, no. 18, pp. 8271–8295, 2016.

Chapter 8. General discussion, conclusions and future perspectives

This chapter is divided in three parts, the general discussion, where it is presented the main properties of the materials developed in the previous chapters (chapter 3 to chapter 7) and a brief comparison with other materials reported in literature. The main conclusions of the work developed in the last 4 years and several suggestions for future work were provided.

8.1. General discussion

The main contribution of this work consists in the development of novel hybrid structures based on cellular materials, producing materials with multiple functions and fill the knowledge gap that exists in its characterization by offering a broader characterization of this type of structures. It is intended to summarize the properties of the hybrid structures developed in the scope of this PhD, focusing in the density, mechanic, thermal and acoustic properties and compare them with the materials that already exists on the market and that are reported in the literature.

In order to simplify and make the discussion easier, here the designations of some specimens were changed. BC/GO10, HS-BC/GO10, PUF/GNPs2.5 and HS- PUF/GNPs2.5 were substituted by nBC, HS-nBC, nPUF and HS-nPUF, respectively.

8.1.1. Mechanical characterization

Figure 8.1 presents the Ashby chart constructed using the CES EduPack 2018, showing the compressive strength vs density chart. In this chart, the hybrid structures presented in the previous chapters are placed according to their compressive strength and density and are compared with the data gathered in the program database.

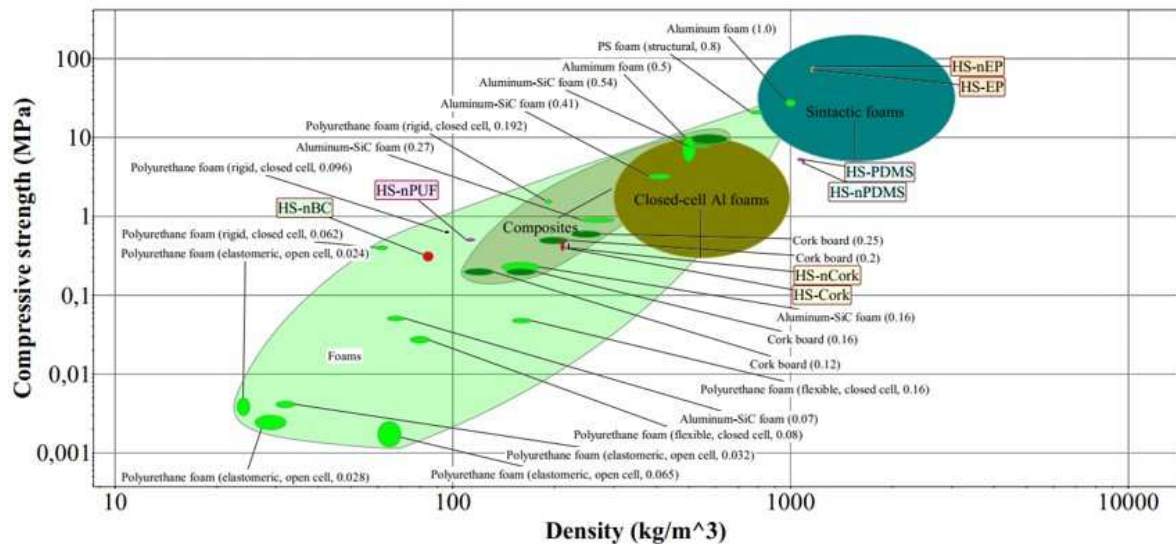


Figure 8.1 “Charts created using CES EduPack 2018, Granta Design Ltd: compressive strength vs density.

As expected, the developed hybrid structures within this PhD thesis occupy different areas in this chart, depending on the type of void filler (e.g. nanocomposites made of GBMs

with different polymers: BC foam, PUF, agglomerated cork, PDMS and EP). They show a wide range of densities, where the less dense materials, OCF filled with BC and PUF nanocomposites have densities closer to 100 kg/m^3 and compressive strength between 0.30 and 0.50 MPa. These materials are located inside de region of the foams, closely to rigid PUFs. HS-Cork and HS-nCork are in the composite's region near of the cork-based products, with densities around 220 kg/m^3 and compressive strength of 0.45 MPa. The hybrid structures prepared with EP have comparable compressive strength to syntactic foams and higher than the closed-cell metal foams. HS-PDMS and HS-nPDMS are placed between closed-cell metal foams and syntactic foams. Syntactic foams are clearly the ones presenting high compressive strength however having also high density. The energy absorption density (EAD) and specific energy absorption (SEA) of the specimens for strain 0.5 is shown in Figure 8.2. The materials that exhibit high compressive behaviour have potential to absorb more energy (as corroborated by EDA and SEA).

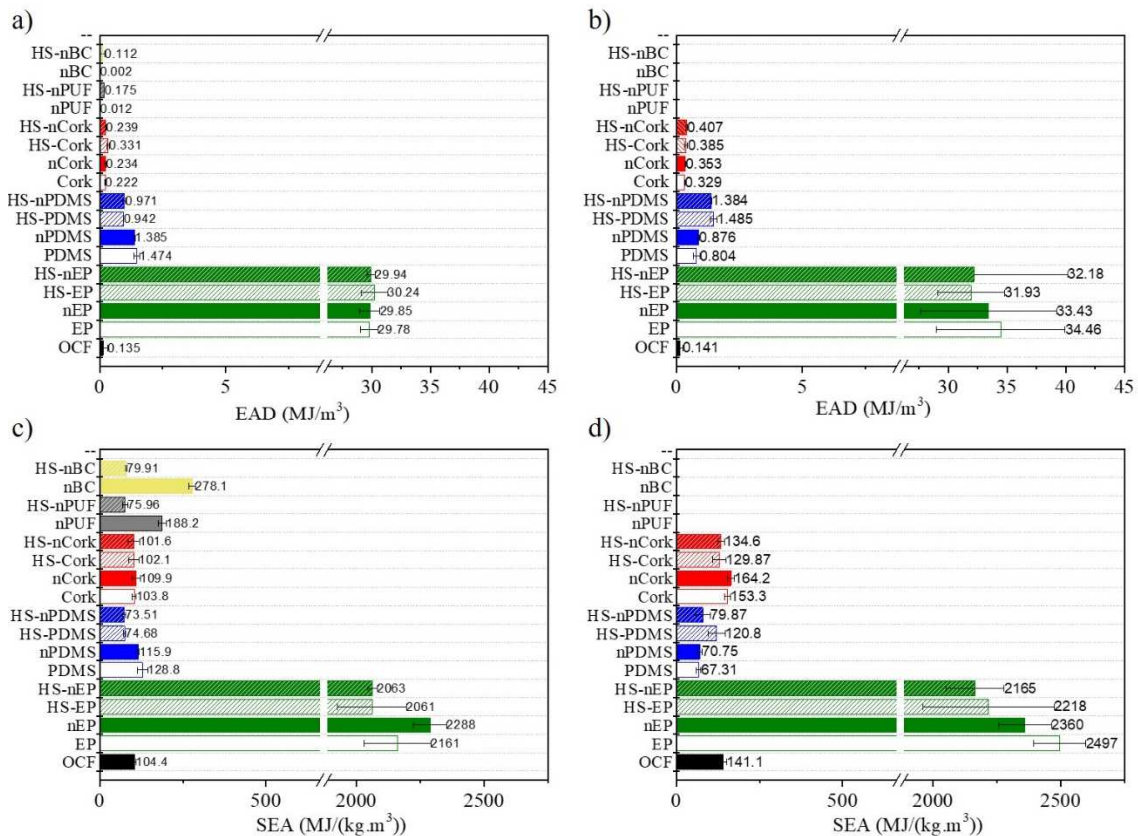


Figure 8.2 Averaged values with the standard deviation of EAD and SEA for a strain of 0.5 for quasi-static (a, c) and dynamic loading conditions (b, d).

Results have clearly show that the void filler type used to fill the OCF are mainly affected the compressive strength of the resulting nanocomposite hybrid structures and their sensitive of the strain rate. For the quasi-static loading condition, the values of the peak stress of HS-Cork, HS-nCork, HS-PDMS, HS-nPDMS, HS-EP and HS-nEP are 0.446 MPa, 0.421 MPa, 5.25 MPa, 4.93 MPa, 66.21 MPa and 77.39 MPa, respectively. For the dynamic loading condition, the values of the peak stress of HS-Cork, HS-nCork, HS-PDMS, HS-nPDMS, HS-EP and HS-nEP are 0.456 MPa, 0.471 MPa, 13.94 MPa, 12.97 MPa, 73.95 MPa, 84.25 MPa, respectively. For example, the peak stress values of HS-PDMS and HS-EP are 12 and 148 times higher than HS-Cork, respectively. However, the HS-Cork and HS-nCork are much lighter in comparison with the other composite hybrid structures, leading to higher values of specific strength. The density values of HS-Cork, HS-nCork, HS-PDMS, HS-nPDMS, HS-EP and HS-nEP are 224 kg/m³, 222 kg/m³, 1087 kg/m³, 1090 kg/m³, 1162 kg/m³ and 1169 kg/m³, respectively. The specific strength is a material's strength divided by its density, also known by the strength-to-weight ratio. The strength-to-weight ratio values of the HS-Cork, HS-nCork, HS-PDMS, HS-nPDMS and HS-EP and HS-nEP are 502 MPa/(kg/m³), 527 MPa/(kg/m³), 207 MPa/(kg/m³), 221 MPa/(kg/m³), 18 MPa/(kg/m³) and 15 MPa/(kg/m³). The latter shows the clear advantages of the HS-Cork and HS-nCork. All these hybrid structures are extremely sensitive to strain-rate testing in which the quasi-static values are superior to the dynamic values. However, the HS-PDMS and HS-nPDMS are the hybrid structures with more strain rate sensitivity, in which the peak stress values of the HS-nPDMS and HS-PDMS changed from 5.25 MPa (quasi static) to 13.94 MPa (dynamic) and from 4.93 MPa (quasi-static) to 12.97 MPa (dynamic). The additional advantages to use these hybrid structures containing cork in comparison with the other hybrid structures that used EP, PDMS is that cork is 100% natural and can be used to create more ecological products.

8.1.2. Sound absorption coefficient

Figure 8.3 shows the sound absorption coefficient for the specimens tested. Table 8.1 summarizes the main parameters, α_{peak} and the respective frequency, NRC and α_{average} .

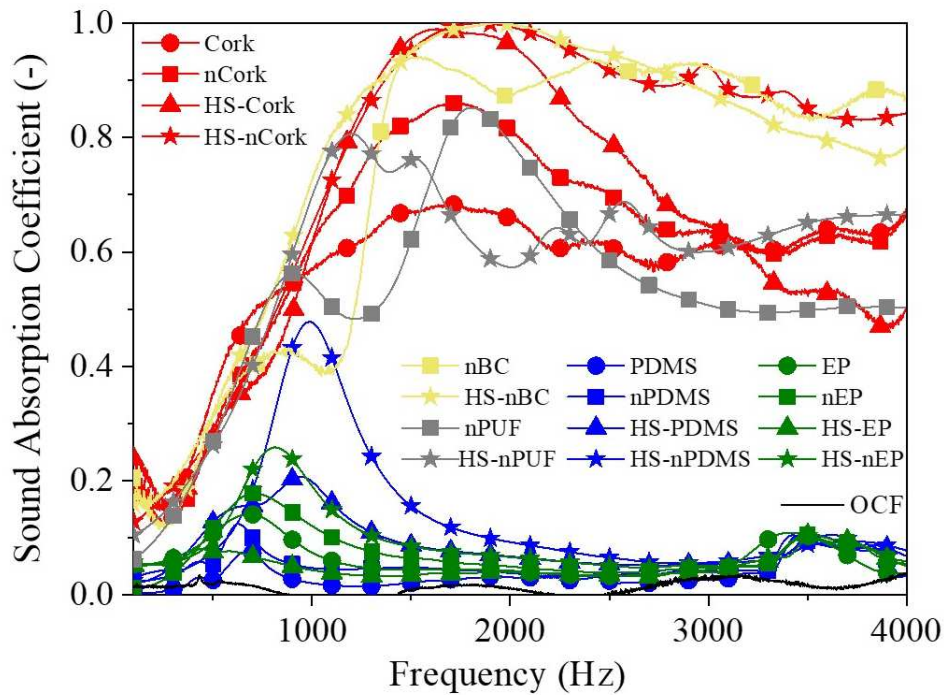


Figure 8.3 Sound absorption coefficient vs Frequency.

The results (Figure 8.3 and Table 8.1) demonstrate that cellular filling materials or its respective hybrid structures have superior behaviour when compared with the materials resulting from OCF and dense polymers. nBC, HS-nBC, and HS-nCork have the highest curves of sound absorption from 1000 Hz to 4000 Hz. This is supported by NRC and the α_{average} values (Table 8.1). Clearly, the dense materials, EP and PDMS, its nanocomposites or correspondent hybrid structures have inferior sound absorption curve and the peak absorption occurs earlier, as shown by the α_{peak} that is located before 1000 Hz. This is due to its compact structure that leads to the faster propagation of the sound waves and less dissipation. NRC is often used to compare the acoustic performance under equal circumstances. Nevertheless, NRC has some limitations as it does not translate the profile of the curve above 2000 Hz. α_{average} , can provide more information since it takes into consideration the sound absorption coefficient until 4000 Hz.

Pedroso et al [1] summarized the NRC values of traditional and innovative acoustic insulating solutions with different densities and thickness. For example, agglomerated cork with thickness of 50 mm and density of 105 kg/m^3 presents NRC of 0.41. Cellulose foam used as insulating materials in houses has NRC of 0.70 for 50 mm of thickness and density of 28 kg/m^3 . More traditional materials like PUF, EPS and XPS present 0.67, 0.50 and 0.33,

respectively for 50 mm of thickness and density 28 kg/m³ (standard deviation ~3 kg/m³). It is worth to mention that sound absorption is highly dependent of thickness. The sound absorption of materials can be improved at low frequencies by increasing the thickness of the materials. For that reason, although the materials developed within this PhD have lower NRC (half of the thickness of the ones described by Pedroso), the results could be improved by increasing the materials thickness.

Table 8.1 Acoustic parameters for fabricated specimens.

	α_{peak} (Frequency, Hz)	NRC	α_{average}
nBC	0.938 (1494)	0.50	0.47
HC-nBC	0.999 (1900)	0.55	0.52
nPUF	0.852 (1804)	0.45	0.38
HS-nPUF	0.807 (1198)	0.45	0.41
Cork	0.682 (1728)	0.40	0.43
nCork	0.861 (1738)	0.45	0.45
HS-Cork	0.990 (1636)	0.55	0.46
HS-nCork	1.000 (1846)	0.50	0.47
PDMS	0.076 (670)	0.05	0.02
nPDMS	0.124 (630)	0.05	0.04
HS-PDMS	0.207 (944)	0.10	0.09
HS-nPDMS	0.478 (988)	0.15	0.13
EP	0.141 (695)	0.05	0.07
nEP	0.177 (718)	0.10	0.06
HS-EP	0.080 (428)	0.10	0.11
HS-nEP	0.258 (809)	0.10	0.09

Results have shown (Table 8.1) that the HS-nBC and HS-nCork are a good sound insulator, in comparison with the other hybrid structures. For example, theHS- nCork has a $\alpha \geq 0.84$ in the frequency range 1261 Hz–4000 Hz. The cork used to minimize noise and vibration problems in mechanical systems, including industrial machines, appliances, vehicles and buildings confer high capacity for thermal and acoustic insulation to the novel hybrid structures.

8.1.3. Thermal conductivity

There is significant industrial interest in the development of innovative and efficient materials for thermal insulation applications. As so, it is important to characterize the thermal conductivity of the materials. Figure 8.4 shows the thermal conductivity values for the specimens tested.

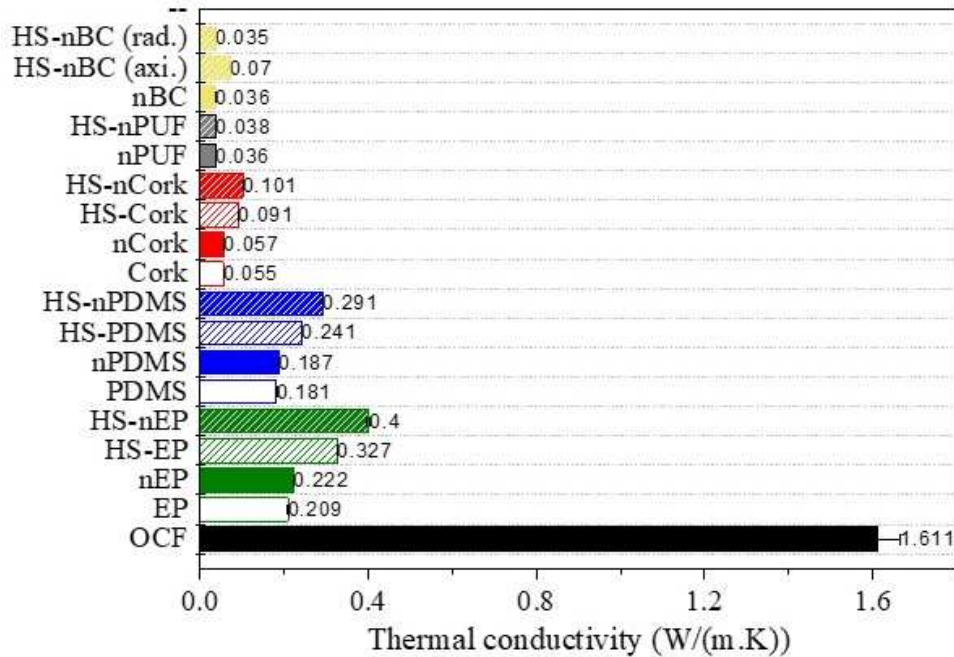


Figure 8.4 Thermal conductivity values of the fabricated materials.

The results presented in Figure 8.4 clearly show that the nanocomposites foams, nBC and nPUF and its hybrid structures have the lowest values of thermal conductivity due to its cellular structure, below 0.04 W/m·K. The thermal conductivity of dense polymers, PDMS and EP, is higher and located between 0.18-0.20 W/m·K, as most of the polymers reported in literature [2], making them good thermal insulators. PDMS and EP have thermal conductivity values around 0.2 W/m·K and this value slightly increases for the respective nanocomposites (with the addition of 0.25% GO). Hybrid structures shows also higher values due to the presence of the OCF. It is also reported that the insulating properties are high for cellular materials and this can be even higher by controlling the pore size and orientation in the foams, for example. BC and PUF are examples of the low thermal conductivity materials presenting thermal conductivity values in the range 0.035 W/m·K. Also, cork agglomerates have thermal conductivity values in accordance with literature,

0.045-0.060 W/m·K [3]. All the materials developed are competitive materials in thermal insulation, when compared, for example, with closed cell metal foams that present significant high values (14-65 W/m·K for materials with densities between 520 and 1350 kg/m³) and syntactic foams (28-43 W/m·K for materials with densities between 1300 and 1550 kg/m³) [4,5]. Globally, hybrid structures are good insulators, since values below 0.4 were obtained.

Overall, the most suitable materials as acoustic and thermal insulators are the materials resulting from two cellular materials (BC, Cork and PUF), while, the materials resulting from the combination of OCF with dense materials (EP and PDMS) are good energy absorbers and with high resistance to compression. Furthermore, the polymeric-based filling materials showed promising fire-retardancy provided by the GBMs incorporation within the matrix.

8.2. Main Conclusions

Multifunctional lightweight materials have tremendous potential to impact new system performance, besides their more complex formulation, by reducing thickness, weight, cost and power consumption, while simultaneously improving efficiency, safety, and versatility. The multifunctional nature of materials is possible at different scales from nano to macro, on various spatial and compositional levels and combining different classes of materials.

The main goal of this PhD thesis was to research and develop innovative hybrid lightweight multifunctional materials using the multimaterial concept by combining cellular metals (open-cell aluminium foam) with other materials (e.g. dense polymers, polyurethane and nanocellulose foams, and cork) to be used/ or to be an alternative to the materials available in the market.

This PhD thesis also contributed with a complete characterization of these type of structures, providing not only the mechanical properties but also the acoustic, thermal and fire-resistant properties. Globally, high-end acoustic and thermal properties, adequate stiffness and strength associated with high energy absorption ability and fire-retardancy were the target properties (Figure 8.5).

Prior to the incorporation of the OCF voids, polymeric materials were combined with GBMs aiming to improve mechanical and sound absorption performance and to confer fire-retardancy property by taking advantage of these nanomaterials' properties. Hereafter, the main conclusions for each chapter as well as the open issues that deserve further research are summarized. Although the main goal of the thesis was accomplished, there are improvements that could be performed in order to achieve superior results. It is worth mentioning that the challenges beyond this research are many and are pointed out, for a better understanding of the limitations through this work.

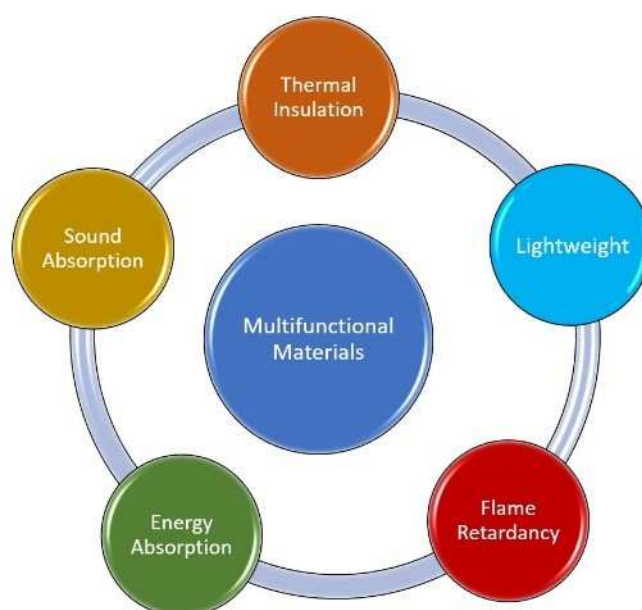


Figure 8.5 Main properties presented by the materials developed under the scope of this thesis.

The following main conclusions can be taken:

- The incorporation of the GBMs, like GNPs or GO/rGO, improved sound absorption coefficient and conferred fire-retardancy, while maintaining the thermal conductivity values. GBMs also provided mechanical reinforcement to the polymeric foams (BC and PUF). The same was not observed in the case of dense polymers like PDMS and EP so their dispersion needed to be improved;
- An excellent form-fitting connection of the polymeric filling materials to the metal surface of OCF in the hybrid structures was verified by μ CT;

- Sustainable and greener BC/GO and BC/rGO based foams were obtained by freeze-drying. Different reducing methods of GO, wet with hydroxylamine and hydrazine and dry with NH₃ vapour, were efficient to decrease water absorption ability. Furthermore, the exposition of BC/GO to MTMS vapour revealed to be efficient to increase the hydrophobicity of the material. A small amount of DMSO allowed the control of the final porous structure of the BC based aerogels;
- The hybrid structures, HS-BC/GO10, presented low weight, good sound absorption, especially between 1000-400 Hz, with NRC of 0.55 and low thermal conductivity values. OCF provided an adequate mechanical support to BC/GO aerogels for easier handling. The compressive behaviour was governed by the OCF;
- The properties of PUF could be tailored by the addition of GO and GNPs. The HS-PUF/GNPs2.5 presented good sound absorption coefficient (NRC ~ 0.45), low thermal conductivity and the mechanical compressive response was mainly governed by the OCF;
- The GO inclusion into granulated cork was successfully achieved by LbL method as verified by SEM images. Filling the voids of OCF with granulated cork was facilitated by reducing the cork grain size and also with the help of a vibratory platform. HS-Cork and HS-nCork proved to be interesting sustainable materials displaying improvements in strength and energy absorption values as well as good sound absorbers coefficients (NRC of 0.55), comparatively to the individual materials;
- The hybrid structures composed by the dense polymer and its nanocomposites filling the OCF presented higher density when compared with the materials prepared in previous chapters obtained by the combination of two cellular materials. Due to the high strength presented by both polymers and high energy absorption capacity, both can be used with structural purposes. PDMS showed a rubber behaviour contrary to the brittleness nature of epoxy.

8.3. Future Perspectives

Due to the constant evolution of technology, society needs are changing, and it is up to the scientific world to adjust its research to those needs, providing new solutions

(manufacturing methods and products). Materials science is a world of infinite possibilities where there is much to discover and plenty to do. Following the line of investigation of this work many opportunities were identified for further exploration. Thereby, some research topics are suggested with the expectation of providing support for new work in this area:

- Despite of the promising preliminary fire-retardancy tests achieved by the incorporation of GBMs, new standard assays should be carried out;
- New approaches to incorporate GBMs into the polymeric matrices should be considered in order to ensure better dispersion, namely by functionalizing the GBMs using straightforward and reproducible methods;
- New hybrid structures of agglomerated cork could be developed, using different percentages and types of binder (environmentally friendly) and types of cork, including the use of cork waste and by-products from different industrial sectors, as well as different dimensions. Also, it would be important to consider the combination of cork with other type cellular metals;
- Changing the operating conditions (curing time and temperature) of the dense polymers (PDMS and EP) could influence the properties of the hybrid structures;
- Different lightweight but stronger polymeric filling materials could be considered to fill OCF. However, natural or recyclable sources should be also considered.

8.4. References

- [1] M. Pedroso, J. de Brito, and J. D. Silvestre, “Characterization of eco-efficient acoustic insulation materials (traditional and innovative),” *Constr. Build. Mater.*, vol. 140, pp. 221–228, 2017.
- [2] M. R. S. and S. M. Z. Craig Dixon, “Transient Plane Source Technique for Measuring Thermal Properties of Silicone Materials Used in Electronic Assemblies,” *Int. Microelectron. Packag. Soc.*, vol. 23, 2000.
- [3] S. Knapic, C. P. dos Santos, H. Pereira, and J. S. Machado, “Performance of Expanded High-Density Cork Agglomerates,” *J. Mater. Civ. Eng.*, vol. 29, no. 2, p. 04016198, Feb. 2017.
- [4] T. Fiedler, I. V. Belova, and G. E. Murch, “On the thermal properties of expanded perlite – Metallic syntactic foam,” *Int. J. Heat Mass Transf.*, vol. 90, pp. 1009–1014, Nov. 2015.
- [5] E. Solórzano, J. A. Reglero, M. A. Rodríguez-Pérez, D. Lehmus, M. Wichmann, and J. A. de Saja, “An experimental study on the thermal conductivity of aluminium foams by using the transient plane source method,” *Int. J. Heat Mass Transf.*, vol. 51, no. 25–26, pp. 6259–6267, Dec. 2008.

Chapter 9. Appendices

Appendix S1 Theoretic Principles

Mechanical properties

The compressive behaviour of the specimens was assessed using testing machines at different crosshead rates (Figure S1.1a). The recorded load (F)-displacement (L) data obtained in compression tests were converted to stress-strain data. The engineering stress (σ) and engineering strain (ε) values were determined by dividing the load with the initial cross-section (Eq. S1.1), and by dividing the displacement with the initial specimen height (Eq. S1.2), respectively.

$$\sigma = \frac{F}{A_0} \quad (\text{Eq. S1.1})$$

$$\varepsilon = \frac{L-L_0}{L_0} \quad (\text{Eq. S1.2})$$

where σ is the engineering stress, F is the applied load, A_0 is the original area of test specimen, ε is the engineering strain, L is the length at any point during compression and L_0 original length. The typical curve σ vs ε for cellular materials is presented in Figure S1.1b.

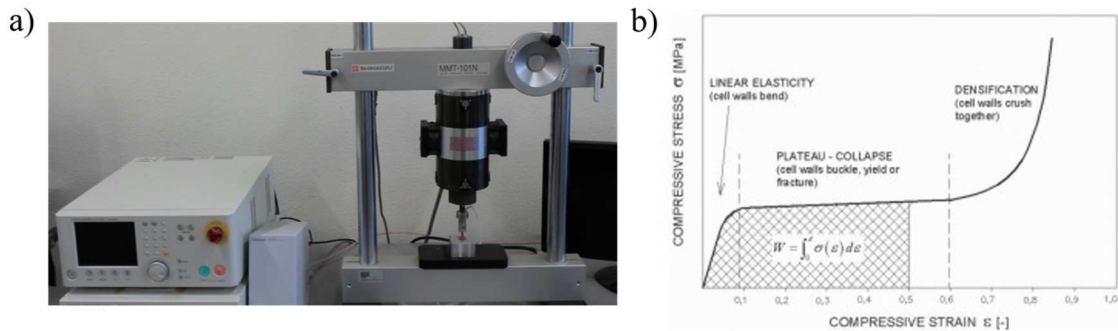


Figure S1. 1 Example of mechanical testing machine and (a) and typical compressive curve for cellular materials (b).

In the stress-strain responses there is an initial region of linear elasticity that follows the Hook law. The Young's modulus (E) is the initial slope of the stress-strain response of the cellular specimen (Eq. S1.3).

$$E = \frac{\sigma}{\varepsilon} \quad (\text{Eq. S1.3})$$

For low density cellular materials, Gibson and Ashby related the Young's modulus (E) young modulus with density (ρ) for open (Eq. S1.4) and closed cell foams (Eq. S1.5).

$$\frac{E}{E_s} \approx \left(\frac{\rho}{\rho_s}\right)^2 \quad (\text{Eq. S1.4})$$

$$\frac{E}{E_s} \approx \Phi^2 \left(\frac{\rho}{\rho_s}\right)^2 + (1 - \Phi) \frac{\rho}{\rho_s} \quad (\text{Eq. S1.5})$$

Where, the subscript “s” is related with the properties of the solid material that constitute the cell walls and Φ is the fraction of the solid. Linear elasticity is controlled by cell wall bending and, in case of closed cells, by stretching of the cell walls.

The elastic region is followed by a long collapse plateau defined by the stress has a near constant value and ending in the densification region in which the stress rises steeply. The stress plateau for low density cellular materials is given by Eq. S1.6 and Eq. S1.7 for open and closed cell foams, respectively.

$$\frac{\sigma_{pl}}{\sigma_s} \approx 0.3 \left(\frac{\rho}{\rho_s}\right)^{3/2} \quad (\text{Eq. S1.6})$$

$$\frac{\sigma_{pl}}{\sigma_s} \approx 0.3 \left(\Phi \frac{\rho}{\rho_s}\right)^{3/2} + 0.4(1 - \Phi) \frac{\rho}{\rho_s} \quad (\text{Eq. S1.7})$$

The energy absorption density (EAD) curves and the specific energy absorption (SEA) values were calculated according to the ISO 13314: 2011 [1] by integrating the engineering stress-strain curves (Eq. S1.8) and by dividing the EAD values by the specimen mass, respectively [1–4].

$$\text{EAD} = \int_0^{\epsilon} \sigma(\epsilon) \, d\epsilon \quad (\text{Eq. S1.8})$$

Thermal conductivity - Transient Plane Source (TPS)

The determination of thermal conductivity was carried out according the ISO 22007-2.2 [5] using Hot Disk Analyser, TPS 2500 S. The TPS method was reported to be capable for measuring materials with thermal conductivity ranging from 0.005 to 500 W/m·K. Figure S1.2a shows the apparatus used to measure the thermal conductivity by a transient plane heat source approach suitable for testing small samples. The apparatus consists on a sensor placed between two similar samples, like a sandwiched configuration, Figure S1.2b. The type of the sensor used in this measurement involves a thin nickel foil folded in a double spiral pattern, which is coated by two thin layers of Kapton protective films. A small current for a short period is applied to the sensor. This time period is generally only a few seconds so that the

metal disk can be considered in contact with infinite size samples throughout the transient signal recording process.

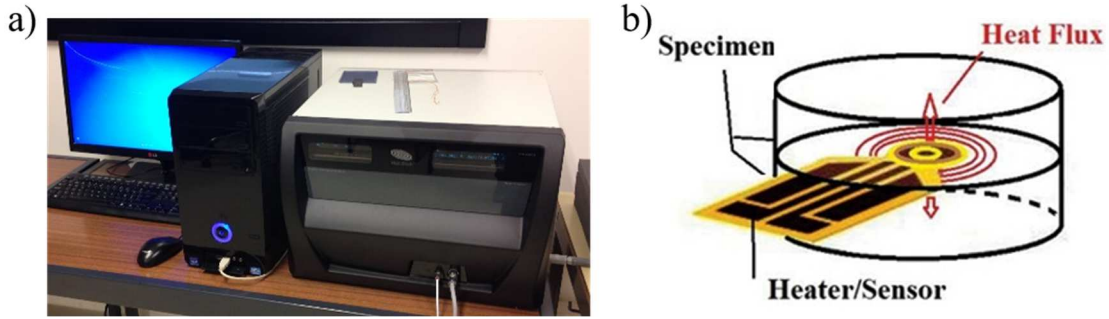


Figure S1. 2.TPS 2500 S equipment and (a) and specimen measurement apparatus (b).

The variation in the sensor resistance $R(t)$ is calculated using Eq. 9 and is directly related to the electrical heat current that passes through the nickel spiral during the measurement and that creates an increase in temperature $\Delta T(t)$ of the sensor as function of time (Eq. S1.9).

$$R(t) = R_0[1 + \alpha \Delta T(t)] \quad (\text{Eq. S1.9})$$

Where, R_0 is the initial nickel electrical resistance at initial time (t_0), α is the temperature coefficient of the resistance of the nickel foil. The energy generated (in the form of heat) spreads and dissipates through both specimens at a rate that is dependent on the thermal transport characteristics of the specimen material. In conductor materials (solid metals) the dissipation is fast, while for insulating materials (for example polymeric foams) this phenomenon is slow. Another important parameter is the temperature increase of the sensor and can be obtained using Eq. S1.10.

$$\overline{\Delta T(\tau)} = P_0 (\pi^{3/2} \alpha \lambda)^{-1} D(\tau) \quad (\text{Eq. S1.10})$$

Where, P_0 is the total output of power from the sensor, a is the overall sensor radius, λ is the thermal conductivity of the specimen that is being measured and $D(\tau)$ is a dimensionless time dependent function with the variable τ , defined by Eq. S1.11.

$$\tau = \left(\frac{t}{\theta}\right)^{1/2} \quad (\text{Eq. S1.11})$$

Where, t is the time measured from the beginning of the transient heating and θ is the characteristic time, which depends both on the parameters of the sensor and the specimen, as defined by the Eq. S1.12.

$$\theta = \frac{\alpha^2}{\kappa} \quad (\text{Eq. S1.12})$$

Where, κ is the thermal diffusivity of the specimen in mm^2/s .

Through a computational algorithm based on specific analyser software, these parameters can accurately be calculated. It is worth to mention that the correctly calculation of the thermal conductivity implies a series of computational plots of $\Delta T(t)$ versus $D(\tau)$, usually made for a range of κ values. The correct value of κ will result in a straight line for the $\Delta T(t)$ versus $D(\tau)$ [6–9].

Sound absorption coefficient

The method used to determine the sound absorption coefficient is defined in the ASTM E 1050 standard [10], based on the Kundt tube. The conductive tube has a sound source in one of the ends, a test piece at the other end and a set of two microphones for reading the pressure variations inside the tube. The source emits a random noise, with continuous spectrum in the frequency range under analysis. Pressure variations are caused by the incidence of sound waves in the test specimen, which cause the dissipation of part of it, through the transfer of sound energy to mechanical energy, thus decreasing the reflected pressure. Microphones are responsible for reading these variations, which with the aid of a digital frequency analyser, that serves as a transducer and a software that processes the data, make possible to determine the sound absorption coefficient [11].

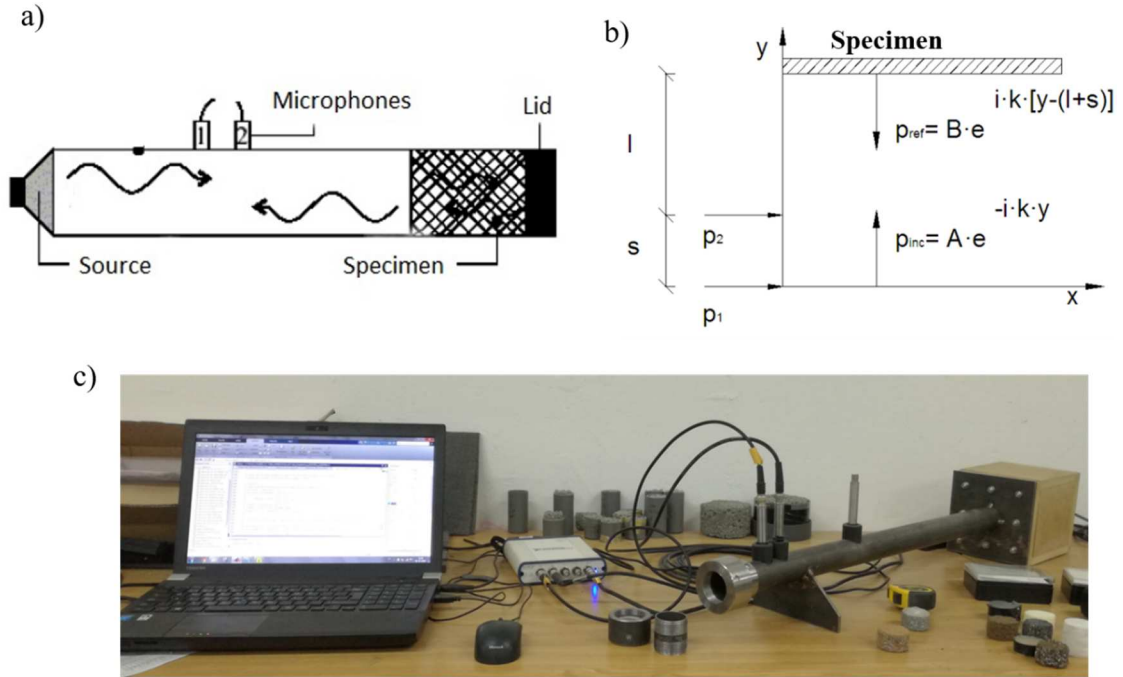


Figure S1. 3. Impedance tube scheme (a); sound wave propagation inside the impedance tube (b) and photograph of the equipment used in the measurements (c) (adapted from [11]).

The incident energy is calculated according the Eq. S1.13 and S1.14 and based in the scheme of the Figure 3b.

$$P_{inc} = A e^{-i k y} \quad (\text{Eq. S1.13})$$

$$P_{inc} = B e^{i k [y - (l+s)]} \quad (\text{Eq. S1.14})$$

Where, A and B are amplitude of sound wave; k is the wavenumber, s the distance between microphones, l is the distance between specimen and microphone, P_{inc} is the energy emitted by the source, P_{ref} is the energy reflected. The sound reflection coefficient (R) is determined by the relation between the reflected and the incident fields (Eq. S1.15).

$$R = \frac{P_{ref}}{P_{inc}} \quad (\text{Eq. S1.15})$$

According to the specimen position the reflection coefficient is calculated by Eq. S1.16.

$$R = \frac{B}{A e^{-i k (1+s)}} \quad (\text{Eq. S1.16})$$

The sound absorption coefficient, α , is related to the sound reflection coefficient by Eq. S1.17.

$$\alpha = 1 - |R|^2 \quad (\text{Eq. S1.17})$$

References

- [1] “ISO 13314:2011 - Mechanical testing of metals— Ductility testing— Compression test for porous and cellular metals.”
- [2] L. J. Gibson and M. F. Ashby, *Cellular Solids: Structure and Properties*. Cambridge University Press, 1999.
- [3] B. Degischer, H.P., Kriszt, *Handbook of Cellular Metals: Production, Processing, Applications*. Wiley-VCH Verlag GmbH, 2002.
- [4] D. Vries, “Characterization of polymeric foams,” Eindhoven University of Technology, 2009.
- [5] “ISO 22007-2.2. Plastics - Determination of thermal conductivity and thermal diffusivity - Part 2: Transient plane heat source (hot disc) method.”
- [6] Y. He, “Rapid thermal conductivity measurement with a hot disk sensor,” *Thermochim. Acta*, vol. 436, no. 1–2, pp. 122–129, Oct. 2005.
- [7] R. Coquard, E. Coment, G. Flasquin, and D. Baillis, “Analysis of the hot-disk technique applied to low-density insulating materials,” *Int. J. Therm. Sci.*, vol. 65, pp. 242–253, Mar. 2013.
- [8] C. R. C. Rao, H. Niyas, and P. Muthukumar, “Performance tests on lab-scale sensible heat storage prototypes,” *Appl. Therm. Eng.*, vol. 129, pp. 953–967, Jan. 2018.
- [9] M. Gustavsson, E. Karawacki, and S. E. Gustafsson, “Thermal conductivity, thermal diffusivity, and specific heat of thin samples from transient measurements with hot disk sensors,” *Rev. Sci. Instrum.*, vol. 65, no. 12, pp. 3856–3859, Dec. 1994.
- [10] “ASTM E1050-12 Standard Test Method for Impedance and Absorption of Acoustical Materials Using a Tube, Two Microphones and a Digital Frequency Analysis System.”
- [11] J. da Silva, “Metodologias experimentais para a determinação do coeficiente de absorção de sonora em materiais de construção,” University of Coimbra, 2008.

Appendix S2.1 Supplementary information for Chapter 3.1

Table S2.1.1. Apparent density (kg/m^3) of cellulose-based nanocomposite foams prepared with GBMs (GO or rGO) and with and without microencapsulated PCMs.

Defibrillated bacterial cellulose														
PCMs 0%					PCMs 5%					PCMs 10%				
0	GO													
	2.5%	5.0%	7.5%	10.0%	0	2.5%	5.0%	7.5%	10.0%	0	2.5%	5.0%	7.5%	10.0%
	11.3	9.5	10.4	10.1	12.5	12.7	14.5	15.1	13.1	15.1	15.3	13.5	14.8	15.1
	± 1.3	± 0.5	± 0.1	± 0.5	± 2.2	± 1.8	± 0.2	± 0.6	± 0.9	± 2.2	± 1.2	± 1.8	± 2.1	± 1.5
9.8 ± 1.3	rGO													
	13.6	13.4	16.8	16.0	12.5	10.3	15.9	20.4	21.9	15.2	13.81	13.40	29.97	29.9
	± 1.9	± 2.2	± 4.5	± 1.0	± 2.2	± 0.3	± 0.6	± 1.2	± 2.6	± 2.2	± 3.7	± 3.67	± 2.6	± 3.6

Table S2.1.2. DSC of cellulose-based nanocomposite foams.

Specimens	Heating			Cooling		
	Peak (°C)	Onset (°C)	ΔH (J/g)	Peak (°C)	Onset (°C)	ΔH (J/g)
PCMs	26.04	23.33	84.15	23.11	24.23	78.44
BC	-	-	-	-	-	-
BC/PCMs10	23.66	22.00	4.86	22.63	23.05	4.64
BC/GO10/PCMs10	23.75	21.77	6.73	22.58	23.08	6.58
BCrGO10/PCMs10	23.61	22.52	4.24	22.42	22.99	3.94

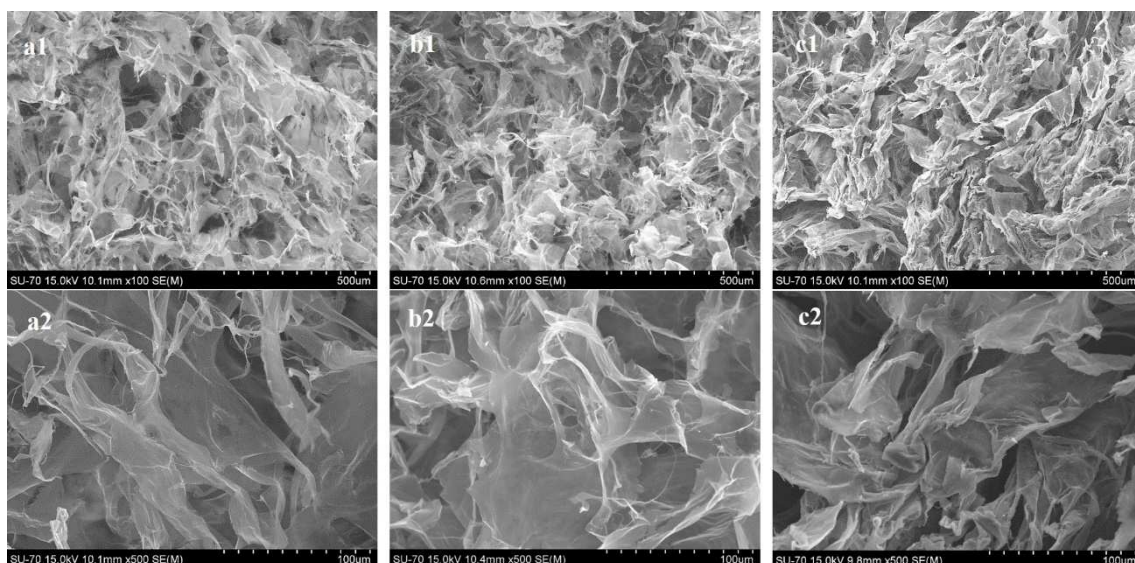


Figure S2.1.1. SEM of BC (a1 and a2), BC/GO10 (b1 and b2) and BC/rGO10 (c1 and c2).

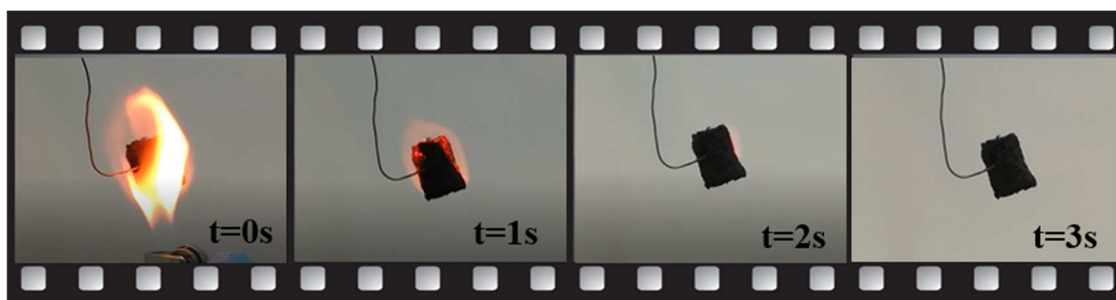


Figure S2.1.2. Photographs of flame test results for BC/GO5.

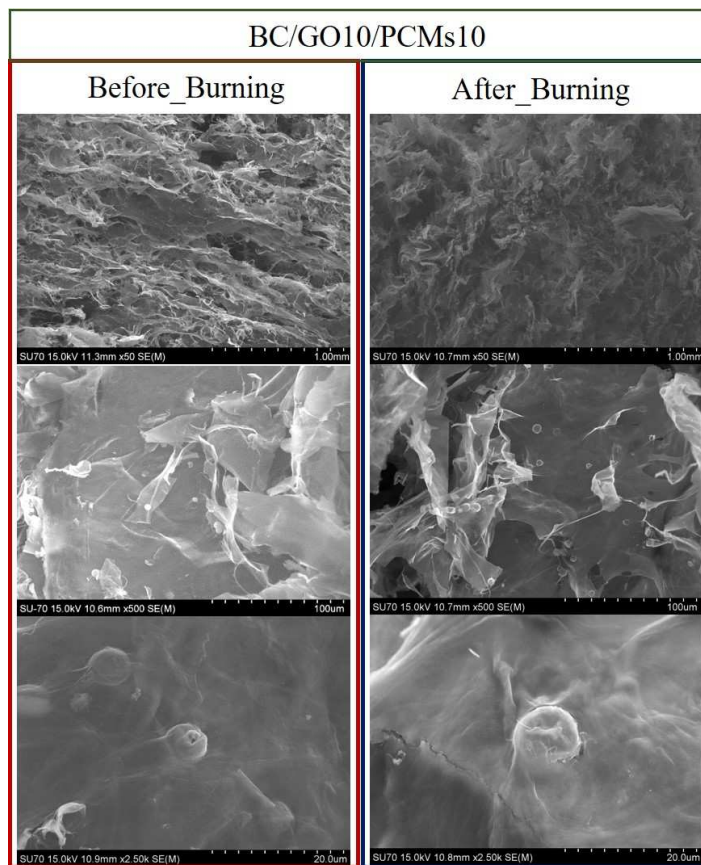


Figure S2.1 3. Flame tests.

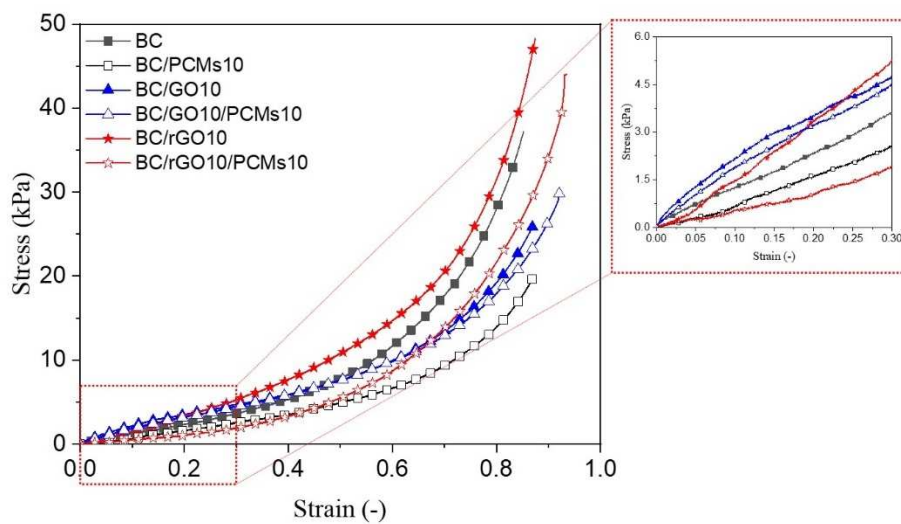


Figure 2.1 4 Average stress-strain compressive curves of the foams.

Appendix S2.2 Supplementary information for Chapter 3.2

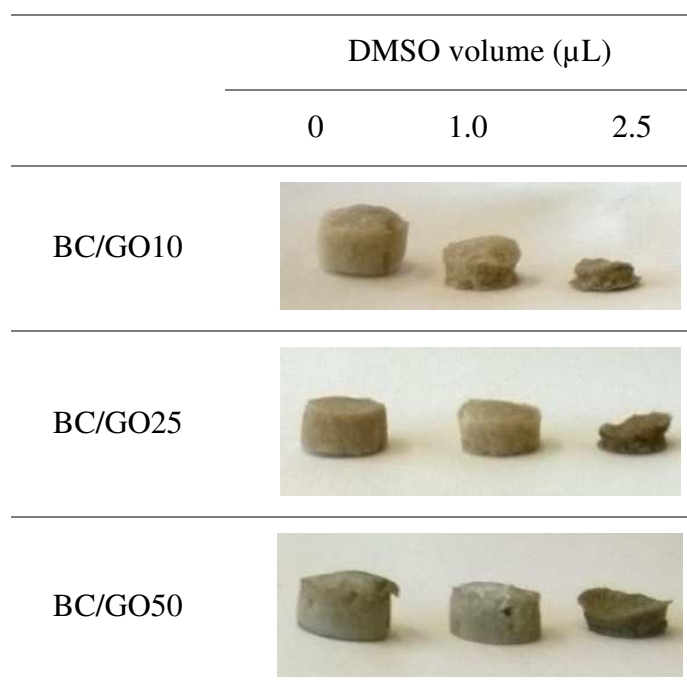


Figure S2.2.1. Photographs of lyophilized BC/GO samples prepared with different quantities of DMSO (0.0, 1.0 and 2.5 μl) added to the aqueous suspension of BC and GO mixture.

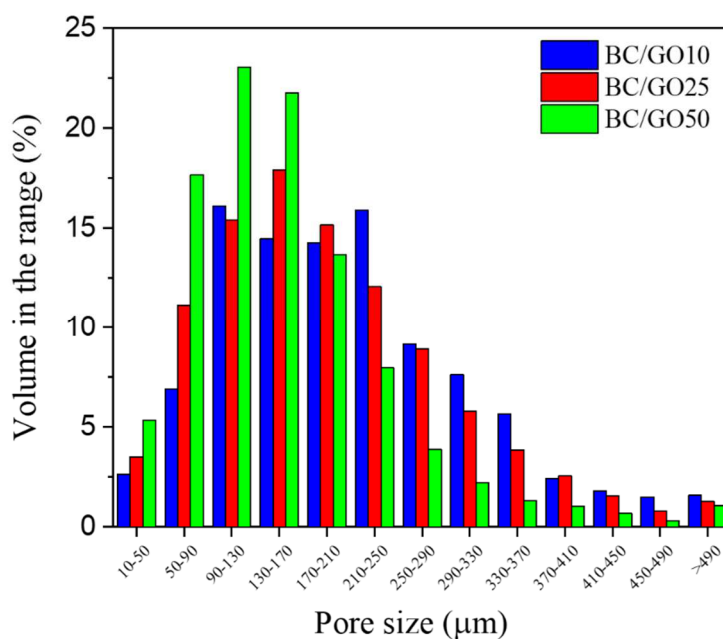


Figure S2.2.2. Pore volume distribution in BC/GO samples determined from μCT analysis.

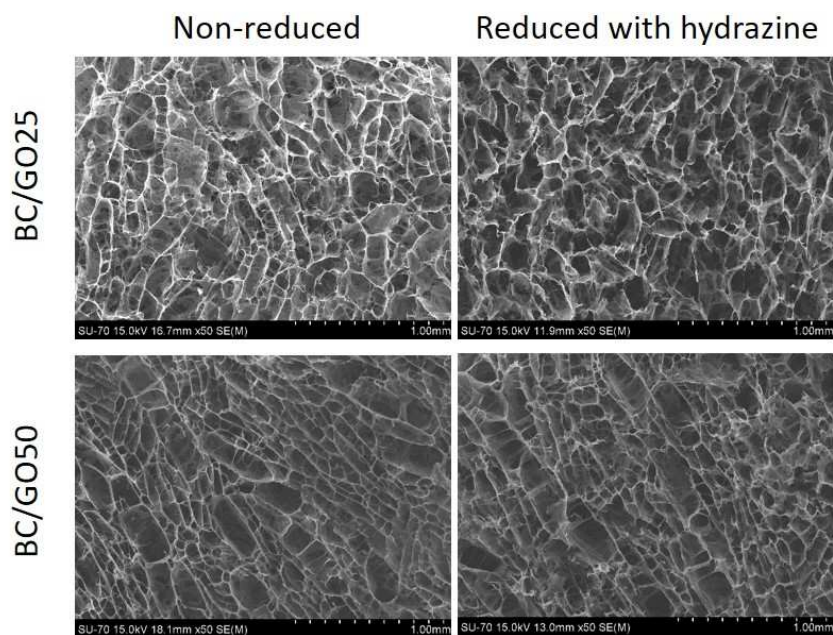


Figure S2.2.3. SEM images of BC/GO aerogels before and after reduction with hydrazine.

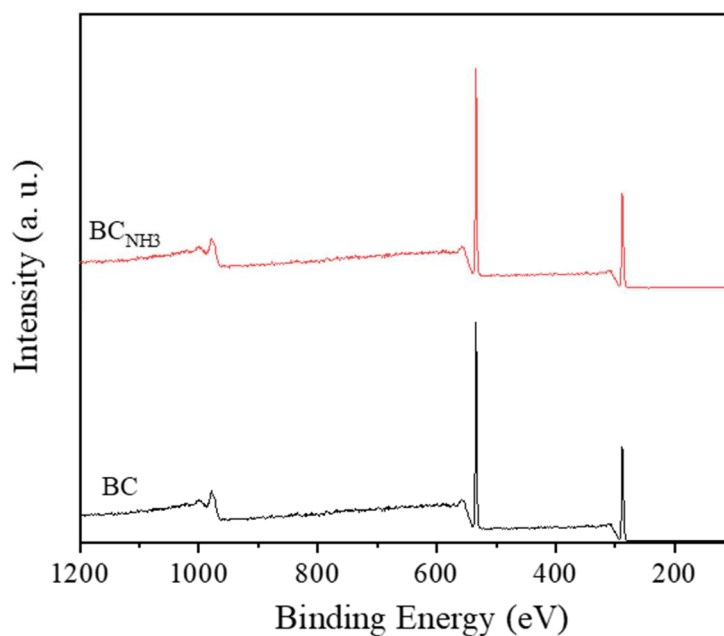


Figure S2.2.4. Survey XPS spectra of bacterial cellulose aerogel (BC) and bacterial cellulose treated with ammonia flow at 220C (BC_{NH3}).

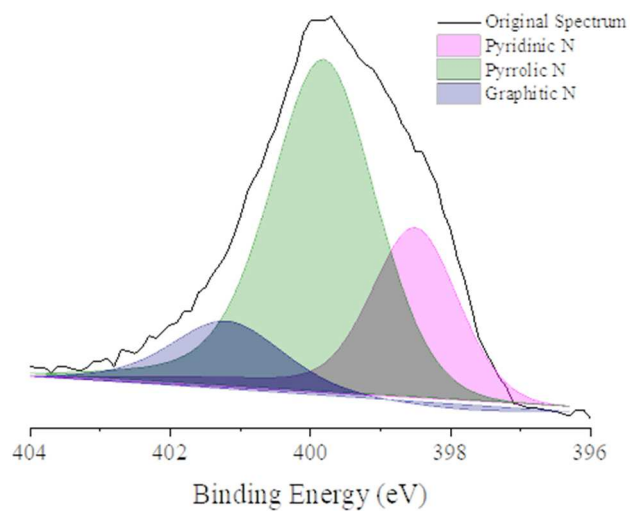


Figure S2.2.5. XPS spectrum of N1s with peak fitting for BC/rGO25NH₃ sample.

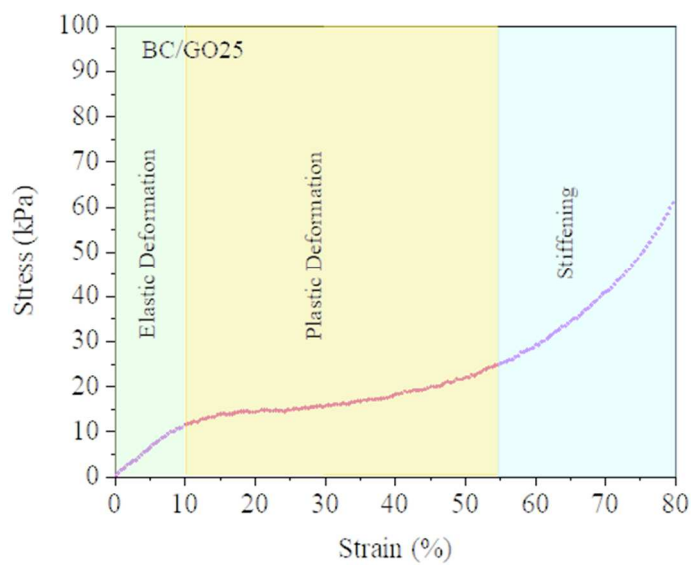


Figure S2.2.6. Profile Stress-Strain curve for BC/GO25.

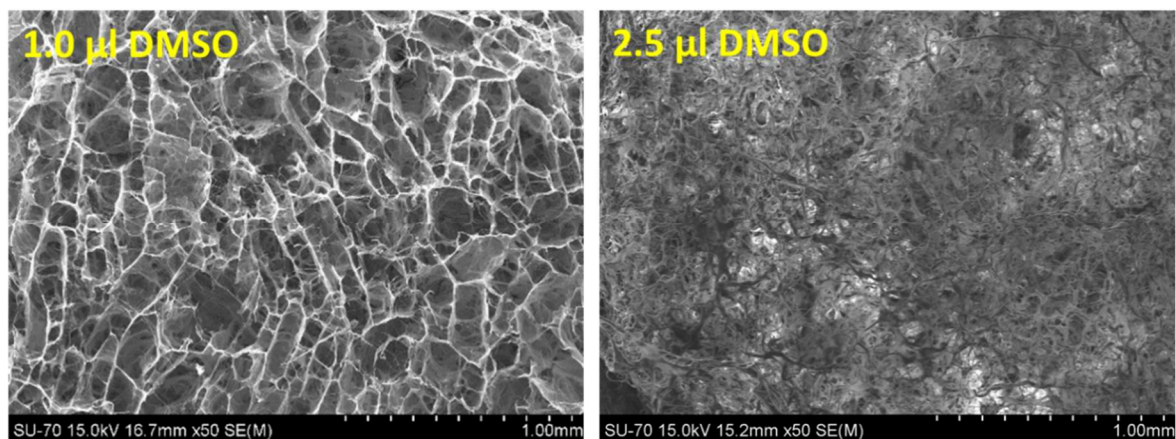


Figure S2.2.7. SEM images of the BC/GO25 aerogels prepared with different amounts of DMSO (1.0 and 2.5 μ l).

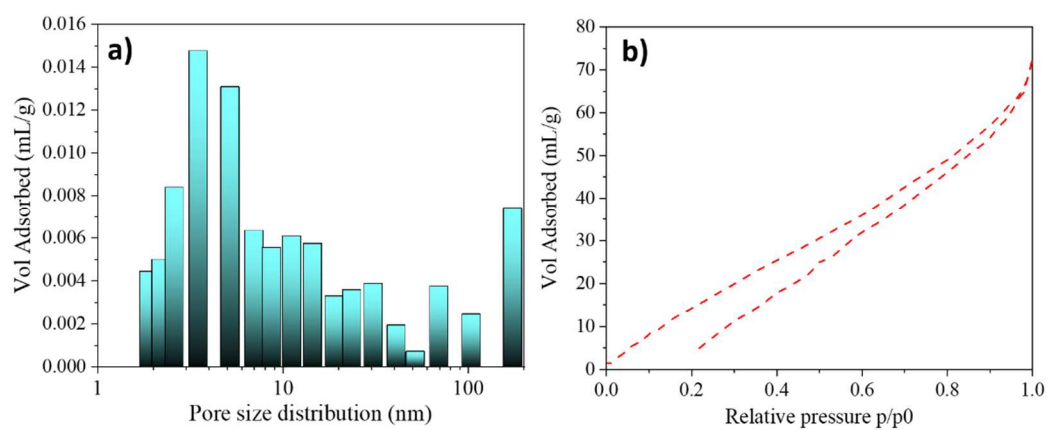


Figure S2.2.8. BJH pore size distribution (a) BET Isotherm of the sample BC/GO25 (b).

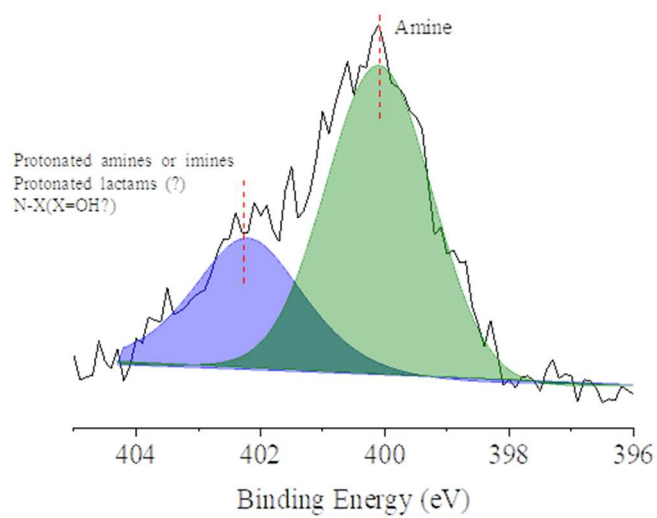


Figure S2.2.9. XPS spectrum of N1s with peak fitting for BC aerogel treated with ammonia at 220C.

Appendix S3 Supplementary information for Chapter 4

Figure S1 shows the normalized FTIR spectra of the polyol, MDI, PUF and PUF nanocomposites prepared with 2.5 wt.% of GNPs (PUF/GNPs2.5) and with 2.5 wt.% of GO (PUF/GO2.5). The MDI spectrum shows a sharp and strong peak at 2250 cm^{-1} assigned to isocyanate groups that disappear after the foam formation suggesting its complete consumption through the reaction with the hydroxyl groups from the polyol (band located between 3150 and 3600 cm^{-1}). Pristine PUF and PUF nanocomposite spectra show bands at 3150 and 3600 cm^{-1} from N–H stretching, a strong and sharp peak located at 1710 cm^{-1} due to the stretching vibrations of the C=O and the bands between 1540 and 1517 cm^{-1} , attributed respectively to C–N and N–H of the urethane groups, confirming the formation of urethane and urea groups [1]. In the spectra of the PUF nanocomposite, the band located between 3200 – 3600 cm^{-1} region is narrower, with high intensity at 3250 cm^{-1} . This could be explained by possible interactions between fillers and MDI, as reported by Gama et al [2]. The 1595 cm^{-1} absorption peak is caused by the vibration of C=C in benzene ring from graphene and MDI structure and the strong peak around 1100 cm^{-1} from the ether bond C–O–C stretch. It is worthwhile to note the difficulty related with the identification of the GBMs in the PUF nanocomposites, not only due to the overlap of the bands of these fillers and the polymer, but also due to its low content when compared with the polymeric matrix [1–3].

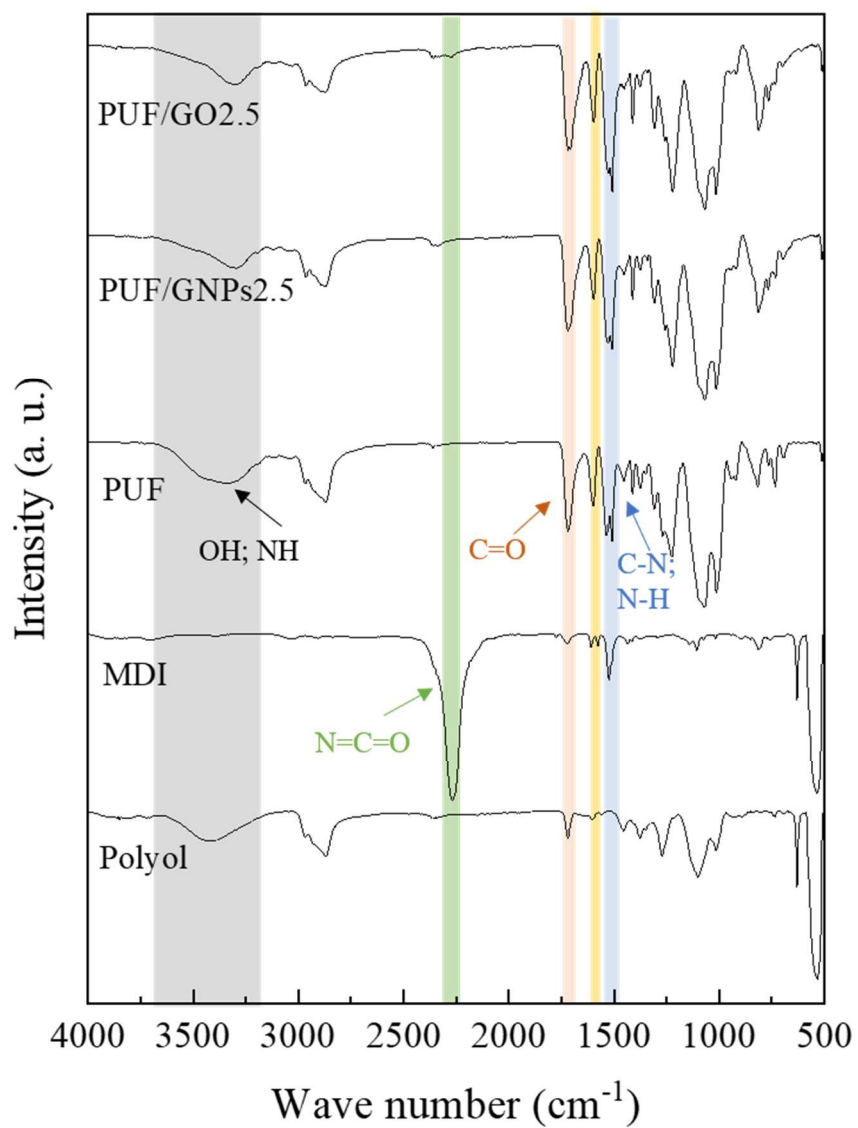


Figure S3. 1Normalized FT-IR spectra of MDI, Polyol, PUF, PUF/GNPs2.5 and PUF/GO2.5.

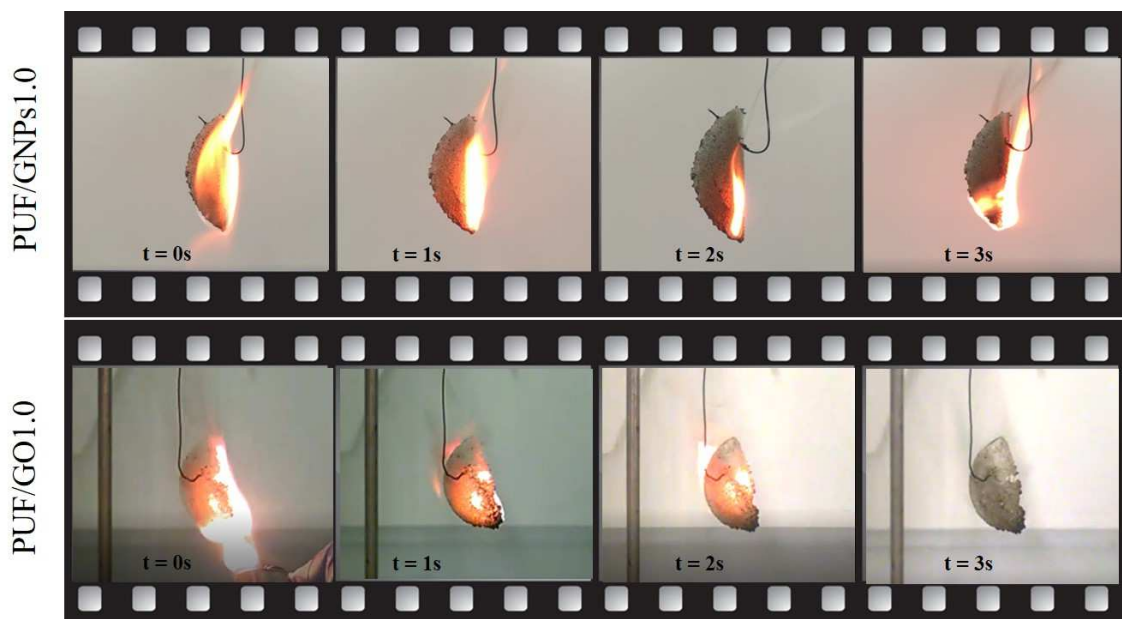


Figure S3. 2 Flame response of PU/GNPs1.0 and PU/GO1.0.

The difference in the thermal stability of GBMs-filled foams opposed to unfilled PUF was in the weight loss percentage associated to each step. A slight weight loss before 160 °C was verified for all the specimens corresponding to adsorbed water evaporation. The second stage of weight loss (around 25%), in the temperature range between 250 to 380 °C, is mainly attributed to the break of urethane bonds and precursors, such as polyols and isocyanates release. From 500° to 620 °C, there is a third weight loss from the oxidative decomposition of isocyanate and aromatic compound and CO₂, HCN or NO₂ formation [4–7].

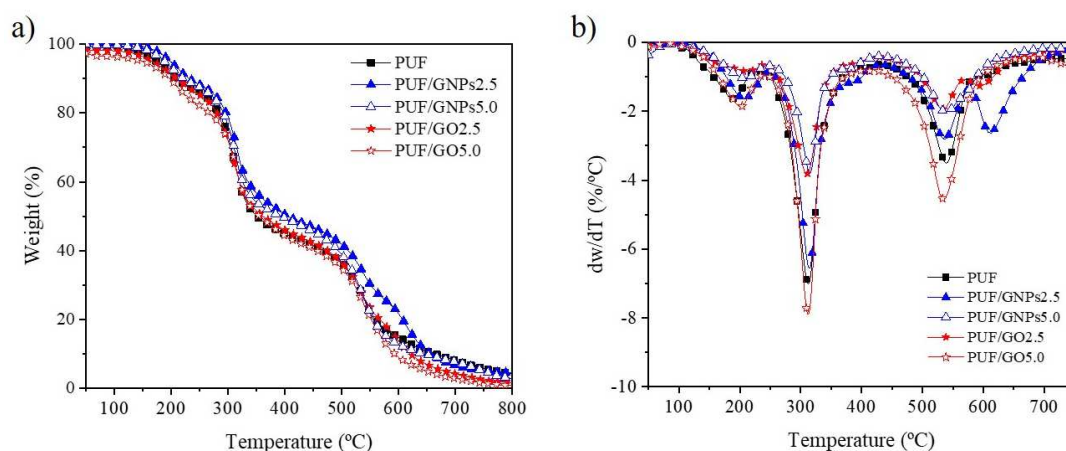


Figure S3. 3 TG and (a) DTG (b) curve of PUF with different GBMs additives (under oxidative atmosphere).

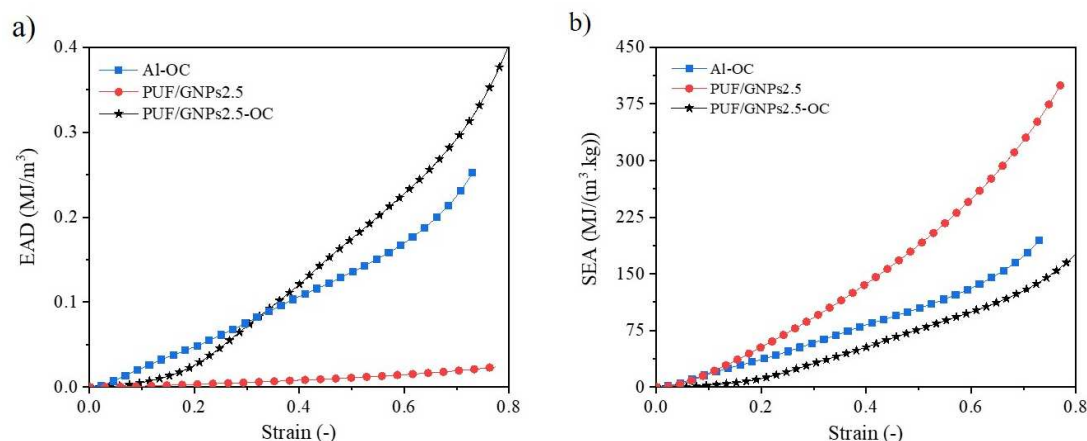


Figure S3. 4 EAD (a) and SEA (b) curves of OCF; PUF/GNPs2.5 and HS-PUF/GNPs2.5.

References

- [1] N. Gama, R. Silva, A. P. O. Carvalho, A. Ferreira, and A. Barros-Timmons, “Sound absorption properties of polyurethane foams derived from crude glycerol and liquefied coffee grounds polyol,” *Polym. Test.*, vol. 62, pp. 13–22, 2017.
- [2] N. V Gama et al., “Enhancement of physical and reaction to fire properties of crude glycerol polyurethane foams filled with expanded graphite,” *Polym. Test.*, vol. 69, pp. 199–207, 2018.
- [3] J. N. Gavvani, H. Adelnia, D. Zaarei, and M. Moazzami Gudarzi, “Lightweight flexible polyurethane/reduced ultralarge graphene oxide composite foams for electromagnetic interference shielding,” *RSC Adv.*, vol. 6, no. 33, pp. 27517–27527, 2016.
- [4] D. K. Chattopadhyay and D. C. Webster, “Thermal stability and flame retardancy of polyurethanes,” *Prog. Polym. Sci.*, vol. 34, no. 10, pp. 1068–1133, Oct. 2009.
- [5] X. Chen, J. Li, and M. Gao, “Thermal Degradation and Flame Retardant Mechanism of the Rigid Polyurethane Foam Including Functionalized Graphene Oxide,” *Polymers (Basel)*, vol. 11, no. 1, p. 78, Jan. 2019.
- [6] P. Acuña, Z. Li, M. Santiago-Calvo, F. Villafañe, M. Rodríguez-Perez, and D.-Y. Wang, “Influence of the Characteristics of Expandable Graphite on the Morphology, Thermal Properties, Fire Behaviour and Compression Performance of a Rigid Polyurethane Foam,” *Polymers (Basel)*, vol. 11, no. 1, p. 168, Jan. 2019.
- [7] E. Ciecierska, M. Jurczyk-Kowalska, P. Bazarnik, M. Kowalski, S. Krauze, and M. Lewandowska, “The influence of carbon fillers on the thermal properties of polyurethane foam,” *J. Therm. Anal. Calorim.*, vol. 123, no. 1, pp. 283–291, Jan. 2016.